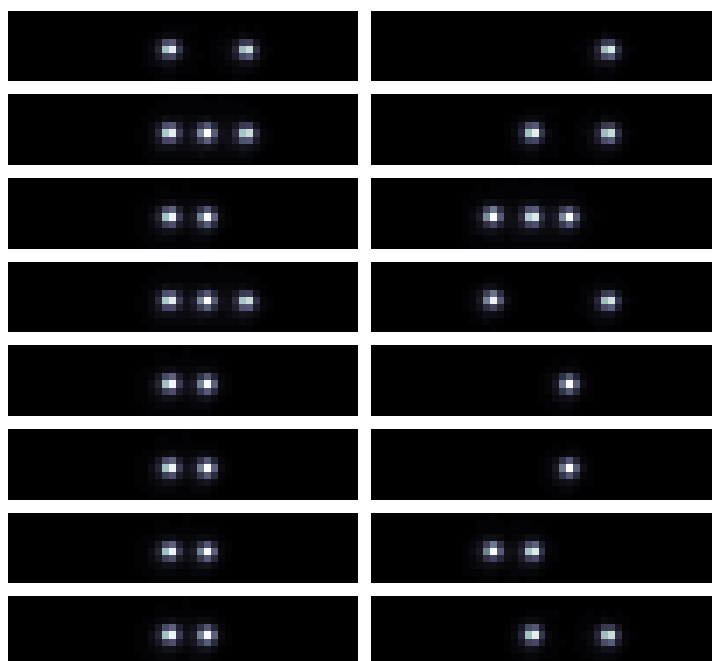

High Fidelity Readout of Trapped Ion Qubits

A thesis submitted for the degree of
Doctor of Philosophy



Alice Heather Burrell

Trinity Term
2010

Exeter College
Oxford

Abstract

High Fidelity Readout of Trapped Ion Qubits

A thesis submitted for the degree of Doctor of Philosophy, Trinity Term 2010

Alice Heather Burrell

Exeter College, Oxford

This thesis describes experimental demonstrations of high-fidelity readout of trapped ion quantum bits (“qubits”) for quantum information processing.

We present direct single-shot measurement of an “optical” qubit stored in a single $^{40}\text{Ca}^+$ ion by the process of resonance fluorescence with a fidelity of 99.991(1)% (surpassing the level necessary for fault-tolerant quantum computation). A time-resolved maximum likelihood method is used to discriminate efficiently between the two qubit states based on photon-counting information, even in the presence of qubit decay from one state to the other. It also screens out errors due to cosmic ray events in the detector, a phenomenon investigated in this work. An adaptive method allows the 99.99% level to be reached in 145 μs average detection time. The readout fidelity is asymmetric: 99.9998% is possible for the “bright” qubit state, while retaining 99.98% for the “dark” state. This asymmetry could be exploited in quantum error correction (by encoding the “no-error” syndrome of the ancilla qubits in the “bright” state), as could the likelihood values computed (which quantify confidence in the measurement outcome).

We then extend the work to parallel readout of a four-ion string using a CCD camera and achieve the same 99.99% net fidelity, limited by qubit decay in the 400 μs exposure time. The behaviour of the camera is characterised by fitting experimental data with a model. The additional readout error due to cross-talk between ion images on the CCD is measured in an experiment designed to remove the effect of qubit decay; a spatial maximum likelihood technique is used to reduce this error to only $0.2(1) \times 10^{-4}$ per qubit, despite the presence of $\approx 4\%$ optical cross-talk between neighbouring qubits. Studies of the cross-talk indicate that the readout method would scale with negligible loss of fidelity to parallel readout of $\sim 10\,000$ qubits with a readout time of $\sim 3\,\mu\text{s}$ per qubit.

Monte-Carlo simulations of the readout process are presented for comparison with experimental data; these are also used to explore the parameter space associated with fluorescence detection and to optimise experimental and analysis parameters.

Applications of the analysis methods to readout of other atomic and solid-state qubits are discussed.

Acknowledgements

I am extremely grateful to my supervisor Dr David Lucas who has collaborated with me on the readout work presented in this thesis. He has provided me with invaluable help and guidance during my time at Oxford, and I would also like to thank him for his enthusiasm and helpful comments and suggestions while proof-reading this thesis. I would also like to thank Professors Andrew Steane and Derek Stacey for all their advice, on both matters of research and of teaching. I am also grateful to Derek Stacey for comments on chapters 3 and 4. I feel very fortunate to have had the guidance of three such inspirational mentors during my time at Oxford.

This thesis would not have been possible without the work of all the members of the Oxford ion-trap group who have built the experiment up to what it is today. I would like to thank both past group members and also those who I have had the pleasure of working with since I joined the group;- Dr. Jonathan Home, Dr. Nicholas Thomas, Dr. Eoin Phillips, Dr. Ben Keitch, Dr. Gergely Imreh, Dr. Simon Webster, Dr. Jeff Sherman, Dr. David Szwer, Dr. Michael (Spike W.) Curtis, David Allcock, Norbert Linke and more recently Tom Harty and Hugo Janacek. Thank you all for the advice and for conversation over tea. In particular I would like to mention David Szwer who has also collaborated with me on readout work: his work on readout in $^{43}\text{Ca}^+$ is mentioned in this thesis and I am grateful for his help with apparatus descriptions (his thesis is copiously referenced in chapter 2). I worked with Norbert Linke and Jeff Sherman on assembly of the gold-on-alumina MicroTrap (“Serious Microtrap Business”); I would also like to thank Paul Pattinson and Peter Clack for technical assistance on this project.

Thanks also go to Graham Quelch for technical assistance, and to Rob Harris and all of the team in the research workshop for help and advice with machine work. I am grateful to Andor for the loan of a “demo” camera, with which a large quantity of data in this thesis was taken. Thanks are due to Dominic Ford and Ross Church for writing and providing support for the PyXPlot plotting package which produced most of the graphs in this thesis.

Finally, I thank my husband Christian, and my family and friends for all their love, encouragement and support throughout.

Contents

Abstract	iii
Acknowledgements	v
1 Introduction	1
1.1 Quantum computation in ion traps	1
1.1.1 Fidelity and speed of computation	8
1.1.2 Other progress with trapped ions	8
1.2 Qubit readout in other architectures	10
1.2.1 Neutral atoms	11
1.2.2 Superconducting qubits	12
1.2.3 Quantum dots	16
1.2.4 Atomic impurities in semiconductors	18
1.2.5 Rare-earth ions in solid-state hosts	19
1.2.6 Linear optics/photonics	20
1.2.7 NMR	21
1.3 Structure of this thesis	22
2 Apparatus	27
2.1 Linear Paul trap	27
2.2 Calcium	30
2.3 Lasers	32
2.4 Imaging system	35
2.4.1 Imaging system A	36
2.4.2 Imaging system B	37
2.4.3 Imaging system C	38
2.5 Experimental control	42
2.5.1 Photon counting	43
3 Ion readout by time-resolved photon counting	47
3.1 Readout of qubits in calcium	47
3.1.1 $^{40}\text{Ca}^+$ Optical qubit	47
3.1.2 $^{40}\text{Ca}^+$ Zeeman level qubit	49
3.1.3 $^{43}\text{Ca}^+$ hyperfine qubit	50
3.2 Analysis techniques	52
3.2.1 Quantifying the readout error	52
3.2.2 Threshold method	53
3.2.3 Maximum likelihood method	57
3.2.4 Adaptive maximum likelihood method	60
3.3 Simulations	63
3.3.1 Justifications for analysis approximations	64
3.3.2 Sensitivity to analysis parameters	68

3.3.3	Dependence of error on experimental parameters	69
3.4	Conclusions for photon counting readout	76
4	Time-resolved photon counting experiments	77
4.1	Investigating non-Poissonian dark counts	77
4.2	Ion readout experimental methods	82
4.3	Accounting for systematic errors	86
4.3.1	Imperfect population preparation	86
4.3.2	Dark to bright transitions	88
4.3.3	Bright to dark transitions	89
4.4	Results and analysis	95
4.4.1	Threshold method	96
4.4.2	Maximum likelihood method	97
4.4.3	Adaptive maximum likelihood method	101
4.5	Comparison with double measurement schemes	102
4.6	Summary of experimental readout results	108
5	Ion readout using a CCD camera	111
5.1	EMCCD cameras	111
5.1.1	Noise sources in the camera	113
5.1.2	Comparison with other detectors	116
5.1.3	Count distributions from the camera	118
5.2	Analysis techniques	122
5.2.1	Selecting a “region-of-interest” in an image	122
5.2.2	Single exposure: spatial resolution	123
5.2.3	Multiple exposures: spatial and temporal resolution	126
5.2.4	Extension to multiple ion readout	129
5.2.5	Quantifying the readout error	132
5.3	Simulation methods	133
5.3.1	Obtaining thresholds from simulated distributions	133
5.3.2	Monte-Carlo simulations	135
6	CCD readout experiments	137
6.1	Experimental methods	137
6.1.1	Characterisation of camera properties	140
6.2	Single qubit, single exposure experiment	142
6.3	Single qubit, multiple exposure experiment	147
6.4	Four ion “qunybble” experiment, single exposure	151
6.5	Simulations	158
6.5.1	Changing cross-talk (ion separation)	159
6.5.2	Spatial resolution on the CCD	160
6.5.3	Discussion of photon arrival rates and exposure times	165
6.5.4	The EMCCD in photon-counting mode	166
6.5.5	Imaging ions in a surface trap	167
6.6	Conclusions for EMCCD readout	169
7	Conclusion	175
7.1	Scalable readout of trapped ions	175
7.1.1	Towards a large-scale architecture	176
7.2	Application of methods to other ions	178
7.2.1	Direct readout of an optical qubit	179
7.2.2	Readout of hyperfine qubits	180
7.3	Application of methods to other systems	185

7.3.1	Neutral atoms	185
7.3.2	Superconducting qubits	185
7.3.3	Quantum dots	186
7.3.4	Atomic impurities in semiconductors	186
7.4	Measurement-based quantum computation	186
7.5	Final remarks	187
A	Monte-Carlo Simulation Code	189
B	Photon counting publication	191
C	CCD camera publication	197

Chapter 1

Introduction

1.1 Quantum computation in ion traps

The smallest unit of classical information is a “bit” which can have the value 0 or 1. It could perhaps represent the answer to a simple true-or-false question. We can encode much more complicated information in this binary representation, and indeed this is how information is stored in a classical computer. Computations proceed by operating on the bits with a succession of logic gates. Such gates may, for example, flip the state of a bit dependent on the state of a different “control” bit. After the computational sequence has finished, we can examine the states of the bits to see how the information contained within them has changed. These computations proceed according to classical laws of physics.

Nature has provided a much more powerful way to represent information: as quantum bits, or “qubits”. These qubits obey the laws of quantum mechanics and can exist in a “superposition” of the states $|0\rangle$ and $|1\rangle$ (in contrast, the classical bit can only be in one of these states at any time). Manipulating this quantum information to perform a quantum computation (QC) was suggested by Feynman [1] and Deutsch [2]. If built, a quantum computer could exploit the quantum phenomena of superposition and entanglement between qubits to perform certain kinds of computations very much faster than a classical computer.

Historically the first well-defined algorithm for a quantum computer which gave a speed-up over classical computation was the Deutsch-Josza algorithm, a toy problem proposed by David Deutsch and Richard Josza [3, 4]. Many other algorithms have

followed, among them are Shor’s factoring algorithm [5, 6] (notable as it offers an exponential speed-up in the time taken to break the RSA cryptosystem¹), and Grover’s search algorithm [8] which reduces the time taken to search an unsorted database with N entries from $O(N)$ to $O(\sqrt{N})$. Quantum computers themselves were first suggested by Feynman in the context of simulating quantum systems, a task which is difficult classically since the complexity increases exponentially as particles are added to the system. A related area (although not strictly a quantum computation) is the use of a quantum system to exchange a *guaranteed* secure key for encrypting communication, suggested by Bennett and Brassard [9]. Quantum cryptography provides absolute secrecy in a way which is not possible classically.

Ion trapping is currently one of the most promising systems with which to realize a quantum computer, being the most technologically mature to-date [10] with some simple algorithms already demonstrated. A comprehensive review of the area has recently been published by Häffner *et al.* [11]. Qubits are encoded in two of the internal electronic states of ions which are held under vacuum in free space confined by electric (and possibly also magnetic) fields.



Figure 1.1: A linear Coulomb crystal of trapped $^{40}\text{Ca}^+$ ions held in a linear Paul trap.

DiVincenzo identified a list of five requirements which a physical system must satisfy in order to build a universal quantum computer [12]. These requirements are summarised below, with brief details of how each need is met in an ion-trap quantum computer.

A scalable physical system with well characterised qubits

As already mentioned, long-lived internal states of the ions are used to store the qubits. The exact choice of states to store the qubit depends on the details of the atomic energy-level structure which depends on the choice of ion. Various possible qubits are discussed in section 3.1 for calcium ions (currently used in our group at Oxford); other alkali earth ions (e.g. Sr^+ , Ba^+) have a similar level structure.

A small qubit register can be created by holding many ions in the same trap and

¹RSA cryptography [7] relies on the fact that it takes a classical computer an unfeasibly long time to factorise a large number into its prime factors.

adjusting the trapping potentials to form them into a (linear) crystal, figure 1.1. This approach is only satisfactory for small numbers of ions: with too many ions the vibrational mode structure becomes too complicated and the mass of the string becomes large. One approach which could avoid these problems is that of holding small groups of ions in separate traps, possibly created in microscale segmented architectures which can support multiple trapping zones [13, 14], see for example figures 1.2 and 1.3. Ions can then be shuttled between trapping zones, with groups of ions being merged and separated. Rowe *et al.* [15] experimentally demonstrated shuttling of ${}^9\text{Be}^+$ ions over 1.2 mm in approximately $50\,\mu\text{s}$ while preserving the coherence of a qubit stored in the internal hyperfine states. They also demonstrated splitting of ion strings, albeit slowly ($\sim 10\,\text{ms}$) and with some heating of the ions' motional state, problems later overcome by Barrett *et al.* [16]. Transport through junctions and around corners has also been implemented, first by Pearson *et al.* with charged micro-particles [17], and later with Cd^+ ions by Hensinger *et al.* [18].

The community has not yet reached a consensus as to the optimum fabrication methods for these microscale traps and work on their development continues through several collaborations and involving many research groups including our group at Oxford.

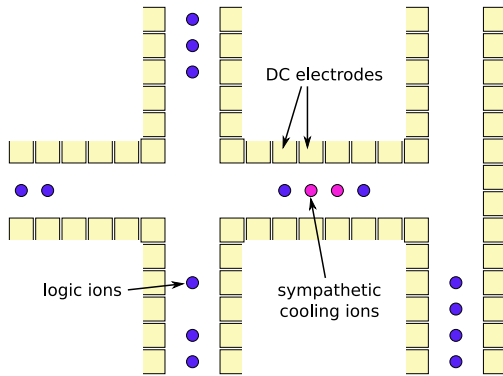


Figure 1.2: Schematic of a multi-zone ion trap similar to the one envisioned by Wineland *et al.* [13] and Kielpinski *et al.* [14].

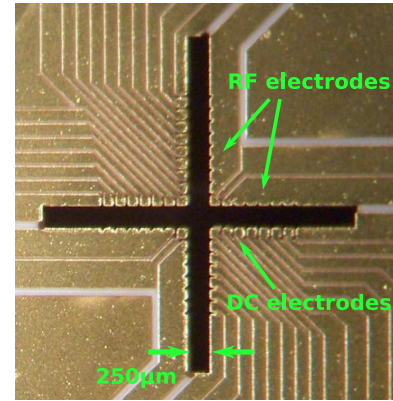


Figure 1.3: Photograph of the upper surface of an assembled multi-zone gold-on-alumina “cross” trap (fabricated by the EU MicroTrap consortium).

The ability to initialise the state of the qubits to a simple fiducial state, such as $|000\dots\rangle$

Preparation of the ions into a well-defined state is achieved with optical pumping, a method first suggested by Kastler [19], and later demonstrated by Brossel *et al.* [20] and

Hawkins and Dicke [21]. The method involves using light to pump the atomic population to a higher internal level from which it can decay to a “dark” state not addressed by the laser. Roos *et al.* achieved a fidelity of 99.9% using frequency-resolved excitation on the quadrupole transition in $^{40}\text{Ca}^+$ to prepare the ion in one of the Zeeman ground states [22].

Long decoherence times, much longer than the gate operation time

For successful computation, the quantum information stored in the qubits must remain “coherent” for a reasonable time: long enough so that gates can be performed between qubits before the information is lost. Qubits stored in the ground-level hyperfine “clock” states of ions (which are independent of the external magnetic field to first order) exhibit some of the longest coherence times measured. Our group has measured a coherence time of 1.2(2) s for a qubit in the $S_{1/2}$ clock states of a $^{43}\text{Ca}^+$ ion; using the spin-echo technique to “re-phase” the internal state, the coherence time was estimated to be ≥ 45 s [23]. Langer *et al.* [24] achieved a decoherence time of 14.7(1.6) s for the clock states in $^9\text{Be}^+$ without a spin-echo. These decoherence times are orders of magnitude longer than typical gate times of 10^{-5} – 10^{-4} s (see below).

A “universal” set of quantum gates

A “universal” set of quantum gates allows one to perform any unitary quantum operation within the system’s computational space. Several different decompositions can be chosen, but a set comprising arbitrary single-qubit gates and a single entangling two-qubit gate would be sufficient, providing the gates can be applied repeatedly between arbitrary pairs of qubits [25].

Single qubit gates can be accomplished by driving Rabi oscillations between qubit states by application of laser light, microwaves or radio waves.

Since ions couple strongly via the Coulomb interaction, they share collective motional modes. The motional state of the ion string can be used as a quantum bus to transfer information between the ions and entangle their internal states. Various protocols exist to realise a quantum gate between the ions which use the bus to mediate a phase shift or bit-flip.

The first two-qubit gate to be proposed for trapped ions was the Cirac-Zoller gate

[26]. A laser pulse maps information from the first ion into the motional state of the ion string, a second laser pulse performs a phase shift on the second ion that is conditional on the ions' collective motional state followed by a final laser pulse which maps information in the motional mode back onto the first ion; the net result is a phase gate between the two ions.

The original proposal requires single ion addressing and cooling of the ions to their motional ground state. Other gates have since been proposed which relax these requirements and are less technically demanding, for example the Mølmer-Sørensen gate [27] and the geometric phase gate [28] (although all gates have their different strengths and weaknesses [11]). Benhelm *et al.* [29] have performed a Mølmer-Sørensen gate operation between “optical”² qubits stored in two $^{40}\text{Ca}^+$ ions with a fidelity of 99.3(1)% in 50 μs , the highest gate fidelity achieved to date. Our group has performed a geometric phase gate between two $^{40}\text{Ca}^+$ ions with a fidelity of 83(2)% in 88 μs (see Home *et al.* [30]), while Leibfried *et al.* [28] report a fidelity of 97% in 39 μs to entangle two Be^+ ions in a Bell state with a similar gate.

Some laserless gates have been proposed, for example magnetic field mediated gates [31] or long wavelength microwave/radio-frequency (RF) mediated gates [32, 33] which eliminate spontaneous photon scattering (a source of decoherence in laser mediated two qubit gates).

Selective addressing of single qubits and pairs of qubits must be possible within the string in order to perform gates on specific ions. For gate times to be as fast as possible the frequencies of the ions' motional modes in the trap must be high. To achieve this, the trapping potential must be tightly confining, meaning the ions in a string will be very close together. For laser driven gates, this amounts to a requirement that the laser must be tightly focused; for single-qubit gates the spot size must be smaller than the ion-ion separation. Alternately the distance between ions can be increased by weakening the trap [34], or by physically separating and shuttling ions in a multi-zone trap [35]. For longer wavelength radiation (microwaves or RF) discrimination must be obtained by frequency selectivity. This could be achieved by shifting the resonance of a particular qubit relative to the others by using a focussed laser to apply different light shifts to ions receiving differing intensities [36, 37] or by applying a magnetic field gradient across the

²See section 3.1.1 for a description of this qubit

whole ion string to shift the resonances relative to each other [32]. Individual and pairs of qubits could also be addressed by using near-field microwaves [31] whose size scale is proportional to the size of the current-carrying waveguides producing them (typically $\sim 40\ \mu\text{m}$), rather than the much larger microwave wavelength.

A qubit-specific measurement capability

It is the fifth DiVincenzo requirement which is the topic of this thesis. In ion traps measurement occurs by the process of resonance fluorescence, whereby radiation is applied that couples one qubit state to a short-lived auxiliary level via a closed transition, while not coupling to the other qubit state. As a consequence, ions in the state which is coupled to the transition will fluoresce, while the ions in the alternate qubit state appear dark; discrimination between the two is by detection of the scattered photons. We define the fidelity of the measurement as $\mathcal{F} = 1 - \epsilon$, where ϵ is the probability of determining the state incorrectly. Fidelities greater than 99% are routinely achieved [38, 39, 35, 29, 40]; the fidelity is usually limited by the rate at which population in the “dark” qubit state is off-resonantly pumped to the “bright” manifold or vice versa. The discrimination methods implemented in this thesis allow higher fidelities (99.99% in an average of $145\ \mu\text{s}$) to be attained by identification of some occasions where this pumping has occurred (chapters 3 and 4) [41].

A variation on the basic resonance fluorescence method was implemented by Hume *et al.* [42] who measure a single qubit state indirectly via an ancilla ion held in the same trap. The qubit is stored in an $^{27}\text{Al}^+$ ion. Laser pulses are used to entangle the state of the $^{27}\text{Al}^+$ ion with the state of a $^9\text{Be}^+$ ancilla ion via the collective motional mode, after which the state of the $^9\text{Be}^+$ ion is detected by resonance fluorescence as usual; this performs a projective measurement on the $^{27}\text{Al}^+$ qubit. The scheme is arranged to be quantum non-demolition (QND): the collapsed state in the $^{27}\text{Al}^+$ ion is preserved and the mapping to the ancilla can be repeated, followed by a further detection step. Using an adaptive method, they achieve an average fidelity of 99.965% in an average of 6.54 sequence repeats (each repeat takes $\approx 1.83\ \text{ms}$).

For simultaneous measurement of all qubits in a string of ions, the whole string can be illuminated with the resonance fluorescence lasers and photons counted using a CCD camera. Haljan *et al.* [37] achieve 97% fidelity to determine the state of a two-ion string

of $^{111}\text{Cd}^+$ in 15 ms (limited by readout electronics). Acton *et al.* [39] achieve a fidelity of 98% based on readout of a three-ion $^{111}\text{Cd}^+$ string. Multiple qubit readout is also investigated in this thesis (chapters 5 and 6), a fidelity of 99.99% is possible for a four ion $^{40}\text{Ca}^+$ string [43].

For selective readout of an individual qubit within a string similar considerations apply as for qubit-specific single-ion gates (above): the separation between ions can be increased to make individual laser addressing easier [16]. An alternate method is to “hide” ions that one does not wish to measure by mapping those qubits to a quantum state not addressed by the detection lasers [44, 45].

An alternate readout method has been proposed by Stock and James [46] which would allow readout on a nanosecond timescale. The scheme involves a state-dependent ionisation of the Ca^+ ions, followed by subsequent detection of the ejected electron. Monochromatic light at 397 nm, 383 nm or 403 nm results in four-photon ionisation from the ground state, while excitation of the other (optical) qubit state is highly suppressed. The separated electron is unstable in the trapping potential (which is effectively a mass filter [47]) and is ejected; the potential can guide the electron towards a high efficiency detector. Fidelities above 99% in 3 ns are estimated, although the remaining Ca^{2+} ion may be lost.

DiVincenzo identified two additional criteria which are relevant to the construction of a quantum network:

The ability to interconvert stationary and flying qubits

The ability to faithfully transmit flying qubits between specified locations

These criteria recognise the need for high-fidelity transmission of quantum information over relatively large distances at high speeds; this is relevant to transfer of information within a quantum computer and is also necessary for secure key distribution in quantum cryptography. Photons can act as flying qubits as quantum information can be stored in (for example) their polarisation state; low-loss polarisation-preserving optical fibres can transmit the photonic qubits over long distances. Transfer of quantum information between photons and ions (stationary qubits) is possible by coupling the ion to the radiation field in a high-finesse cavity [48].

1.1.1 Fidelity and speed of computation

For a successful quantum computation, the requirements above not only have to be fulfilled, but all operations have to be performed fast and with high fidelity. Some errors can be corrected by the application of fault-tolerant quantum error correction (QEC) protocols, but nevertheless a certain “fault-tolerant threshold” for all operations must be attained to make this possible [49]. Lower fidelities can be tolerated by encoding one logical qubit over several physical qubits; the penalty is a large overhead in the number of physical qubits required [50].

The speed of operations is important: slow operations not only result in a long computational time but also increase the time that idle qubits must be kept coherent. The adaptive techniques for high-fidelity detection described in chapter 3 are an important tool to reduce measurement time. Performing many operations in parallel is also an important way to reduce computational time [49]; chapter 6 presents work on single-shot simultaneous readout of a multi-qubit register.

The relevant timescales for comparison with the readout time are the coherence times T_1 and T_2 for a qubit. The T_1 time describes the lifetime of the populations of the two qubit states. In the optical qubit in Ca^+ , this is given by the lifetime of the upper qubit level against decay to the lower level. T_2 is the time over which the phase relationship between the two eigenstates becomes randomised.

1.1.2 Other progress with trapped ions

All the DiVincenzo requirements for building a quantum computer with trapped ions have been individually met although not all operations have reached a fault-tolerant threshold. Hanneke *et al.* [51] at NIST have demonstrated the combination of all the above requirements (although not at fault-tolerant levels) into a programmable two-qubit quantum processor capable of performing all possible unitary operations on two qubits. The logical qubits were stored in the “clock” states of $^9\text{Be}^+$ ions (these have a long coherence time), with two “refrigerant” $^{24}\text{Mg}^+$ ions held in the same trap. The $^{24}\text{Mg}^+$ ions could be laser-cooled near to their ground state of motion without affecting the coherence of the qubits in $^9\text{Be}^+$; the cooling of the collective motional mode means that the $^9\text{Be}^+$ ions are sympathetically cooled, minimising logic gate errors due to heating. The four-ion string could be deterministically ordered to have the $^9\text{Be}^+$ ions at the

ends of the string [52]. The mean fidelity of the output states produced was 79.1(4.5)%, averaged over 160 different operations on random input states. The same research group (see Home *et al.* [53]) have also combined one- and two-qubit logic gates with transport, separation and recombination of ions in a linear multi-zone Paul trap. In one repeat of a process \hat{U} , each of the ${}^9\text{Be}^+ - {}^{24}\text{Mg}^+$ pairs travelled a total distance of $960\,\mu\text{m}$. One application of \hat{U} resulted in an entanglement of the two ${}^9\text{Be}^+$ qubits with a state fidelity of 94.0(4)%; two repeats (\hat{U}^2) gave 89.0(4)%.

Some simple quantum algorithms have already been demonstrated. Gulde *et al.* [54] at Innsbruck have implemented the Deutsch-Josza algorithm with a single ${}^{40}\text{Ca}^+$ ion. Chiaverini *et al.* [55] (NIST) have implemented a semiclassical quantum Fourier transform with three ${}^9\text{Be}^+$ qubits in a segmented trap. (The semiclassical version could replace the fully quantum Fourier transform in an implementation of Shor's algorithm and only requires single-qubit operations, conditioned on measurement results.) The same group have also implemented a rudimentary error correction protocol with three ${}^9\text{Be}^+$ qubits [56]; two of the ions acted as ancillae to protect the primary qubit from spin-flip errors introduced to test the implementation. The protocol increased the fidelity of the primary qubit relative to an encoded qubit without correction, although for small errors the protocol reduced the fidelity more than for an unencoded qubit (with no error correction) due to the limited fidelity of the encoding and decoding gates ($\sim 90\%$). Brickman *et al.* [57] at Michigan implemented Grover's search algorithm with two ions, recovering the marked element with an average probability of 60(2)% which exceeds the classical 50% probability.

Simple quantum simulations have also been performed, for example Friedenauer *et al.* [58] have simulated a phase transition in a two-qubit quantum magnet. Interesting quantum states have been constructed: Häffner *et al.* (Innsbruck) [59] created entangled states of up to 8 particles, while several groups have demonstrated teleportation of quantum information between ions. For some groups, this involves a direct two-qubit entangling gate [45, 16], while the group at Maryland [60] used photonic qubits to entangle two ${}^{171}\text{Yb}^+$ ions in separate traps separated by 1 m. The entanglement was heralded with a post-selected fidelity of 89(2)%.

1.2 Qubit readout in other architectures

Several other architectures exist in which a quantum computer could be realised. An overview of each will be given here, including a description of the physical system and the methods for qubit readout. Readout fidelities and times reported in the literature are summarised in tables 1.1 and 1.2 and plotted in figure 1.4 for comparison. I begin by defining some measurement features which will be relevant.

Quantum non-demolition (QND) A QND measurement is one in which there is minimal excess perturbation of the quantum state outside the state collapse required by the measurement postulate of quantum mechanics [61]. Repeated QND measurements should give the same eigenvalue; this repetition can be used to characterise the QND nature of a measurement and a “QND fidelity” can be defined. Examples of measurements which are *not* QND include photodetection (the photonic qubit is absorbed) and readout scenarios where the coupling between qubit and detector results in transitions between the two qubit states during readout.

Weak or strong Measurements do not necessarily have to involve a full collapse to one of the qubit eigenstates. In some cases the coupling strength to the measuring device can be tuned so that only partial collapse results: this is a “weak” measurement; see Michael Curtis’s thesis for an example in trapped ions [62]. For quantum computation a strong measurement is usually required.

Single-shot I define a single-shot measurement as one in which the state of a qubit can be obtained in a single readout step with a reasonable fidelity. In the case of a strong measurement, the single step can involve a state collapse followed by (sometimes repeated) interrogation of the qubit state to integrate enough classical information to discriminate between eigenstates. If a reasonable fidelity cannot be attained without re-preparing the qubit state followed by another measurement then the process is not single-shot; repeated preparations and measurements are not scalable for quantum computation. Unless otherwise stated, the fidelities and processes mentioned in this section are single-shot.

Resonance fluorescence readout of trapped ions consists of interrogation with laser

light which causes a “strong” projection onto one of the qubit eigenstates; scattered photons are collected to obtain classical information to determine the result. Off-resonant excitation of the “dark” qubit state would reduce the QND fidelity: the electron shelving technique for ground state qubits (see section 3.1) is a route to increasing the QND fidelity.

1.2.1 Neutral atoms

Neutral atoms can be confined either by electric and magnetic potentials created by current-carrying structures or by light fields or a combination of the two. Arrays of atoms can be held in optical lattices created by interfering laser beams, or in specially tailored light fields created by microfabricated arrays of optical elements [63]. Two internal states are chosen to store the qubit in a similar manner to trapped ions.

Direct readout of a single atomic qubit by resonance fluorescence (as used in ion readout) does not lead to similarly high fidelities as it is often not possible to scatter enough photons on the optical transition before the atom is off-resonantly excited to the other qubit state. One solution is to remove all atoms in one qubit state from the trap, followed by fluorescence detection to determine which atoms remain. Selective removal of atoms is achieved by a laser resonant with one of the qubit states which creates a radiation force which exceeds the optical dipole force confining the atom. This step is often accompanied by a lowering of the trapping potential to make ejection faster [64, 65]. Fidelities and detection times taken from references [66, 64, 65] which use this scheme are shown in table 1.1 and figure 1.4. Since atoms are removed from the trap during the detection step, the “push-out” scheme does not represent a QND measurement.

A related problem is that of determining which sites in an optical lattice are occupied by an atom. This has applications not only in the “push-out” readout scheme, but also in initial loading of the lattice and when observing subsequent interactions between atoms in neighbouring lattice sites. This issue has been addressed experimentally by Karski *et al.* [67], Nelson *et al.* [68] and Bakr *et al.* [69] by imaging the lattice on a CCD camera and is a subject that we shall return to later in this thesis.

More recently, a state-dependent ionisation scheme for neutral atoms has been demonstrated [70] which is similar to the photoionisation scheme for ions mentioned earlier. Henkel *et al.* hold ^{87}Rb atoms in an optical dipole trap and employ a two-colour

photoionisation process to selectively ionise atoms in one of the hyperfine qubit states. The ejected photoelectron and $^{87}\text{Rb}^+$ are each detected with $\eta = 98.2(2)\%$ by opposing channel electron multipliers. This method is fast ($< 1\ \mu\text{s}$) although necessarily involves qubit loss.

An alternative non-destructive approach to qubit readout is to use a cavity to increase the number of scattered photons collected via the Purcell effect [71]. When the atom is resonant with a cavity mode, the spontaneous emission rate into the cavity mode is increased; this allows enough photons to be collected for state inference before the atom is lost [72]. The atom also gives a state-dependent shift in the resonance frequency of the cavity which can be exploited for readout. Gehr *et al.* [73] measure the transmission and reflection of the cavity with a probe laser and implement the maximum likelihood protocols to be discussed in this thesis (and published in [41]) to achieve 99.92% readout fidelity.

The above protocols use photons to probe the state of atoms in cavities. In a rôle reversal, atoms can be used as probes to detect the photonic state in a cavity. Gleyzes *et al.* [74] demonstrate a measurement of the photon number (0 or 1) in a microwave cavity at 0.8 K by measuring the state of successive Rydberg atoms sent through in a Ramsey-type experiment. This scheme can be extended to the detection of many-photon states, where each atom gives one bit of information about the cavity state [75].

1.2.2 Superconducting qubits

A wide variety of superconducting circuits have been proposed and demonstrated in which one can realize a qubit. The building blocks of such circuits are Josephson Junctions: a thin insulating barrier between two semiconductors across which charge can tunnel. A junction can sustain a tunnelling supercurrent of $I = I_0 \sin(\delta)$, where δ is the phase difference across the junction and I_0 is the maximum (critical current) that the junction can sustain. For $I < I_0$ the junction exhibits no resistance, but for $I > I_0$ the junction becomes resistive and a voltage appears across it (this is often exploited for qubit readout).

When the junction is within a superconducting loop, the value of δ across the junction (and hence I_0) depends on the magnetic flux Φ inside the loop. The quantisation of flux within the loop (in units of $\Phi = h/2e$) is an important phenomenon for the construction

of qubits in such circuits. Josephson junctions also have a capacitance across them which can result in a difference in the number of Cooper pairs of electrons on each side: a charge Q which is quantised in units of $2e$. Q and δ do not commute and are subject to Heisenberg’s uncertainty principle. The types of qubits realised in such circuits fall into three broad categories, depending on which of these variables provides a good quantum number. Clarke and Wilhelm [61] have recently written a review of superconducting qubits.

Decoherence times for superconducting qubits are often short (typically hundreds of ns) but readout and gate times in such systems are also very fast. Qubits from the three main families will be discussed below, along with their relevant readout methods. Gambetta *et al.* [76] classify the measurement methods for superconducting qubits into two sorts: those that involve a fast, strong measurement of the qubit state (some of which involve a sample-and-hold latching technique); and those where the measurement involves a sequence of repeated or weak continuous QND measurements.

Phase qubits

Phase qubits consist of a single current-biased Josephson junction in which the phase δ is a good quantum number. The junction’s inductance and capacitance form an anharmonic “LC” resonator with quantised energy levels labelled $|0\rangle \dots |n\rangle$. For a current I just below I_0 the anharmonic potential can be approximated by a cubic potential; crucially the energy difference between the levels $|n\rangle$ and $|n+1\rangle$ is different for each value of n . The lowest levels $|0\rangle$ and $|1\rangle$ are used to store the qubit.

Readout of the qubit begins by selectively removing population in $|1\rangle$ from the well (the state $|0\rangle$ is ideally not disturbed). The potential barrier to escape from the well is lower for states with higher n and can also be tuned: the barrier height decreases as the bias current I is increased. Population is either removed by driving a microwave transition from $|1\rangle$ to a higher level (which has a higher tunnelling rate) [77], or by a pulse of current which lowers the barrier so that population in $|1\rangle$ can tunnel directly [78]. In the paper by Martinis *et al.* [77], the tunnelling makes the junction switch to the “voltage” state: a non-zero voltage measured across the junction implies the qubit was in state $|1\rangle$.

Alternately the tunnelling of state $|1\rangle$ can result in a difference of flux in the super-

conducting loop by one quantum, as in Ansmann *et al.* [78]. This can then be measured by a dc SQUID. A SQUID is a device consisting of two Josephson junctions in parallel on a superconducting ring. A change in flux in the loop (caused by a nearby qubit for example) will change the critical current I_0 for the SQUID. Readout can either involve finding the change in I_0 (by acquiring an I - V curve) or by biasing the SQUID so that the change in flux caused by the qubit is enough to transfer the SQUID to the voltage state. The final readout step of the SQUID can be slower after the initial tunnelling of the qubit state has been completed.

Although these measurements are of the strong/latching kind, the tunnelling rate can be adjusted to enable measurements with varying strength [79] so that the wavefunction only undergoes partial collapse.

Flux qubits

Flux qubits consist of a superconducting loop interrupted by one or three Josephson junctions. The phase δ (or equivalently, the flux Φ in the loop) is a good quantum number and the two qubit states correspond to the flux in the loop pointing upwards (supercurrent flowing anticlockwise, $|\uparrow\rangle$) and down (supercurrent flowing clockwise, $|\downarrow\rangle$). The flux state of the qubit is detected by a dc SQUID. Lupaşcu *et al.* [80] use the SQUID in a bistable regime to perform a latching readout where the qubit state is mapped onto the inductance of the SQUID which is later measured by interrogation with microwaves.

Bennett *et al.* [81] demonstrate a different sort of flux qubit (an rf SQUID) where the qubit states have the same flux. The state of the qubit is detected by a fast pulse which maps the upper qubit level onto a state with different flux which is then detected by a dc SQUID.

Charge qubits

The first type of charge qubit demonstrated was the “Cooper-pair box” (CPB) [82] which consists of a superconducting island onto which Cooper-pairs of electrons can tunnel; accordingly the charge Q is a good quantum number for these circuits. The qubit states correspond to the number of Cooper-pairs on the island, e.g. 0 and 1. CPBs are susceptible to decoherence from charge noise. More advanced qubits have since been developed, such as the “transmon” [83] and “quantronium” [84] qubits, although these

would more properly be described as charge-phase qubits.

A wide variety of methods have been developed for reading out charge qubits. A more comprehensive list of methods is given in the review by Girvin *et al.* [85].

A measurement of the weak continuous sort was demonstrated on a CPB by Wallraff *et al.* [86]. The qubit was non-resonantly coupled to a transmission line resonator; the cavity showed a shift of resonance frequency dependent on the qubit state which was probed by measuring the phase and amplitude of coherent microwaves transmitted through the cavity.

Aassime *et al.* [87] study the radio-frequency single-electron transistor (rf-SET) as a readout device for charge qubits in a CPB. The rf-SET is a sensitive electrometer which can continuously measure the charge in a CPB (see Lehnert *et al.* [88]) although the coupling can cause transitions to occur between the qubit states. This “backaction” is assessed in [87]. Astafiev *et al.* [89] electrostatically decouple the rf-SET from their qubit by using a separate readout pulse to transfer charge from the qubit to a separate charge trap where it remains for $\sim 300 \mu\text{s}$ and can be measured by the SET.

Many of the superconducting readout methods that have been described utilise the switching of Josephson junctions or SQUIDS to the “voltage” state; in this state energy is deposited, often near to the qubit. Although measurement times can be small with such systems, there can be a long $\sim 1 \text{ ms}$ “reset-time” following readout as one must wait for equilibrium to be restored [90, 61]. The Josephson bifurcation amplifier (JBA) [91] overcomes these limitations as the readout is dispersive and the junction always remains in the zero-voltage state; there is no heating and so repetition rates can reach 10 MHz [92].

The JBA is a non-linear resonator which has two metastable oscillation states with different amplitudes and phases. The JBA can be made to bifurcate between the two states depending on the state of a nearby qubit. In Siddiqi *et al.* [92] the JBA comprises a Josephson junction with a capacitor connected across it. A “sampling” pulse of current causes the JBA to bifurcate depending on the quantonium-qubit’s state. The current is then reduced but the state of the JBA then remains latched for a further period during which it is repeatedly interrogated with microwaves to determine its state. Boulant *et al.* [93] quantify to what extent a measurement of this sort is QND.

A similar system was used by Mallet *et al.* [94] who construct a JBA with a Josephson

junction in the middle of a coplanar waveguide and use it to measure the state of a transmon qubit. The fidelity was limited by relaxation of the $|1\rangle$ state before latching of the JBA could occur: this was improved by mapping $|1\rangle \rightarrow |2\rangle$ with a resonant π -pulse in a similar fashion to the electron-shelving technique used in trapped ions.

The technique employed by Lupaşcu [80] to measure a flux qubit (above) is similar to the JBA method.

Circuit QED

Coplanar waveguides have already been mentioned above in the context of single qubit readout; they can also be employed as a single bus for multiplexed readout of several qubits [95]. Such waveguides are important in superconducting implementations of circuit QED and can be used to couple two qubits [78]. There has been a recent demonstration of the (90%) QND readout of single photons from such cavities [96]. The experiment involved mapping the presence of a single photon in the “storage” cavity onto a transmon qubit using a C-NOT gate (with a 2–3% error), followed by readout of the transmon using a separate readout cavity with a single-shot fidelity of 55%.

1.2.3 Quantum dots

“Artificial atoms” can be built by confining charge carriers in semiconductors to a small spatial region known as a quantum dot. If the region is approximately the same size as the wavelength of the charge carrier, the energy levels inside the dot will be quantised. One technique to manufacture such dots involves the growth of the semiconductor crystal into small islands; another method is to confine a two-dimensional electron gas in the remaining two spatial dimensions by electric fields from electrodes patterned onto the surface of the semiconductor. Adjusting the electrode voltages can tune the energy levels in the dot.

When the quantum dot is populated with one electron, the Coulomb repulsion creates an energy barrier for subsequent electrons to tunnel onto the dot; at low temperature the tunnelling is suppressed, leading to an effective limit on the number of electrons. By tuning the potentials the limit can be set at one or two electrons, depending on requirements. The qubit is usually stored in the spin state of one or two electrons on the dot. Review articles describing the manipulation of spins in such architectures can

be found in [97] and [98].

Qubit measurements can be performed optically or electronically. Optical measurements of single confined spins have been achieved, where differentiation between qubit states is by the detection of photons of a certain polarisation [99] or by monitoring the Faraday or Kerr rotation of a laser beam [100, 101]. Electrical measurements are performed either as a measurement of the current transport through the dot or by sensing the charge on the dot (after a conversion which maps the spin state to the charge); the second of these is more widely used and will be described below for different qubits.

Single quantum dot: single electron spin state

The quantum dot is tuned so that it can support only 0 or 1 electron. When a large magnetic field is applied, the spin states of a single electron on the dot are split in energy and can be used to store a qubit. Elzerman *et al.* [102] used a 10 T field so that $|\uparrow\rangle$ and $|\downarrow\rangle$ formed the ground and excited states of the qubit respectively. For readout, a spin-to-charge conversion was made by tuning the dot potential so that the two energy levels representing the two qubit states were either side of the Fermi energy of the reservoir. This meant that the electron would tunnel off the dot if the qubit was in the excited $|\downarrow\rangle$ state, and remain confined if in the lower $|\uparrow\rangle$ state. A quantum point contact (QPC) was fabricated near to the dot; the current through such a device is dependent on the electrostatic potential from the dot. Steps observed in the current through the QPC indicated the tunnelling of electrons on and off the dot. The current was continuously monitored for ~ 0.11 ms and compared with a threshold to determine the qubit state. Several issues limit the fidelity of this method of spin-to-charge conversion, including thermally activated tunnelling, electrical noise and magnetic fields. The same research group later demonstrated a more robust spin/charge mapping, to be described next.

Single quantum dot: two electron spin state

Hanson *et al.* [103] describe readout of a qubit stored in the two-electron spin state inside a quantum dot. The lower state $|S\rangle$ of the qubit is the antisymmetric “singlet” state $\frac{1}{\sqrt{2}}(|\uparrow\downarrow\rangle - |\downarrow\uparrow\rangle)$. The upper qubit state $|T\rangle$ is the “triplet” state $\{|\uparrow\uparrow\rangle, |\downarrow\downarrow\rangle, \frac{1}{\sqrt{2}}(|\uparrow\downarrow\rangle + |\downarrow\uparrow\rangle)\}$, where one electron must reside in a higher energy orbital due to the requirement that the wavefunction be overall antisymmetric. The magnetic field need no longer be

high to separate the qubit states. Mapping of the qubit state to the charge in the dot is achieved by a difference in tunnelling rates to the reservoir. The potential of the dot is adjusted so that both qubit levels are above the Fermi level and tunnelling is energetically allowed for either state. The tunnelling rate for the triplet state is much higher than for the singlet state; the time allowed for tunnelling is carefully chosen so that if the qubit is in $|T\rangle$ the electrons will most likely have tunnelled out of the dot, while a qubit in $|S\rangle$ will be unaffected. The measurement is completed by a detection of the number of electrons (1 or 2) on the dot by a QPC.

The above measurements are destructive since electrons are necessarily removed from the dot in order to determine the qubit state. Meunier *et al.* [104] note that after the measurement of the singlet-triplet qubit is over and the qubit energy levels are returned to below the Fermi energy, if the dot is left with only one electron then a second will tunnel back in, preferentially to the triplet state (restoring the original qubit state). This realizes a non-destructive qubit measurement (although not strictly QND).

Double quantum dot: two electron spin state

Single electrons in two neighbouring quantum dots can couple by the spin-spin interaction to form singlet and triplet states. Barthel *et al.* [105] demonstrate readout of such a qubit by using a voltage pulse to transfer both the electrons into the same dot [a charge state denoted by (0,2)] if the qubit is in the singlet state. If the qubit is in the triplet state, the electrons remain in the charge state (1,1). The charge state is then detected by sensing a change in conductance of a nearby rf-QPC; the successive voltage readings from the QPC are integrated over a certain time and then a threshold voltage is used to determine the qubit state. The fidelity is limited by relaxation of the state (1,1) during the measurement interval.

Double-dot systems could also be used in principle to make QND measurements of single-electron qubits; the spin-to-charge mapping would then involve moving the electron to the neighbouring dot, rather than allowing tunnelling to the reservoir [98].

1.2.4 Atomic impurities in semiconductors

In common with quantum dots, qubits in these systems are stored in single-spins in semiconductors. Single dopant sites can themselves have nuclear spin, or can act as a

potential trap for electrons or holes. Low concentrations of dopant mean that single-site addressing can be possible. An example of one such impurity is phosphorus dopants in silicon. Morello *et al.* [106] demonstrate the single-shot readout of an electron spin on a P dopant site. Readout is achieved in a similar way to quantum dots: the electron is made to leave the site if it is in $|\uparrow\rangle$, while an electron in $|\downarrow\rangle$ can remain. The charge on the site affects the current through a nearby rf-SET. A spike in the current above a chosen threshold indicates the presence of an electron in $|\uparrow\rangle$ (which tunnelled off, to be replaced by an electron in $|\downarrow\rangle$).

More complicated sites are created from a combination of several impurities, such as the nitrogen-vacancy (N-V) colour-centre in diamond. In this case, a substituted nitrogen dopant is found next to a missing carbon atom. For an electron on the site there exists a ground and excited state, both of which are triplets. The ground state is often chosen to store a qubit, where the $|m_S = 0\rangle$ and $|m_S = \pm 1\rangle$ states are the qubit states. When excited by a resonant laser, fluorescence can be driven between the two $m_S = 0$ states which appear bright, while the other qubit state remains dark. Spin-flips can cause unwanted bright \rightarrow dark transitions; the relaxation of the qubit states can be on the order of 1 s at the low (< 2 K) temperatures used by Wrachtrup *et al.* [107], but at higher temperatures coupling to nearby spins (either N dopants or naturally occurring ^{13}C) can decrease the coherence times [97]. Decay via metastable levels can also cause spin-flips [108]. Various techniques have been proposed to overcome this so that more photons can be detected before a flip occurs; these involve coupling the electron spin to a nearby nuclear spin. The nuclear spin can be used as an ancilla to repeatedly re-set the electron's state [109] or the coupling can be used to decrease the spin-flip rate [108]. A qubit can also be stored in nearby nuclear spins and read out through the N-V centre [110].

1.2.5 Rare-earth ions in solid-state hosts

In this system rare-earth dopant ions are embedded in cryogenic crystals or glasses. These ions have spin and their internal hyperfine ground states can be manipulated to store quantum information; examples include Pr^{3+} or Eu^{3+} dopants in Y_2SiO_5 (yttrium orthosilicate).

Since quantum information can be stored in the hyperfine-split ground level, coher-

ence times can be very long. The dominant source of dephasing is due to the interaction of the rare-earth spins with spins of the yttrium nuclei in the host material. Fraval *et al.* [111] have demonstrated phase coherence times in $\text{Pr}^{3+}:\text{Y}_2\text{SiO}_5$ as long as 82 ms by applying an external magnetic field to minimise the sensitivity of the qubit transition to magnetic field fluctuations; these can be extended further (up to several seconds) by the use of dynamic decoupling techniques [112, 113].

The hyperfine-split ground level of the dopant ions is coupled to an excited state via an optical transition. Since the optical transition is inhomogeneously broadened, sub-groups of ions can be selected based on the frequency of this transition, termed "channels" [114]. The channels are selected with a separation in frequency so that they can be individually addressed with the population in each channel acting as a qubit. The readout process is therefore an ensemble measurement on all ions in a channel; this is similar to the measurements in an NMR implementation (to be described in section 1.2.7), however the scheme does not share the initialisation problems that beset NMR since the ions can be prepared in a pure state by optical pumping.

State detection can be performed using the optical Raman heterodyne technique [115]. Applying a radio frequency (RF) field between the two qubit levels along with an optical field between the upper qubit level and a higher excited state results in the generation of a second anti-Stokes optical field at the sum of these frequencies. The RF beat between the two optical frequencies can then be detected on a photodiode and is proportional to the coherence between the ground qubit levels. Longdell *et al.* [116] have used this method and performed state tomography on several input states in $\text{Eu}^{3+}:\text{Y}_2\text{SiO}_5$ with an average 90% fidelity for preparation and measurement combined.

1.2.6 Linear optics/photonics

Qubits can be encoded in the spatial or polarisation state of photons, or alternatively on the basis of photon location or timing. This scheme is appealing since photons are relatively free of decoherence; the main decoherence source is photon loss which is the closest comparison to T_2 in matter qubits. A review of linear optical quantum computation can be found in [117].

Making two photons interact is a challenge. It was initially thought this would require a strong optically non-linear medium, but a proposal by Knill, Laflamme and Milburn

(KLM) removes this requirement by achieving interactions between two photons using only single-photon sources, detectors and linear optics. The scheme relies on interference with auxiliary photons at detectors, followed by measurements of the ancilla photons and it is non-deterministic: that is, the desired interaction occurs only with a certain probability, although success is often “heralded”. This is in contrast to “push-button” on-demand interactions in other architectures.

The main method of quantum measurement in photonic schemes is photon detection. When detecting the presence/absence of a single photon, the measurement fidelity is dependent on the quantum efficiency (causing photons to be missed) and the “dark counts” of the detector (positive detections when no photon is present). Typical unfiltered detection efficiencies are 85% at 660 nm, with dark counts at $\sim 6\,000\text{ s}^{-1}$ at room temperature, or only 25 s^{-1} at cryogenic temperatures [117]. Superconducting detectors can reach 95% efficiency, but are relatively slow [118]. Not all detectors can measure photon number; most have some recovery time during which subsequent photons are not counted. The KLM scheme requires high-efficiency photon-number discriminating detectors; these are currently being developed, for example the visible light photon counter (VLPC) which has 88% quantum efficiency at 694 nm [119].

Typical photon detection is destructive, however a QND measurement of a photon has been performed by Pryde *et al.* [120]. The destructive polarisation measurement was performed on an ancilla “meter” photon, leaving a propagating “signal” photon in the apparatus. The coupling between the meter and signal photons had been achieved via the KLM protocol, so the measurement was non-deterministic and heralded. The detection fidelities were 97(3)% and 81(4)% for the $|H\rangle, |V\rangle$ polarisation states, and the probability that a measurement of the signal would yield the same result as the meter was 88(5)%.

1.2.7 NMR

The qubits in liquid-state NMR are implemented using the spins of nuclei in complex molecules in a bulk sample ($\sim 10^{20}$ molecules) at room temperature [121, 122]. Computations involve the manipulation of “pseudo-pure states”: mixed states that provide the same signal as pure states to within a constant scaling factor.

Measurements in a liquid-state system are ensemble measurements of the mean mag-

netisation of the whole sample and as such do not form the sort of projective measurements usually involved in quantum computation. The measurement usually proceeds by exciting the qubits with an RF pulse; after a phase correction, the integrated intensity of the signal can be examined to see if there is net absorption or emission and the strength of the signal determines the population in each qubit state. If the qubits are left in a superposition state at the end of the computation, each qubit collapses individually and the measurement returns an ensemble average over all possible answers. It is not clear that one can solve every sort of problem with a measurement like this, but sometimes an algorithm can be re-cast so that the measurement will give a well-defined result [123, 124]. By repeating the computation with various qubit rotations before detection, a full quantum picture of the state can be built up (the density matrix) using “state tomography”, although this is only practical for a few spins.

Despite rapid early progress in the field, prospects for NMR quantum computation are generally thought to be limited. Since selective excitation of qubits is accomplished by separating the transitions in frequency space, the available frequency range soon fills up; this limits NMR implementations to $\lesssim 30$ qubits. A second (although less critical) problem is related to the lack of a projective measurement: it is difficult to selectively re-initialise individual qubits mid-computation, a process which is important for quantum error correction protocols.

1.3 Structure of this thesis

During the course of my doctoral studies I have been involved in other work, mainly concerning apparatus development for the new microfabricated ion traps which are also investigated at Oxford. This included the construction and characterisation of two other imaging systems (of similar design to the imaging systems described in the following chapter) and the installation of a micromotion compensation system. I also made some investigations into calcium neutral fluorescence before loading ions into the Sandia microtrap. This work will not be presented in this thesis, but a description of some of it can be found in my first-year report [126].

I was involved in the assembly of the gold-on-alumina microfabricated “cross” trap (obtained through the EU MicroTrap consortium) together with Norbert Linke. This novel trap features ~ 80 electrodes arranged in four arms which join at a junction (figure

Qubit	readout fidelity	readout time	QND	coherence time		ref.	notes
				T_1	T_2		
Trapped ions	99.990(1)%	145 μ s	✓	1.168 s	~ 1 ms	[this work]	$^{40}\text{Ca}^+$ optical qubit.
	99.965%	11.9 ms	✓	21 s	–	[42]	Adaptive $^{27}\text{Al}^+$ measurement via $^9\text{Be}^+$ ancilla.
	99.925%	3 ms	✓	1.168 s	~ 1 ms	[29]	$^{40}\text{Ca}^+$ optical qubit.
	99.87(4)%	10 ms	✓	35 s	120 μ s	[40]	$^{137}\text{Ba}^+$ optical qubit.
	99.77(3)%	2.4 ms	✓	$\sim 10^3$ s	1.2(2) s	[41, 23]	$^{43}\text{Ca}^+$ ground-state qubit.
	> 99.4%	~ 15 ms	✓	$\sim 10^3$ s	–	[39]	$^{111}\text{Cd}^+$ hyperfine ground-state qubit (single ion ICCD readout).
	99%	200 μ s	✓	$\sim 10^3$ s	–	[38]	$^9\text{Be}^+$ hyperfine ground-state qubits
	97.9(2)%	1 ms	✓	$\sim 10^3$ s	2.5(3) s	[125]	$^{171}\text{Yb}^+$ hyperfine ground-state qubit.
	97%	200 μ s	✓	$\sim 10^3$ s	–	[35]	$^9\text{Be}^+$ hyperfine ground-state qubits
Neutral atoms	99.921(3)%	100 μ s	✓	–	–	[73]	^{87}Rb cavity transmission/reflection.
	99.4(1)%	85 μ s	✓	–	–	[72]	^{87}Rb cavity-enhanced fluorescence.
	99.19(5)%	802(17) ns	×	–	–	[70]	^{87}Rb photoionisation measurement.
	> 99%	~ 500 ms	×	–	–	[66]	Cs “push-out” measurement.
	> 98%	10 ms	×	–	–	[65]	^{87}Rb “push-out” measurement.
	98(1)%	~ 130 ms	×	~ 220 s	16.7 ms	[64]	Cs “push-out” measurement.
Cavity photon	$\sim 99.92\%$	7.8 ms	✓	–	–	[74]	Microwave cavity; Rydberg atom interferometer.

Table 1.1: Readout fidelities, measurement times and coherence times for atomic or photonic qubits in different architectures. Fidelities are quoted as an average for the two qubit states. Coherence times are given where reported. The $T_1 \sim 10^3$ s time for hyperfine qubits in trapped ions assumes a typical time between collisions in UHV which could cause collisional spin flips.

Qubit	readout fidelity	readout time	QND	decoherence time		ref.	notes
				T_1	T_2		
Superconducting	$\sim 98\%$	5 ns*	?	~ 20 ns	–	[81]	Flux qubit.
	$\sim 97\%$	< 30 ns*	?	~ 400 ns	~ 140 ns	[78]	Two coupled phase qubits.
	$\sim 96\%$	250 ns*, 700 ns	✓	$0.5 \mu\text{s}$	$0.4\text{--}0.6 \mu\text{s}$	[94]	Transmon (charge); latched JBA measurement.
	$\sim 95.1(4)\%$	150 ns	88%	~ 470 ns	–	[80]	Flux qubit.
	$\sim 92\%$	25 ns	?	~ 10 ns	–	[77]	Phase qubit.
	$\sim 90\%$	300 ns*	?✓	–	–	[89]	Cooper-pair box (charge); latched rf-SET measurement.
	$\sim 69\%$	250 ns	$\sim 67\%$	$\sim 1.3 \mu\text{s}$	–	[93]	Quantronium (charge); latched JBA measurement.
	$\sim 65\%$	$7.3 \mu\text{s}$	✓	$\sim 7.3 \mu\text{s}$	~ 500 ns	[86]	Cooper-pair box (charge); continuous measurement.
Quantum dots	$\gtrsim 95\%$	$\sim 6 \mu\text{s}$	†?	$34 \mu\text{s}$	27 ns	[105]	Two-electron double quantum dot qubit; charge measurement.
	$\sim 91\%$	$\sim 70 \mu\text{s}$	×	2.58(9) ms	–	[103]	Two-electron quantum dot qubit at 0.02 T; charge measurement.
	$\sim 87\%$	$\sim 20 \mu\text{s}$	91%†	1.8(1) ms	–	[104]	Two-electron quantum dot qubit; charge measurement.
	$\sim 83\%$	~ 0.11 ms	×	$< 0.55(7)$ ms	–	[102]	Single-electron quantum dot at 10 T; charge measurement.
Semicond. spins	$\sim 96\%$	$\sim 100 \mu\text{s}$	×	~ 39 ms	–	[106]	Electron in P-doped Si; charge measurement at $B = 5$ T.
	$\sim 95\%$	5 ms	?	~ 1 s	$< 350 \mu\text{s}$	[107]	Electron in N-V centre at 2 K; optical measurement.

Table 1.2: Readout fidelities, measurement times and coherence times (where reported) for solid-state qubits in different architectures. Fidelities are quoted as an average for the two qubit states. Readout times marked by (*) are state-latching times only and do not include the time taken to read the classical binary answer. Entries marked by (†) indicate a non-destructive measurement which is not necessarily QND by definition.

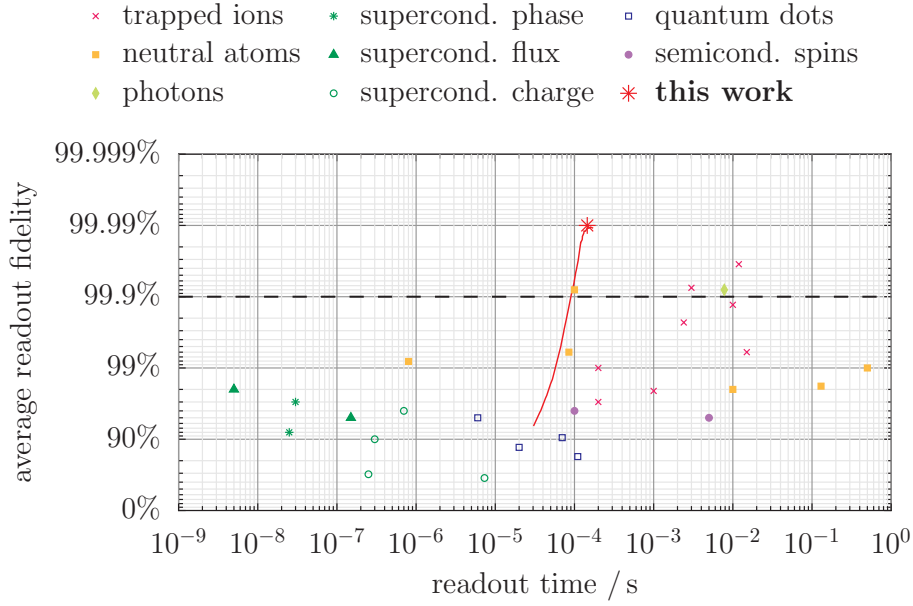


Figure 1.4: Readout fidelities and measurement times for qubits in different implementations, see tables 1.1 and 1.2. The fidelity/time trade-off achieved with the adaptive detection method in this work (chapters 3, 4) is shown as a solid red line. The horizontal dashed line indicates the fidelity required by Steane in [49] for a fault-tolerant quantum computer.

1.3). The trap was designed to test ion shuttling algorithms and was fabricated in a three-layer design which required manual assembly³ using UHV-compatible adhesives. The trap is now under vacuum but has not been tested to date.

This thesis presents only work on high-fidelity readout of trapped ion qubits. Chapter 2 presents the apparatus used in the experiments described in this thesis. Chapters 3 and 4 describe readout of a single trapped $^{40}\text{Ca}^+$ ion by time-resolved photon counting with a photomultiplier tube (PMT); the work was published in [41], which is included here as appendix B. Chapters 5 and 6 describe an extension of the work to readout of a four-ion string using an EMCCD camera, a brief account of which was published in [43], included here as appendix C. Chapter 7 concludes with a discussion of how the methods described in this work might be applied to readout of qubits in other architectures.

³There were also some fabrication issues which required correction before assembly.

Chapter 2

Apparatus

This thesis concerns experiments with $^{40}\text{Ca}^+$ ions at Oxford. The ions are held in a linear Paul trap under ultra-high vacuum (UHV). All optics and detection systems are outside: light enters and leaves the system through viewports on the vacuum can while electrical connections to the ion trap enter via UHV electrical feedthroughs. The main control of the experimental sequence is handled by a PC which can trigger laser pulses and adjust the laser frequencies.

Most experiments with this system involve some manipulation of the atomic population by lasers, followed by a readout of the atomic state by resonance fluorescence. The scattered photons are detected by the imaging optics and recorded by the computer. The readout step is the focus of this thesis.

2.1 Linear Paul trap

Electric fields can be used to confine ions or other charged particles. When trapping neutral atoms, the trapping potential depends on the internal state of the atom. This is not the case with ions so the populations of various internal states can be manipulated while the ion is held tightly confined in a deep trap.

It is not possible to confine ions in all three dimensions using only static electric fields since Gauss's Law states that $\nabla \cdot \mathbf{E} = 0$, meaning that there cannot be a potential minimum in all three directions in free space as the electric potential V must satisfy $\nabla^2 V = 0$. There are two common types of ion trap which confine the ions in different ways: Penning traps and Paul traps. Penning traps confine the ions axially (along z) using a static electric field and the addition of a strong homogeneous magnetic field

in the z direction confines the ions radially by the Lorentz force. Thompson *et al.* discuss work with $^{40}\text{Ca}^+$ in a Penning trap [127]. The high magnetic field results in the ions performing two circular motions and causes relatively large Zeeman shifts which complicate the cooling of ions in the trap.

Paul traps are a more common choice for experiments in ion trap quantum computation, and it is this sort that we use at Oxford. As for the Penning trap, a static electric field is used to confine the ions axially, but the radial confinement is instead achieved with a time-varying radio-frequency (RF) electric field. A diagram of our linear Paul trap is shown in figure 2.1, where the DC endcap electrodes provide the axial confinement along z . The RF electrodes (arranged at the corners of a square) provide an oscillating quadrupole¹ field in the x - y plane. When one pair of electrodes is at a maximum voltage, the ion will be confined along one direction (say, y) but will begin to be expelled along the direction that is anti-trapping (x). At a later time, when the phase of the RF has advanced by π , the opposite will be true: the ion will be confined along x and expelled along y . As the ion starts to accelerate along the anti-trapping direction, the RF field switches to provide a restoring force toward the centre of the trap. Since the electric potential is quadratic, the further the ion gets from the centre of the trap, the greater the restoring force will be. The net result (when averaged over the RF cycles) is that the ion feels a confining “pseudopotential” centred on the null point of the field. This holds the ion at the centre of the trap despite the fact that the oscillating potential averages to zero over time everywhere in the trap. The angular frequencies of the harmonic pseudopotentials confining the ion in the radial and axial directions are denoted ω_r and ω_z respectively and are known as the secular frequencies.

The RF null is along a line down the trap z axis; the ions can be pushed away from this null by stray DC electric fields. Outside the RF null, the oscillating force felt by the ion causes it to perform a periodic movement at the RF frequency, known as “micromotion”. The full motion of the ion is described by the Mathieu differential equations, these are included in many review papers on ion trapping as well as the book by Ghosh [128]. To minimise the micromotion, the static field in the x - y plane can be corrected by applying DC voltages to the compensation electrodes which are shown in figure 2.1, outside the RF electrodes. To detect the micromotion we look for correlations

¹Higher order multipole terms may be present, but the quadrupole term dominates.

between the phase of the RF voltages and the fluorescence photons being scattered by the ion. The scattering rate depends on the detuning of the laser from the transition resonance. As the ion performs micromotion it will see the detuning vary (due to a changing Doppler shift) with the same period as the RF field in which it moves. For our purposes it is important to minimise the ion micromotion in order to maximise the fluorescence signal.

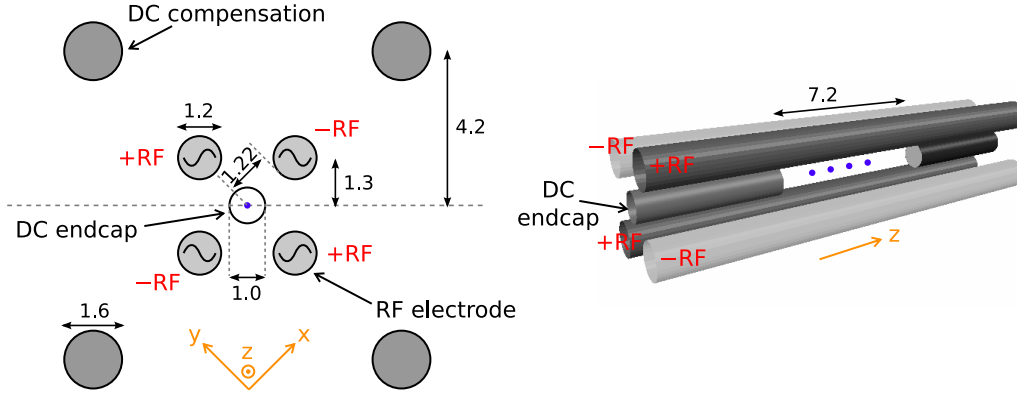


Figure 2.1: LEFT: cross-sectional diagram (to scale) of the electrodes in our linear Paul trap with their dimensions in mm. RIGHT: perspective view of the trap showing only the radio-frequency (RF) electrodes and DC endcaps. The separation between the four trapped ions is exaggerated enormously.

More details of the design of our ion trap can be found in the thesis of Dr Charles Donald [129]. The DC electrodes are held at a positive voltage to confine our positively charged ion, usually 30–700 V. The RF voltages are applied at 6.4 MHz with a typical amplitude of $\approx 170 \text{ V}_{\text{pk-pk}}$. The compensation electrodes normally require $< 100 \text{ V}$. Typical radial and axial frequencies for this trap are $\omega_r/2\pi \approx 0.7\text{--}0.9 \text{ MHz}$ and $\omega_z/2\pi \approx 0.2\text{--}0.8 \text{ MHz}$. When multiple ions are in the trap they arrange themselves so that the Coulomb repulsion between them is balanced by the axial potential they see in the trap. We can alter the radial and axial frequencies of the trap to change the shape of the resulting “Coulomb crystal” that is formed; to create a linear crystal along the axis the trap must be tighter radially than in the axial direction. To create a larger spacing between the ions along the axis for the experiments described in chapter 6 we reduced the axial confinement slightly.

The trap potential is so deep (many eV) that even when ions in the trap are heated (by collisions with background gas, for example) they remain trapped, albeit with a lot of energy so that they are in a large orbit away from the trap centre. It is possible to cool the ions back into the centre of the trap although sometimes this can take several

minutes as cooling is very inefficient: the ions spend very little time in the laser beam and see a very large Doppler shift, making the light far off resonance with the cooling transition during most of the orbit. Anomalous heating of ions has been observed in ion traps, possibly due to noisy patch potentials on the electrodes which are thermally driven. The heating rate was investigated experimentally by Deslauriers *et al.* [130] and found to scale with trap size approximately as r^{-4} where r is the distance from the ion to the nearest electrode surface. Since our trap is large ($r = 1.2$ mm), this heating rate is very low, around ~ 10 quanta s^{-1} (for microfabricated traps the higher heating rate presents more of a challenge).

The ion trap is installed in a stainless steel vacuum can which is maintained at ultra-high vacuum (UHV) by an ion pump and a getter pump. The ion gauge pressure reads around 1.0×10^{-11} Torr (10^{-9} Pa) although pressure gauges are unreliable at such low pressure. The lifetime of an ion in the trap can be as long as days; such long lifetimes are an advantage for the experiments presented in this thesis, where data acquisition often lasted for up to 10 hours.

In order to define a quantisation axis and prevent optical pumping of the ion into dark states [131], a magnetic field of ~ 2 G is applied to the ion by magnetic field coils placed around the vacuum can [132].

Aside from the linear Paul trap described above, other ion traps (including microfabricated designs) are used at Oxford. The only one of these traps mentioned in this thesis in the context of readout is a surface trap in section 6.5.5. Full details of this trap can be found in Allcock *et al.* [133].

2.2 Calcium

Calcium ions are loaded directly into our ion trap by in-situ photoionisation of neutral atoms which emanate from a heated calcium oven pointing towards the trap. The photoionisation is a two-step process: the atoms are first excited to a higher-lying energy level by light at 423 nm, then ionised by light at ≈ 389 nm which excites the electron to the continuum. This scheme is illustrated in figure 2.2(a). The first stage can be used to predominantly excite one particular isotope (the transitions for different isotopes differ in frequency slightly due to the isotope shift) and hence preferentially load a certain isotope, such as $^{43}\text{Ca}^+$ [134]. The experiments in this thesis were done with $^{40}\text{Ca}^+$

which has the highest natural abundance and so is relatively easy to load. The $^{43}\text{Ca}^+$ isotope is used in other experiments at Oxford but was not used for the experiments presented in this thesis. A readout method for qubits stored in $^{43}\text{Ca}^+$ is described in section 3.1 for completeness.

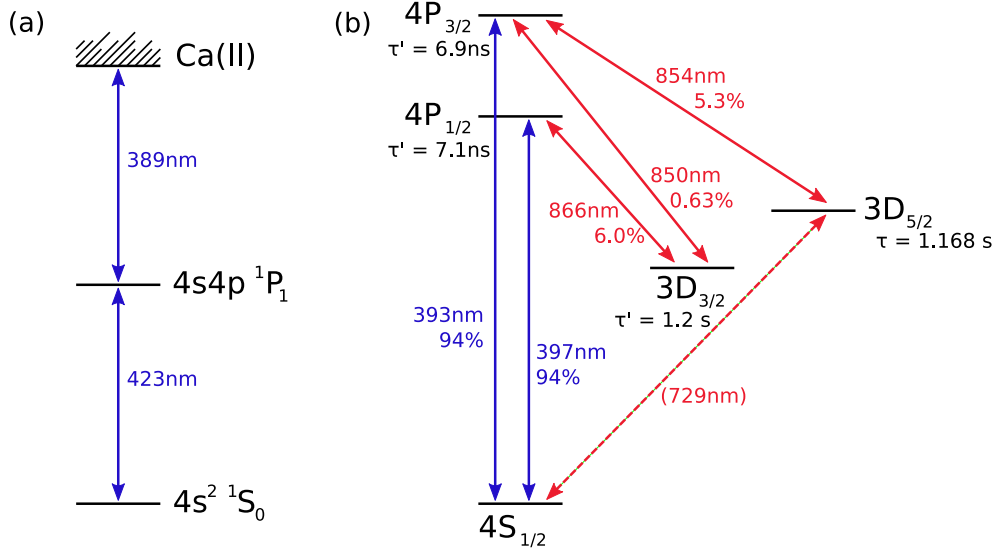


Figure 2.2: Energy level diagrams for (a) neutral calcium Ca(I) and (b) singly ionised calcium Ca(II) (or Ca^+). Wavelengths and branching ratios of important transitions are shown, along with the lifetimes of some levels.

A diagram showing the energy level structure of $^{40}\text{Ca}^+$ is shown in figure 2.2(b). Two energy levels can be chosen to store a qubit: this thesis concentrates on readout of the “optical” qubit stored in the $\{S_{1/2}, D_{5/2}\}$ levels. Longer-lived qubits can be stored in the $S_{1/2}$ ground level which is split into the two different m_j states by the Zeeman effect in $^{40}\text{Ca}^+$ (or two hyperfine-split sub-levels with different F in $^{43}\text{Ca}^+$). More detail on these qubits can be found in section 3.1. Two Zeeman states in the $D_{5/2}$ level can also be used to store a qubit; experiments involving this qubit can be found in the thesis of Michael Curtis [62, chapter 7]. Readout for all qubits involves first mapping to the “optical” qubit by state-selective shelving (in the case of $S_{1/2}$ level qubits) or state-selective deshelling (in the case of the $D_{5/2}$ qubit).

Section 3.1 describes the state-selective shelving process for ground state qubits. The transitions which are important are the same as those used for state-preparation of the optical qubit: population in the $S_{1/2}$ level can be moved to the $D_{5/2}$ “shelf” (via the $P_{3/2}$ level) by driving the transition at 393 nm. An additional laser at 866 nm is needed to remove population that decays to the $D_{3/2}$ level (which has a lifetime of $\approx 1.2\text{ s}$). The Oxford group do not have a 729 nm laser to excite ions directly on the narrow linewidth

$S_{1/2} \rightarrow D_{5/2}$ transition, although there are groups who do use this transition in calcium [135, 136]. De-shelving from $D_{5/2}$ is accomplished by light at 854 nm which returns the population to the ground state.

Readout from the optical qubit is via the process of resonant fluorescence on the 397 nm transition; this transition is also used for Doppler cooling the ion. Light at 866 nm is needed to form a closed cycling transition by removing population that decays to the $D_{3/2}$ level (there is a branching ratio of 6% to this level).

The wavelengths and saturation intensities of the various transitions are summarised in table 2.1, where the saturation intensity I_{sat} is defined as the intensity at which the spontaneous and stimulated transition rates are equal for a cycling transition on resonance:

$$I_{sat} = \frac{\hbar \omega_{ij}^3 \Gamma_j}{6\pi c^2} \quad (2.1)$$

where ω_{ij} is the angular frequency of the $i \leftrightarrow j$ transition and $\Gamma_j = 1/\tau_j$ is the total decay rate out of state j .

Transition	Wavelength / nm	Einstein A coefficient / s ⁻¹	Saturation Intensity / W m ⁻²
$4S_{1/2} \rightarrow 4P_{1/2}$	396.958 978 8(9)	132×10^6	933.82
$4S_{1/2} \rightarrow 4P_{3/2}$	393.477 471 6(3)	$135.0(4) \times 10^6$	987.58
$3D_{3/2} \rightarrow 4P_{1/2}$	866.452	8.4×10^6	89.798
$3D_{3/2} \rightarrow 4P_{3/2}$	850.036	$0.955(6) \times 10^6$	97.954
$3D_{5/2} \rightarrow 4P_{3/2}$	854.444	$8.48(4) \times 10^6$	96.446
$4S_{1/2} \rightarrow 3D_{5/2}$	729.347 276 793 955(2)	0.856(5)	9.181×10^{-7}
$4S_{1/2} \rightarrow 3D_{3/2}$	732.591	0.850(8)	8.818×10^{-7}

Table 2.1: Wavelengths, Einstein A coefficients and saturation intensities (2.1) for important transitions in $^{40}\text{Ca}^+$, for a more complete list, see Szwer [137, table 3.2].

2.3 Lasers

The full laser set-up is described in detail by Dr David Szwer in his thesis [137]. A summary of the lasers used for the experiments presented in this thesis is provided here.

One of the advantages of using calcium is that the wavelengths required to address all the necessary transitions can be obtained with diode lasers. None of the lasers used for work in this thesis required frequency doubling as short-wavelength blue diodes capable

of operating at (397 nm, 393 nm 389 nm and 423 nm) were purchased by the group in the past. Although these diodes are no longer manufactured, it will still be possible to obtain these wavelengths in the future by frequency doubling light from infra-red laser diodes.

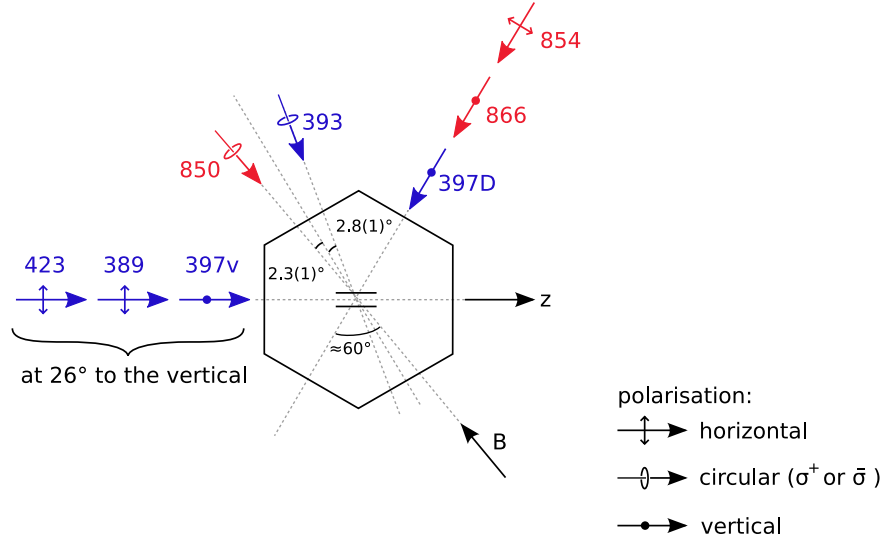


Figure 2.3: Directions and polarisations of laser beams as they enter the hexagonal vacuum chamber, including the approximate magnetic field direction (B) and trap axis (z). Adapted from D. J. Szwed [137, figure 2.5]. The imaging system for collecting ion fluorescence is perpendicular to the page.

The directions and polarisations of the laser beams as they enter the trap are shown in figure 2.3. The exact orientation of the magnetic field is not important for the experiments presented in this thesis: figure 2.3 shows the approximate direction based on settings used for other experiments in the trap. The “vertical” beams enter the vacuum system through the same window that the ions are imaged through; a small black paper flag is used to prevent reflections from the beams entering the imaging system. The 423 nm and 389 nm beams enter at this angle so that they cross perpendicular to the atomic beam used for loading; this minimises Doppler-broadening so that loading can be isotope selective [134]. The vertical 397 nm beam (“397v”) is used only to detect vertical micromotion.

A summary of the various lasers mentioned in this thesis is provided in table 2.2. With the exception of the 389 nm laser, all of the lasers are grating stabilised in the Littrow configuration. (The second stage of photoionisation is not frequency selective, so neither locking nor stabilisation of the 389 nm laser is necessary.) The lasers at 397 nm and 866 nm also have a second, external, grating to reduce the amount of amplified

Name, λ / nm	Lock	Extinction	Notes
423	—	shutter	Isotope-selective excitation for photoionisation.
389	—	shutter	Non-selective second stage for photoionisation.
397D40	PDH	2×AOM & 1×AOM	Doppler-cooling, state-preparation and readout, but also provides 397v beam for micromotion detection.
397D43	PDH	1×AOM & shutter	Doppler-cooling and state-preparation of $^{43}\text{Ca}^+$, but also provides 397v beam for micromotion detection.
866	s-o-f	2×AOM	Repumping from $D_{3/2}$.
393	PDH	2×AOM	Shelves ions into $D_{5/2}$ for readout.
854old	—	1×AOM & shutter	Des shelves ions from $D_{5/2}$ back to $S_{1/2}$. This laser used for the PMT readout experiments.
854new	—	2×AOM & shutter	Temporary replacement for 854old, delivered by fibre from the laboratory next-door and used for CCD readout experiments.
850	s-o-f	1×AOM	Used for readout of $^{40}\text{Ca}^+$ and $^{43}\text{Ca}^+$ $S_{1/2}$ qubits, see section 3.1

Table 2.2: Summary of lasers used for experiments presented in this thesis, including any locking arrangement [Pound-Drever-Hall (PDH) or side-of-fringe (s-o-f)] and extinction method, where 1×AOM indicates a single-pass acousto-optic modulator and 2×AOM indicates a double-pass AOM.

spontaneous emission (ASE) present (specifically at 393 nm and 854 nm respectively) which would cause unwanted shelving to or deshelfing of the ion from the $D_{5/2}$ level [138].

All lasers (except the 389 nm and 854 nm lasers) are locked to their own temperature-stabilised external reference cavity, either with a side-of-fringe or Pound-Drever-Hall (PDH) lock. The cavities are low-drift (≤ 1 MHz/hr) etalons made by the National Physical Laboratory (NPL). One of the mirrors in each cavity is attached to a piezo-electric actuator to which a voltage can be applied in order to translate the mirror and hence change the cavity length. Frequency scanning of the lasers in experiments is achieved by control of this voltage by a digital-to-analogue converter (DAC) in the computer (see section 2.5). Provided the scan is slow compared to the lock bandwidth, the locked laser will follow the cavity. The laser frequency diagnostics are described in [137, section 2.4.3]. Laser powers are measured from pick-off diagnostic beams sent to photodiodes which are monitored by the experimental control computer (see below), while the laser spot sizes are measured on a camera positioned at an equivalent position on the diagnostic beam to where the main beam hits ions in the trap. Together these measurements allow an estimate of the laser intensity.

Fast extinction of laser beams within experimental sequences is provided by acousto-optic modulators (AOMs). These devices are made from materials such as quartz whose refractive index changes significantly as the material is compressed. A piezo-electric transducer is used to set up a travelling acoustic wave within the crystal at RF frequencies, typically at 80–100 MHz. The longitudinal waves create a travelling diffraction grating; light passing through the AOM is then diffracted with the m^{th} order diffracted beams being Doppler shifted by m times the drive frequency. The AOMs are set up so that the first-order diffracted beam continues to the ion while the zeroth order is often blocked or used as a diagnostic. Even when the AOM is nominally switched off, the power in the diffracted beam does not disappear completely: this is due either to imperfect extinction of the RF drive or to scattering within the crystal. Using the AOM in a double-pass configuration improves extinction, nevertheless some leakage may still occur. Dr. Szwer has made measurements of the extinction ratio of the 850 nm and 397 nm beams [137, section 2.7], while measurements in section 4.3.3 of this thesis indicate that the extinction of the 393 nm laser by its double-pass AOM could be as high as $\sim 10^{-8}$. When total extinction of a beam is important (for example the 854 nm light, where leakage can cause unwanted deshelling during readout) shutters can be used to almost completely extinguish the beam. These come with their own technical difficulties as they tend to “bounce”, meaning the beam may not be fully blocked/unblocked when it ought to be. In addition there is a wide variation in the time it takes the shutter to open and close (up to several ms), so any experimental sequence where shutters are used must be carefully designed with this in mind (see figure 4.5 for example).

2.4 Imaging system

The imaging system is used to collect fluorescence at 397 nm from the ions in the trap and focus it onto a detection device in order to determine the presence (and later, the internal state) of the ions held in the trap. For photon detection either a photomultiplier tube (PMT) or a charge-coupled device (CCD) camera is used. The imaging system was modified several times through this work with the aim of improving the photon collection efficiency; each system will be described here.

2.4.1 Imaging system A

The initial imaging system (A) used for the first PMT readout experiments (series I, in chapter 4) is shown in figure 2.4 and is essentially the same as that described by C. J. S. Donald [129, §3.7]. Light from the ion(s) is collected by a wide-aperture compound objective lens² which is not optimised for 397 nm, the wavelength we are interested in detecting. The nominal focal length of the lens is 65 mm, although the object and image distances in [129, figure 3.30] suggest it is ≈ 68 mm. The position of the focal planes is not known as the measured physical length of the lens does not seem to agree with that shown in [129, figure 3.30]. Figure 2.4 shows estimates of their position based on experimental measurements of magnification, object and image distances, assuming a focal length of 68 mm.

The objective lens collects light over a solid angle of $\Omega = 2\pi(1 - \cos \alpha)$, where α is the half-angle subtended by the useful diameter of the lens at the ion. This is more usually quoted in terms of the numerical aperture which is $\sin \alpha$. The light passes through a light-tight tube and is imaged with a magnification of $\mathcal{M} \approx 4.1$ onto a moveable ≈ 1 mm aperture which is used to filter out stray light. A shutter is installed at this position although its purpose is historic: it was used to protect the PMT and camera from bright light during the loading of ions by electron bombardment. Now that ions are loaded by photoionisation the shutter is obsolete.

The ion(s) image is then re-imaged via secondary lenses onto the PMT³ with unity magnification, and optionally a CCD camera⁴ with magnification 2 via a moveable beamsplitter (power transmission 18% at 397 nm). The total magnification at the CCD is then ≈ 8.2 . The two detectors in this system serve different purposes: the PMT is used for state measurement, while the CCD is used to determine the number of ions held in the centre of the trap and to check that they have formed a crystal. The beamsplitter can be removed from the optical path so that all the light is incident on the PMT for higher detection efficiency. An arrangement of translation stages allows x - y - z adjustment of the imaging system position to focus on electrodes in the trap and hence locate the trap centre.

Coloured-glass blue band-pass filters are installed in front of the PMT and CCD to

²Nikon ED PLAN 1.5 \times SM2-U

³Hamamatsu H6180-01

⁴Andor DU-437-BU2 conventional back-illuminated CCD

cut down the amount of background room light and scattered background laser light, in particular suppressing the 866 nm light to which the camera is sensitive (although the PMT is not). The filters are installed in the collimated part of the beam path to reduce aberrations. A 200 μm diameter pinhole in front of the PMT further reduces background light by spatial filtering. The transmission of each component in the system is shown in table 2.3, along with the calculated net collection efficiency $\eta = 0.10(1)\%$ for the system when all the light is incident on the PMT. For the same imaging system, Donald calculates $\eta = 0.13(2)\%$; the discrepancy can be explained by the change in solid angle (the object distances are different for the two systems). Donald measured $\eta = 0.11\%$ experimentally by comparing the maximum count rate from a $^{40}\text{Ca}^+$ ion with a 3-level rate-equations model.

Imaging system:			A	B	C
...see figure			2.4	2.5	2.6
Experiment:			PMT	PMT	EMCCD
Magnification, \mathcal{M}			(<i>series I</i>)	(<i>series II</i>)	
Numerical aperture ($\sin \alpha$)			≈ 4.1	≈ 5	6.2(1)
Solid angle fraction $\Omega/(4\pi)$			0.014(1)	0.015(1)	0.016(1)
Window	T	0.92 [‡]	•	•	•
Nikon lens	T	0.73 [‡]	•	•	•
Comar lens 50PS25	T	0.875(3) [†]	•		
Comar lens 50DQ16	T	0.866(3) [†]	•		
Blue filter BG37	T	0.83(2) [†]	•		
Interference filter	T	0.94(5)			•
PMT (spec.)	Q	0.16	•	•	
EMCCD (spec.)	Q	0.55			•
net η (from components)			0.10(1)%	0.17(2)%	0.56(7)%
measured η			[0.13(2)%]*	0.22(2)%	[0.67(8)%]*

Table 2.3: Comparison of the imaging systems used in this work, where • indicates inclusion of a particular component. The transmissions T and quantum efficiencies Q of various components are used to make an estimate of the net collection efficiency η of the system. The values of η and magnification \mathcal{M} relate to the detection device used for readout. The last line of the table relates to an independent measurement of η for system B which implies that the PMT efficiency is higher, at $Q = 0.21$, implying the camera efficiency is $Q = 0.65$ (for further discussion, see text). * Estimates of η assuming PMT $Q = 0.21$. † Power transmissions measured by D. J. Szwed [137, §2.6]. ‡ Values taken from Donald [129, §3.7].

2.4.2 Imaging system B

The imaging system was then altered to increase the collection efficiency by removing unnecessary elements which absorbed or reflected light from the ions. The secondary lenses were removed, as was the filter since the PMT is insensitive to 866 nm background

light. (Room lights were extinguished to minimise background). The aperture and shutter were also removed and the objective lens was moved 3 mm closer to the ions, increasing the solid angle collected. The ions were imaged directly onto the PMT via a $200\text{ }\mu\text{m}$ diameter pinhole to reduce background scatter. The camera and beamsplitter were (temporarily) removed, although these were replaced in a later re-build of the system by D. J. Szwer, see [137, figure 2.9]. The modified system (B) used for the second PMT readout experiments (series II) is shown in figure 2.5.

The efficiencies of the components in table 2.3 give an estimated efficiency for imaging system B of $\eta = 0.17(2)\%$. D. N. Stacey has used Bloch equations⁵ to fit the observed 397 nm fluorescence level from a $^{40}\text{Ca}^+$ ion with changing 866 nm frequency, recorded using this imaging system. These fits imply a rather higher efficiency of $0.22(2)\%$; this higher η could be explained if the quantum efficiency of the PMT was $Q = 0.21$. This is plausible since the manufacturers do not quote an error on their specification of $Q = 0.16$ and the absolute value of Q can vary within each manufactured batch, as well as depending on temperature and magnetic field [139]. This higher Q would imply that the net efficiency for system A was also higher, at $\eta = 0.13(2)\%$ (see table 2.3, last line).

2.4.3 Imaging system C

The system was modified to imaging system C shown in figure 2.6 following the installation of a new EMCCD camera⁶ to investigate ion readout with spatial resolution (chapter 6). The positions of the camera and PMT were swapped so that the highest η could be obtained at the CCD with the beamsplitter removed from the optical path. The EMCCD has a nominal quantum efficiency of $Q = 0.55$, giving an estimate of $\eta = 0.56(7)\%$ for the net efficiency of imaging system C. In section 6.2 we measure the quantum efficiency of the camera to be $Q = 0.50$ relative to the PMT, assuming $Q_{\text{PMT}} = 0.16$. The higher value $Q_{\text{PMT}} = 0.21$ would imply $Q = 0.65$, giving a net $\eta = 0.67(8)\%$.

⁵This model includes the effects of coherent population trapping in $\text{D}_{3/2}$ [131]. Simply using rate equations which do not model coherent effects means that reduced fluorescence due to population trapping could be misinterpreted as a lower η .

⁶Andor iXon^{EM}+ DU-897; see chapter 5 for the motivation for choosing this model.

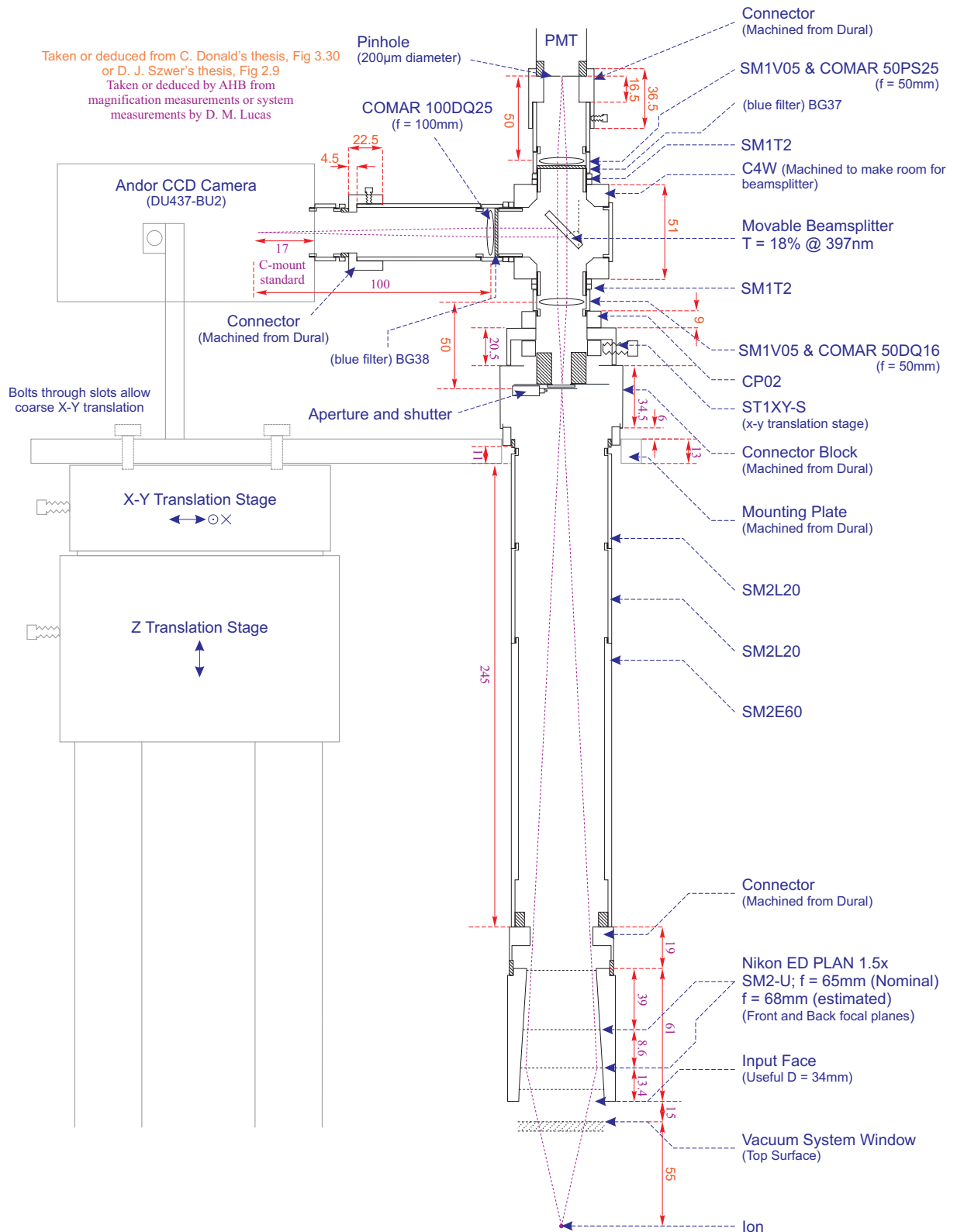


Figure 2.4: Imaging system A, as used for the PMT (series I) set of readout experiments described in chapter 4. All dimensions are in mm. Part numbers for the Thorlabs lens tubing parts are given. Dimensions taken or deduced from the theses of C. J. S. Donald [129] or D. J. Szwer [137] are shown in orange sans-serif font; dimensions deduced by AHB from magnification measurements or system measurements by D. M. Lucas are shown in purple serif font. Diagram adapted from Szwer [137, figure 2.9].

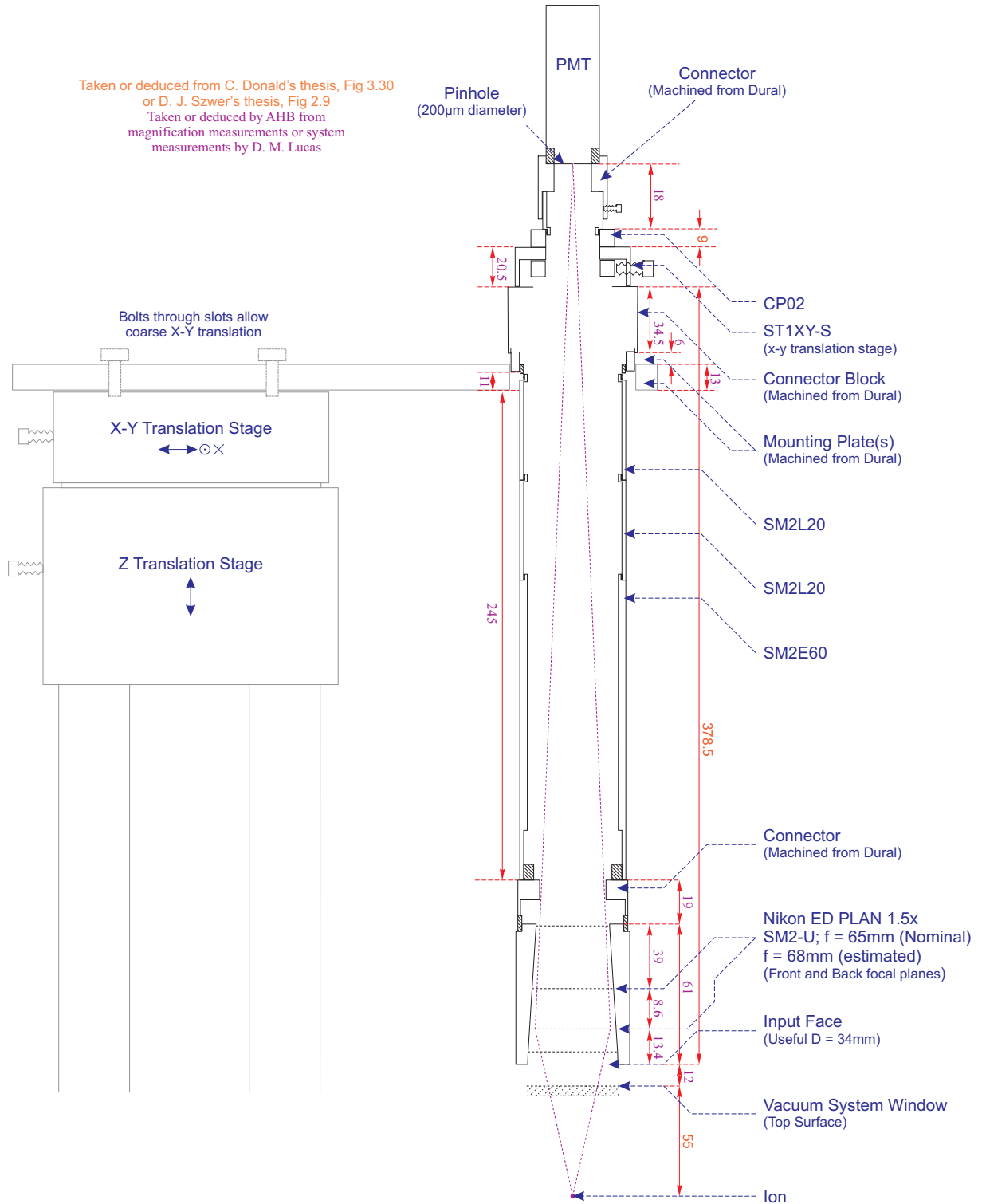


Figure 2.5: Imaging system B, as used for the PMT (series II) set of readout experiments described in chapter 4. All dimensions are in mm.

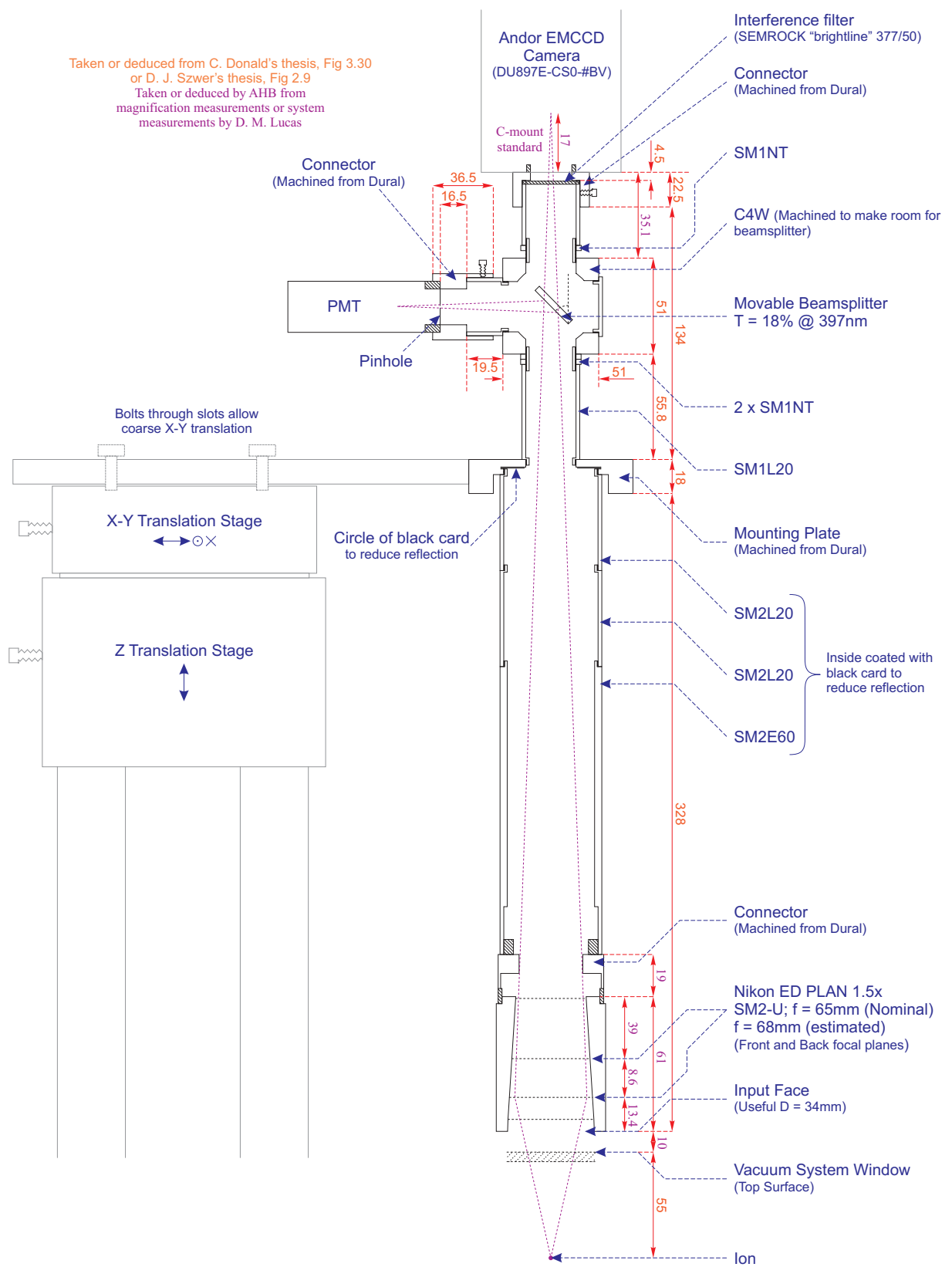


Figure 2.6: Imaging system C, as used for the EMCCD set of readout experiments described in chapter 6. All dimensions are in mm.

2.5 Experimental control

The overall control of experiments is handled by a program written in Turbo Pascal 7.0 running under MS-DOS 6.2 on a PC. Connection to the experimental hardware is made by various commercially available ISA/PCI interface cards, via the Laser Control Unit (LCU) designed and built by Dr Ben Keitch [132] which provides additional real-time synchronisation, buffering and logic. This system was chosen because it allows adaptive, yet robust, timing: the computer's interrupts can be disabled during an experimental sequence, allowing real-time control of experimental pulses to a resolution of $0.1\ \mu\text{s}$ and with a precision $\sim 10\ \text{ns}$.

The experimental control system has the capability to control the various lasers: turning them on or off via acousto-optic modulators (AOMs) or mechanical shutters, tuning their frequencies and intensities via digital-to-analogue converters (DACs) and recording their intensities via power measurements on calibrated photodiodes. It can also control microwaves and RF for manipulation of $^{43}\text{Ca}^+$ or $^{40}\text{Ca}^+$ qubits by magnetic resonance. The system has the facility to turn on and off the calcium ovens and trap RF for ion loading, and can alter the voltages on the trap end-cap and DC compensation electrodes via DACs. The pressure inside the vacuum system is continuously displayed while the control program is running. The 50 Hz AC mains signal can be monitored and used to trigger the experiment at the same phase each time to reduce magnetic field uncertainty. The output of the PMT is also connected to the system; the number of detected photons within time bins of a chosen length is continuously displayed and the results of analyses on them (or the raw counts themselves) can be saved to disc or over ethernet. The photon counting arrangement is described in more detail in section 2.5.1, below. Another feature of the system is the ability to record time-correlations between the RF phase and the arrival time of photons scattered from the ion. This allows the ion micromotion to be detected and compensated (see section 2.1 and [126, 137]).

The control program provides the ability to edit and run experimental pulse sequences as well as monitoring and displaying inputs on-the-fly. For example the photon count rate can be continuously monitored while scanning a DAC which controls the frequency of a laser in order to find the resonant frequency of a transition. Timed “sequences” consisting of a list of many different instructions can be run. Such a sequence may consist of a pulse of laser light to prepare the ion in a certain state, followed by

pulses of laser light, microwaves or RF to further manipulate the ion’s state and finally a “readout” period where photons are counted for a fixed time or (for time-resolved readout) many consecutive fixed-time bins. The value of DACs controlling a certain parameter can also be changed in a “scan”: for each scan point, the sequence is repeated several times with the same DAC value to give one data point. For example the length of a 393 nm shelving pulse could be scanned and the number of times the ion is shelved in 512 sequence repeats recorded. The number of shelvings for each 393 nm pulse-length is recorded to build a data set such as that in figure 4.7(a). The timed sequences can also be executed in “whizzo-interactive” mode enabling parameters to be tuned as the sequence is running. For the PMT readout experiments presented in this thesis, the parameters were kept constant between each sequence repeat and the raw photon counts were saved to disc.

The main experimental control PC does not control the acquisition of data from the camera: this is performed through proprietary software on a separate PC running Windows XP and containing a special interface card. In this case, the camera was used to trigger pulse sequences on the main control PC; more detail on synchronising the camera with the rest of the sequence can be found in chapter 6. Since the beamsplitter was removed from the optical path, the PMT could not detect signal from the ion during camera experiments so the experimental control PC saved nothing but a record of the sequence executed and laser power measurements. Image data was saved on the dedicated camera-control PC.

2.5.1 Photon counting

The hardware arrangement for counting photons detected by the PMT is shown in figure 2.7. The PMT outputs ~ 9 ns long TTL-compatible pulses which are then “stretched” in time by a custom-made circuit⁷ which outputs a TTL pulse with an adjustable width between 25 and 100 ns followed by a period held “low” for the same time. The pulse width was set at 50 ns, which allowed us to reach the 10 MHz maximum specified counting rate of the counters on the Intel 82C54 chip to which the pulses are sent.

The Intel 82C54 chip contains three programmable counters and is part of a data acquisition ISA card⁸ installed in the experimental control computer. The three counters

⁷Built by Johan Fopma, Central Electronics, Oxford Physics Department.

⁸Keithley DAS-8AO

are wired to record contiguous counting bins as follows. Counter C2 is used to provide a square wave whose period (usually $2 \times 10 \mu\text{s}$) is set by programming C2 to record a certain number of 1 MHz oscillations from a crystal on the ISA card. The output of C2 is used to alternately gate counters C0 and C1 so that they alternately record incoming counts from the PMT (via the pulse-stretcher) with very small dead time (see below). While C0 is counting, the contents of C1 are read into the control program via the PC's ISA bus, and vice-versa. In order to get reliable timing, the PC's interrupts must be disabled during the counting periods, but they are restored in between successive pulse-sequences in order for the PC to respond to input from the computer keyboard.

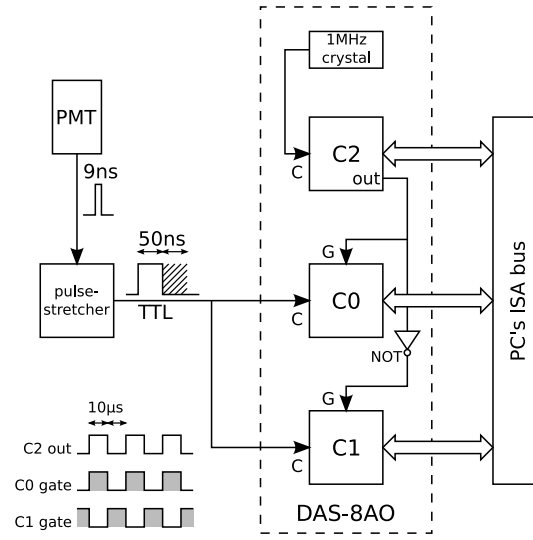


Figure 2.7: Experimental arrangement for counting photon pulses from the PMT in contiguous $10 \mu\text{s}$ counting bins using three counters (C0, C1 and C2) on an Intel 82C54 chip. C = clock input, G = gate input.

When detecting photons with a Poissonian average arrival rate R_0 for an interval of length t , a dead-time of T will lead to an *average* observed number of counts n [140]:

$$n = \frac{R_0 t}{1 + R_0 T}$$

The observed count rate $R = n/t$ will be reduced (compared to R_0) as a fraction of the counts ($\approx R_0 T$) are not recorded. There are two sources of photon losses in this system:

1. Pulses which arrive while the gate is changing from C0 to C1 and are not counted by either counter, giving an effective dead-time which was measured to be $T \approx 43 \text{ ns}$ when counting with $10 \mu\text{s}$ long bins.
2. The finite counting rate of the 10 MHz ($\approx 1/T$) counters.

A typical observed count rate for $^{40}\text{Ca}^+$ is $R_B = 55\,800\,\text{s}^{-1}$ (see chapter 4), implying we lose 0.80% of the counts in total.

Note that we cannot simply correct for these lost counts by adding R_0RTt to n (a “dead time correction”): this adds no information and therefore cannot increase readout fidelity.

Chapter 3

Ion readout by time-resolved photon counting

3.1 Readout of qubits in calcium

3.1.1 $^{40}\text{Ca}^+$ Optical qubit

The experiments described in this thesis concern the readout of the “optical” qubit stored in the $S_{1/2}$ and $D_{5/2}$ levels of $^{40}\text{Ca}^+$, shown in figure 3.1¹. Qubit measurement is performed by the process of state-dependent resonance fluorescence. To measure the state of an ion, a resonant laser is applied which couples one qubit state to a closed transition, but does not couple to the other qubit state. This performs a projective measurement, collapsing the wavefunction of the ion into one of the qubit eigenstates. If the ion collapses to the state addressed by the laser it scatters millions of photons per second on the cycling transition which can be detected and the ion appears bright. If the ion collapses to the state not addressed by the laser it does not scatter photons and appears dark. The state of the ion can therefore be determined by counting how many photons are scattered from the ion during a fixed interval.

For the optical qubit in calcium, laser radiation at 397 nm is applied resonant with the $S_{1/2} \leftrightarrow P_{1/2}$ transition. Because of the small (6.0%) branching ratio from $P_{1/2}$ to $D_{3/2}$, an additional laser is needed at 866 nm to form a closed cycling transition by re-pumping any population that decays to the $D_{3/2}$ level. If the ion is in the $S_{1/2}$ “bright” state it

¹A particular choice of m_j state has to be made for each level, but the readout method is not sensitive to this choice.

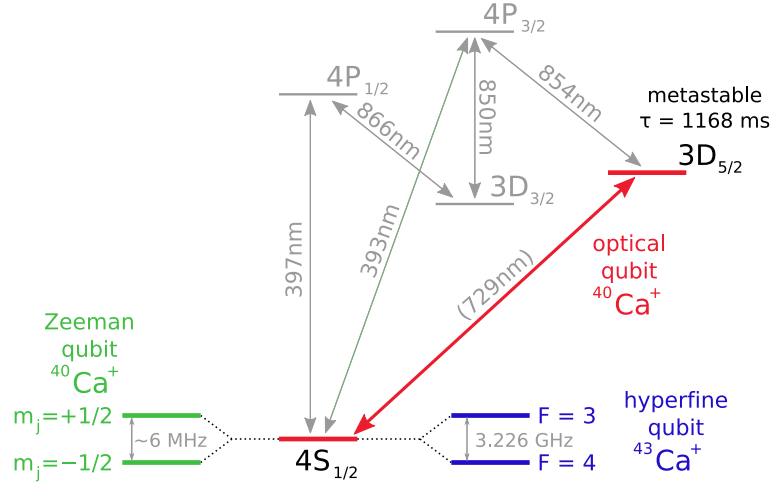


Figure 3.1: Level diagram showing various qubits in $^{40}\text{Ca}^+$ and $^{43}\text{Ca}^+$ along with the wavelengths of important transitions. The Zeeman qubit splitting shown is for a typical applied field $B \sim 2$ G.

scatters photons at 397 nm which we detect. If the ion is in the $D_{5/2}$ level then it is not addressed by either of the lasers and appears “dark”.

The optical qubit in $^{40}\text{Ca}^+$ suffers from two drawbacks. Firstly, the lifetime of the qubit itself is fundamentally limited by the 1.168(7) s lifetime [138] of the metastable $D_{5/2}$ upper qubit level. Secondly, the narrow linewidth of the quadrupole transition between the two qubit states means that high frequency stability and narrow bandwidth lasers are needed to manipulate the qubit coherently. Qubits stored in the $S_{1/2}$ ground level of $^{40}\text{Ca}^+$ or $^{43}\text{Ca}^+$ (see figure 3.1) avoid these problems and are described in sections 3.1.2 and 3.1.3 below. Our interest in the optical qubit is because of its use in the readout process, as follows.

The readout process for both ground-level qubits involves initially mapping the qubit to the optical qubit configuration by moving population from one of the qubit states to the $D_{5/2}$ “shelf”. This technique is known as electron shelving and was initially suggested by Dehmelt [141], and first demonstrated by Sauter, Nagourney and Bergquist [142, 143, 144]. Detection then proceeds by driving the cycling transition at 397 nm as for the optical qubit. The advantage of the shelving method over trying to perform resonant fluorescence on one of the ground qubit states directly is the reduced rate of unwanted dark to bright (or bright→dark) excitations possible with the shelving method. When a dark to bright transition occurs, the population from the “dark” qubit state begins to participate in the cycling transition, scattering photons and appearing bright; this will cause a measurement error. In the shelving method, only relatively few excitations

are needed to transfer the population from one of the ground level qubit states to the long-lived metastable shelf, after which the cycling transition can be driven millions of times before the population in the shelf decays. This enables many photons to be detected, even with a poor collection efficiency. In contrast, if one were trying to excite directly one of the ground level qubit states, far fewer photons would be scattered before an unwanted off-resonant excitation of the other qubit state occurred. This means that the shelving process gives a significant advantage.

Studying the readout fidelity achievable with the optical qubit is therefore also relevant to the readout of ground-level qubits. Nevertheless the optical qubit is still interesting for quantum information in its own right; it has already been used at Innsbruck University to demonstrate the production of an entangled Bell state of two ions with a very high 99.3(1)% fidelity, the highest fidelity quantum logic gate to date [29].

Descriptions of two sorts of ground-level qubit in calcium and details of shelving procedures for them follow.

3.1.2 $^{40}\text{Ca}^+$ Zeeman level qubit

In $^{40}\text{Ca}^+$, qubits can be stored in the two Zeeman-split sub-levels of the $S_{1/2}$ ground level. The ion can be initialised into either qubit state by optical pumping of the population with a σ -polarised 397 nm beam and an 866 nm repumper. The qubit state can then be manipulated by driving Raman laser transitions or by magnetic resonance [145]. The coherence time of the qubit can be ~ 1 ms without magnetic field shielding.

To read out the state of the qubit, the Zeeman qubit is first mapped to the optical qubit by moving the population from one of the Zeeman states to the $D_{5/2}$ “shelf”. Various ways one could achieve this are considered in Matthew McDonnell’s thesis [146], but most require high stability and narrow linewidth lasers. The EIT (electromagnetically induced transparency) method, however, does not have such demanding requirements. Full details of this method are given in [146]. A brief description follows, which has polarisations chosen to achieve shelving of the $|\downarrow\rangle$ state ($m_s = -\frac{1}{2}$). Choosing the opposite polarisations would produce shelving of the $|\uparrow\rangle$ state. The scheme is illustrated in figure 3.2.

To shelve the $|\downarrow\rangle$ state, weak σ^- polarised light at 393 nm is applied to the ion. This drives a cycling transition between $S_{1/2}$, $m_j = -1/2$ and $P_{3/2}$, $m_j = -3/2$, from

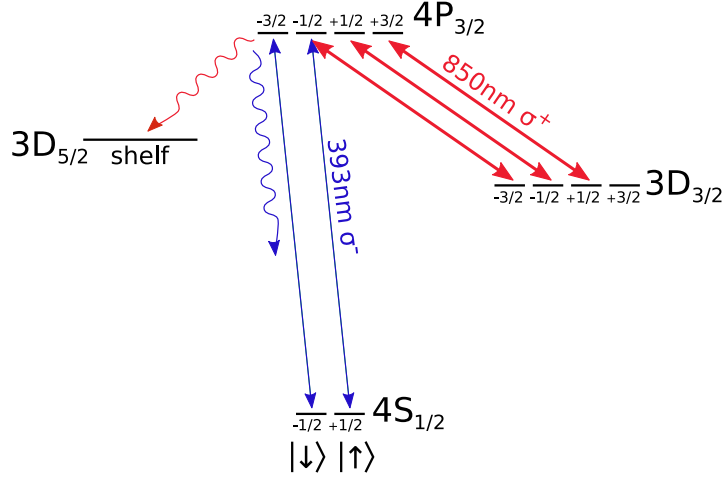


Figure 3.2: Level diagram for $^{40}\text{Ca}^+$, showing transitions for the EIT shelving scheme to map the Zeeman-level qubit to the optical qubit. Not shown is the $P_{3/2} \rightarrow D_{3/2}$ decay route, which leads to 11% loss in the scheme.

where population can decay to the $D_{5/2}$ shelf. However, the 393 nm light can also excite population in the $|\uparrow\rangle$ state as the typical qubit splitting (~ 6 MHz) is small compared with the transition's natural linewidth (23 MHz). To avoid this, high intensity σ^+ polarised light at 850 nm is applied to the ion. With this choice of polarisation, the $P_{3/2}, m_j = -3/2$ state does not couple to the 850 nm light, so the $|\downarrow\rangle$ state is unaffected while excitations from the $|\uparrow\rangle$ state are prevented by the formation of a dark state. Only population in $|\downarrow\rangle$ is ever excited to the $P_{3/2}$ level, from which 6% of the time it will decay to one of the D-states. Of these decays, 89% are to the required $D_{5/2}$ level, successfully shelving the ion. The other 11% of decays are to the $D_{3/2}$ level, where they may not necessarily be correctly re-pumped back to the $|\downarrow\rangle$ state. This represents a loss mechanism in the scheme and limits the average readout fidelity to a maximum of 92.85%.

3.1.3 $^{43}\text{Ca}^+$ hyperfine qubit

Calcium-43 is an odd isotope of calcium and has nuclear spin $I = 7/2$, giving rise to hyperfine splitting of the energy levels. The $S_{1/2}$ ground level is split into states with different quantum numbers F, M_F (referred to as $S_{1/2}^{F, M_F}$), which form two sub-levels with the two different values of F , (denoted by $S_{1/2}^F$), split by ~ 3.226 GHz. The hyperfine structure of the $S_{1/2}$ ground level can therefore be chosen to store a qubit, with one qubit state in each F sub-level. This scenario has been modelled using rate

equations by Simon Webster [145], and more extensively by David Szwer [147, 137]. Only a summary is provided here; more details can be found in David Szwer’s thesis [137]. Ground level hyperfine qubits have been used to demonstrate some of the longest coherence times ever measured [23, 24].

Transitions between different $S_{1/2}^{F,M_F}$ states can be made by microwave pulses or Raman transitions, which allow coherent manipulation of the hyperfine qubit. Any pair of M_F states can be chosen to store the qubit, but selection rules mean that the “stretched states” $S_{1/2}^{3,+3}$ and $S_{1/2}^{4,+4}$ are the easiest to prepare and read out. Preparation of the ion in $S_{1/2}^{4,+4}$ is achieved by optical pumping with σ^+ polarised 397 nm light with an 866 nm repumper. Since the splitting of the two F sub-levels is so large, two 397 nm frequencies are needed to pump from both sub-levels. This is achieved by adding sidebands onto the 397 nm laser with an electro-optical modulator (EOM) and having the carrier address $S_{1/2}^4$ to $P_{1/2}^4$ with one of the sidebands addressing $S_{1/2}^3$ to $P_{1/2}^4$.

The population in $S_{1/2}^{4,+4}$ is moved to the $D_{5/2}$ shelf to map the stretched state qubit to the optical qubit for readout. This could be accomplished by directly driving the narrow quadrupole transition at 729 nm [135, 136], but an excellent fidelity can be achieved without the need for a technically demanding laser with such a narrow linewidth and high frequency stability. David Szwer has devised a state selective shelving scheme to transfer the population from the $S_{1/2}^{4,+4}$ state to the shelf via the $P_{3/2}^{5,+5}$ state by simple optical pumping. A σ^+ polarised 393 nm pulse would achieve a transfer to the shelf with $\sim 95\%$ accuracy, but the addition of an 850 nm repumper allows a higher fidelity to be reached by removing population from the $D_{3/2}$ level in such a way that it does not fall into the $S_{1/2}^3$ sub-level. The levels involved are shown in figure 3.3. The optimal solution is a pulsed repeated sequence of (393 nm σ^+ , 850 nm σ^+ , 850 nm π), but a continuous beam of 850 nm σ^+ at a small angle (2.3°) to the B-field (giving a small admixture of π light but negligible σ^- light) gives a fidelity almost as high. Theoretically, a transfer fidelity of 99.95% is attainable with 10 μ s of optical pumping. Experimentally, a transfer fidelity of 99.87(4)% was achieved for the continuous method. This scheme is described in more detail in [137] and was published in [41] which is included as appendix B.

The advantage of choosing the $S_{1/2}^{3,0}$ and $S_{1/2}^{4,0}$ states (“clock states”) to store a qubit (rather than states with a non-zero M_F) is that they are insensitive to magnetic field noise to first order. The $S_{1/2}^{4,0}$ state can be prepared by pumping with a π polarised 397 nm

beam, as the selection rules mean that this state is a dark state in which population will build up. Readout of the clock states is more complicated, as the polarisation/selection rules do not protect one qubit state and the optical pumping transfer scheme above is limited to 99.64% fidelity. One possibility to read out the qubit is first to move the population coherently to the stretched states described above, before mapping to the optical qubit.

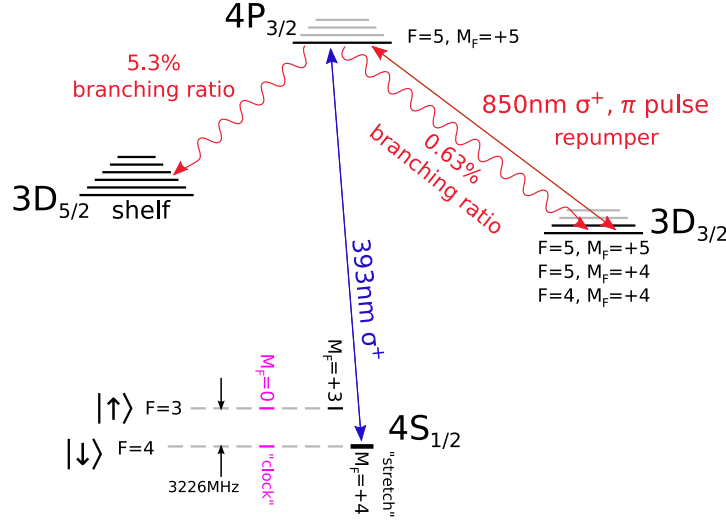


Figure 3.3: Level diagram for $^{43}\text{Ca}^+$, showing transitions for the shelving scheme to map the ground-level hyperfine qubit to the optical qubit. Selection rules and laser polarisations mean that only certain (F, M_F) states are involved in the transitions, these are listed explicitly for the S_{1/2}, P_{3/2} and D_{3/2} levels (but not for the D_{5/2} level).

3.2 Analysis techniques

Several different analysis protocols will be introduced in this section. The outcomes of each protocol are labelled in figures using the following abbreviations:

- T** Threshold method
- M** Maximum likelihood method
- A** Adaptive maximum likelihood method (ignoring dark→bright decay)
- AD** Adaptive maximum likelihood method (including dark→bright decay)

3.2.1 Quantifying the readout error

Section 3.1 described the readout both of the optical qubit and also two types of ground-level qubits in calcium. All of these qubits involved a measurement of photons scattered

in state-dependent resonance fluorescence of the optical qubit. It is therefore of interest to quantify the fidelity achieved in this readout step.

To make a measurement of this fidelity, a single ion is repeatedly prepared with high fidelity in a known initial state. The state is then measured and the result compared with the known preparation. The errors for the bright ($S_{1/2}$) and dark ($D_{5/2}$) states are measured separately and the average readout error is defined as $\epsilon = (\epsilon_B + \epsilon_D)/2$, where ϵ_B is the fraction of trials where an ion prepared in the bright state was incorrectly measured to be dark (and similarly for ϵ_D). The error ϵ_B and its uncertainty are given by:

$$\epsilon_B = \frac{n_{\text{err}}^B}{N_{\text{exp}}^B} \pm \frac{\sqrt{n_{\text{err}}^B}}{N_{\text{exp}}^B}$$

where n_{err}^B represents the number of trials prepared in the bright state which were incorrectly measured as dark, from a total of N_{exp}^B bright preparations. The uncertainty is an estimate that should be valid for small ϵ_B and large N_{exp}^B .

The average readout fidelity is defined as $\mathcal{F} = 1 - \epsilon$.

3.2.2 Threshold method

When an ion is in the bright state $|B\rangle$, it will scatter photons which will be detected (using a photomultiplier tube, for example) with some level of detection efficiency η , at a count rate of R_B . Background light and detector dark counts will add additional counts at a rate of R_D . When the ion is in the dark state $|D\rangle$, only the background counts will be detected. The state of the ion can therefore be determined by examining how many counts n have been recorded during a fixed interval, the “bin time” t_b . The standard way to discriminate between the two states is to choose some threshold n_c . Trials with $n \geq n_c$ are determined to be in state $|B\rangle$, those with $n < n_c$ are identified as $|D\rangle$. The optimum threshold n_c which minimises the discrimination error ϵ is at the value of n where the distributions $B_0(n)$ and $D_0(n)$ cross (as shown in figure 3.4) where $B_0(n)$ and $D_0(n)$ give the probability of recording n counts in a time t_b from states prepared in $|B\rangle$ and $|D\rangle$ respectively and are assumed to be monotonic. Note that the minimum ϵ does not necessarily imply that $\epsilon_B = \epsilon_D$ since the distributions are asymmetric.

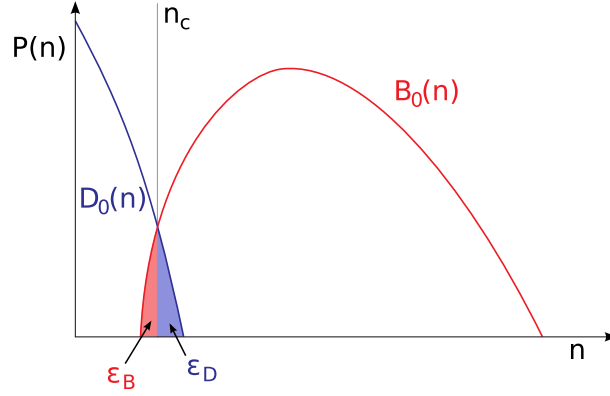


Figure 3.4: Discrimination errors ϵ_B and ϵ_D for ions prepared in $|B\rangle$ and $|D\rangle$ due to the overlap of distributions $B_0(n)$ and $D_0(n)$ with the optimum discrimination threshold n_c .

Statistical errors

Assuming the rates of $|B\rangle \rightarrow |D\rangle$ and $|D\rangle \rightarrow |B\rangle$ pumping are both zero, and we have an ideal detector, the probability distributions $B_0(n)$ and $D_0(n)$ will be Poisson distributions with means $(R_B + R_D)t_b$ and $R_D t_b$ for states prepared in $|B\rangle$ and $|D\rangle$ respectively. In this special case, the optimum threshold n_c can be found analytically as the point at which the two Poisson distributions intersect:

$$n_c = \frac{R_B t_b}{\ln \left(1 + \frac{R_B}{R_D} \right)} \quad (3.1)$$

The discrimination error ϵ for this special case is entirely due to the statistical nature of photon counting and is proportional to the overlap of the two Poisson distributions. The means of the two distributions are separated by $R_B t_b$ so the error can be reduced by increasing t_b as this moves the two distributions further apart; this is shown in figure 3.5 (dashed lines) for typical fluorescence rates in our experiment, $R_B = 55800 \text{ s}^{-1}$ and $R_D = 442 \text{ s}^{-1}$. The threshold defined in (3.1) is labelled n_{c*} and the discrimination error is labelled $\epsilon*$.

Finite qubit lifetime

In general, the rates for pumping between the qubit states will not be zero. For the calcium optical qubit the $|B\rangle \rightarrow |D\rangle$ pumping rate remains negligible (section 4.3.3), but the rate of $|D\rangle \rightarrow |B\rangle$ pumping due to decay from the metastable $D_{5/2}$ state is appreciable at $1/\tau$ where $\tau = 1.168(7) \text{ s}$ is the average lifetime of the shelf state [138].

The count distribution $B_0(n)$ for trials prepared in the $|B\rangle$ state remains Poisson

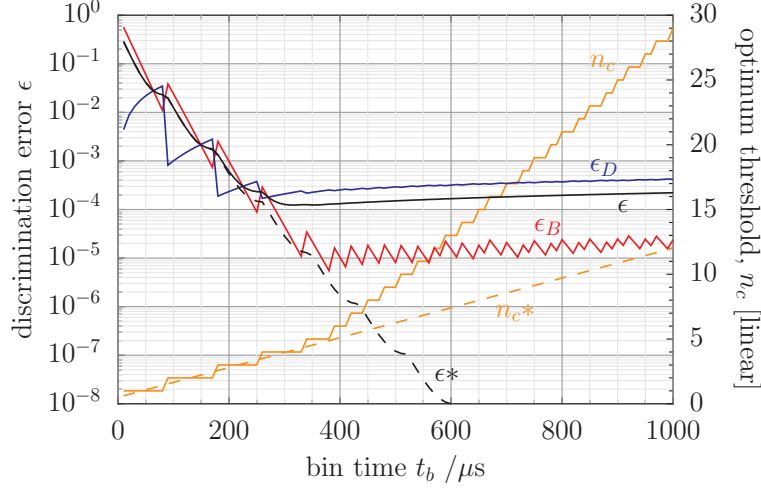


Figure 3.5: Variation of discrimination error with bin time simulated for the threshold method for typical rates $R_B = 55800 \text{ s}^{-1}$ and $R_D = 442 \text{ s}^{-1}$ in our experiment. Dashed lines show the error (ϵ^*) and threshold (n_c^*) for an ideal system with no decay. Solid lines show the threshold n_c (orange) and error ϵ (black) for the system with decay, including contributions ϵ_D (blue) and ϵ_B (red). Note the linear scale for the threshold axis.

distributed with mean $(R_B + R_D)t_b$, but the distribution for trials initially prepared in the $|D\rangle$ state is modified to contain two terms:

$$D_0(n) = e^{-t_b/\tau} \frac{(R_D t_b)^n e^{-R_D t_b}}{n!} + X_0(n) \quad (3.2)$$

The first term is a Poisson distribution with mean $R_D t_b$ for a dark ion, weighted by the probability $e^{-t_b/\tau}$ that the ion remains shelved throughout t_b . The second term $X_0(n)$ is made up of weighted amounts of Poisson distributions with means between $R_D t_b$ and $(R_B + R_D)t_b$ for occasions when the ion decays at a time $t < t_b$ and begins to fluoresce at a rate R_B . To derive the shape of this distribution, we follow the procedure of C. Langer in [148].

The number of counts n recorded in t_b when an ion decays at a time t is Poisson distributed with mean $\lambda(t)$:

$$\lambda(t) = R_D t_b + R_B(t_b - t) \quad \text{for } 0 \leq t < t_b \quad (3.3)$$

and the probability that the ion decays between t and $t + dt$ is given by:

$$f(t) dt = \frac{1}{\tau} e^{-t/\tau} dt \quad (3.4)$$

We can find the density of means, $g(\lambda)$ in the case that t is a continuous random variable

and $\lambda(t)$ has a simple inverse by [149]:

$$\begin{aligned} g(\lambda) &= f(t(\lambda)) \left| \frac{dt}{d\lambda} \right| \\ &= \frac{1}{R_B \tau} \exp \left(\frac{\lambda - (R_D + R_B)t_b}{R_B \tau} \right) \end{aligned} \quad (3.5)$$

We can then find the $X_0(n)$ term in (3.2) by integrating over all Poisson distributions with means $R_D t_b < \lambda \leq (R_B + R_D)t_b$, weighted by the density of means $g(\lambda)$ from (3.5).

$$\begin{aligned} X_0(n) &= \int_{R_D t_b}^{(R_B + R_D)t_b} g(\lambda) \frac{\lambda^n e^{-\lambda}}{n!} d\lambda \\ &= \frac{e^{-\xi} (R_B \tau)^n}{n!} (R_B \tau - 1)^{-(n+1)} \Gamma(n+1) \times \dots \\ &\quad \dots \left\{ P(\xi(R_B \tau - 1), n+1) - P\left(\frac{R_D t_b}{R_B \tau} (R_B \tau - 1), n+1\right) \right\} \end{aligned} \quad (3.6)$$

where ξ has been used to condense the expression:

$$\xi = \frac{(R_B + R_D)t_b}{R_B \tau}$$

$\Gamma(a)$ is the gamma function and $P(x, a)$ the incomplete gamma function, defined as:

$$P(x, a) = \frac{1}{\Gamma(a)} \int_0^x e^{-m} m^{a-1} dm$$

Figure 3.6 shows plots of $B_0(n)$ and $D_0(n)$ for $t_b = 420 \mu s$ and typical fluorescence rates in our experiment. The optimum threshold n_c where $B_0(n)$ and $D_0(n)$ cross must now be found numerically rather than analytically. Figure 3.5 (solid lines) shows the variation of ϵ (and n_c) with t_b . For short t_b , ϵ is dominated by the statistical errors discussed earlier. Beyond about $320 \mu s$ there is now a penalty to increasing t_b : the increased probability of a $|D\rangle \rightarrow |B\rangle$ transition during the detection period which causes the ion to fluoresce and may cause a count $n > n_c$. Accordingly, ϵ_D is larger than ϵ_B . The cusps in ϵ and sawtooths in ϵ_B and ϵ_D are due to the discrete nature of the distribution and occur when the threshold n_c changes between integer values.

Non-Poissonian counts

In addition to the previous sources of errors discussed, there may be other non-Poissonian noise sources that cannot be included as a simple increase in the background rate R_D but

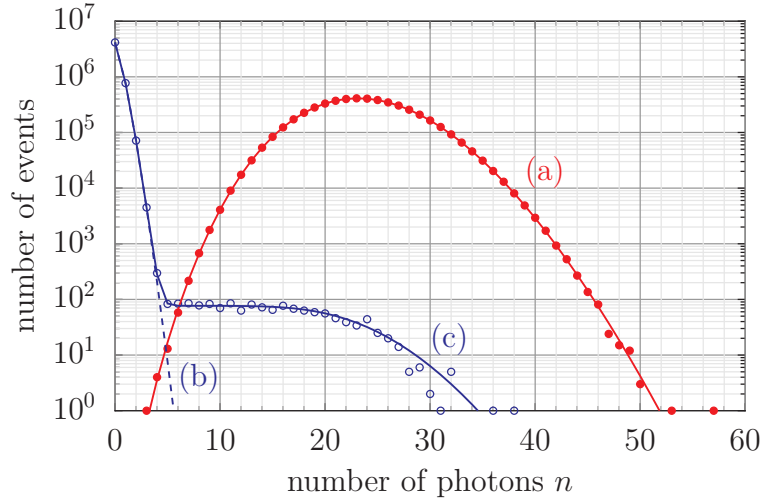


Figure 3.6: Simulated data for 10^7 readout trials, half prepared in $|B\rangle$ (\bullet) and half in $|D\rangle$ (\circ) for typical R_B , R_D and $t_b = 420 \mu\text{s}$. Probability distributions (solid or dashed lines) for (a) $B_0(n)$ (b) $D_0(n)$ with no decay (c) $D_0(n)$ with decay. The asymmetry between ϵ_B and ϵ_D caused by the $|D\rangle \rightarrow |B\rangle$ decay is clear.

instead must be included as alterations to the shapes of $B_0(n)$ and $D_0(n)$. These extra noise sources may cause an increase in ϵ . For photon counting with a photomultiplier tube (PMT) we found an extra non-Poissonian noise source due to cosmic rays, discussed in detail in section 4.1.

3.2.3 Maximum likelihood method

The threshold method does not make use of the information contained in the arrival time of the photons. Using this information we can hope to identify the occasions when the ion decays from the dark to bright state during the counting bin. The bin may contain $n > n_c$ photons in total, but these will tend to be clustered towards the end of the detection period. The use of time-resolved readout for qubit measurement was first suggested by C. Monroe [38] and modelled theoretically by C. Langer [148] and J. Gambetta *et al.* [76].

We gather arrival time information by splitting the total bin time t_b into N short sub-bins of length t_s and recording the set of counts $\{n_i\}$ from sub-bins indexed by i . Dealing with discrete arrival times greatly simplifies the treatment in [148], but otherwise we follow a similar process.

We calculate the likelihood p_B that a particular set of counts $\{n_i\}$ could be generated by an ion prepared in $|B\rangle$ and compare it with p_D , the likelihood that the set could be generated by an ion prepared in $|D\rangle$. If $p_D > p_B$ then the ion is determined to have

been in the state $|D\rangle$ at the start of the counting bin. $p_B = P(\{n_i\} | |B\rangle)$ is calculated as the product of the probabilities of observing n_i counts in each sub-bin i :

$$p_B = \prod_{i=1}^N B(n_i) \quad (3.7)$$

where $B(n_i)$ is the probability of observing n_i counts in a sub-bin from a bright ion. In the ideal case, $B(n_i)$ is a Poisson distribution with mean $(R_B + R_D)t_s$.

The calculation of $p_D = P(\{n_i\} | |D\rangle)$ involves a sum over all possible sub-bins $j = 1, \dots, N$ in which the ion could decay:

$$p_D = e^{-t_b/\tau} \prod_{i=1}^N D(n_i) + \sum_{j=1}^N X(n_j) \prod_{i=1}^{j-1} D(n_i) \prod_{i=j+1}^N B(n_i) \quad (3.8)$$

where $t_b = Nt_s$ and in the ideal case, $D(n_i)$ is a Poisson distribution with mean $R_D t_s$. (Note that we intend that when $j = 1$, the product $\prod_{i=1}^0 D(n_i) = 1$ and when $j = N$ the product $\prod_{i=N+1}^N B(n_i) = 1$.) The quantity $e^{-t_b/\tau}$ is the probability that the ion decays after the last sub-bin has ended. The distribution $X(n_j)$ is the probability that the ion decays in sub-bin j and that n_j counts are recorded in that sub-bin. Since the ion could decay at any time $(j-1)t_s < t \leq jt_s$ in the sub-bin, the distribution $X(n_j)$ can be calculated in a similar way to (3.6) and is given by:

$$\begin{aligned} X(n) &= e^{(1-j)t_s/\tau} \frac{e^{-\zeta} (R_B \tau)^n}{n!} (R_B \tau - 1)^{-(n+1)} \Gamma(n+1) \times \dots \\ &\dots \left\{ P(\zeta(R_B \tau - 1), n+1) - P\left(\frac{R_D t_s}{R_B \tau} (R_B \tau - 1), n+1\right) \right\} \end{aligned} \quad (3.9)$$

where ζ has been used to condense the expression:

$$\zeta = \frac{(R_B + R_D)t_s}{R_B \tau}$$

The probability that the ion decays in sub-bin j is $e^{-jt_s/\tau}(e^{t_s/\tau} - 1)$ and this is included in (3.9) during the derivation. Equation (3.9) correctly reduces to the form for $X_0(n)$ given in (3.6) by making the substitution $t_s \rightarrow t_b$ and setting $j = 1$.

Using the following recursion relation reduces the calculation of p_D from $O(N^2)$ to

$O(N)$ operations which makes real-time readout (and simulations) much faster:

$$p_D = e^{-t_b/\tau} M_N + S_N \quad \text{where} \quad (3.10)$$

$$\begin{aligned} M_0 &= 1, & M_k &= M_{k-1} D(n_k) \\ S_0 &= 0, & S_k &= M_{k-1} X(n_k) + S_{k-1} B(n_k) \end{aligned}$$

Furthermore, various approximations can be made with negligible effect on the analysis results (see section 3.3.1 for justification) and which can speed up calculations. Since $t_s, t_b \ll \tau$ the probability that the ion decays after t_b is approximately $(1 - t_b/\tau)$ and the probability that the ion decays in any sub-bin is approximately (t_s/τ) . If the sub-bins are short then we can also assume that when a decay happens, the count rate changes from R_D to R_B at the start of the sub-bin; this eliminates the need for the complicated distribution $X(n_j)$ in (3.9). We can then substitute $(t_s/\tau)B(n_j)$ for $X(n_j)$ in (3.8) and the calculation of p_D becomes:

$$p_D = \left(1 - \frac{t_b}{\tau}\right) \prod_{i=1}^N D(n_i) + \left(\frac{t_s}{\tau}\right) \sum_{j=1}^N \prod_{i=1}^{j-1} D(n_i) \prod_{i=j}^N B(n_i) \quad (3.11)$$

The recursion relations are now simplified to:

$$p_D = (1 - t_b/\tau) M_N + (t_s/\tau) S_N \quad \text{where} \quad (3.12)$$

$$\begin{aligned} M_0 &= 1, & M_k &= M_{k-1} D(n_k) \\ S_0 &= 0, & S_k &= (S_{k-1} + M_{k-1}) B(n_k) \end{aligned}$$

Figure 3.7 shows the variation of ϵ with t_b for a maximum likelihood analysis of 10^8 simulated trials. In common with the threshold method for short t_b , ϵ is dominated by statistical errors. However, beyond $320 \mu\text{s}$ there is now no penalty to increasing t_b : the increasing number of $|D\rangle \rightarrow |B\rangle$ transitions are recognised by the maximum likelihood method and correctly identified.

If there were additionally an appreciable rate of pumping $|B\rangle \rightarrow |D\rangle$, we could also modify p_B to include this and take a form similar to (3.8). We do not include these extra terms in p_B for this thesis as the rate is so low in our experiments; see section 3.3.1.

The maximum likelihood method can still be used when there is no state-to-state

pumping at all. In this case it is exactly equivalent to the threshold method discussed in section 3.2.2 when there are statistical errors only. For this scenario, we use $p_B = \prod_{i=1}^N B(n_i)$ and $p_D = \prod_{i=1}^N D(n_i)$. For the special case when $B(n_i)$ and $D(n_i)$ are both Poisson distributions then it is easy to show that requiring $p_B/p_D > 1$ is the same as the condition $n_{tot} > n_c$ where the total number of counts in t_b is $n_{tot} = \sum_{i=1}^N n_i$ and n_c is the same count threshold that we derived in (3.1).

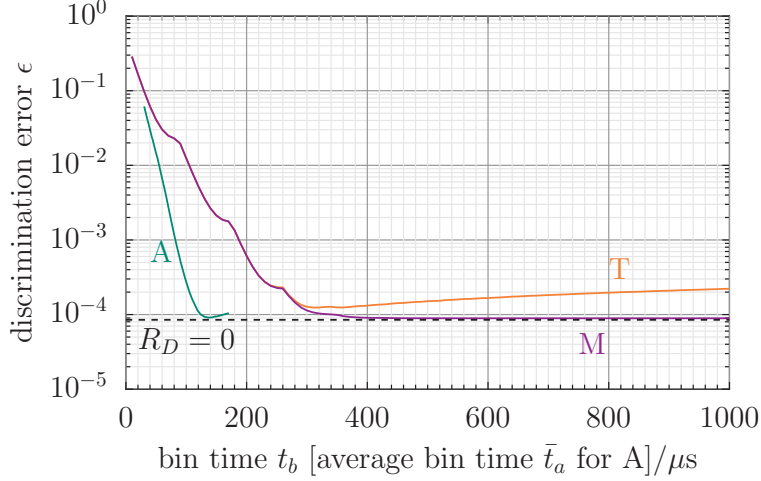


Figure 3.7: Variation of discrimination error with bin time simulated for typical R_B , R_D in our experiment using the simulation methods described in section 3.3 with 10^8 simulated trials. T: Threshold method (orange), M: Maximum likelihood method (purple), A: Adaptive maximum likelihood method (green). Dashed line: minimum error possible for zero background ($R_D = 0$).

3.2.4 Adaptive maximum likelihood method

The values of p_B and p_D calculated in a maximum likelihood procedure can give us a measure of confidence about the individual readout measurement that we are analysing. The quantity $p_B = P(\{n_i\} | |B\rangle)$ is the probability of recording the counts $\{n_i\}$ from an ion that was prepared in $|B\rangle$. We can use Bayes' theorem to calculate the inverse, namely the probability that the ion was prepared in $|B\rangle$, given that we recorded a signature $\{n_i\}$:

$$P(|B\rangle | \{n_i\}) = \frac{P(\{n_i\} | |B\rangle)}{P(\{n_i\})} = \frac{p_B}{p_B + p_D}$$

We can use this to calculate the *estimated* error probability e_B that we have incorrectly deduced the ion to be bright when $p_B/p_D > 1$:

$$e_B = 1 - P(|B\rangle | \{n_i\}) = \frac{p_D}{p_B + p_D} \quad (3.13)$$

and similarly for e_D . Using the recursion relations (3.12) we can evaluate p_B , p_D in $< 1 \mu s$, which is $< t_s$, so there is negligible classical computing time overhead and we can evaluate the estimated error while the measurement is in progress. This information can be used to terminate detection at $t_a < t_b$ when the estimated error for the state (the lower of e_B and e_D) falls below some required cutoff e_c . This “adaptive” technique was suggested and demonstrated by Hume *et al.* in [42]. It is also necessary to impose a cutoff time $t_c \leq t_b$ in case the threshold error is not reached. t_c is therefore the worst-case readout time, but most trials will be terminated before this time is reached, resulting in an average readout time \bar{t}_a which is shorter than when the bin-length is fixed.

We find that faster detection is possible with little increase in ϵ by omitting the effect of spontaneous decay in the calculation of p_D , instead using $p_D = \prod_{i=1}^N D(n_i)$. This is discussed further in section 3.3.1. The variation of ϵ with average readout time \bar{t}_a is shown in figure 3.7, where simulations were made for different values of e_c in the range 10^{-6} to 10^{-1} and fixed $t_c = 650 \mu s$. The adaptive method reaches $\epsilon = 10^{-4}$ at $e_c = 0.7 \times 10^{-4}$, where $\bar{t}_a = 124 \mu s$.

In section 3.2.3 we noted that when the effect of spontaneous decay is omitted in the analysis, requiring $p_B/p_D > 1$ is the same as the condition $n_{tot} > n_c$ where n_c is given by (3.1). In the adaptive method, then, requiring $e_B \leq e_c$ is approximately the same as requiring $p_B/p_D \geq 1/e_c$ (since $p_B \gg p_D$) which is equivalent to the condition $n_{tot} \geq n_c^B$ where:

$$n_c^B(t_b) = \frac{R_B t_b - \ln(e_c)}{\ln\left(1 + \frac{R_B}{R_D}\right)} \quad (3.14)$$

Similarly, $e_D \leq e_c$ is approximately equivalent to the condition $n_{tot} \leq n_c^D$ where:

$$n_c^D(t_b) = \frac{R_B t_b + \ln(e_c)}{\ln\left(1 + \frac{R_B}{R_D}\right)} \quad (3.15)$$

The two thresholds n_c^B and n_c^D are equally spaced about n_c by $\pm \ln(e_c)/\ln(1 + R_B/R_D)$ and all three thresholds increase linearly as t_b increases. The adaptive method then becomes simply a case of counting photons until n_{tot} is greater than n_c^B or less than n_c^D —a simple extension of the threshold method to three time-dependent thresholds. If neither n_c^B nor n_c^D is reached before the time t_c , the measurement can still be assigned a state by comparing n with the central threshold n_c . Each trial can be visualised as a

trajectory of cumulative photon counts on a diagram similar to that in figure 3.8.

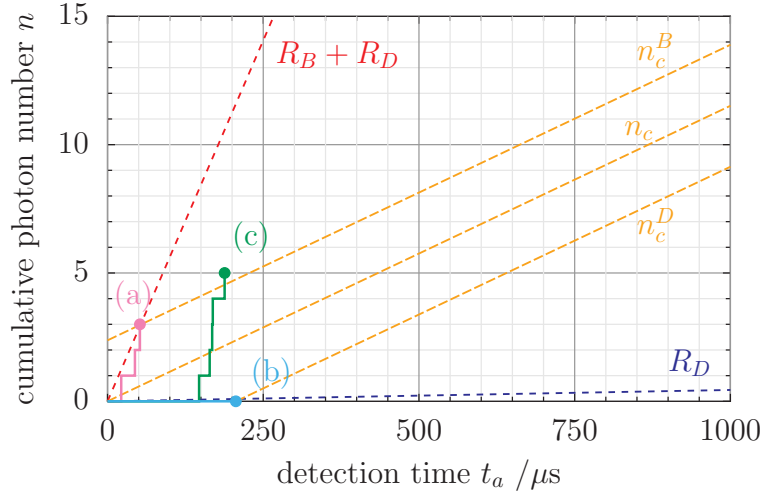


Figure 3.8: Visualising the adaptive analysis as a triple-threshold method. Threshold n_c lines (orange, dashed) are shown for $e_c = 10^{-5}$ and average trajectories for readout trials with typical photon count rates ($R_B + R_D$) (red, dashed) and R_D (blue, dashed) in our experiment are shown. Three simulated example trajectories are shown (solid lines): (a) bright trial prepared in $|B\rangle$, (b) dark trial prepared in $|D\rangle$, (c) trial prepared in $|D\rangle$ which decays 144 μs into the trial and is incorrectly identified as bright. The dot (\bullet) at the end of each trajectory indicates where the measurement is terminated as sufficient confidence is reached.

Trials prepared in $|B\rangle$ will on average follow a trajectory with a gradient $R_B + R_D$, while trials prepared in $|D\rangle$ will follow a trajectory with a gradient R_D unless a decay occurs, after which the gradient will change to $R_B + R_D$. One can immediately see that in general only decays that occur before the intercept of n_c^D with the time axis can cause an error and that almost all such decays will do so. This occurs at $t_a = -\ln(e_c)/R_B \approx 206 \mu\text{s}$. From this, we can make an estimate of the upper limit of the decay contribution to ϵ_D , assuming all trials with decays before 206 μs cause errors. The probability of a shelved ion decaying before this time gives an upper contribution to ϵ_D of 1.77×10^{-4} . From simulations of 10^8 trials, $\epsilon_D = 1.67(2) \times 10^{-4}$ which is close to our simple estimate.

It is also apparent from the typical trajectories in figure 3.8 that average detection times for the $|D\rangle$ state will be longer than for the $|B\rangle$ state. This is because to attain a level of certainty for $|D\rangle$ state measurement, one must wait for a sufficient number of bins with $n = 0$ photons in and these are also fairly common from our typical R_B rate for an ion in $|B\rangle$.

One can also see that a bright \rightarrow dark rate, if present, will lead to fewer errors than the same dark \rightarrow bright rate, since the bright \rightarrow dark transition must occur within a shorter average detection time for the $|B\rangle$ state.

3.3 Simulations

The data plotted in the figures in the preceding section 3.2 were produced by computationally simulating the readout process. The discrimination error ϵ achievable with the threshold method described in section 3.2.2 and plotted in figure 3.5 can be found directly from knowledge of the distributions $B_0(n)$ and $D_0(n)$ for trials prepared in $|B\rangle$ and $|D\rangle$ respectively. In the case of no pumping between states, the threshold n_c for a given t_b is given by (3.1) and ϵ is found by combining ϵ_B and ϵ_D , calculated as:

$$\epsilon = (\epsilon_B + \epsilon_D)/2; \quad \epsilon_B = \sum_{n < n_c} B_0(n), \quad \epsilon_D = \sum_{n > n_c} D_0(n) \quad (3.16)$$

When $|D\rangle \rightarrow |B\rangle$ decay is included, $D_0(n)$ is calculated by (3.2) and the optimum threshold n_c must be obtained computationally by finding where $B_0(n)$ and $D_0(n)$ cross which minimises ϵ in (3.16).

The errors achieved in maximum likelihood analyses such as those in sections 3.2.3 and 3.2.4 cannot be found analytically, so Monte Carlo (M-C) simulations were performed using a program written in the Fortran 95 language and using the NAG Fortran library² to provide a more reliable random number generator than the standard Fortran routine.

Simulations proceeded by generating trials consisting of N_{tot} sub-bins of length t_s . As each trial was generated it was immediately analysed by a selection of analysis methods; the number of incorrect measurement outcomes for each method was recorded to give a measurement of ϵ . For each trial the analysis was performed for a variety of bin times $t_b = Nt_s$ by changing the number of sub-bins included $1 \leq N \leq N_{\text{tot}}$. For most simulations, including those plotted in figure 3.7, $N_{\text{tot}} = 200$ and $t_s = 10 \mu\text{s}$ to match the experiment described in section 4.2. As M-C trials were generated, the counts $n = \sum_{i=1}^N n_i$ for a range of N were histogrammed to provide simulated histograms such as the example in figure 3.6. These histograms could be used to perform another threshold analysis on the simulated data to check consistency with the analytical method above (3.16).

Bright trials prepared in $|B\rangle$ were created by picking N_{tot} random numbers from $B(n)$, a Poisson distribution of mean $(R_B + R_D)t_s$. To generate a trial initially prepared

²Numerical Algorithms Group: <http://www.nag.co.uk/>

in $|D\rangle$, a random number was first picked from an exponential distribution (3.4) to provide the decay time t_* of the ion. If this was larger than $N_{\text{tot}}t_s$ then a completely dark trial was generated by picking N_{tot} random numbers from $D(n)$, a Poisson distribution of mean $R_D t_s$. However, if the decay of the ion occurred earlier, in sub-bin j , then for sub-bins before j random numbers were picked from $D(n)$ and for sub-bins after j numbers were picked from $B(n)$. For sub-bin j itself, a random number was picked from a Poisson distribution with mean $(R_D + (jt_s - t_*)R_B)t_s$.

Example code for M-C simulations is included in appendix A. A selection of simulation results were checked by comparing the results with output from an independent simulation program written by Dr David Lucas. This program generated trials by picking photon arrival-times from exponential distributions e^{-Rt} using an independent random number generator. The results agreed within the statistical error.

3.3.1 Justifications for analysis approximations

Approximations in calculating likelihoods

In calculating the likelihoods p_B, p_D for the maximum likelihood analysis using (3.12) we made two assumptions: that $t_s, t_b \ll \tau$ and that when a decay happens, the count rate changes from R_D to R_B at the start of the sub-bin. To check that these simplifications would not significantly alter the value of ϵ obtained, the results of maximum likelihood analyses with and without the approximations (using (3.12) and (3.10) respectively) were compared for the same set of 10^7 M-C simulated trials with $N_{\text{tot}} = 200$, $t_s = 10 \mu\text{s}$, $R_B = 55800 \text{ s}^{-1}$ and $R_D = 442 \text{ s}^{-1}$. There were some slight differences in ϵ_B and ϵ_D between the methods but these variations were always smaller than the statistical uncertainties. The deviations in ϵ_B and ϵ_D for each t_b usually occurred in opposite directions meaning that overall there was little change to ϵ . The largest overall deviation in ϵ was seen at $t_b = 370 \mu\text{s}$, where $\epsilon = 8.9(3) \times 10^{-5}$ and the difference between the two methods was 2×10^{-7} , more than an order of magnitude below the statistical uncertainty.

Neglecting $|B\rangle \rightarrow |D\rangle$ pumping rate in simulations and analyses

The discussion of analysis methods in this chapter has assumed the rate of $|B\rangle \rightarrow |D\rangle$ pumping is negligible, so it has been excluded from both simulations and likelihood calculations. Only $|D\rangle \rightarrow |B\rangle$ pumping has been considered. Section 4.3.3 discusses

measurement of the $|B\rangle \rightarrow |D\rangle$ pumping rate in our experiment and finds an upper limit³ on this rate of 10^{-3} s^{-1} . Would this rate of transitions have a significant effect on the value of ϵ deduced from our experiment? To answer this question, two sets of 10^7 M-C simulated trials were generated with parameters chosen to match the experimental data presented in chapter 4. The first set included $|B\rangle \rightarrow |D\rangle$ transitions at a rate of 10^{-3} s^{-1} as well as $|D\rangle \rightarrow |B\rangle$ decays at a rate of $1/\tau$, while the second set had only the $|D\rangle \rightarrow |B\rangle$ decays. In the first set of simulated data, $|B\rangle \rightarrow |D\rangle$ transitions occurred in 9 trials and the optimum discrimination error was found to be $\epsilon = 8.9(3) \times 10^{-5}$ at $t_b = 530 \mu\text{s}$ using a maximum likelihood analysis. There was no statistically significant difference in ϵ found for the first data set whether or not $|B\rangle \rightarrow |D\rangle$ transitions were included in the calculation of p_B . In the second data set, the optimum error was found to be $\epsilon = 8.5(3) \times 10^{-5}$ with the same bin time. The values of ϵ for the two simulations agree within the uncertainties, so $|B\rangle \rightarrow |D\rangle$ pumping was not included in any further simulations or analyses.

Neglecting $|D\rangle \rightarrow |B\rangle$ pumping in the adaptive analysis method

When using the adaptive analysis method, we find that faster detection is possible with little increase in ϵ by omitting the effect of spontaneous decay in the calculation of p_D using $p_D = \prod_{i=1}^N D(n_i)$. This is because the adaptive technique allows detection to finish on a timescale even shorter compared with the decay time τ , so negligible improvement is gained by the inclusion of decay terms in (3.8). Rather, these extra terms slow the progress of the estimated error towards e_c as extra information must be collected to distinguish between an ion initially in $|B\rangle$ and an ion which has decayed to that state. Using M-C simulations, a comparison was made between adaptive analyses with and without the inclusion of decay in the likelihood calculation. A large range of parameters was explored (see section 3.3.3) and a selection of representative plots is shown in figure 3.9.

An analysis omitting decay (method A) still reaches a minimum ϵ that is within 10% of the asymptotic error obtained using the method which includes decay (method AD). Method A reaches this minimum in a shorter average detection time (visible in figure 3.9), typically $\sim 30\%$ shorter than the time it takes method AD to reach within 10% of

³The rate of $|B\rangle \rightarrow |D\rangle$ transitions seen in our experimental data is expected to be even lower than this, for reasons discussed in section 4.3.3.

its asymptote.

Requiring an estimated error cutoff e_c that is too low results in a larger \bar{t}_a . When decay is included in the analysis, this has no effect on the final ϵ reached. However, when decay is omitted, this larger \bar{t}_a results in an increase in ϵ due to the increased probability of decay during the detection period; this is the reason for the slight upwards curve for method A on figure 3.9 at larger \bar{t}_a . We must therefore make a careful choice of e_c to attain the lowest ϵ . We gain a speed-up in detection by omitting decay from the likelihood calculations, but this comes at the expense of increased sensitivity to the analysis parameters (namely, choice of e_c).

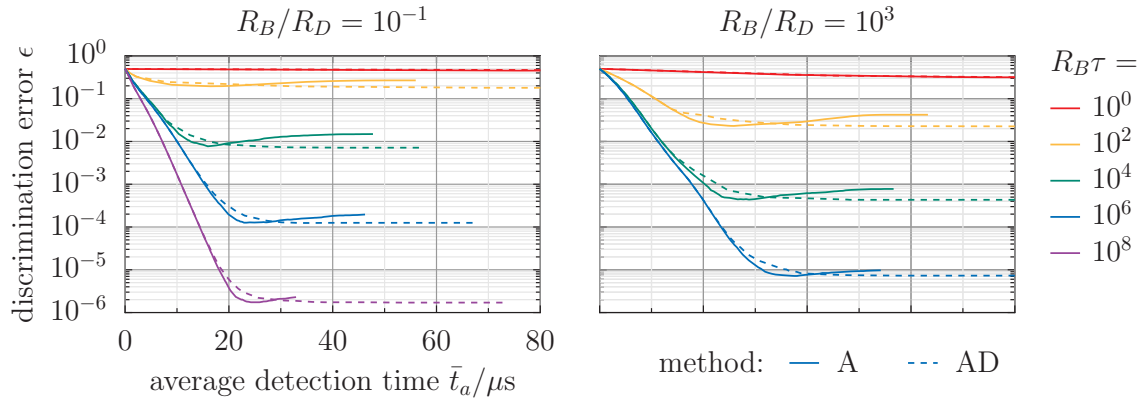


Figure 3.9: The variation of ϵ with average readout time \bar{t}_a for adaptive analyses of simulated trials, both including (AD) and ignoring (A) decay in the calculation of p_D . The data points comprising each curve are generated by varying e_c in the range 10^0 to 10^{-9} , where demanding a lower e_c results in a longer average bin time \bar{t}_a . Error bars due to statistical uncertainty are too small to show on the plot.

Number of sub-bins required for maximum likelihood analysis

When preparing to read out a qubit using a maximum likelihood analysis we gather arrival time information by splitting the total bin time t_b into N short sub-bins of length t_s . The integration time t_b necessary to reach the minimum possible discrimination error ϵ is determined by the rates R_B and R_D (investigated in more detail in the following section 3.3.3); however to reach this minimum ϵ , t_b must be divided into enough sub-bins which are also of short enough length compared with τ . In principle there is no limit to how short t_s may be, as long as N can be made large enough to enable the required integration time $t_b = Nt_s$ to be attained. If t_s is chosen to be too long then decays within the first sub-bin will start to contribute significantly, raising ϵ . As well as satisfying $t_b = Nt_s$, the number of sub-bins N must be large enough to provide good

temporal resolution when calculating the likelihoods.

Figure 3.10 shows the results of several sets of 10^7 simulated trials with different values of t_s between $10\ \mu\text{s}$ and $1\ \text{ms}$ for typical rates in our apparatus $R_B = 55800\ \text{s}^{-1}$ and $R_D = 442\ \text{s}^{-1}$. Each set of simulations was analysed with $1 \leq N \leq 100$ and a selection of these analyses are shown in the figure. For low t_s the lowest possible ϵ (marked “target”) should be accessible, but for analyses which also have a low N the short integration time prevents this limit being reached. At longer t_s , the ϵ achieved increases as decays within the first sub-bin begin to contribute. An upper limit on the contribution to ϵ from decays is marked on the plot as $\frac{1}{2}(1 - e^{-t_s/\tau})$, which assumes all decays within t_s cause an error.

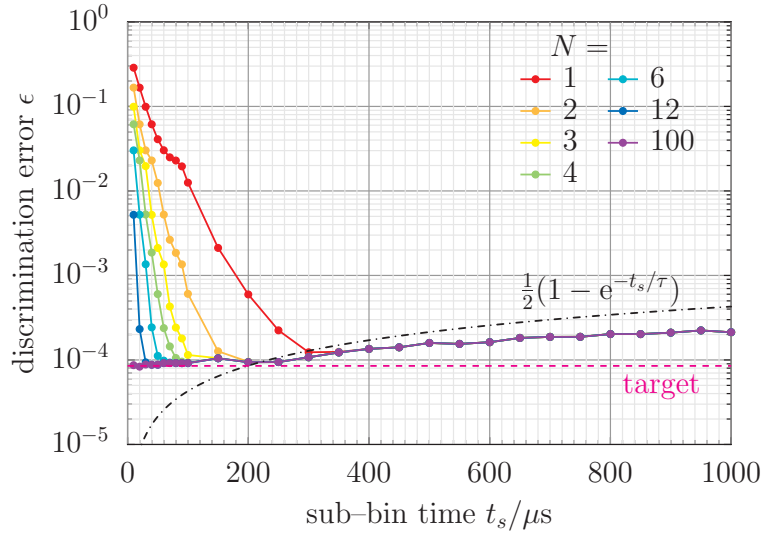


Figure 3.10: Analyses of sets of 10^7 simulated trials with varying t_s and varying numbers of sub-bins N . An upper limit on the contribution to ϵ from decays is shown (dash-dotted line) and the lowest possible ϵ is marked as “target” (dashed line). Statistical errors are at most the size of the symbols.

It is clear from figure 3.10 that an analysis with $N = 100$ enables us to reach the lowest ϵ possible. Is it possible to reach this error with a smaller N ? Figure 3.11 shows the lowest ϵ it is possible to reach for an analysis with N sub-bins when the optimum t_s is chosen. These data are the lowest points on each curve in figure 3.10. The lowest ϵ is reached when we have $N \geq 24$ for $t_s = 20\ \mu\text{s}$.⁴ Therefore, a choice of $t_s \leq 20\ \mu\text{s}$ and N sufficiently large to enable us to reach $t_b \geq (24 \times 20)\ \mu\text{s}$ will enable the lowest possible ϵ to be measured for the rates R_B and R_D seen in our apparatus. However, it is remarkable that even $N = 2$ sub-bins are sufficient to achieve $\epsilon < 10^{-4}$, provided the

⁴One would expect the optimum t_s to be $10\ \mu\text{s}$, the smallest value simulated. The difference in ϵ between the simulations with $t_s = 10, 20\ \mu\text{s}$ is within the statistical error.

correct t_s is chosen.

With only one sub-bin ($N = 1$) the maximum likelihood method is identical to the threshold method and the right choice of $t_s = t_b$ is critical to achieve the lowest ϵ . This is true in general—fewer sub-bins imply more sensitivity to the choice of t_s , as can be seen by the widths of the minima in figure 3.10. Subdividing t_b into more sub-bins than is strictly necessary (i.e. a larger N) makes the choice of t_s less critical whilst providing a finer time resolution to spot cosmic rays (see section 4.1).

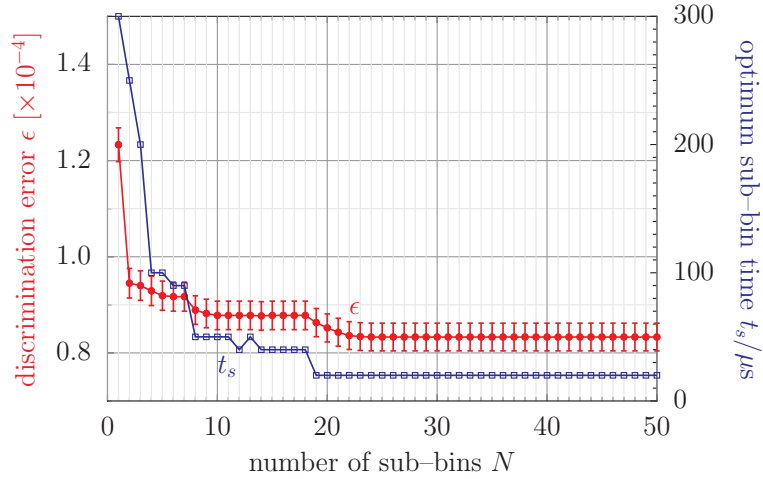


Figure 3.11: The lowest discrimination error ϵ attainable in experiments including N_{tot} sub-bins when the optimum sub-bin time t_s is chosen. The lowest ϵ is reached by $N = 24$. Based on sets of 10^7 simulated trials with varying t_s .

3.3.2 Sensitivity to analysis parameters

The simulations presented above demonstrate that the maximum likelihood method becomes relatively insensitive to the exact choice of t_s and t_b when the time resolution is fine enough. In contrast, the threshold method requires a more precise choice of t_b and also a threshold n_c (to which it is *very* sensitive). The maximum likelihood method requires instead the rates R_B and R_D to build the analysis distributions. We now investigate the sensitivity of the maximum likelihood method to these rates by performing M-C simulations with rates and parameters to match the series II experimental run described in the following chapter: $N_{\text{tot}} = 200$, $t_s = 10 \mu\text{s}$, $R_B = 55800 \text{ s}^{-1}$ and $R_D = 442 \text{ s}^{-1}$. These simulated trials were then analysed with the maximum likelihood method using a choice of $\{R'_B, R'_D\}$ which did not match the input parameters. R'_B and R'_D were varied separately and the results are shown in figure 3.12 where they are compared with the effect of varying t_b and n_c for the threshold method. The data in

figure 3.12(c) are formed from 10^9 simulations, half prepared in $|B\rangle$ and half in $|D\rangle$. Outside this region, only 10^8 simulations were made. Overall, the threshold method is more sensitive to its input parameters than the maximum likelihood method. Indeed, the choice of R'_D hardly affects the outcome for our simulation parameters. Although changing R_B by $\sim 10\%$ generates a comparable percentage change in the discrimination error ϵ , we emphasise that since the minimum value $\epsilon = 8.85(3) \times 10^{-5}$ is already very small in absolute terms, a 10% increase still does not take it above the 10^{-4} level.

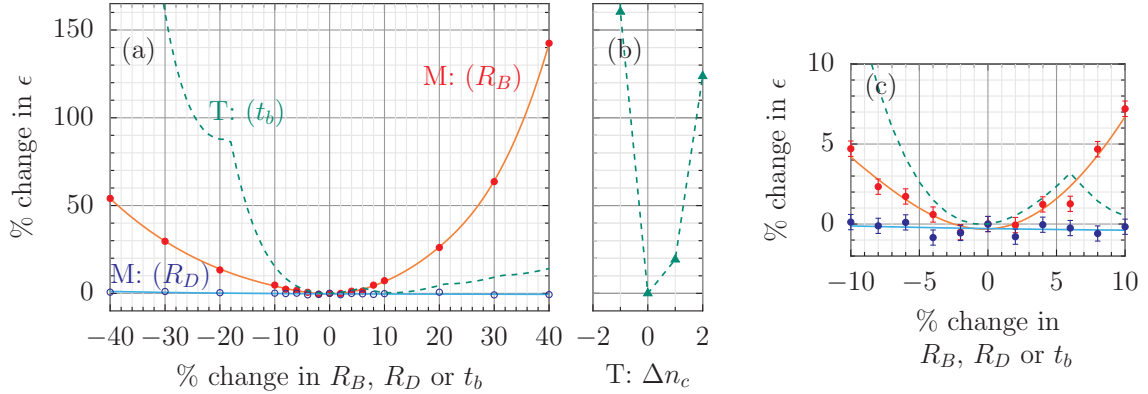


Figure 3.12: Simulations showing sensitivity of analysis methods to input parameters. (a) Consequence for discrimination error ϵ when varying analysis parameters R_B and R_D for the maximum likelihood method M away from their true values and for the threshold method T (dashed lines) when choosing non-optimal t_b and (b) threshold n_c . (c) Central region of plot (a) in more detail. Solid lines show spline fits to guide the eye, data points are from M-C simulations. If not shown, error bars are smaller than the point size.

3.3.3 Dependence of error on experimental parameters

If it were not for the $|D\rangle \rightarrow |B\rangle$ pumping, we would be able to reach an arbitrarily low discrimination error ϵ by increasing the bin time t_b . The lifetime τ of the $|D\rangle$ state against decay effectively limits ϵ and sets the timescale for the detection problem. The fidelity and speed of detection are also limited by the rates at which we collect fluorescence and background photons compared to τ , given by $R_B\tau$ and $R_D\tau$ respectively. These effects are considered in the remainder of this chapter.

No background counts

The special case where $R_D = 0$ provides an insight into how ϵ depends on the fluorescence rate $R_B\tau$. This has been studied analytically by Langer [148] for continuous detection based on photon arrival times; a summary of his work is provided here. When $R_D = 0$, once the first photon has been detected at t_1 then the ion must be in the bright state

$|B\rangle$ for the remainder of the counting period. The probabilities of detecting photons after t_1 are taken from the bright distribution, so the likelihood is the same for p_B and p_D . Therefore, we need only consider the arrival time of the first photon at t_1 . The probability of detecting a photon from an ion in state $|B\rangle$ between t and $t + dt$ is given by:

$$p_B(t) dt = R_B e^{-R_B t} dt \quad (3.17)$$

If the ion was initialised in $|D\rangle$ at $t = 0$ then the probability of detecting a photon between t and $t + dt$ is given by:

$$\begin{aligned} p_D(t) dt &= \left(\int_0^t f(t') p_B(t - t') dt' \right) dt \\ &= \left(\int_0^t f(t') e^{R_B t'} dt' \right) p_B(t) dt \\ &= M(t) p_B(t) dt \end{aligned} \quad (3.18)$$

where $f(t')$ is the probability that the ion decayed from $|D\rangle$ to $|B\rangle$ between t' and $t' + dt'$ (see (3.4)) and $p_B(t - t')$ is the probability of detecting a photon a certain time after the decay (this is (3.17) with a shifted origin). The product of these is then integrated over all possible decay times up to when the photon was detected. The criterion to decide if the ion was prepared in $|D\rangle$ is $p_D/p_B > 1$ or $M(t) > 1$. $M(t)$ is a monotonically increasing function with t , so the criterion for an ion to be identified as dark is equivalent to the first photon arriving with $t_1 > t_c$ where $M(t_c) = 1$, giving:

$$t_c = \frac{\tau}{R_B \tau - 1} \ln(R_B \tau) \quad (3.19)$$

The discrimination error for state $|D\rangle$ is $\epsilon_D = \int_0^{t_c} p_D(t) dt$, the probability of detecting a photon before t_c , and similarly for $\epsilon_B = \int_{t_c}^{\infty} p_B(t) dt$. This gives a total error of:

$$\begin{aligned} \epsilon &= \frac{1}{2} (1 - e^{-t_c/\tau}) \\ &= \frac{1}{2} \left(1 - (R_B \tau)^{(1 - R_B \tau)^{-1}} \right) \end{aligned} \quad (3.20)$$

It is interesting to note that ϵ is one-half times the probability that an ion prepared in $|D\rangle$ decays before t_c . Since for reasonable values of $R_B \tau$ we have $t_c \ll \tau$, then $\epsilon \approx \frac{1}{2} (t_c/\tau)$. This limiting error (3.20) is plotted in figure 3.13 and decreases as $R_B \tau$

increases. This is because photons can be detected more rapidly compared with the $|D\rangle$ state lifetime τ .

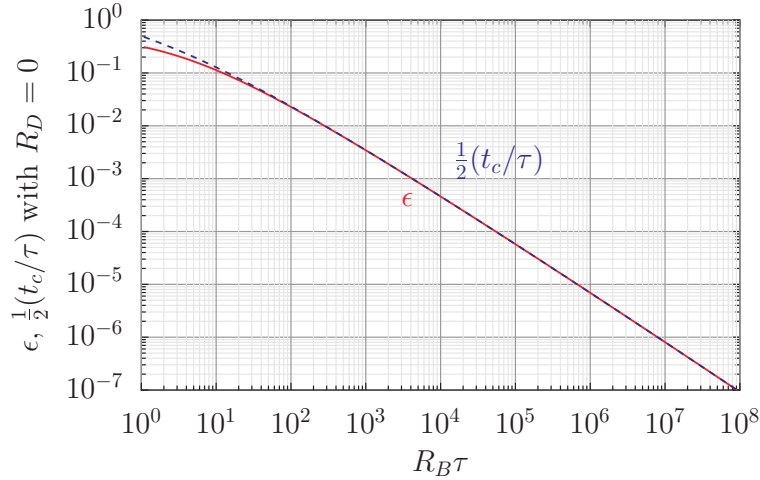


Figure 3.13: The variation of ϵ with changing $R_B\tau$ for $R_D = 0$ using (3.20) and the threshold time in (3.19) from Langer [148].

This limiting error is also shown on figure 3.7 for typical R_B in our experiment, and also on figure 3.14, where it is labelled as $R_B/R_D = \infty$.

Non-zero background counts

The value of ϵ in (3.20) gives a lower limit to the discrimination error possible; in general there will be a non-zero R_D that will affect the fidelity and speed of state detection. The effects of changing R_B and R_D were investigated using the simulation methods described at the start of section 3.3. The rates and times are all given in units of τ^{-1} and τ .

The effects of changing R_B and R_D for the maximum likelihood protocol were investigated by performing M-C simulations. The total number of sub-bins simulated was set to be $N_{\text{tot}} = 200$, and the sub-bin length t_s was chosen so that there would be $N \approx 100$ at the optimum t_b (lowest ϵ) to provide adequate time resolution for the likelihood calculations. The value of t_s was also chosen short enough that the estimated error caused by decays within the first sub-bin $\frac{1}{2}[1 - \exp(-t_s/\tau)]$ was at least an order of magnitude lower than the final ϵ attained. The version of p_D given in (3.8) was used without the approximations discussed in section 3.3.1 as t_s could be an appreciable fraction of τ . The number of M-C trials generated for each point was chosen so that the statistical uncertainty in ϵ was an order of magnitude smaller than its value⁵.

⁵The choice of t_s and the number of trials do take a few iterations to get right!

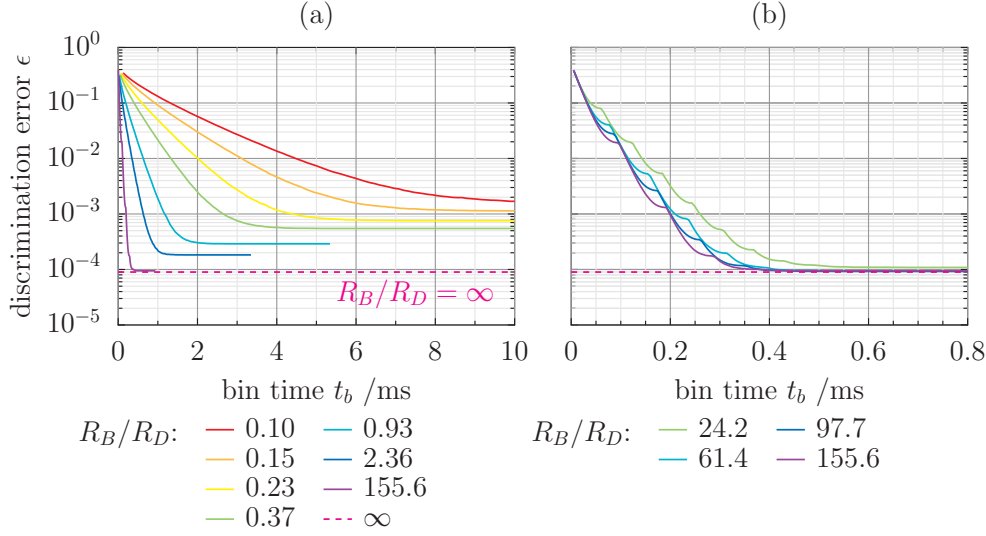


Figure 3.14: Results of a maximum likelihood analysis of simulated data showing discrimination error ϵ with bin time t_b for $R_B = 52500 \text{ s}^{-1}$ ($\tau = 1.168 \text{ s}$) and increasing R_D . (a) Variation over wide range of signal-to-background ratios. (b) Variation with reasonably large signal-to-background ratios.

Figure 3.14 shows the results of several simulations with a constant value of R_B and increasing signal to background ratios R_B/R_D . Figure 3.14(a) shows the results of simulations over a wide range of R_B/R_D . As the rate of background counts R_D increases, both the minimum ϵ and the time taken to reach it increase. This is because as R_D increases the difference between the net count rates R_D and $R_D + R_B$ (for ions in $|D\rangle$ and $|B\rangle$ respectively) does not change, but the variance σ^2 of both the Poisson distributions increases so a longer integration time is required to gather enough photons to distinguish between them. The longer detection period increases the probability of decay during the counting bin; the result is a higher ϵ . As R_D becomes small, ϵ tends towards the limit in (3.20).

The variation of the discrimination error ϵ (reached asymptotically for long t_b) with $R_B\tau$ and R_B/R_D is shown for the maximum likelihood method in figure 3.15, while figure 3.16 shows the time $t_{1.1}/\tau$ necessary to reach within 10% of this asymptotic error. Once a reasonable R_B/R_D has been reached the contours on figure 3.15 become nearly vertical indicating that the discrimination error becomes largely independent of the background count rate R_D and tends towards that for the $R_D = 0$ case, shown on the upper bar of the plot. The solid curve shows the parameter range accessible in our apparatus by varying the laser power at 397 nm, modelled by equation (4.2). This curve reaches a maximum signal-to-background ratio R_B/R_D , after which it decreases due to

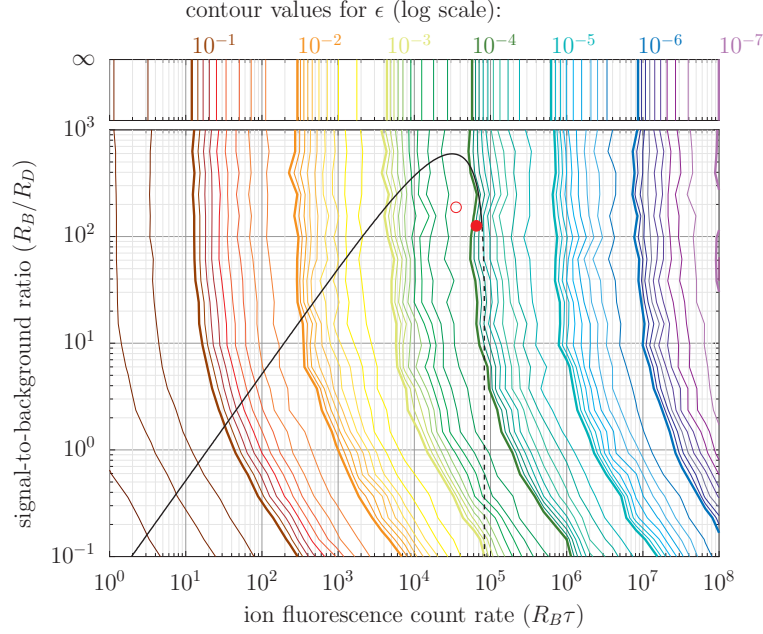


Figure 3.15: Contours showing the minimum ϵ possible (asymptotically approached as $t_b/\tau \rightarrow \infty$) for the *maximum likelihood method* from M-C simulations over a 28×21 grid. We express the fluorescence rate R_B in units of the $|D\rangle \rightarrow |B\rangle$ decay rate τ^{-1} so that the plot is a “universal” one for all similar ion species. Values of the bold contours are labelled at the top of the plot. The upper bar shows ϵ at $R_D = 0$. The solid black line shows the upper boundary of the region accessible by varying 397 nm laser power in our apparatus as used for the series II set of experiments described in chapter 4; the dotted line is an extrapolation to extreme laser powers. Also marked are the parameters for our experiments: (○) series I, (●) series II.

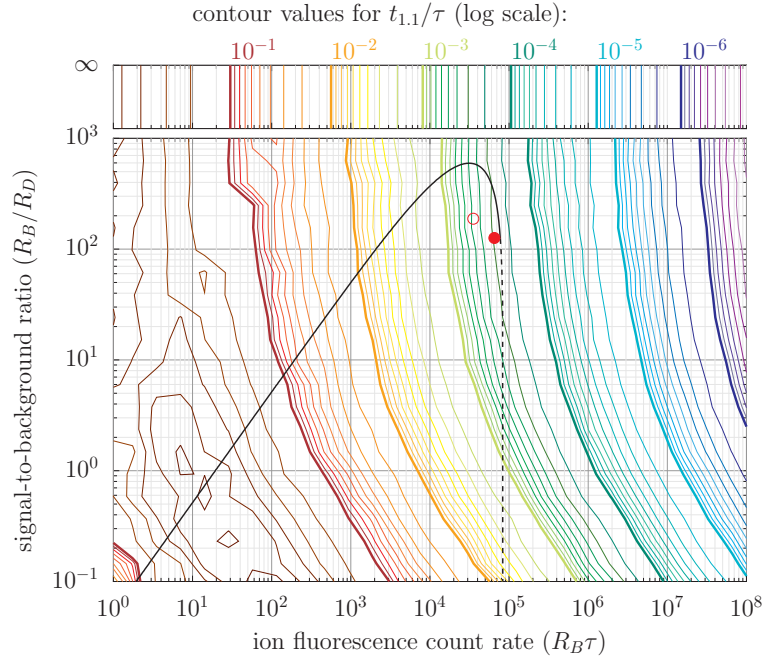


Figure 3.16: Contour plot showing $t_{1.1}/\tau$ necessary for the *maximum likelihood method* to reach within 10% of the asymptotic error shown in figure 3.15. The somewhat disrupted shapes of the contours in the region with low R_B/R_D and low $R_B\tau$ (bottom left corner of the plot) are due to the coarse grid used and the statistical error in the simulations (see text).

saturation of the atomic transition. However, because ϵ is almost independent of R_D in this region, the lowest discrimination error is obtained by using a higher laser power to reach a higher R_B , *rather than optimising the signal-to-background!* The minimum ϵ occurs with R_B/R_D about an order-of-magnitude below its optimum. In this case, we can reach a lower ϵ because photons can be detected more rapidly compared with τ . Above $R_B/R_D \approx 10$, the best figure of merit is $R_B\tau$, rather than R_B/R_D .

In our experiment, typically $R_B/R_D > 100$ and we find that slightly increasing R_D only acts to slow detection of the $|D\rangle$ state. Figure 3.14(b) shows the results of simulations with a variety of R_B/R_D values and R_B similar to that in our experiments. The plot shows that increasing R_D in this regime mostly causes an increase in the time t_b taken to reach minimum ϵ .

The kinks in the contours in figures 3.15 and 3.16 are due in part to the coarse grid used, but are mostly due to the relatively large ($\sim 10\%$) statistical error in ϵ from the simulations⁶.

Figure 3.17 shows the variation of ϵ with $R_B\tau$ and R_B/R_D for simulations of the threshold method over a 133×100 grid. These simulations do not involve the slow generation of simulated trials, so there is negligible uncertainty in the values of ϵ plotted. The contours of ϵ are smoother and tend towards those for $R_D = 0$. Figure 3.18 shows the optimum (t_b/τ) needed to reach the lowest ϵ ; the kinks in the contours are due to the discrete changes in the integer threshold.

Since ϵ decreases with increasing $R_B\tau$, a significant improvement could be made to readout fidelity and speed by increasing collection efficiency. Figure 3.19 shows the result of simulations investigating the relationship between the net collection efficiency η and the asymptotic error ϵ_∞ possible with the maximum likelihood method; also shown is the time $t_{1.1}/\tau$ required to reach within 10% of the asymptotic error. The simulations required as their input the rates R_B , R_D for our experiment with efficiency η predicted by (4.2). The M-C simulated data was analysed using the maximum likelihood method and the plot shows almost an order of magnitude decrease in ϵ_∞ and $t_{1.1}/\tau$ for each order of magnitude increase in η . A fit of the form $a\eta^b$ to the data provides exponents $b = 0.915(3)$ and $b = 0.920(2)$ for ϵ_∞ and $t_{1.1}/\tau$ respectively.

⁶The number of simulations for each point could be increased, but the simulation is very slow!

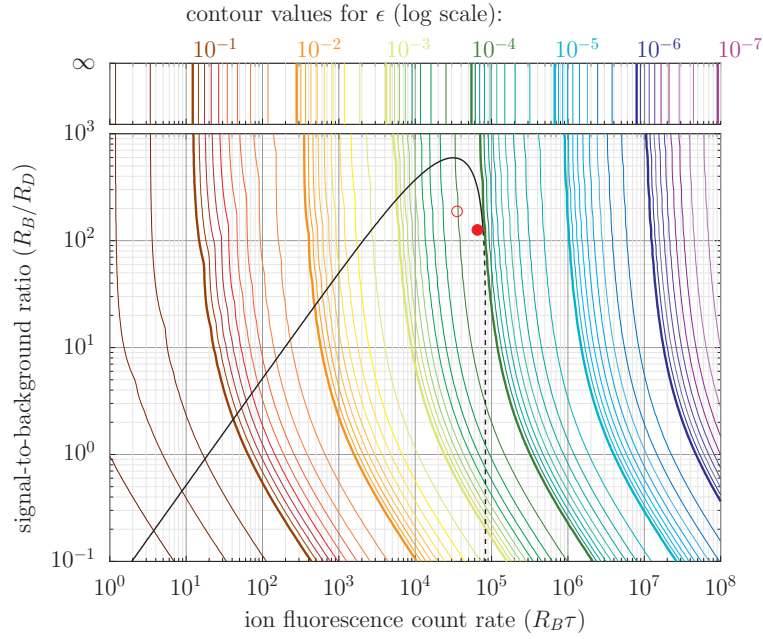


Figure 3.17: Contour plot showing minimum ϵ reached at the optimum t_b for the *threshold method* from simulations over a 133×100 grid. Other markings as for figure 3.15.

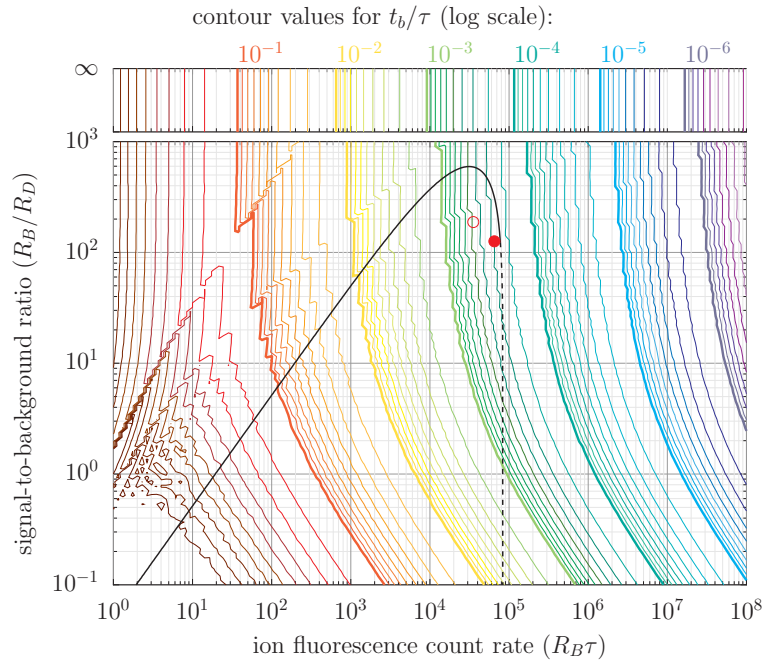


Figure 3.18: Contour plot showing the optimum t_b in units of τ for the *threshold method*. Other markings as for figure 3.15.

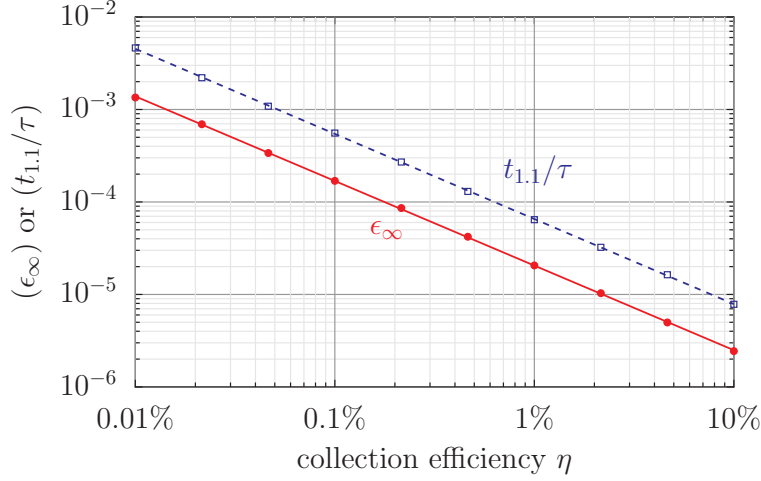


Figure 3.19: Simulations of readout using the maximum likelihood method showing the asymptotic average error ϵ_∞ and the time $t_{1.1}/\tau$ required to reach within 10% of ϵ_∞ as functions of η , the net collection efficiency. The statistical uncertainty is at most the size of the symbols. The lines show fits of the form $y = a\eta^b$, where y is the ordinate.

3.4 Conclusions for photon counting readout

In this chapter we have presented various protocols to discriminate between a bright and dark ion based on photon counting information, in the presence of a dark \rightarrow bright decay rate $1/\tau$. A maximum likelihood method was described which makes use of photon arrival times to identify occasions where the ion has decayed; this method also benefits from a reduced sensitivity to analysis parameters when compared with a simpler threshold method. An adaptive version of the protocol uses the calculated likelihoods to achieve an average speed up in state-identification by terminating the detection period once a desired confidence level is reached. We have shown that the adaptive protocol is faster when decay is omitted from the likelihood calculations; in this case the method is equivalent to a triple-threshold method. We have presented simulations to justify various analysis approximations and to investigate the time resolution necessary for the maximum likelihood method. We have also presented “universal” plots showing the dependence of the discrimination error ϵ and detection time on the fluorescence rate (compared to the decay rate) $R_B\tau$ and signal-to-background level R_B/R_D . We found that for $R_B/R_D \gtrsim 10$, the lowest ϵ is obtained by maximising $R_B\tau$ rather than optimising signal-to-background. Finally, we investigated ϵ with changing photon detection efficiency.

Chapter 4

Time-resolved photon counting experiments

This chapter describes experiments performed to measure the readout fidelity possible for the optical qubit in a single $^{40}\text{Ca}^+$ ion using a photomultiplier tube (PMT) to count scattered photons. In common with precision-measurement experiments, the systematic effects must be studied carefully; these are discussed in the first half of the chapter, starting with a characterisation of non-Poissonian noise sources observed in our detector. The main experiment and results are then presented. Our method relies on our ability to prepare the qubit states with an error much smaller than the readout error. In systems where this is not possible, high-fidelity readout can be measured by performing two successive measurements of the same state; we conclude the chapter by comparing our results to those expected from a double measurement scheme and identifying systematic differences between the two methods.

4.1 Investigating non-Poissonian dark counts

For photon counting with a PMT we found an extra non-Poissonian noise source that could not be treated as a simple increase in the background rate R_D during analysis (see section 3.2.2 in chapter 3). This manifested itself as a “tail” at high photon counts in a histogram of PMT dark counts, such as the example in figure 4.1. This tail was also present when using different PMTs and counting electronics.

To investigate the source of these extra counts, we performed experiments to deter-

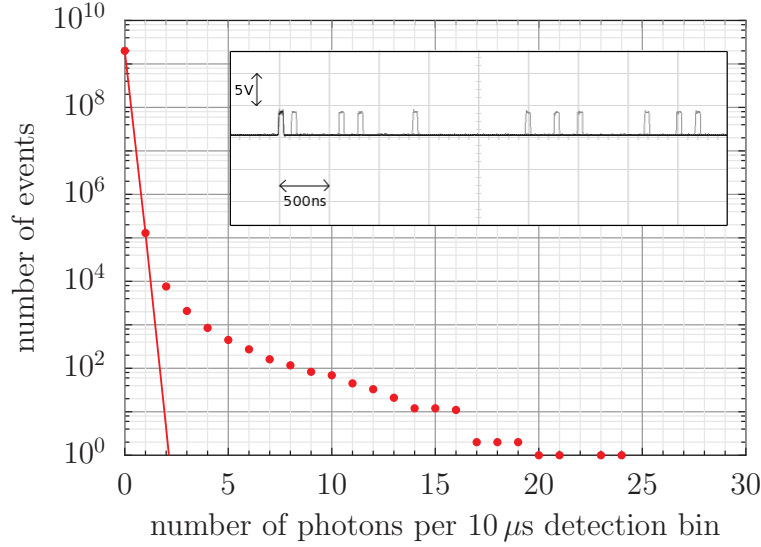


Figure 4.1: Example histogram of dark counts with no ion in the trap and all lasers and roomlights switched off. $R_D = 8.2 \text{ s}^{-1}$, $t_b = 10 \mu\text{s}$. Data points (●) for $N_{\text{exp}} = 2,000,001,889$ contiguous bins. Solid line: Poisson distribution with the same mean as the data. INSET: example pulse burst viewed on an oscilloscope.

mine if the size of the non-Poissonian tail was dependent on the bin time t_b and whether it scaled with the number of “real” photons arriving at the PMT. For each set of conditions, N bins of length t_b were recorded and a histogram was made of the counts. The size of the non-Poissonian tail δ was estimated by choosing a count threshold n_c and calculating the area of the histogram δ_{exp} above this threshold¹, then subtracting that expected from a Poisson distribution δ_{thr} :

$$\delta = \delta_{\text{exp}} - \delta_{\text{thr}}$$

The value n_c was chosen to be the smallest value at which $\delta_{\text{thr}} < \ell$, where we chose $\ell = 10^{-7}$. The exact value of δ was found to depend very sensitively on the choice of ℓ but the qualitative behaviour of δ should remain the same.

Figure 4.2 shows the variation of δ with bin time² t_b . For each value of t_b , $N \geq 10^6$ bins³ were recorded with no ion in the trap and all lasers turned off in a darkened laboratory. The mean background count rate was $R_D = 8.2 \text{ s}^{-1}$. The data show a linear increase in δ with t_b , indicating that the non-Poissonian counts are not due to noise in some PMT readout process, but instead are due to some independent phenomenon of

¹This is the proportion of trials recording a count $n > n_c$

²The bin time t_b was not divided into sub-bins, but recorded as a single long counting period.

³The exact values of N for each data point are corrected for in the analysis and changes in N only manifest themselves in the size of the uncertainty.

which more is recorded during longer counting periods.

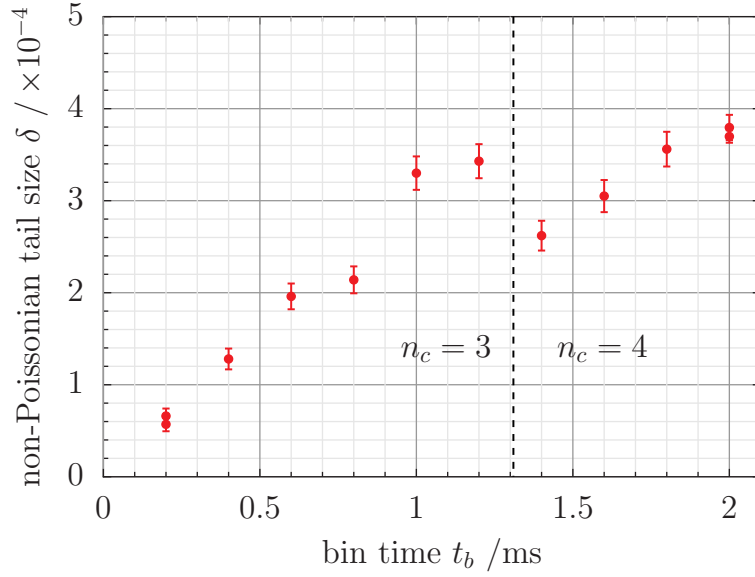


Figure 4.2: Variation of the amount δ of non-Poissonian histogram tail with counting bin time t_b for PMT dark counts with $R_D = 8.2 \text{ s}^{-1}$. The dashed line indicates the change in threshold n_c from 3 to 4.

The variation of δ with background photon arrival rate R_D is shown in figure 4.3 where the sudden changes in δ are due to changes in the choice of n_c . For each value of R_D , $N = 10^6$ bins were recorded with $t_b = 0.5 \text{ ms}$ and no ion in the trap. Changes to R_D were achieved by changing the power of a 397 nm laser beam scattering light off the trap electrode surfaces and vacuum viewports. Light at the same wavelength as the ion fluorescence was deliberately used to eliminate any dependence of the phenomenon on wavelength.

For comparison, figure 4.3 also shows the value of δ obtained from simulated histograms in which the non-Poissonian behaviour is assumed independent of R_D . These histograms were generated by convolving Poissonian histograms of varying mean R_D with an experimentally derived non-Poissonian histogram created from 8,192,000 trials in a darkened laboratory with no lasers and $t_b = 0.5 \text{ ms}$. The experimental data shows a similar trend to the simulation implying that the non-Poissonian phenomenon is not related to the arrival rate of 397 nm photons at the PMT.

To investigate the temporal characteristics of the non-Poissonian counts, photon counts n were recorded for 2,000,001,889 contiguous⁴ bins each of length $t_b = 10 \mu\text{s}$.

⁴This was achieved using the same counting hardware as described in section 2.5.1 and by disabling interrupts on the PC and compressing the data in real time to store it all within 640 kB without needing to write to disc.

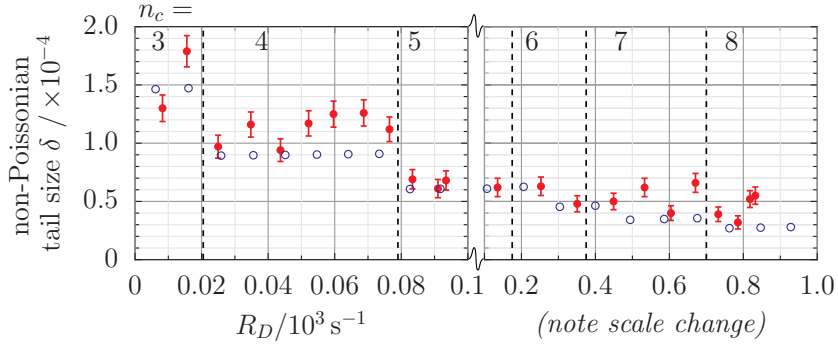


Figure 4.3: Variation of the amount δ of non-Poissonian histogram tail in PMT dark counts with photon arrival rate R_D for $t_b = 0.5$ ms. Experimental data points (\bullet) show a similar trend to a theoretical prediction (\circ) which assumes that the non-Poissonian behaviour is independent of R_D . Error bars in the theoretical prediction are at most the size of the symbols. Dashed lines indicate changes in the tail threshold n_c .

The counts were recorded in a darkened laboratory with no ions in the trap and no lasers on. The distribution of dark gap lengths *between* bins which contain $n \geq 1$ photons is shown in figure 4.4. The fitted line assumes an exponential distribution of gap lengths appropriate to a Poisson distribution and gives a mean arrival rate of $6.35(4) \text{ s}^{-1}$ — the underlying Poisson count rate. The excess of events with short gap-lengths indicate that the spurious events occur as bursts of many pulses over a short timescale and that the statistics are affected for up to ~ 2 ms after the bursts. An example of such a burst viewed on an oscilloscope is shown in the inset of figure 4.1. This shows 11 pulses occurring in under $5 \mu\text{s}$; the probability of this event occurring for a true Poisson distribution with $R_D = 8.2 \text{ s}^{-1}$ is of order 10^{-56} (meaning this would have occurred with a probability 10^{-33} in the time since the universe began!). The example PMT output is viewed after the pulse-stretching circuit described in section 2.4, which stretches the PMT pulses from $\sim 9 \text{ ns}$ to 50 ns TTL pulses, with a 50 ns “low” period after each, so pulses separated by less than 100 ns are not visible.

In summary, the non-Poissonian counts were found to occur in bursts of up to ~ 2 ms in length, and the effects of these increased roughly linearly with bin time t_b while being independent of the number of 397 nm photons arriving at the PMT. The literature also records such a phenomenon [150, 151], attributing it to cosmic-rays passing through the PMT; this leads to a cascade shower which results in pulse trains in the PMT. The relatively long timescale (compared to the cosmic ray event itself) of the pulse bunching observed in figure 4.4 may be due to slow processes such as luminescence excited in the glass envelope of the PMT.

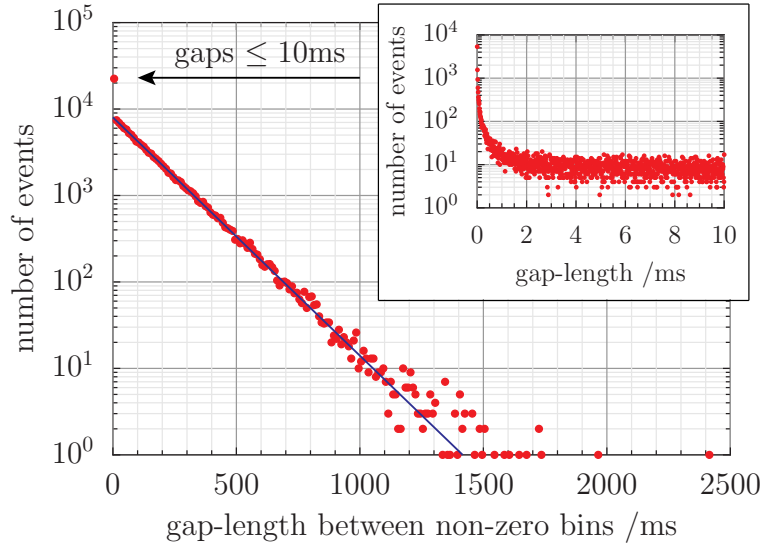


Figure 4.4: Histogram of the gap lengths between bins with a non-zero count ($n \geq 1$) showing a non-Poissonian excess of trials with short (≤ 10 ms) gap lengths. $t_b = 10 \mu\text{s}$ and $R_D = 8.2 \text{ s}^{-1}$. The line fitted to data > 10 ms assumes an exponential distribution of gap lengths appropriate to a Poisson distribution.

These cosmic ray effects will cause an increase in the discrimination error ϵ when trying to read out the state of an ion using simple count thresholding. The additional “cosmic ray errors” mainly act to increase ϵ_D as they can look like fluorescence photons, making a dark ion appear bright. Despite this, the maximum likelihood protocol can correctly identify many cosmic ray events. The effect of cosmic rays on ϵ is discussed further in section 4.4.

The pulse-stretcher described in section 2.4 may help to screen out extra pulses from cosmic rays that occur within 100 ns of each other; however the correlated bursts of pulses are difficult to screen out entirely over a longer timescale (even using more sophisticated counting electronics) due to their similarity to real photons from a fluorescing ion.

It is difficult to add the effect of the cosmic ray bursts into maximum likelihood analyses or simulations of the readout process due to their non-Poissonian time behaviour. However, we can partially take them into account in theoretical distributions by convolving an experimentally derived probability distribution including the non-Poissonian tail (recorded at the appropriate t_b)⁵ with the Poisson distributions $B(n)$ and $D(n)$ defined in section 3.2. This includes only the counting statistics of the bursts, neglecting the time correlations. Theoretical distributions such as these were used in analyses of ex-

⁵One might initially suppose that convolving the experimentally recorded histogram for $t_b = 10 \mu\text{s}$ with itself would result in a histogram appropriate for $t_b = 20 \mu\text{s}$. This is not the case for cosmic rays due to the time correlations of the bursts; nevertheless appropriate distributions for any t_b can be created by summing adjacent $10 \mu\text{s}$ bins from our contiguous background count data.

perimental data, but all simulations of the readout process were produced and analysed using pure Poisson distributions.

4.2 Ion readout experimental methods

To make a measurement of the readout fidelity, a single $^{40}\text{Ca}^+$ ion was repeatedly prepared with high fidelity in a known initial state. A detection period then followed where photon counts coming from the ion were recorded and saved for later analysis. This enabled us to test many different analysis protocols on the same data set for determining the ion's state from the recorded photon counts. The results of the analyses were compared with the known initial state of the ion to make a measurement of ϵ and hence determine the optimal protocol.

The experimental apparatus is described in more detail in chapter 2. The ion is Doppler cooled on the $S_{1/2} \leftrightarrow P_{1/2}$ transition by a laser at 397 nm and re-pumped on the $D_{3/2} \leftrightarrow P_{1/2}$ transition by a laser at 866 nm. Light from the ion is imaged on to the PMT via a large numerical aperture objective lens; more details of the imaging system can be found in section 2.4.

The experimental sequence is shown in figure 4.5. The ion is first illuminated with 393 nm and 886 nm light for 1 ms. This moves all population to the $D_{5/2}$ “shelf” via spontaneous decay from the $P_{3/2}$ level. The 866 nm light acts to re-pump any population from the $D_{3/2}$ metastable level (which has a lifetime of 1.20(1) s) back into the $S_{1/2} \leftrightarrow P_{3/2}$ cycle. During this period, the 397 nm beam is extinguished to make the shelving rate faster and more stable. After the population has been prepared in qubit state $|D\rangle$, the 393 nm beam is extinguished and the ion is illuminated with light at 397 nm and 866 nm which drives a cycling transition in the $(4S_{1/2}, 4P_{1/2}, 3D_{3/2})$ manifold. After a delay of 20(2) μs (to ensure complete extinction of the 393 nm light) we begin to record counts at the PMT.

The PMT counts photons for a total bin time $t_b = 2\text{ ms}$, divided up into 200 sub-bins each of length $t_s = 10\text{ }\mu\text{s}$. Two alternately-gated 10 MHz counters are used to count the signal from the PMT so that there is negligible ($\approx 43\text{ ns}$) dead-time between the sub-bins. The counts $\{n_i\}$ in each sub-bin i are recorded by the computer in time order and are available to the control program $\sim 5\text{ }\mu\text{s}$ after the end of the sub-bin which would enable real-time processing (e.g. adaptive analysis) in a real QC experiment. The

contiguous sub-bins can later be added together to give a varying length t_b trial for a threshold analysis.

The population is then removed from the shelf and prepared in state $|B\rangle$ by a laser at 854 nm which illuminates the ion for ~ 3 ms. A further $200 \times 10 \mu\text{s}$ counting bin follows, during which the ion is expected to fluoresce. The 854 nm laser remains on during this second counting period to avoid shelving of the ion due to leakage from the 393 nm laser which is extinguished only by a double-pass AOM (see also section 4.3.3 below). At other times, a shutter is used to properly eliminate the 854 nm light as there can be leakage through the single-pass AOM which will reduce the apparent lifetime of the $|D\rangle$ state.

The whole sequence is repeated many times to give a total of N_{exp} trials, half prepared in state $|D\rangle$ and half prepared in state $|B\rangle$. The advantage of interleaving the trials on the two qubit states in this way is twofold; the periods in which the ion fluoresces provide Doppler cooling and the “B” trials also provide a check on the presence of the ion after a dark “D” trial (several consecutive “B” trials with low fluorescence indicate the ion has been heated, e.g. by a background gas collision).

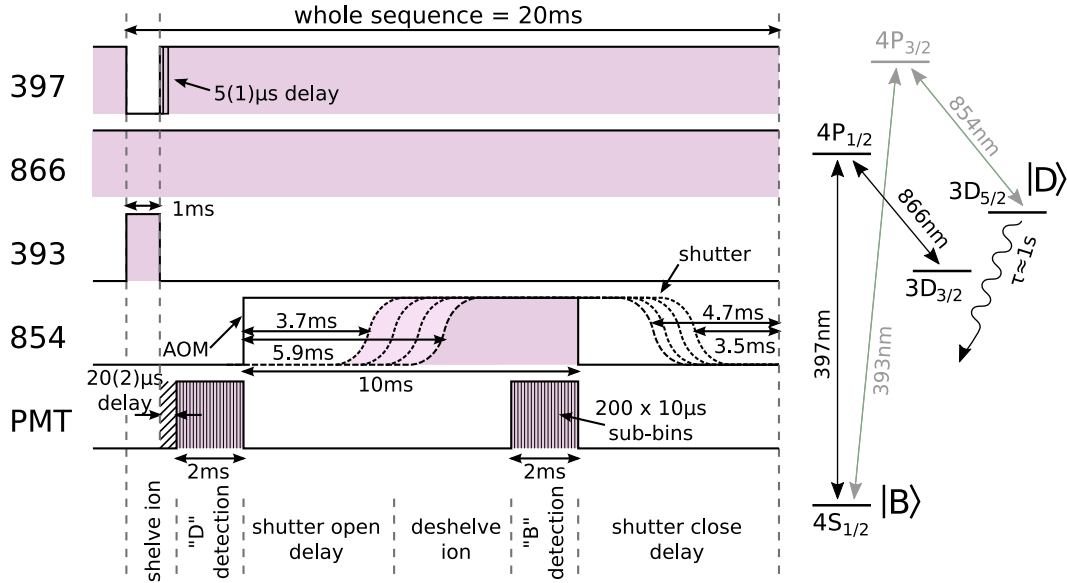


Figure 4.5: Diagram showing timing of laser pulses and detection periods for both series of PMT ion readout experiments. Timing jitter is $< 0.1 \mu\text{s}$ except where indicated. RIGHT: Level diagram showing important transitions in $^{40}\text{Ca}^+$.

Two series of experiments were performed. The first data set (“Series I”) was taken with imaging system A and the second (“Series II”) with imaging system B where modifications had been made to increase the collection efficiency η in order to achieve

a higher R_B . Series II was also performed with an increased magnetic field and 866 nm laser power which increases fluorescence from the ion by reducing coherent population trapping in $D_{3/2}$ [131]. Typical measured fluorescence rates and experimental settings for the two data sets are given in table 4.1. The 397 nm and 866 nm lasers were tuned as close to resonance as possible in order to maximise fluorescence. The 397 nm laser is tuned slightly to the red of the transition to avoid heating the ion which would cause a drop in fluorescence or ion loss. The 393 nm and 854 nm lasers were also tuned as close to resonance as possible to maximise shelving and deshelling rates to avoid state preparation errors. The 854 nm laser is not locked to a cavity and therefore tends to drift in frequency. Over the course of each series of experiments the detuning drifted by < 60 MHz, the resolution of the wavemeter.

	Series I	Series II
R_B	$30\,200\text{ s}^{-1}$	$55\,800\text{ s}^{-1}$
R_D	161 s^{-1}	442 s^{-1}
η	$0.12(2)\%$	$0.22(2)\%$
Imaging system	A	B
...see figure	2.4	2.5
N_{exp}	$1,022,976 \approx 1.023 \times 10^6$	$1024 \times 1000 = 1.024 \times 10^6$
B field	$1.64(1)\text{ G}$	$3.0(1)\text{ G}$
Δ_{397}	-17 MHz	-17 MHz
I_{397}	$7.9I_{\text{sat}}$	$5.4I_{\text{sat}}$
I_{866}	$36I_{\text{sat}}$	$89I_{\text{sat}}$
I_{393}	$0.06I_{\text{sat}}$	$0.06I_{\text{sat}}$
I_{854}	$4.5I_{\text{sat}}$	$2.3I_{\text{sat}}$

Table 4.1: Parameters for the two series of PMT readout experiments. Total collection efficiency η includes the quantum efficiency (nominally $\sim 16\%$) of the PMT at 397 nm. Frequency detuning is given as $\Delta = f - f_0$ where f_0 is the resonant frequency of the transition. The saturation intensity I_{sat} is that for the relevant transition in each case; the definition used is that given in (2.1).

The rates R_B and R_D in the experiment are in general dependent on the intensity of the lasers at 397 nm and 866 nm. The fluorescence of the three-level ($4S_{1/2}$, $4P_{1/2}$, $3D_{3/2}$) manifold was studied by Derek Stacey [152] using rate equations (see also [129, Appendix B]). The detected fluorescence rate is given by $R_B = \eta A_{21} n_2$ where n_2 is the population of the $P_{1/2}$ state which can be found by solving the rate equations. For a high 866 nm laser power, n_2 is only dependent on I , the intensity of the laser at 397 nm. Assuming the detuning Δ_{397} from the $S_{1/2} \leftrightarrow P_{1/2}$ transition is small, the population in $P_{1/2}$ is given by:

$$n_2 = \frac{(I/I_{sat})}{1 + 4(I/I_{sat})} \quad (4.1)$$

This result assumes linearly polarised lasers that excite transitions involving all Zeeman substates. The model does not include coherent effects (these can be modelled using Bloch equations but this is not necessary for our purpose).

The PMT is very insensitive to light at 866 nm, so the background count rate R_D is primarily dependent on the intensity of the 397 nm laser which has been scattered off the trap electrodes. The variation of R_B and R_D with the power P of the 397 nm laser is given in (4.2), where $I \propto P$, the power measured experimentally as the voltage on a photodiode.

$$R_B = \eta A_{21} \frac{(P/P_{sat})}{1 + 4(P/P_{sat})} \quad ; \quad R_D = m\eta P + c \quad (4.2)$$

The parameter c is the contribution to R_D when the lasers are turned off, which includes the PMT dark count rate of 8.2 s^{-1} at 20°C and any scattered room-light in the laboratory. The value of m (the increase in scatter with laser power) is highly dependent on beam pointing. The Einstein coefficient for the $S_{1/2} \leftrightarrow P_{1/2}$ transition has value $A_{21} = 1.32 \times 10^8 \text{ s}^{-1}$ and P_{sat} is proportional to the saturation intensity of the $S_{1/2} \leftrightarrow P_{1/2}$ transition.

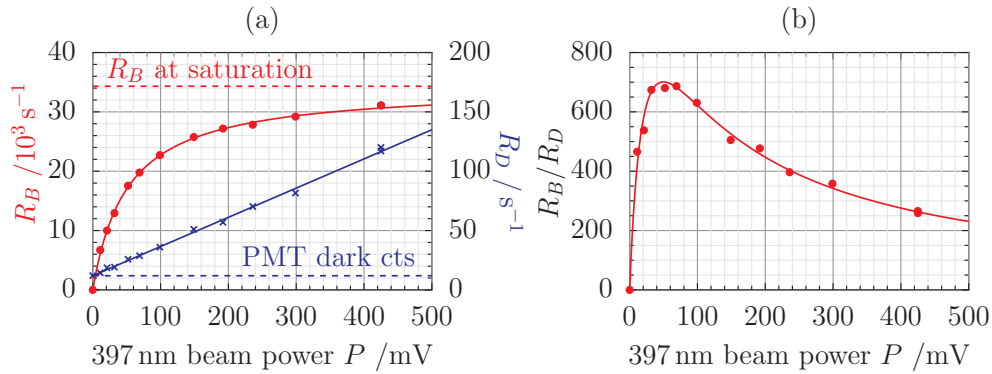


Figure 4.6: (a) Variation of R_B (●) and R_D (×) with 397 nm laser power P (measured as a reading in mV from a photodiode), for imaging system A. The solid lines show fits to the data. (b) Variation of signal-to-background ratio R_B/R_D with 397 nm laser power.

The values of P_{sat} , m and c were found by fitting the functions in (4.2) to measured values of R_B and R_D at varying 397 nm laser power, P . The value of η was also allowed to float during the fit and the values of all the parameters are shown in table 4.2. The values of η from the fit are comparable with the values given in table 4.1, although to

obtain a more reliable measure of η one would need to include coherent effects in the model for n_2 . A better method to determine η would be to use a trapped $^{40}\text{Ca}^+$ ion to produce a single photon per “trial” and measure the number of trials in which a photon is detected in a scheme similar to that used by Shu *et al.* [153].

An example plot showing the variation of R_B and R_D with 397 nm laser power is shown in figure 4.6 for series I. The parameters in table 4.2 were used with (4.2) to add the R_B/R_D curve to figures 3.15, 3.16, 3.17 and 3.18 in section 3.3.3.

	Series I	Series II
η (fit)	0.1044(3)%	0.228(1)%
P_{sat}	204(2) mV	377(6) mV
m	237(3) s ⁻¹ /mV	234(8) s ⁻¹ /mV
c	11.9(5) s ⁻¹	17(2) s ⁻¹
maximum R_B/R_D	702	603
... at $P =$	50 mV	54 mV
397 nm P used:	439 mV	380 mV

Table 4.2: Values of parameters in (4.2) and associated uncertainties found from fits. The last row gives the 397 nm power used in the readout experiments.

In the qubit readout experiments, the 397 nm laser power was set to be much higher than that which optimised the signal-to-background ratio R_B/R_D . This is because the highest readout fidelity is actually achieved at higher laser power since the increased fluorescence R_B can be detected more rapidly compared with τ : maximising R_B is more important than maximising R_B/R_D (see section 3.3.3).

4.3 Accounting for systematic errors

4.3.1 Imperfect population preparation

The process by which we measure the readout fidelity assumes that we know with certainty the initial state in which we prepared the ion at the beginning of each trial. However, in general the state preparation may be imperfect and these incorrectly prepared trials will result in errors that are indistinguishable from the real measurement error ϵ that we are aiming to quantify. Therefore the state preparation error must be estimated separately and corrected for. An alternative is to make a double measurement, as done by Hume *et al.* [42], but this comes with its own complications, see section 4.5. A “triple” measurement scheme is used in the camera detection experiments described in chapter 6.

Dark state

There are two contributions to ϵ_D from errors in preparing the $|D\rangle$ state. The first is from the finite shelving rate of the 393 nm laser which must compete against the decay from the $D_{5/2}$ state which has a lifetime of τ . The shelving rate was measured by varying the length of the 393 nm shelving pulse from $t_{393} : 0 \rightarrow 100 \mu\text{s}$ in a sequence similar to that in figure 4.5. The number of successful shelvings for each t_{393} was measured as the fraction of the “D” trials which appeared dark in 512 sequence repeats; an example of such an experiment is shown in figure 4.7(a). This data was fitted with a model which treated the $D_{5/2}$ level and $(S_{1/2}, P_{1/2}, D_{3/2})$ manifold as a two-level system. The rate of shelving was measured to be $1/t_{shelve}$ where $t_{shelve} = 12(2) \mu\text{s}$. The correction to ϵ_D is given by:

$$\begin{aligned} \delta_{shelve} &= 1 - \frac{1/t_{shelve}}{1/t_{shelve} + 1/\tau} \left(1 - e^{-(1/t_{shelve} + 1/\tau)t_{393}} \right) \\ &\approx \frac{t_{shelve}}{\tau} \end{aligned} \quad (4.3)$$

The second contribution to the $|D\rangle$ preparation error is from the $t_{delay} = 20(2) \mu\text{s}$ delay after the shelving period before photon counting is started; there is a small probability that the ion will decay back to the $|B\rangle$ ground state before the counting bin has begun. The correction to ϵ_D is given by (4.4).

$$\begin{aligned} \delta_{delay} &= 1 - e^{-t_{delay}/\tau} \\ &\approx \frac{t_{delay}}{\tau} \end{aligned} \quad (4.4)$$

The total correction to ϵ_D is therefore $\delta = (t_{delay} + t_{shelve})/\tau = 2.7(8) \times 10^{-5}$ where the uncertainty is given by combining the systematic uncertainty⁶ in δ of 0.2×10^{-5} with the statistical uncertainty $\sqrt{\delta/N_{\text{exp}}^D}$ expected in $N_{\text{exp}}^D = 512000$ trials prepared in $|D\rangle$. This correction factor has been subtracted for all values of ϵ_D and ϵ that follow.

Bright state

State preparation errors for $|B\rangle$ state could be caused by the 854 nm pulse failing to deshelve the ion. The rate of deshelling was measured by scanning the length of the

⁶due to the uncertainties or jitter in the measurements of t_{shelve} and t_{delay} .

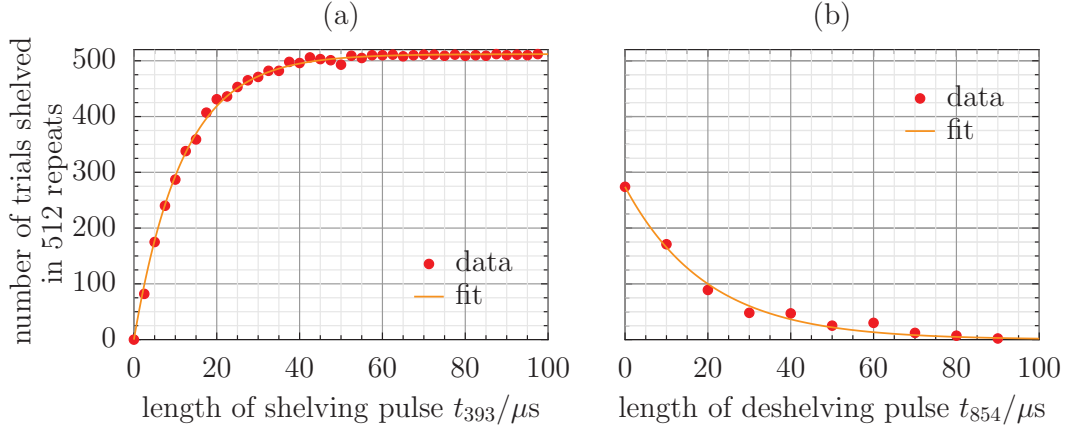


Figure 4.7: Results of experiments to measure (a) the rate of shelving by the 393 nm laser, (b) the rate of deshelling by the 854 nm laser. The reduced number of shelved trials at $t_{854} = 0$ can be explained by 854 nm light leaking through the AOM giving a background deshelling rate. Statistical uncertainty in the data points are at most the size of the symbols.

AOM “on” pulse which allows the 854 nm beam through in the sequence shown in figure 4.5. The AOM pulse was scanned for $t_{854} : 0 \rightarrow 100 \mu\text{s}$ directly before the “B” trial and the number of unsuccessful deshellings for each t_{854} was measured as the fraction of the “B” trials which still appeared dark in 500 sequence repeats. The shutter behaviour was not altered, so there was some 854 nm light leaking through the AOM which gave a background deshelling rate. The data is shown in figure 4.7(b) and was fitted by an exponential decay with time constant $t_{\text{deshelve}} = 20(1) \mu\text{s}$ which, for the $\sim 3 \text{ ms}$ period allowed for deshelling in our experiments, gives an entirely negligible state preparation error of order 10^{-66} . For this measurement of the deshelling rate the 854 nm intensity was $\sim 5.4I_{\text{sat}}$ with $\Delta_{854} = -120 \text{ MHz}$. When the detuning was altered to be closer to resonance then the light leaking through the AOM was enough to deshelve the ion before the AOM “on” pulse. Since we kept $|\Delta_{854}| \lesssim 100 \text{ MHz}$ during the readout experiments, we can assume there are negligible state preparation errors for the $|B\rangle$ state and no correction is needed to ϵ_B . It is much more likely that the ion would appear to be dark due to collisional heating, see below.

4.3.2 Dark to bright transitions

We assume in the rest of this thesis that the dominant source of $|D\rangle \rightarrow |B\rangle$ pumping in trials prepared in $|D\rangle$ state is due to decays from the $D_{5/2}$ state which has a lifetime of $\tau = 1168(7) \text{ ms}$; nevertheless off-resonant pumping (e.g. by 866 nm light on the $D_{5/2} \leftrightarrow P_{3/2}$ transition at 854 nm) could cause an additional deshelling rate. In the maximum $t_b =$

2 ms detection period used in our readout experiments, we expect 876(30) decays due to the finite lifetime τ , where the statistical uncertainty is given for 512 000 trials prepared in $|D\rangle$. The number of decays seen in each experimental series can be estimated from a histogram of the photon counts n seen in 2 ms by counting the number of trials in the “tail” of the histogram with large n . Using a threshold of $n_c = 7.5$, there are an estimated 827(29) decays in the series I set of experiments, and 910(30) in series II. The statistical uncertainties quoted are based on the number of “D” trials; the crude method of estimation means that the uncertainty is likely to be larger than this. The number of decays appears to be consistent with a $D_{5/2}$ lifetime of $\tau = 1168(7)$ ms, meaning other contributions to this pumping rate are comparatively small.

4.3.3 Bright to dark transitions

We have assumed that the rate of $|B\rangle \rightarrow |D\rangle$ pumping in trials prepared in $|B\rangle$ is sufficiently low to be omitted in simulations and analyses. We now estimate an upper limit on this transition rate.

During the PMT readout experiments described above the 854 nm laser continued to illuminate the ion during the “B” trials when the ion was prepared in $|B\rangle = S_{1/2}$. This laser acts to rapidly (with time constant $\sim 20 \mu\text{s}$) deshelve the ion in the event that some shelving process should occur which transfers the population into $D_{5/2}$. For completeness, however, we consider all processes which could make the ion appear dark when it should be bright.

Shelving by 393 nm leakage

One such shelving process is excitation due to leakage from the 393 nm laser which is only extinguished with a double-pass AOM. The rate of this process was estimated by looking for quantum jumps ($D_{5/2}$ shelving events) while continually monitoring the ion’s fluorescence using counting bins with a resolution of $t_b = 167$ ms. The ion was illuminated by 397 nm light (detuned from resonance to give efficient cooling) and the 866 nm repumper while the 393 nm beam was extinguished only by its AOM. The 854 nm beam was completely extinguished by its shutter. No quantum jumps were seen in 10.5 minutes, putting an upper limit on this shelving rate of $1.6 \times 10^{-3} \text{ s}^{-1}$. Thus, even if the 854 nm laser had not been left on for the “B” trials, we would expect at most ~ 2

shelving events in each of our data sets due to this process. In contrast, with the 393 nm beam unblocked a shelving rate of $1/(12\ \mu\text{s}) \approx 8.3 \times 10^4\ \text{s}^{-1}$ was observed, meaning the double-pass AOM gives a net extinction of $\sim 10^{-8}$. It is unlikely this extinction ratio could be improved upon without the addition of a mechanical shutter.

Off-resonant shelving

Aside from the 393 nm leakage, shelving could occur by far off-resonant excitation on the $S_{1/2} \leftrightarrow P_{3/2}$ 393 nm transition by the 397 nm light, or on the $D_{3/2} \leftrightarrow P_{3/2}$ 850 nm transition by the 866 nm light, followed by a decay to $D_{5/2}$. The shelving rates for these two processes were estimated using the standard theory of atom-light interaction to calculate the transition rates from each initial state (“level 1”) to the $P_{3/2}$ level (“level 2”) from an off-resonant laser, averaging over all Zeeman components (see for example [138]). This is then multiplied by the branching ratio b to $D_{5/2}$ (5.3%) and a further factor to take into account the saturated population N_1 of the initial state ($\approx 1/4$ and $\approx 1/2$ for $S_{1/2}$ and $D_{3/2}$ respectively). The shelving rate is given by:

$$R_{\text{shelve}} = N_1 \times b \times \frac{2J_2 + 1}{2J_1 + 1} \frac{\pi^2 c^3}{\hbar \omega_{12}^3} A_{21} \frac{I}{c} g(\omega_L - \omega_{12}) \quad (4.5)$$

where ω_L and ω_{12} are the frequencies of the laser and the transition respectively, I is the laser intensity and $g(\omega_L - \omega_{12})$ is the normalised Lorentzian lineshape. J_1 and J_2 denote the total angular momenta of levels 1 and 2 respectively.

The rate of excitation by the 397 nm light is estimated to be $< 2.7 \times 10^{-5}\ \text{s}^{-1}$ for the highest laser intensities used in our experiments, with that from the 866 nm light an order of magnitude lower. The rates match well with those produced from a full rate-equations simulation by Dr David Szwer. These rates are much lower than the shelving rate from 393 nm leakage.

This estimate assumes monochromatic lasers. The diode lasers are not monochromatic but both beams are filtered by diffraction gratings which we expect to reduce shelving to a rate comparable to that for monochromatic lasers (see [138]).

Doppler heating

There are also heating processes which cause the ion to move out of resonance with the 397 nm laser due to an increased Doppler shift. This causes a low photon scattering rate

meaning the ion appears dark even when it is not in the $D_{5/2}$ state. Once the photon scattering rate is lowered, Doppler cooling becomes less efficient so the dark periods can be fairly long as the ion is slowly cooled back into resonance. We include processes which heat the ion in estimations of the $|B\rangle \rightarrow |D\rangle$ transition rate.

In order to obtain the highest fluorescence for our experiments we had the 397 nm laser tuned very close to resonance. One cause of heating is jitter in the 397 nm laser frequency which can heat the ion if it becomes detuned blue of the resonance. With the laser tuned so close to resonance the cooling of a hot ion is very inefficient. During our experiments we continually monitored the ion fluorescence in the “B” trials and paused data collection if we saw low fluorescence in several consecutive trials. We then briefly tuned the 397 nm laser further red to cool the ion back down before continuing data collection. At analysis time we could identify further missed heating events by searching for consecutive “B” trials which appeared dark. These were removed along with “D” events nearby in the sequence which could bias ϵ_D as they would never show errors from $|D\rangle \rightarrow |B\rangle$ decay. This removal ensured that heating effects are minimal in our data set. In a real QC experiment this heating source could also be removed by detuning the 397 nm laser further from resonance and increasing photon collection efficiency to maintain a high R_B . Additionally, a sympathetic cooling ion of a different species could be held in the same trap ensuring the $^{40}\text{Ca}^+$ remained cold [154]. Use of an ion of a different species ensures that the lasers required to cool it will be very far from resonance with important transitions in $^{40}\text{Ca}^+$.

Collisional effects

Another cause of $|B\rangle \rightarrow |D\rangle$ transitions is that the ion can experience collisions with the background gas. There are two processes which can lead to loss of ion fluorescence. Short-range collisions can impart significant kinetic energy to the ion, heating it up and leading to a loss of fluorescence as described above. These sorts of collisions can often be recognised by a gradual return in fluorescence as the ion is cooled back into resonance with the lasers. The second sort of collision is a fine-structure changing interaction where the ion is perturbed leading to population in the $3D_{3/2}$ level being transferred to the $3D_{5/2}$ shelf. The ion may not gain significant kinetic energy from the collision, so is not necessarily heated. The return of fluorescence is sudden as the ion makes a

quantum jump after a dark period with average length $\sim \tau$. In general these two kinds of collisional effects are difficult to eliminate in a real QC experiment, although the addition of sympathetic cooling ions may speed up ion recoiling after the short-range collisions and reduce the length of the dark periods somewhat.

It is difficult to estimate the rates of these collisional processes from a measurement of the pressure in our vacuum system as pressure gauges are unreliable in ultra high vacuum. In order to estimate the rate of these processes in our apparatus we monitored the fluorescence of a single ion illuminated only by the 397 nm and 866 nm lasers. The 397 nm laser was detuned to the half-fluorescence point to give the most efficient Doppler cooling. When monitoring the ion with $t_b = 1$ ms for 35 minutes, four collisional events were recorded; these were observed as dark periods which included bins with $n = 0$ counts ($\approx 4\sigma$ below the mean count rate) and are shown in figure 4.8. The dark periods last between 1 ms and 250 ms and, of the four events seen, two show a gradual return in fluorescence indicating a heating event. However, in general it is difficult to distinguish between the two collisional processes so only the total rate $\approx 2(1) \times 10^{-3} \text{ s}^{-1}$ can be reliably determined. A second experiment with reduced resolution ($t_b = 10$ ms) recorded four events with counts more than 5σ below the mean in 85 minutes, giving a rate of $\approx 8(4) \times 10^{-4} \text{ s}^{-1}$. Barton *et al.* [138] measured 17 events in 8 hours (a rate of $6 \times 10^{-4} \text{ s}^{-1}$) in the same ion trap in 1999, using the same method⁷. These collisional effects dominate over any off-resonant shelving by the 397 nm and 866 nm lasers that may be present in these experiments.

Forbidden transitions to $D_{5/2}$

In addition to the rates of off-resonant excitation to $3D_{5/2}$ already considered there are forbidden transitions into the shelf state.

One such transition is the 871 nm decay $4P_{1/2} \rightarrow 3D_{5/2}$ which is forbidden by the E2 and M1 selection rules. The transition has $\Delta J = 2$ and $\Delta l = 1$ with a parity change and therefore is allowed by the M2 and E3 selection rules [155]. No data is available for the rate of this transition in $^{40}\text{Ca}^+$, however it is likely to be highly suppressed. The NIST atomic physics [156] database lists 6 transitions in various atoms over the wavelength range 800–950 nm which are allowed only by the M2 selection rules. These

⁷In the 1999 experiment, the 397 nm laser was a frequency-doubled source, expected to be highly monochromatic.

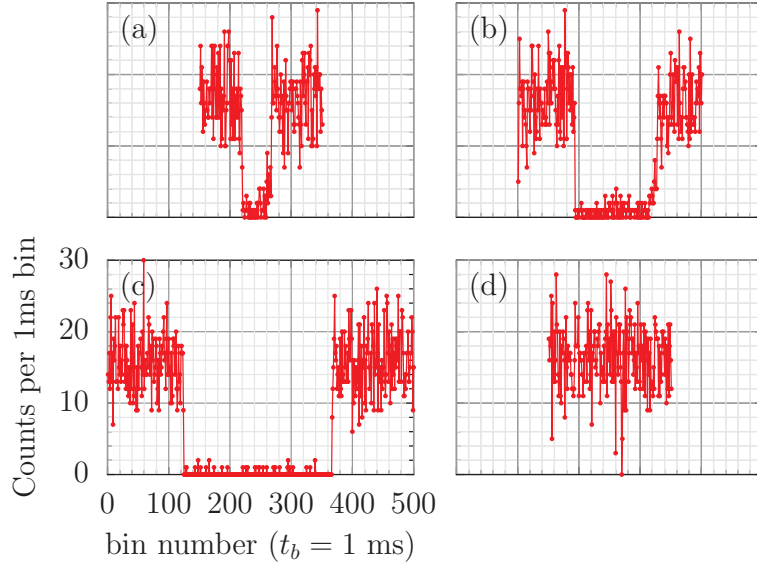


Figure 4.8: Four bright→dark transitions recorded over 35 minutes with $t_b = 1$ ms and attributed to collisions with background gas. Events (a) and (b) show a gradual return in fluorescence indicating the ion had been heated. Event (d) contains only a single bin with zero counts.

have calculated A_{21} spontaneous transition rates between 10^{-5} and 10^{-12} s^{-1} . The highest transition rate was $A_{21} = 1.97 \times 10^{-5} \text{ s}^{-1}$ [157] for the $3P_{1/2} \rightarrow 3D_{5/2}$ transition in Na(I) with $\lambda = 818 \text{ nm}$. An example of an E3 allowed transition from the world of ion trapping is the $^2S_{1/2} \rightarrow ^2F_{7/2}$ transition at 467 nm in $^{171}\text{Yb}^+$ which has a lifetime of ~ 6 years [158, 159], or $A_{21} \sim 10^{-9} \text{ s}^{-1}$. Therefore, it is likely that the rate of shelving transitions from $P_{1/2}$ in $^{40}\text{Ca}^+$ is of order 10^{-5} s^{-1} or less.

Other “forbidden” transitions to $D_{5/2}$ include direct excitation from $S_{1/2}$ on the 729 nm electric quadrupole transition (E2), and direct excitation from $D_{3/2}$ which is an M1 transition. These could be excited by blackbody radiation, or off-resonantly by lasers nearby in frequency. The rate of excitation between two levels by blackbody radiation at a temperature T is calculated as:

$$R_{shelve} = N_1 \frac{2J_2 + 1}{2J_1 + 1} A_{21} \left(e^{\hbar\omega/kT} - 1 \right)^{-1} \quad (4.6)$$

where N_1 is the fraction of the population in the initial (lower) state, as in (4.5). For the M1 transition at room temperature⁸ this gives a transition rate of $\sim 5 \times 10^{-6} \text{ s}^{-1}$. For the quadrupole transition at 729 nm the rate is instead dominated by off-resonant excitation from the 866 nm laser light. Using (4.5) we find the rate is only of order

⁸The vacuum system also houses an ion gauge filament at $T \approx 1700 \text{ K}$, although this is not in the ion’s line-of-sight (see Barton *et al.* [138]).

10^{-21} s^{-1} due to the very narrow linewidth.

The estimated rates for these forbidden transitions are summarised in table 4.3. Transitions of these sorts would also contribute to the $|B\rangle \rightarrow |D\rangle$ rate seen in the experiment described above to measure collisional shelving and heating, which gave an upper limit on the total transition rate of $\sim 10^{-3} \text{ s}^{-1}$.

transition		λ / nm	A_{21} / s^{-1}	ref.	rate estimation
$P_{1/2} \rightarrow D_{5/2}$	M2/E3	871	$< 10^{-5}$	[156, 157]	$\lesssim 10^{-5} \text{ s}^{-1}$
$S_{1/2} \rightarrow D_{5/2}$	E2	729	0.86	[138]	$\sim 10^{-21} \text{ s}^{-1}$
$D_{3/2} \rightarrow D_{5/2}$	M1	164 771	2.41×10^{-6}	[160]	$\sim 5 \times 10^{-6} \text{ s}^{-1}$

Table 4.3: Table showing estimated rates of “forbidden” shelving transitions.

B-field state mixing

The $P_{1/2} \rightarrow D_{5/2}$ decay is normally an electric-dipole forbidden $\Delta J = 2$ transition; however at large magnetic fields B (such as those required in Penning traps), there is some magnetically induced J -mixing of states with the same m_J but different J . This results in a small amplitude of the $P_{1/2}$ to $D_{5/2}$ transition becoming electric-dipole allowed, resulting in unwanted shelving of the ion in $D_{5/2}$ during the normal $\{S_{1/2}, P_{1/2}, D_{3/2}\}$ cooling cycle. Crick *et al.* [161] have observed this effect in their Penning trap and calculate the branching ratio from $P_{1/2}$ between the $S_{1/2}$ and $D_{5/2}$ decay channels to be:

$$\frac{\Gamma(P_{1/2}, D_{5/2})}{\Gamma(P_{1/2}, S_{1/2})} = 4.2 \times 10^{-7} (B[\text{T}])^2 = n^{-1}$$

where n is the average number of 397 nm photons which will be emitted before the unwanted shelving process occurs. At the maximum B field used in this work ($3 \text{ G} = 3 \times 10^{-4} \text{ T}$) we expect an approximate shelving rate of $3 \times 10^{-6} \text{ s}^{-1}$ due to this process.

Total transition rate

The rates of all the processes discussed above are summarised in table 4.4. In a future ion-trap quantum computer with sympathetic cooling ions, only fine-structure changing collisions remain as a potentially significant source of bright \rightarrow dark pumping. These were present in the experiment described above (titled “collisional effects”) which found a net rate of order $\sim 10^{-3} \text{ s}^{-1}$, but this also includes short-range collisions. Section 3.3.1

discussed why a rate this low can be omitted from our simulations and analysis.

In our readout experiments most sources of $|B\rangle \rightarrow |D\rangle$ pumping are minimised. The 854 nm laser during the “B” trials means that population is immediately removed from $D_{5/2}$ after any shelving processes (including fine-structure altering collisions); therefore only heating processes (including short-range collisions) will lead to spurious dark “B” trials. Most of these are identified and removed before analysis to enable us to assess the fidelity of the measurement process alone. The overall rate of $|B\rangle \rightarrow |D\rangle$ pumping in our experiment is thus expected to be below 10^{-3} s^{-1} , i.e. below 1 event in a run with 0.5×10^6 bright state readout trials, each of duration 2 ms.

Mechanism	Rate estimation
Shelving by 393 nm leakage through AOM	$< 1.6 \times 10^{-3} \text{ s}^{-1}$
Off-resonant shelving by 397 nm light	$\sim 2.7 \times 10^{-5} \text{ s}^{-1}$
Off-resonant shelving by 866 nm light	$\sim 2.1 \times 10^{-6} \text{ s}^{-1}$
Heating by 397 nm laser jitter	<i>eliminated before analysis</i>
Collisional shelving and heating	$\sim 10^{-3} \text{ s}^{-1}$
“Forbidden” shelving transitions	$< 10^{-5} \text{ s}^{-1}$
B-field state mixing	$\sim 3 \times 10^{-6} \text{ s}^{-1}$

Table 4.4: Table showing estimated rates of $|B\rangle \rightarrow |D\rangle$ pumping processes.

4.4 Results and analysis

Unless specified, the numerical values quoted in the text of this section refer to those obtained from analysis of the data in the series II set of experiments for which a smaller discrimination error ϵ was obtained due to the higher fluorescence rate R_B .

The discrimination errors ϵ obtained with varying bin time t_b for both series of experiments are shown in figure 4.9 for the three analysis techniques described in section 3.2. The statistical uncertainties in the data are at most the size of the symbols. The errors expected from M-C simulations of the readout process with ideal Poisson statistics are shown for comparison as solid lines and in general these show good agreement with the experimental results. At short t_b the experimental ϵ is greater than that for the simulations due to super-Poissonian noise in the data caused by for example cosmic rays and drifts in R_B over the course of the data collection (each series took several hours to acquire). The changes in R_B (at the $\sim 5\%$ level) could have been caused by drifts in 397 nm laser frequency or beam position on the ion, or drifts in imaging system

alignment.

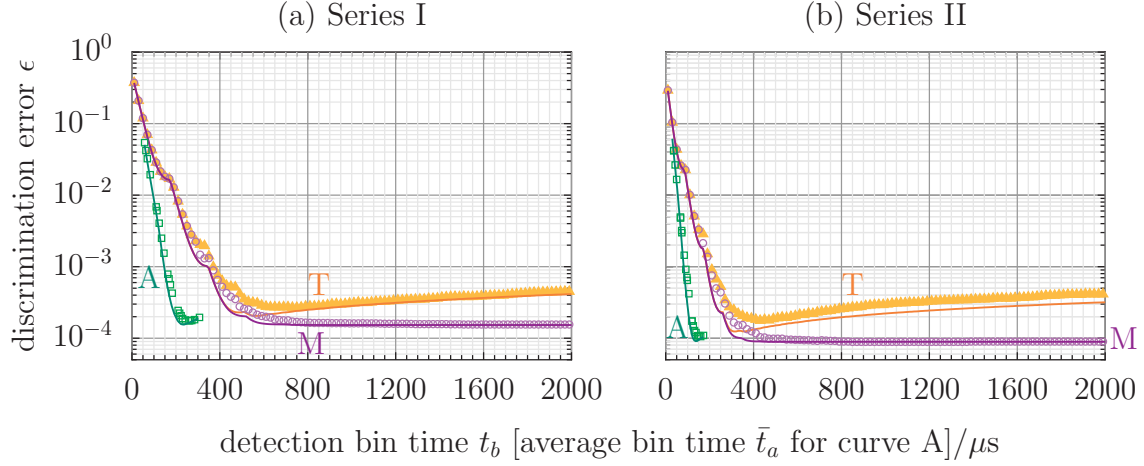


Figure 4.9: Variation of discrimination error with bin time for the two series of readout experiments; statistical uncertainties are at most the size of the datapoints. Solid lines show the results of a simulation of 10^8 trials using the methods described in section 3.3. T: Threshold method (orange), M: Maximum likelihood method (purple), A: Adaptive maximum likelihood method (green).

4.4.1 Threshold method

The time-resolved data enables us to find the optimum detection bin length t_b at analysis time. We find that the threshold method reaches a minimum error of $\epsilon = 1.8(1) \times 10^{-4}$ at $t_b = 420 \mu\text{s}$ using a threshold at $n_c = 5\frac{1}{2}$. The majority of the error is due to above-threshold events in the dark $|D\rangle$ -prepared histogram $\epsilon_D = 3.1(3) \times 10^{-4}$; this is mainly due to the $|D\rangle \rightarrow |B\rangle$ decay rate. The histograms for this bin time are shown in figure 4.10. The theoretical distributions are also shown, generated using the rates R_B and R_D measured from this data and listed in table 4.1. The super-Poissonian noise can be seen as the excess width of the experimental histograms relative to these, which increases the histogram overlap and hence ϵ : drifts in R_B widen the $|B\rangle$ histogram and cosmic rays contribute to a tail in both histograms towards higher n . The contribution of cosmic rays to ϵ_D was estimated by applying the threshold method to the theoretical distributions discussed in the previous chapter, with and without an experimental cosmic ray distribution convolved in. An excess error of 0.62×10^{-4} was found in ϵ_D at the theoretical optimum $t_b = 320 \mu\text{s}$, reducing to 0.38×10^{-4} at experimental optimum $t_b = 420 \mu\text{s}$. Comparing this with the values of ϵ_D from the experimental analysis at $t_b = 320 \mu\text{s}$ and $420 \mu\text{s}$, the contribution of cosmic rays is estimated to be between 12% and 20% of ϵ_D .

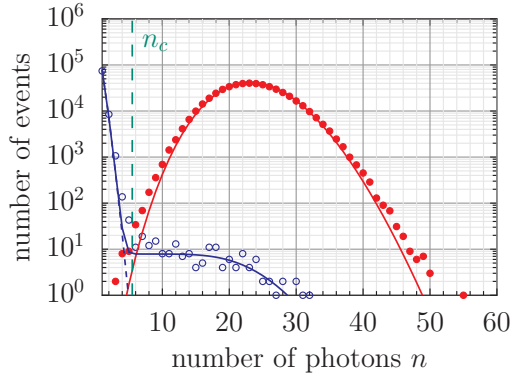


Figure 4.10: Experimental histograms of count data from the series II set of readout experiments, half prepared in $|B\rangle$ (\bullet) and half in $|D\rangle$ (\circ) for $t_b = 420 \mu\text{s}$. Theoretical probability distributions (lines) for $B_0(n)$ (solid, red); $D_0(n)$ with decay (solid, blue); $D_0(n)$ with no decay (dashed, blue). The optimum threshold n_c for discrimination is shown as a vertical dashed line (green).

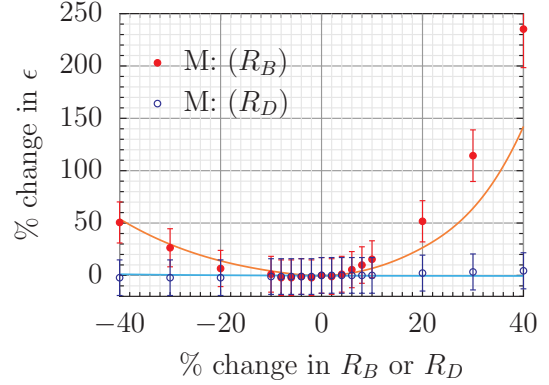


Figure 4.11: Sensitivity of the maximum likelihood analysis method to analysis parameters R_B and R_D . Data points show the discrimination error ϵ obtained from an analysis of the data with R_B and R_D altered from the optimal values listed in table 4.1. Solid lines show the sensitivity expected from simulations (these are the spline fits in figure 3.12).

4.4.2 Maximum likelihood method

The distributions $B(n)$ and $D(n)$ necessary for this analysis protocol (see section 3.2.3) were generated by convolving Poisson distributions with an experimentally derived non-Poissonian tail in order to account partially for the effect of cosmic rays.

For $t_b \gtrsim 200 \mu\text{s}$ the maximum likelihood method gives a lower error than the threshold method as it is able to recognise some of the “D” trials where a $|D\rangle \rightarrow |B\rangle$ decay has occurred. Typical trials taken from the series II data set are shown in figure 4.12, together with the maximum likelihood trajectory of $P(|B\rangle | \{n_i\}) = p_B / (p_B + p_D)$, the probability that the event seen was caused by an ion prepared in $|B\rangle$. Examples (a) and (b) show typical bright and dark trials respectively, while (c) shows a trial in which a $|D\rangle \rightarrow |B\rangle$ decay occurred around $t = 240 \mu\text{s}$. This trial contains 12 counts in the first $420 \mu\text{s}$ and so would be incorrectly identified by the threshold method (where $n_c = 5\frac{1}{2}$); nevertheless the event is correctly recognised as an initially dark ion by the maximum likelihood analysis.

The maximum likelihood error ϵ tends towards an asymptotic value of $\epsilon = 0.89(11) \times 10^{-4}$ (or a fidelity of $\mathcal{F} = 99.9911(11)\%$) which it attains at $t_b \geq 850 \mu\text{s}$; by $t_b = 550 \mu\text{s}$ the error has reached within 10% of this asymptotic value. As for the threshold analysis, more errors are made when measuring the $|D\rangle$ state, with $\epsilon_D = 1.5(2) \times 10^{-4}$ and $\epsilon_B = 0.31(8) \times 10^{-4}$. The value of ϵ reached is consistent with the simulation’s

asymptote $(0.891(9) \times 10^{-4})$ and is close to the minimum possible ϵ predicted by equation (3.20) for $R_D = 0$, $\epsilon = 0.85 \times 10^{-4}$. That the experimental data converges to the simulation's asymptote despite the super-Poissonian noise present is an indication that the maximum likelihood method is less sensitive to cosmic rays and drifts in R_B than the threshold method at long t_b ⁹. Furthermore, the maximum likelihood method only requires knowledge of the rates R_B and R_D , and the choice of a sufficiently long t_b with small enough t_s . The rates R_B and R_D for our analysis were taken from the experimental data but using independently measured values gives the same ϵ . The maximum likelihood method is less sensitive to these input parameters than the threshold method (see section 3.3.2 and figure 4.11), for which n_c and t_b must be carefully tuned from control data to attain the minimum ϵ .

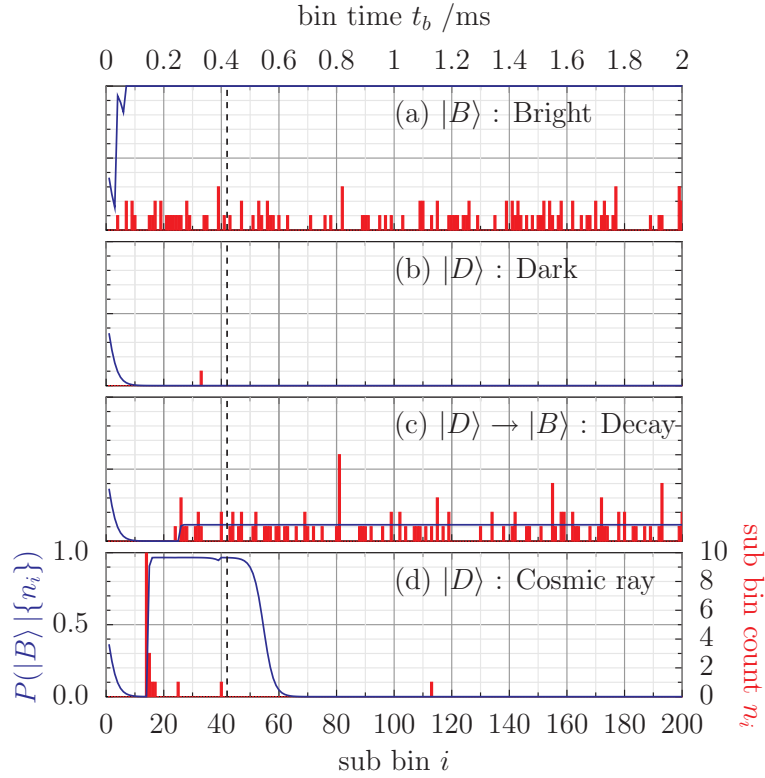


Figure 4.12: Example events (red) from the series II data set with a maximum likelihood analysis (blue) plotted as $P(|B\rangle | \{n_i\}) = p_B / (p_B + p_D)$, the estimated probability that the event seen was caused by an ion prepared in $|B\rangle$. The dashed line shows the optimal $t_b = 420 \mu s$ for the threshold method. Plots (a) and (b) show bright and dark trials, (c) shows a $|D\rangle \rightarrow |B\rangle$ decay around $240 \mu s$ and (d) shows a cosmic ray arriving during a dark trial.

The insensitivity of the maximum likelihood method to some cosmic rays can be understood by considering the example event shown in figure 4.12(d) which shows a cosmic ray arriving in a trial prepared in $|D\rangle$. There is an initial pulse of 12 counts

⁹The agreement also gives us confidence in our correction for imperfect population preparation.

at $t = 140 \mu\text{s}$, followed by “after-pulsing”— occasional single counts over the next ms (possibly the result of luminescence excited in the glass envelope of the PMT). The bin with $n_i = 12$ is highly unlikely from both $B(n_i)$ and $D(n_i)$ distributions; it is the after-pulsing which mimics fluorescence at a rate R_B and causes $P(|B\rangle|\{n_i\}) \rightarrow 1$. If the counting bin were to stop at $t_b = 420 \mu\text{s}$ or the after-pulsing were to continue for longer then the event would be incorrectly identified. However, for $t_b \geq 550 \mu\text{s}$ the event is correctly identified as “D” as the after-pulsing has ceased. If a cosmic ray event occurs late in the counting bin it is likely that the event will still be correctly identified despite the after-pulsing— the event then looks similar to a $|D\rangle \rightarrow |B\rangle$ decay which can be recognised by the maximum likelihood method.

The likelihoods p_B and p_D calculated during the readout process in a maximum likelihood analysis can be used to quantify our confidence in the measurement outcome by calculating the “estimated errors” e_D or e_B (see (3.13) for example); these are the same quantities used in the adaptive analysis technique. These estimated errors could be exploited in quantum error correction algorithms, enabling us to choose to repeat the necessary part of the algorithm if our confidence in an ancilla measurement is judged to be too low.

Figure 4.13 shows the distribution of estimated errors e_B and e_D seen in the experimental data set for each value of $t_b = Nt_s$ as it is analysed with the maximum likelihood method. Plot (a) shows the trials prepared in $|B\rangle$ which are correctly identified. After $t_b \approx 140 \mu\text{s}$, most trials are identified with an estimated error e_B in the region 10^{-4} – 10^{-6} . In contrast, the estimated error e_D shown in plot (b) for correctly identified states prepared in $|D\rangle$ continues to decrease as t_b increases. It is the inclusion of the decay probability in p_D which limits e_B for the bright trials in plot (a). Plots (c) and (d) show the estimated errors for trials that were incorrectly identified. On average, the confidence in these identifications is lower than for states correctly identified: $e_B > 10^{-4}$ for most incorrectly identified “D” trials¹⁰ and of order 10^{-1} for “B” trials. Therefore, at longer t_b , lower confidence in the measurement outcome indeed correlates with an incorrect decision. Figure 4.14 shows the result of demanding a minimum confidence level from trials in our data set. As a higher confidence is required from the analysis (the maximum permissible e_B or e_D is reduced) the resultant error ϵ decreases, at the expense

¹⁰Figure 4.13(d) is expected to include ~ 14 trials mistakenly prepared in $|B\rangle$ due to imperfect population preparation. These are likely to account for the trials with $e_B < 10^{-5}$.

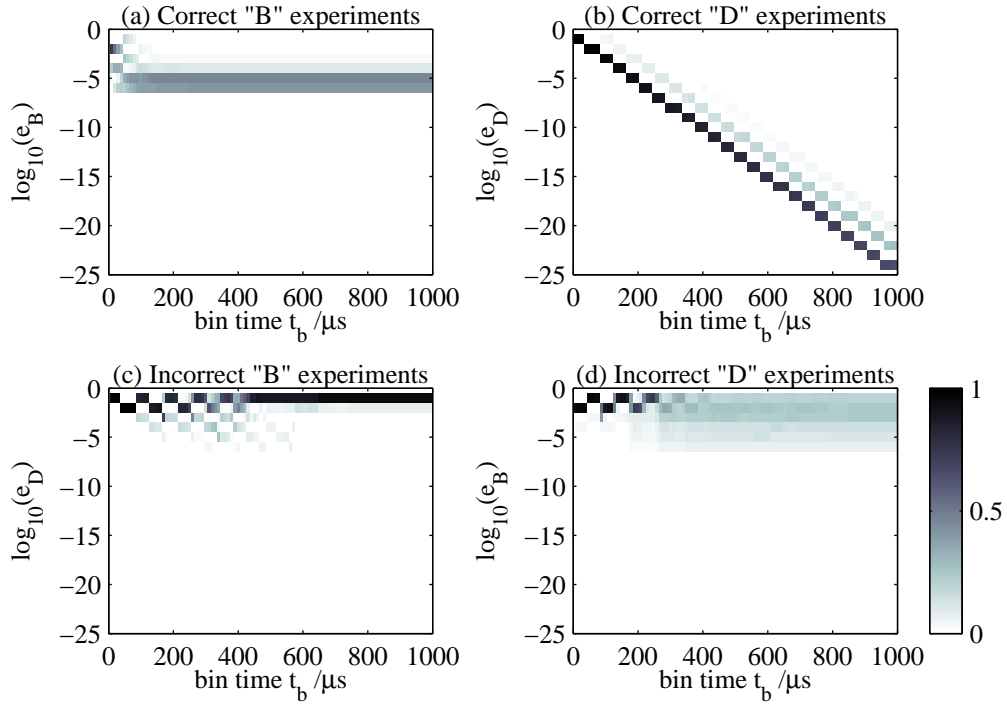


Figure 4.13: Surface plots showing the distribution of estimated errors (e_B or e_D) from the maximum likelihood method at each bin time t_b . At each t_b the trials are divided into four groups; those prepared in $|B\rangle$ or $|D\rangle$ and then further into those correctly or incorrectly identified. The colour shows the proportion of trials with a given e_B (or e_D) at each t_b , normalised by the number of trials in the group.

of rejecting ever more trials from the dataset. By demanding an estimated error lower than 3×10^{-5} we can reduce ϵ for the remaining trials by an order of magnitude, thus achieving 99.999% fidelity at the price of discarding only $\sim 2\%$ of the measurements.

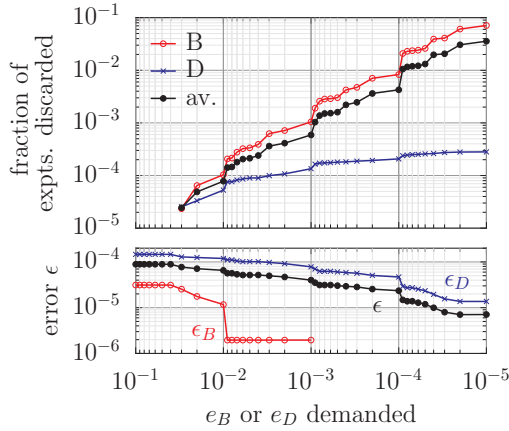


Figure 4.14: The effect on the net discrimination error ϵ (lower plot) as low-confidence events are discarded, shown for a maximum likelihood analysis at $t_b = 850 \mu\text{s}$. The abscissa shows the maximum estimated error allowed, while the upper plot indicates the fraction of trials in the data set which were discarded for having a larger error than this.

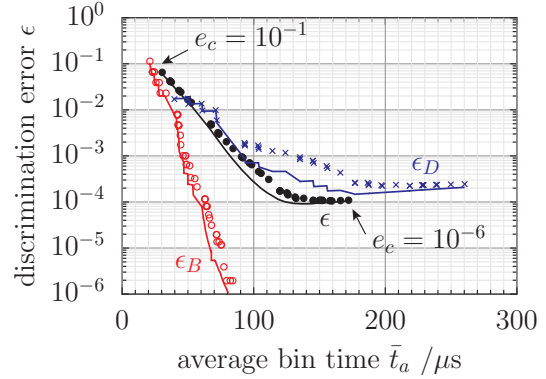


Figure 4.15: Results for the adaptive analysis of the series II set of readout experiments showing average ϵ (\bullet), ϵ_B (\circ) and ϵ_D (\times) together with errors expected from an M-C simulation (solid lines).

4.4.3 Adaptive maximum likelihood method

An adaptive maximum likelihood analysis of the data is shown in figure 4.15 for a range of e_c from 10^{-6} to 10^{-1} and using a cutoff time $t_c = 650 \mu\text{s}$ which was found to give the lowest ϵ in the fastest average time \bar{t}_a . This adaptive analysis shows a substantial reduction in average readout time, reaching a minimum of $\epsilon = 1.1(1) \times 10^{-4}$ in $\bar{t}_a = 145 \mu\text{s}$ (using $e_c = 10^{-5}$) which is ~ 34 times lower than the non-adaptive maximum likelihood analysis, or nearly 3 times as fast to reach the same ϵ . An error of $\epsilon = 1.0(1) \times 10^{-4}$ is possible using a simple additional cosmic-ray veto¹¹. The error for the $|D\rangle$ state is again larger at $\epsilon_D = 2.0(2) \times 10^{-4}$ compared to $\epsilon_B = 2.0(6) \times 10^{-5}$ and the average readout time for the dark state is also longer ($219 \mu\text{s}$) than that for the bright state ($72 \mu\text{s}$) as expected (see section 3.2.4). In fact, it is possible to arrange¹² to get very low ϵ_B at the expense of a slight increase in ϵ_D . The data imply that $\epsilon_B < 2 \times 10^{-6}$

¹¹The veto involves replacing neighbouring sub-bins with zero when their sum is equal to 7 counts or more.

¹²To do this, one must lower e_c which forces \bar{t}_a to increase and ϵ_B becomes smaller at the expense of ϵ_D , which will raise due to the increased likelihood of decays. A non-adaptive version of this would simply be to perform a threshold analysis choosing a threshold n_c below that in (3.1).

(zero events in all 5.12×10^5 $|B\rangle$ trials, or a bright-state fidelity $\mathcal{F}_B > 99.9998\%$) is possible in $\bar{t}_a = 79 \mu\text{s}$ whilst retaining $\epsilon_D = 2.1(2) \times 10^{-4}$ in $239 \mu\text{s}$.

This asymmetric readout error ($\epsilon_B \ll \epsilon_D$) could be exploited for QEC by encoding the “no-error” syndrome of the ancilla qubits in the $|B\rangle$ state which has the higher readout fidelity. The gates performed within the algorithm must have a reasonably high fidelity in order to avoid the use of a large number of physical qubits to encode each logical qubit [49], consequently the “no-error” syndrome of the ancilla qubits will be measured most often. The probability of an error within the algorithm is therefore reduced overall if the most frequently measured qubit state has the highest readout fidelity. A second aspect of the adaptive maximum likelihood method that can be exploited in QEC is the “estimated error” discussed previously. However, the estimated errors for the adaptive analysis in figure 4.15 do not show an obvious correlation between the events with measurement errors and those with low confidence. This could be partly due to ignoring decay in our calculation of p_D and partly due to the short¹³ average measurement time \bar{t}_a . This lack of correlation is only a problem for this particular adaptive protocol and is not true in general. Figure 4.16 shows the estimated errors from a different adaptive analysis of our data when decay is included in the calculation of p_D (method AD discussed in section 3.3.1); this also causes a longer \bar{t}_a . For comparison with figure 4.13, the average measurement time \bar{t}_a increases along the x axis with decreasing e_c . When the lowest e_c is demanded (corresponding to the lowest ϵ) then the incorrectly identified trials also show the largest estimated errors.

4.5 Comparison with double measurement schemes

In situations where high fidelity state preparation is not possible it is difficult to separate errors due to imperfect state preparation from those due to a finite readout fidelity. It may not be possible to compare the outcome from a single measurement with a known initial state. In this case, some measurement of the fidelity can be made by using a double-measurement scheme in which the outcomes of two consecutive measurements $\{M_1 M_2\}$ are compared and the number of trials showing a disagreement between M_1 and M_2 are recorded. This scheme was employed by the NIST ion trap group in the paper by Hume *et al.* [42]. Even though we are able to prepare our single ion qubit

¹³The correlation between errors and low confidence only becomes obvious at longer t_b in figure 4.13.

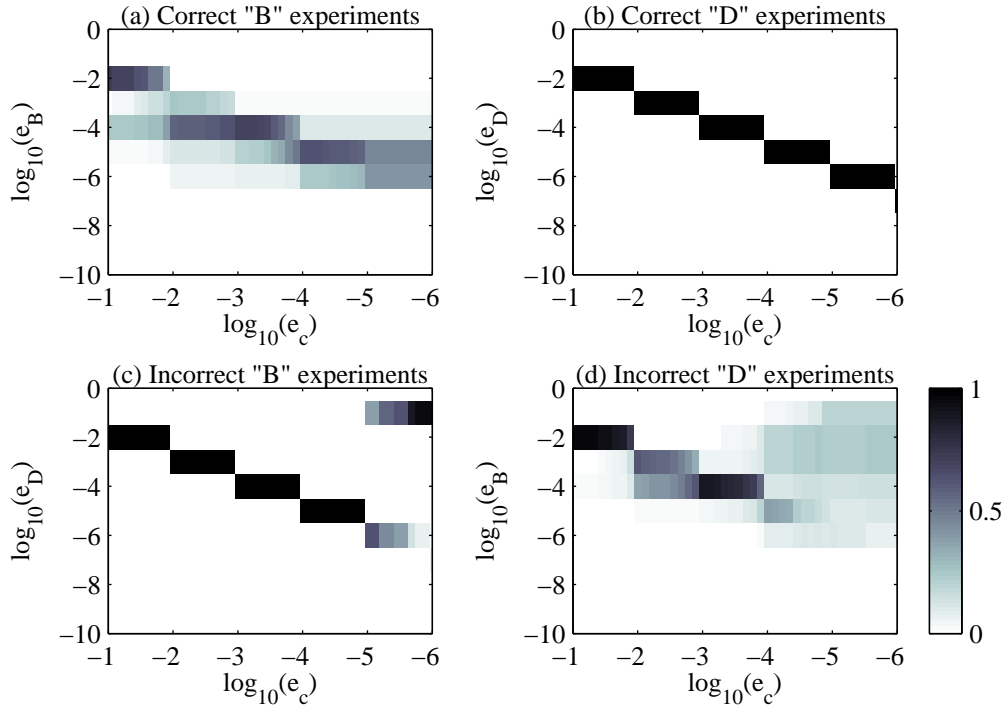


Figure 4.16: Surface plots showing the distribution of estimated errors (e_B or e_D) from the adaptive maximum likelihood method when decay is included in the calculation of p_D (method AD). The cut-off threshold is e_c . In general, average measurement time \bar{t}_a is increasing along the x axis with decreasing e_c ($\bar{t}_a = 555 \mu\text{s}$ at $e_c = 10^{-6}$). The data is displayed in a similar format to figure 4.13.

in both initial states with high fidelity, it is still worth analysing our data in a double measurement scheme to get more insight into the analysis performance. The analysis is non-trivial due to the presence of both random (Poissonian) and systematic (decay) errors.

We can write down the probability of obtaining each possible double-measurement outcome $\{BB, BD, DB, DD\}$ given an initial qubit state $|B\rangle$ or $|D\rangle$. We assume that only statistical errors cause readout errors in trials prepared in $|B\rangle$ and we denote these statistical errors by ϱ_B . Readout errors in trials prepared in $|D\rangle$ are caused by both statistical errors ϱ_D and decay events. The probability of a $|D\rangle \rightarrow |B\rangle$ decay occurring in a measurement of length t_b is $Q \approx t_b/\tau$, and the probability that such a decay then causes an error is x . The value of x depends in general on both the bin time and the analysis method and can vary between 1 (a decaying ion always causes an error) and 0 (decaying ions are always spotted by the analysis method). The probabilities of obtaining each possible measurement outcome from consecutive measurements $M_1 M_2$ are as follows:

Experiments prepared in $|B\rangle$:

$$s(BB) = (1 - \varrho_B)(1 - \varrho_B)$$

$$s(BD) = (1 - \varrho_B)\varrho_B$$

$$s(DB) = \varrho_B(1 - \varrho_B)$$

$$s(DD) = \varrho_B\varrho_B$$

Experiments prepared in $|D\rangle$:

$$q(BB) = (1 - 2Q)\varrho_D\varrho_D + Qx(1 - \varrho_B) + \varrho_D Qx$$

$$q(BD) = (1 - 2Q)\varrho_D(1 - \varrho_D) + Qx\varrho_B + \varrho_D Q(1 - x)$$

$$q(DB) = (1 - 2Q)(1 - \varrho_D)\varrho_D + Q(1 - x)(1 - \varrho_B) + (1 - \varrho_D)Qx$$

$$q(DD) = (1 - 2Q)(1 - \varrho_D)(1 - \varrho_D) + Q(1 - x)\varrho_B + (1 - \varrho_D)Q(1 - x)$$

where the first term applies to no decay, the second term to decays in M_1 and the third to decays in M_2 . If we make the approximation that ϱ_B , ϱ_D and Q are all small then

we can neglect second order terms to find:

Experiments prepared in $B\rangle$:	Experiments prepared in $D\rangle$:
$s(BB) \approx 1 - 2\varrho_B$	$q(BB) \approx Qx$
$s(BD) \approx \varrho_B$	$q(BD) \approx \varrho_D$
$s(DB) \approx \varrho_B$	$q(DB) \approx \varrho_D + Q$
$s(DD) \approx 0$	$q(DD) \approx 1 - 2\varrho_D - Q - Qx$

(4.7)

In general we may wish to quantify the readout errors separately for measurements on the two qubit states $|B\rangle$ and $|D\rangle$ as the fidelities can be quite different, as noted earlier. The two readout fidelities we are aiming to measure are those obtained in a single measurement on a state that we can prepare with high fidelity—these are the values of ϵ_B and ϵ_D measured in the experiments described in this chapter. In terms of the statistical and decay errors, these are:

$$\begin{aligned}
 \epsilon_B &= \varrho_B & \epsilon_D &= (1 - Q)\varrho_D + Qx \\
 & & &\approx \varrho_D + Qx
 \end{aligned}
 \tag{4.8}$$

If we have chosen a double measurement scheme it is presumably because it is not possible to prepare the initial states $|B\rangle$ and $|D\rangle$ with high fidelity. In this case, we must combine the two sets of probabilities $s(M_1M_2)$ and $q(M_1M_2)$ shown in (4.7) for each measurement outcome, weighting them with the probability of preparing each initial state to get $p(M_1M_2)$, the total probability of obtaining the outcome $\{M_1M_2\}$. One might hope that the four resulting equations could be solved to obtain ϱ_B , ϱ_D and x in terms of $\{p(BB), p(BD) \dots\}$, enabling us to reconstruct ϵ_B and ϵ_D from experimental data according to (4.8). Unfortunately this is not possible as $p(BD)$ and $p(DB)$ turn out to be simply related by the state preparation probability, leaving us with only two independent equations for three unknowns.

If we are in a situation where we can initialise our qubit state with only a small infidelity δ then to first order this only affects the probabilities s, q for $\{BB, DD\}$ in (4.7). We can use the number of $\{BD, DB\}$ mismatches we see in our experimental data to determine the statistical errors ϱ_B , ϱ_D . Unless we have a good independent measure of the state preparation infidelity, it may be difficult to extract x from our measurement of $q(BB) \approx Qx + \delta$ for trials prepared mostly in $|D\rangle$. In general, measures of infidelity

from the double-measurement scheme will always include some measure of the state preparation fidelity.

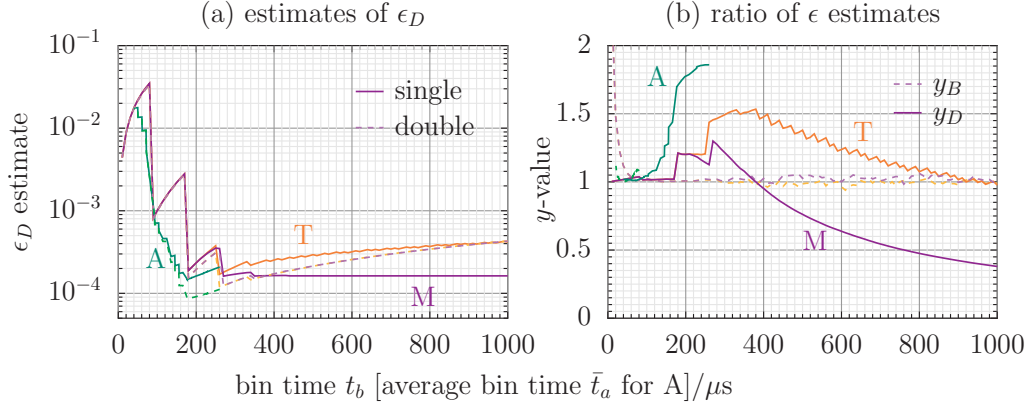


Figure 4.17: (a) Estimates of the discrimination error for states prepared in $|D\rangle$. Solid lines show the true ϵ_D from 5×10^7 simulations with typical R_B , R_D to match the series II set of experiments, analysed as single measurements. Dotted lines show the error measure $W/(2N_{\text{dbl}})$ from the same data analysed with the double-measurement scheme. T: Threshold method (orange), M: Maximum likelihood method (purple), A: Adaptive maximum likelihood method (green). (b) Ratio of the single and double measurement error estimates y_B and y_D as defined in the text. Solid lines show y_D for the simulations in plot (a), dotted lines show y_B for 5×10^7 simulations prepared in $|B\rangle$.

In Hume *et al.* [42] the readout error was quantified by counting the number of $\{BD, DB\}$ mismatches, W in N_{dbl} double-measurement trials. Assuming high fidelity state preparation, how well can we reconstruct our single-measurement values of ϵ_B and ϵ_D by this method? Figure 4.17(a) shows a comparison of the error measure $W/(2N_{\text{dbl}})$ with the readout error ϵ_D for qubits initialised in $|D\rangle$. The data shown is for the same simulated data set, analysed both as single measurements and double trials; a discrepancy is visible between the two error measures for each analysis method. For the adaptive analysis this discrepancy reaches nearly a factor of two (which is $\sim 50\times$ the statistical uncertainty). The double-measurement error estimates are the same¹⁴ for the threshold and maximum likelihood methods at large t_b . The ratio y_D between the error measures ϵ_D and $W/(2N_{\text{dbl}})$ is shown in figure 4.17(b) for simulations prepared in $|D\rangle$ and analysed by different methods. Theoretically this ratio is given by $y_D = 2\epsilon_D/(q(DB) + q(BD))$. The ratio y_B for simulations prepared in $|B\rangle$ is also shown, given by $y_B = 2\epsilon_B/(s(DB) + s(BD))$. Substituting in from (4.7) we see that for qubits initialised in $|B\rangle$ then $y_B = 2\epsilon_B/(2\varrho_B) = 1$ and this is reflected in figure 4.17(b), which shows $y_B \approx 1$ for all methods¹⁵. $W/(2N_{\text{dbl}})$ is thus a good measure of the readout error

¹⁴This can be explained by looking at $(q(DB) + q(BD))$ in (4.7) and noticing that $W \propto Q$ at large t_b when decay will dominate. There is no dependence on x (which varies with analysis method).

¹⁵At very small t_b the values of y plotted are unreliable as the approximations we used to write down

for qubits initialised in $|B\rangle$. For qubits initialised in $|D\rangle$ the statistical error dominates at short t_b so $\epsilon_D \approx \varrho_D$ and the same argument applies: $y_D = 1$ at short t_b . However, for long t_b then the decay effect dominates over ϱ_D and $y_D \rightarrow 2x$. In general, however, both statistical and decay errors will contribute and so neither $W/(2N_{\text{dbl}})$ nor Wx/N_{dbl} will be the correct estimator of the underlying ϵ_D . In addition the factor x varies with both the analysis method and t_b . In figure 4.17(b) $y_D \approx 1$ for all methods at short t_b . At longer t_b the value of y_D begins to reflect the value of x , the ability of the analysis method to spot decays.

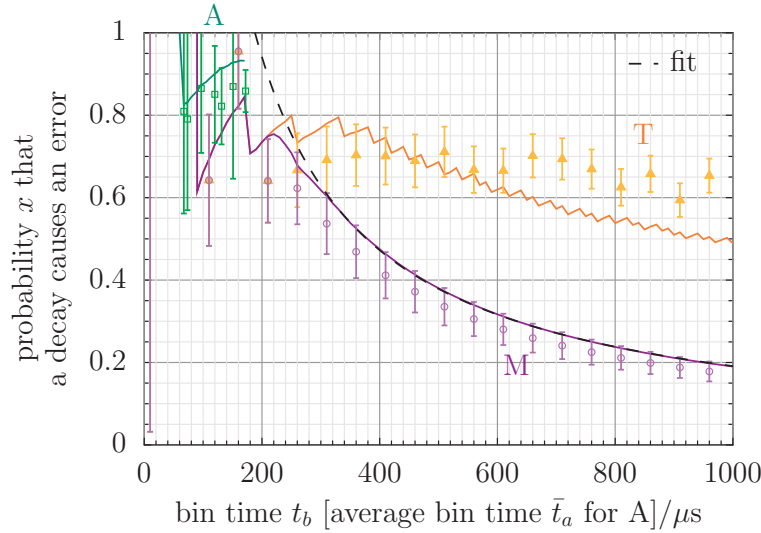


Figure 4.18: The probability x that a $|D\rangle \rightarrow |B\rangle$ decay causes an error when analysed with various analysis protocols. The solid lines show the value of x predicted from 10^8 simulations, data points show x extracted from the series II set of experiments. T: Threshold method (orange), M: Maximum likelihood method (purple), A: Adaptive maximum likelihood method (green).

Since we have a reliable estimate of the preparation infidelity for the $|D\rangle$ state (section 4.3) we can extract x from our experimental data by analysing it with a double measurement scheme and counting the number of $\{BB\}$ trials seen. This is shown in figure 4.18 along with the value of x extracted from our simulations¹⁶. Figure 4.18 shows that at shorter t_b all methods are poor at spotting decay events. The threshold method gets slightly better at longer t_b , with $x \rightarrow 0.5$ indicating that only half of all decay events will cause an error. The maximum likelihood method becomes increasingly effective at long t_b with x decreasing $x \propto 1/(1 - \exp(-t_b/\tau))$ so that the increased number of decays is matched by an increasing efficiency to spot them, resulting in a value of ϵ_D that asymptotically approaches a minimum value, as seen in figure 4.17(a).

(4.7) (namely that ϱ is small) are not valid.

¹⁶As in figure 4.17(b), the value of x plotted is unreliable at very small t_b

This fitted function for x is plotted as a dashed line in figure 4.18. For the adaptive maximum likelihood method the average value of x is plotted¹⁷. This remains close to 1 as the average bin time \bar{t}_a is small, meaning the method is overall poor at spotting decays.

In summary, the quantity $W/(2N_{\text{dbl}})$ reflects the underlying error ϵ_B well for qubits initialised in $|B\rangle$ with high fidelity. For qubits initialised in $|D\rangle$ the complication of decays means that $W/(2N_{\text{dbl}})$ is often a poor estimator of ϵ_D , depending on both the analysis method and t_b . For the threshold and adaptive methods this causes an underestimate of the error at the optimum t_b ; for the adaptive method this underestimate is by nearly a factor of two!

4.6 Summary of experimental readout results

In this chapter we have applied the analysis protocols in chapter 3 to experimental data. We investigated the temporal characteristics of cosmic rays arriving at the PMT: these events were responsible for 12%–20% of the “dark” trials which were incorrectly identified as a bright ion with the threshold method. The maximum likelihood method was able to identify most of these events correctly: using this method we have demonstrated readout of a single $^{40}\text{Ca}^+$ ion with a fidelity of 99.991(1)%.

Analysis method		Experiment	Simulation
T: threshold	ϵ	$1.8(1) \times 10^{-4}$	$1.24(1) \times 10^{-4}$
	t_b	$420 \mu\text{s}$	$320 \mu\text{s}$
M: maximum likelihood	ϵ_∞	$0.89(11) \times 10^{-4}$	$0.891(9) \times 10^{-4}$
	t_b	$\geq 850 \mu\text{s}$	$\geq 570 \mu\text{s}$
	$t_{1.1}$	$550 \mu\text{s}$	$360 \mu\text{s}$
A: adaptive	ϵ	$1.0(1) \times 10^{-4}$	$0.91(1) \times 10^{-4}$
	\bar{t}_a	$145 \mu\text{s}$	$137 \mu\text{s}$

Table 4.5: Summary of the discrimination error ϵ and detection time t_b obtained experimentally and from simulations. The quantity ϵ_∞ is the asymptotic error as $t_b \rightarrow \infty$. $t_{1.1}$ gives the time to reach $\epsilon = 1.1\epsilon_\infty$. \bar{t}_a is the average detection time for an adaptive analysis.

A summary of the discrimination error ϵ obtained experimentally for each analysis protocol is shown in table 4.5 with simulated results for comparison. For all analyses $\epsilon_B < \epsilon_D$, meaning that the $|B\rangle$ state is detected with the highest fidelity; we have discussed how this could be exploited in quantum error correction. We have also in-

¹⁷because we can only find the average value of $Q \approx \bar{t}_a/\tau$

investigated the effect on measurement fidelity when low-confidence measurements are discarded: a fidelity of 99.999% was possible at the price of discarding 2% of our measurement trials.

Finally, we considered how to determine the measurement fidelity in situations where high-fidelity state preparation is not possible. We re-analysed our data in the form of a double measurement scheme and showed that counting the fraction of double-measurement trials that do not match can lead to an under-estimate of the underlying discrimination error for the $|D\rangle$ state. This depends on the analysis method and detection time, but can be as large as a factor of two.

Chapter 5

Ion readout using a CCD camera

The previous chapters concerned high-fidelity readout of a single ion using a PMT. When performing a real quantum computation one may wish to read out several ions held in a single trapping zone. The PMT could be used to determine how many ions are fluorescing and so could provide a measure of the parity of the ion string, but determining the states of individual ions with the PMT would not be possible. Imaging the ion string with a CCD array provides spatial resolution and allows the states of each of the ions to be determined with high fidelity. This allows parallel readout of many qubits at once—an essential step towards scaling up the computation to many ions [49]. It is also necessary for the qubit readout step to be performed fast in comparison with the logic-gate speed to enable quantum error correction to be performed.

In this chapter we begin by describing the architecture of EMCCD cameras and the extra noise sources present in them. We then discuss simulation and analysis methods for camera readout and give some simulation results. The presentation of the main body of simulations is deferred to chapter 6, after the discussion of experimental data.

5.1 EMCCD cameras

The experiments described in the next two chapters concern ion readout using an EMCCD (electron multiplying charge coupled device). This is a high gain, low noise camera which has been available commercially since 2001 [162]. The CCD architecture is pictured in figure 5.1 and is comprised of a standard frame-transfer CCD with the addition of an extra “gain register”. The image is captured on the exposed portion of the CCD array where incident photons are converted (with a certain quantum efficiency, Q) into

photoelectrons. Typical saturation intensities for EMCCDs are at the level of 10^4 – 10^5 photoelectrons per pixel and the CCD arrays can have fill factors of 100%, meaning there are no gaps between pixels. After the image is captured it is rapidly shifted to the covered storage region which prevents any further light being captured while the charge is read out from the pixels (a relatively slow process). This arrangement also allows a faster frame rate as the next exposure can proceed as the previous image is read from the storage region. The readout of charge begins by shifting all the columns vertically down by one row so that the lowest row is moved into the serial readout register. From there, the row is shifted horizontally through the gain register and finally pixel-by-pixel into the readout pre-amplifier, after which it is converted to a “count” at the analogue-to-digital converter (ADC). The primary amplification of the signal occurs as the charge in each pixel is moved through the gain (or “multiplication”) register. The movement of charge between pixels is achieved by altering “clock” voltages on electrodes; in the gain register these clock voltages are arranged so that there is a small probability p that an electron moving to the next “pixel” will generate a secondary electron via impact ionisation. Although the probability per transfer is typically small (0.01–0.02) [163] after many transfers through the r “pixels” in the gain register, the total mean gain $G = (1 + p)^r$ can be fairly large. For our camera, $r = 512$ and gains up to $G \approx 1000$ can be achieved.

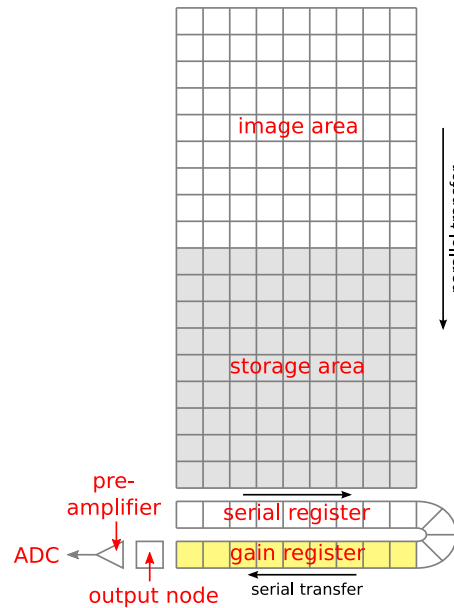


Figure 5.1: Schematic of a frame-transfer EMCCD architecture.

5.1.1 Noise sources in the camera

We now turn to a discussion of the noise sources in the camera. Each extra noise source manifests itself as an extra spread in the count values we record when we are trying to detect the state of an ion. This can be viewed as an increased overlap of the “B” and “D” histograms we discussed in chapter 3 and hence an increased readout error ϵ .

Shot noise

In the previous two chapters, readout using a photomultiplier tube (PMT) was described in which the only source of noise (apart from cosmic rays) was the statistical shot-noise from the photons, including both the ion signal S_B and dark counts S_D (which include scattered laser light). We assume that the noise obeys Poisson statistics so that the variance $\sigma_B^2 = S_B$. This source of noise is also present in data read out from the EMCCD, although the rates S_B and S_D will not be exactly the same as for the PMT. Firstly, the two devices have a different quantum efficiency Q , so we must scale the proportion of scattered signal and background light collected accordingly. Secondly, there are extra contributions to S_D which do not occur in PMTs, which will be discussed below.

Cosmic rays

Although cosmic rays are detected by CCD cameras, the spatial resolution of the CCD means that they will rarely be a problem in readout. Janesick [164] notes that these events occasionally show as tracks across the CCD array, but more often affect only a few pixels as most have a high angle of incidence. He quotes a nominal fluence of $0.025 \text{ cm}^{-2} \text{ s}^{-1}$ at sea-level, therefore the probability of the rays hitting the tiny region of the CCD that an image of one ion occupies is quite small. For this fluence, we estimate the probability of a cosmic ray occurring in a single 500-pixel $400 \mu\text{s}$ exposure is $\sim 10^{-8}$. The probability of recording a cosmic ray amongst all of the data presented in chapter 6 is $\sim 1\%$, we nevertheless did see a single event (see figure 6.8).

Thermal dark current

Apart from scattered laser light, there are contributions to S_D for both the PMT and CCD in the form of thermal dark counts which increase with exposure time. The rate of thermal dark counts R_{therm} can be reduced by cooling the device and, for an EMCCD,

cooling reduces these thermal counts to such a low level that the dark count rate is instead dominated by dark counts from a different mechanism, discussed next.

CIC noise

“Clock-induced charge” (CIC) noise (or “spurious charge”) λ_{CIC} is a noise source which is independent of exposure time and is introduced for each pixel read out from the EMCCD camera. CIC noise is generated by a similar mechanism to that which provides the gain of the EMCCD. As charge is moved from one pixel to the next, there is a possibility that a hole trapped beneath the electrode will be accelerated by the clock voltage and will collide with a silicon atom, producing a new electron-hole pair via impact ionisation. Spurious charge is also generated in conventional CCDs as charge is moved off the pixel array but it is generally swamped by the noise in the readout amplifier. In EMCCDs, however, the extra CIC electrons will be amplified above the noise floor by the gain register and be indistinguishable from real photoelectrons. This phenomenon has been extensively studied in EMCCDs by Tulloch [165, 166, 167] and is discussed in detail by Janesick [164].

The amount of spurious charge generated depends sensitively on the speed and magnitude of the changes in clock voltage and can be minimised by optimisation of the clock waveforms. Most of this work has already been done by the camera manufacturer¹ and only a few parameters are left for user optimisation: the vertical shift-speed and a clock voltage parameter. The vertical shift speed controls how fast the rows are moved down the CCD and a faster shift-speed can result in lower “parallel register” CIC noise; a fast shift-speed demands the clock voltage spends less time in the inverted state (in which holes can be accelerated) so the trapped holes do not have the opportunity to move. However, with increasing shift-speed, charge transfer efficiency can reduce resulting in information being left behind on the CCD. To combat this, one can increase the clock voltages to move charge more efficiently. Unfortunately higher clock voltages result in increased CIC noise so a compromise must be found, namely the minimum possible increase in clock voltage required to move the charge from the CCD as fast as possible.

As well as being generated by parallel shifts, spurious charge is also generated in the gain register. Tulloch [165] found that this “serial register” spurious charge accounted

¹We chose the camera advertised as having the lowest CIC noise rate, assuming they had performed this optimisation the best!

for most of the CIC noise in their particular system. This source of CIC noise increases with increasing gain, nevertheless our experiments operated with maximum gain in order to minimise the effect of noise from the readout amplifier. The amount of CIC noise also increases with decreasing temperature as impact ionisation is more efficient at low temperatures. Despite this, operation at the lowest possible temperature still reduces overall noise from the camera as the dependence of thermal dark current on temperature is much stronger and this is minimised at low temperatures.

Finally the probability of spurious charge being generated depends linearly on the number of transfers made. Therefore when using only a small region of the CCD it is advisable to choose it such that the number of shifts required to reach the readout amplifier is minimised; this also minimises the readout time. The frame-transfer format of the camera presents a disadvantage in this case as the data must be shifted across the whole storage region before readout.

Readout noise

As for all CCD cameras, further noise is introduced during the final readout of the charge at the ADC, including some quantisation noise. In a conventional CCD, this read noise σ_R can be large compared to the signal S_B , however in an EMCCD the gain process amplifies the signal well above this noise floor. The gain process effectively reduces the read noise to σ_R/G , which can be negligible for high gains.

Gain noise

The gain process itself also introduces additional noise: the multiplication mechanism is stochastic, so one electron entering the gain register will result in a spread of possible numbers of electrons leaving it. This excess noise can be quantified by a noise factor F :

$$F = \frac{\sigma_{out}}{G\sigma_{in}}$$

where σ_{in}^2 and σ_{out}^2 are the variances of the input and output signals respectively. This has been studied in detail by Robbins *et al.* [168] who show that it tends towards $F = \sqrt{2}$ for an EMCCD at high gains.

Other noise sources

Fixed pattern noise (pixel-pixel variations in offset or response) can be significant when more than one pixel is considered, but this can be accounted for in experimental analysis. The myriad other noise sources in CCDs have been studied in detail [169, 164] but we shall not quantify them here as they are irrelevant for our purposes.

5.1.2 Comparison with other detectors

We add the various noise sources in quadrature to give the total noise *per pixel* containing both ion signal S_B and dark counts S_D :

$$\begin{aligned}\sigma_{tot} &= \sqrt{F^2(\sigma_B^2 + \sigma_D^2) + \sigma_R^2/G^2} \\ &= \sqrt{F^2(S_B + S_D) + \sigma_R^2/G^2}\end{aligned}\tag{5.1}$$

When reading out fluorescence collected from an ion in state $|B\rangle$, we expect to observe photon numbers distributed with mean $(S_B + S_D)$ and variance σ_{tot}^2 according to (5.1). In the absence of ion signal, the above parameters are modified by setting $S_B = 0$. When all the signal from an ion is incident on one pixel, $S_B = R_B t_b$ and $S_D = R_D t_b + \lambda_{CIC}$ for an exposure of length t_b where R_B is the detected fluorescence rate from a bright ion and R_D is the dark count rate for the single pixel (including thermal dark counts).

Although the bright/dark discrimination error will depend on the detailed shape of the photon-count distributions (section 5.1.3), we can nevertheless construct a figure of merit to make a simple comparison between the EMCCD and other detectors. We wish to discriminate between the “B” and “D” distributions which have means separated by S_B . We add the widths of the distributions in quadrature to give the signal-to-noise ratio (SNR) per pixel:

$$\text{SNR} = \frac{S_B}{\sqrt{F^2(S_B + 2S_D) + 2\sigma_R^2/G^2}}\tag{5.2}$$

Table 5.1 gives typical values for the parameters discussed above, taken from the data sheets for commercially available devices including the model of PMT used in chapter 4, a conventional CCD, an intensified CCD (ICCD) and the EMCCD used for the experiments presented in chapter 6. Read noise is quoted at the maximum possible

readout rate for the device since fast readout is also important for quantum computation.

The gain mechanism for ICCDs is described in [169] and is somewhat similar to that in a PMT: photoelectrons emitted at a photocathode are amplified by a microchannel plate into a cascade of secondary electrons which then hit a phosphor screen where they are converted back to photons before hitting a CCD. This process causes some blurring of the image² and also has an associated noise factor F , varying between 1.6 for a GenIII “filmless” ICCD to as high as 3.52 for the “filmed” version [170].

	Ideal Detector	PMT <i>Hamamatsu H6180-01</i>	CCD <i>Andor iKon-M 934N</i>	ICCD <i>Andor DK740 Gen III (filmless)</i>	EMCCD <i>Andor iXon DU-897 (BI)</i>
Q	100%	16%	60%	35%	55%
σ_R	0	0	10 e^-	15 e^-	50 e^-
Gain G	1	1	1	1000	1000
R_{therm}	0	$\sim 8\text{ s}^{-1}$	0.00012 s^{-1}	0.08 s^{-1}	0.001 s^{-1}
... at T	0	25°C	-100°C	-35°C	-85°C
λ_{CIC}	0	0	—	—	0.005
F	1	1	1	1.6	$\sqrt{2}$
max. R/O	—	—	2.5 MHz	1 MHz	10 MHz

Table 5.1: Parameters for various detectors (*per pixel*), including Q (quantum efficiency at 397 nm), readout noise σ_R quoted at the maximum possible readout rate R/O, thermal dark count rate R_{therm} at the minimum operating temperature T , clock induced charge noise λ_{CIC} and the noise factor, F .

The value of the SNR in (5.2) with changing integration time is shown in figure 5.2 for each device in table 5.1. The “ideal detector” shows the shot-noise quantum limit. Although the conventional CCD gives the highest signal-to-noise for a bright ion at longer t_b , the EMCCD out-performs other detectors in the range $t_b \leq 0.8\text{ ms}$ — a similar range to that investigated for PMT readout in chapter 4. Therefore in the likely range of optimum t_b with our fluorescence rates the EMCCD offers the best SNR; it is plausible that this will result in the lowest discrimination error ϵ . Moreover, the EMCCD offers a much shorter pixel readout time than a conventional CCD.

In section 3.3.3 it was found that the highest readout fidelities are obtained by maximising R_B , and that this could be achieved by increasing collection efficiency. Therefore we chose the camera model with the highest possible quantum efficiency. In general, choosing a back-illuminated CCD array gives a higher quantum efficiency as absorption loss is reduced; an AR coated version also reduces reflection loss. The nominal quantum

²This would increase cross-talk between ion images on the CCD.

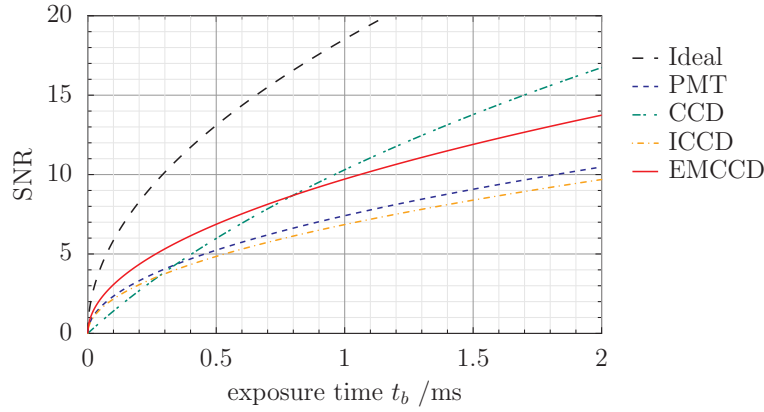


Figure 5.2: Comparison of signal-to-noise ratio (SNR) for various detection devices over various integration times t_b . Typical R_B and R_D rates seen in the series II set of PMT experiments (chapter 4) are assumed; for these rates $t_b \leq 0.6$ ms was found to be the most interesting range.

efficiency of our camera at 397 nm is listed in table 5.1, but the “effective” quantum efficiency of the device turns out to be lower. In the absence of any dark counts or readout noise, we have that $\text{SNR} = \sqrt{S_B}/F$. We see that if we have a noise factor F which is different from unity, then we need to increase S_B to achieve the same SNR as a system with $F = 1$. Hence, a noise factor of $\sqrt{2}$ in an EMCCD is equivalent to effectively halving the quantum efficiency [163].

In addition to choosing a camera with the highest quantum efficiency, it is also advantageous to choose one with a high readout speed and the ability to read out only partial regions of the CCD array in order to minimise the readout time (this is at least as long as the exposure time for our application).

5.1.3 Count distributions from the camera

The more complex operation of the EMCCD means that the counts read out from the camera do not show the same Poisson distribution as the incoming photons. The more complex distributions resulting from the operation of the gain register have been studied in some detail by Tubbs [163, 171] and his model is described below.

Single pixel

Due to the probabilistic nature of the gain stage, an ideal gain register (with no CIC noise within the register itself) will operate on an input of s photoelectrons to give a probabilistic distribution of x electrons at the other end, depending on the gain G . This

operation is described by the function $p_{s,G}(x)$.

$$p_{s,G}(x) = \begin{cases} \delta(x) & \text{if } s = 0 \\ 0 & \text{if } s > 0 \text{ and } x = 0 \\ \frac{(x/G)^{s-1} e^{-x/G}}{G(s-1)!} & \text{and } x > 0 \end{cases} \quad (5.3)$$

We assume the number of photoelectrons s on a pixel is drawn from a Poisson distribution $q_\lambda(s)$ of incoming photons with mean λ . The distribution leaving the gain stage $h_{\lambda,G}(x)$ is therefore a weighted sum over (5.3) for the different values of s :

$$h_{\lambda,G}(x) = \begin{cases} q_\lambda(0) & \text{if } x = 0 \\ \sum_{s=1}^{\infty} q_\lambda(s) p_{s,G}(x) & \text{for } x > 0 \end{cases} \quad (5.4)$$

The charge is then read out from the CCD, a process which adds extra noise with variance σ^2 and an arbitrary offset μ . This can be modelled by convolving (5.4) with a Gaussian distribution to give $f(x) = h_{\lambda,G}(x) * r_{\mu,\sigma}(x)$ with readout noise given by:

$$r_{\mu,\sigma}(x) = \frac{1}{\sigma\sqrt{2\pi}} \exp\left(\frac{-(x-\mu)^2}{2\sigma^2}\right) \quad (5.5)$$

At the ADC the electrons x are converted to “counts” $n = x/\beta$ where β is a scaling factor which depends on the pre-amplifier gain (PAG) setting and whose values are supplied by the camera manufacturer [172]. The final probability distribution $f(n)$ describing the counts read from the camera can then be found by summing blocks of entries in $f(x)$ from x to $x + \beta - 1$, but to a good approximation one can calculate:

$$f(n) = h_{\lambda,G}(n) * r_{\mu,\sigma}(n) \quad (5.6)$$

using values of the parameters G , μ and σ all scaled down by a factor of β since we are working in counts rather than electrons. This set of parameters describes the action of the camera and depends on the camera settings, while the remaining parameter λ varies from pixel to pixel according to the image. The parameters can be extracted from experimental data by fitting the function $f(n)$ to a histogram of count values for each pixel. Examples of the theoretical distribution $f(n)$ are shown in figure 5.3 for varying λ ; it is clearly non-Poissonian. The variance of the distribution with $\lambda = 8$ is $\sigma^2 = 16$, the same as an “ideal” detector with twice the quantum efficiency (which would give a

Poisson distribution with $\lambda = \sigma^2 = 16$), illustrating the excess noise factor F .

The mean count rates λ_i on each pixel i are given in (5.7) for a bright or dark ion:

$$\begin{aligned}\lambda_i^B &= (R_B w_i + R_{Di}) t_b + \lambda_{CIC} && \text{Bright ion} \\ \lambda_i^D &= R_{Di} t_b + \lambda_{CIC} && \text{Dark ion}\end{aligned}\tag{5.7}$$

For a bright ion, the pixel means are dependent on the detected fluorescence rate R_B for an ion in $|B\rangle$, the exposure time t_b and w_i , the fraction of fluorescence collected on pixel i where the sum over the whole image is normalised to unity: $\sum_i w_i = 1$. The dark counts are included in two parts: a rate R_{Di} *per pixel* which includes scattered laser light and thermal dark current and is dependent on t_b ; and the CIC noise λ_{CIC} which is independent of exposure time. The background rate R_{Di} is allowed to vary between pixels in order to incorporate non-uniform background scatter and “fixed pattern noise”; the mean value *per pixel* is denoted by R_D . These effects can be measured and included in simulations or analyses by obtaining the values $\{\lambda_i^D\}$ individually for each pixel from experimental data; an ideal CCD would have the same value of λ_i^D for all pixels. The serial register CIC noise is omitted from this model as it is more complicated: spurious charge can be generated at any point along the gain register, resulting in an excess of events at lower counts which has been modelled by Tulloch [165]. The effect of serial register CIC is visible in our experimental data, see for example figure 6.3.

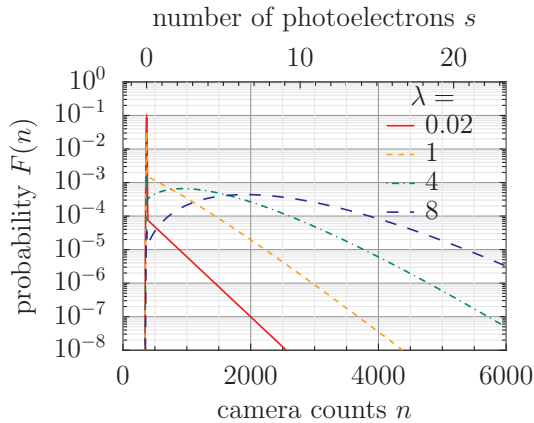


Figure 5.3: Examples of theoretical probability distributions for single pixels on an EM-CCD camera with changing λ . The upper abscissa shows an approximate scaling back to the number of photoelectrons s . $G = 1000 e^-/e^-$, $\mu = 370$ counts, $\sigma = 18.6 e^-$, $\beta = 4.16 e^-$ per count.

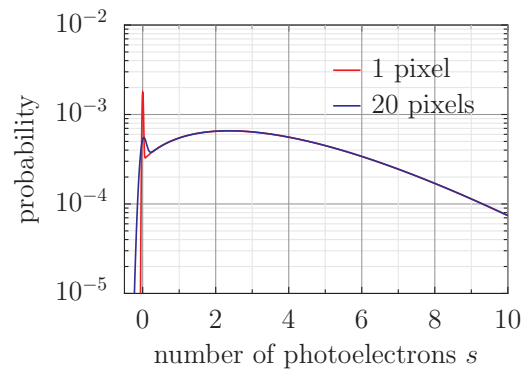


Figure 5.4: Theoretical distributions $f(n)$ for $\lambda = 4$ either on 1 pixel, or divided evenly amongst 20 pixels which have been summed at analysis time. The abscissa shows an approximate scaling back to photoelectrons s .

Combining multiple pixels

In many EMCCDs it is possible to combine the pixel contents on the CCD before readout, known as “binning” [170], which reduces readout time (and readout noise in principle), although it also reduces spatial resolution. There are three places where pixels can be combined: before the gain register, after the gain stage but before the readout amplifier, or after readout from the camera.

When pixels are combined the two probability distributions describing their contents must be convolved together. To combine two pixels vertically, two rows are shifted down into the serial readout register and combined before being moved through the gain register. The contents of each pixel before the gain register is then simply $q_{(\lambda_1+\lambda_2)}(s)$ as the convolution of two Poisson distributions is just another Poisson distribution. Horizontal combination of pixels occurs after the gain register by shifting two pixels into the readout amplifier node to combine their contents before the readout of charge is performed. The resulting distribution is then $(h_{\lambda_1,G}(n) * h_{\lambda_2,G}(n)) * r_{\mu,\sigma}(n)$. This function is more complicated, so if pixels are combined after the gain register then the result must be found numerically and fitting the experimental count distributions is hard. If pixels were instead read out individually and then only combined at analysis time, the probability distribution would be $(h_{\lambda_1,G}(n) * h_{\lambda_2,G}(n)) * r_{2\mu,\sqrt{2}\sigma}(n)$ — the readout noise is increased by \sqrt{N} when N pixels are combined. Therefore, if combination of pixels is required, lowest noise is achieved by doing so before readout from the CCD. An example of this is shown in figure 5.4 which compares the probability distributions achieved for $\lambda = 4$ photoelectrons on a single pixel with the same total count spread over 20 pixels which are summed at analysis time.

On-chip binning was not used for any of the experiments presented in this thesis— pixels were always read individually from the camera and combined at analysis time. This was in order to obtain the most spatial information possible in the hope that this would enable us to improve ion discrimination. The \sqrt{N} increase in readout noise when combining pixels in analyses remains negligible due to the high gain which ensures that σ/G is small. Unless explicitly stated, the rest of the discussion in this thesis assumes no on-chip binning.

5.2 Analysis techniques

The following abbreviations will be used in figures to refer to the different analysis protocols which will be discussed in this section:

- T** Threshold method
- M** Maximum likelihood method
- A** Adaptive maximum likelihood method (ignoring dark→bright decay)
- TN** Iterative threshold method (including states of neighbouring ions)
- MN** Iterative maximum likelihood method (including states of neighbouring ions)

5.2.1 Selecting a “region-of-interest” in an image

As for the PMT readout, we must choose a protocol that allows us to discriminate between the two ion states $|D\rangle$ and $|B\rangle$ (dark and bright respectively) based on the information we retrieve from our measuring device. A single ion imaged onto the CCD measured using a single exposure of duration t_b is analogous to a single continuous counting bin using the PMT, from which we measured a single count value n . However, here we will retrieve a set of counts $\{n_i\}$ from each pixel i on the CCD since the ion image will be spread over several pixels, either because of imaging system imperfections or through use of a high magnification diffraction-limited system.

The discrimination protocol is then applied to a region-of-interest (ROI) consisting of N pixels. To make the process most efficient we label the pixels $i = 1 \dots N$ in order of decreasing average brightness so that the pixels containing the most information are included first in the analysis³. We then vary N to find the optimum ROI size. The pixel order can be obtained experimentally from a single long “test” exposure of the ion, see [figure 5.5(a), inset] which shows the central nine pixels of a diffraction-limited ion image.

For an image containing multiple ions we can still label the pixels in brightness order for each ion; the pixel order for a particular ion can be obtained by examining a long exposure image in which *only* that ion is fluorescing.

³This method allows arbitrarily shaped ROIs and is more efficient than just defining a square region around the ion.

5.2.2 Single exposure: spatial resolution

We start by considering the simplest case: a single ion imaged onto the CCD, measured using a single exposure of duration t_b .

Threshold method

The simplest protocol to determine the state of the ion is to apply a threshold to the total number of counts $n = \sum_{i=1}^N n_i$ contained in an ROI consisting of N pixels. The threshold chosen is that which optimises discrimination between histograms of the total counts obtained from the bright and dark state preparations in a similar way to that discussed in section 3.2.2.

The histograms reflect the underlying probability distributions $B(n)$ and $D(n)$ for obtaining n counts in an N -pixel ROI from trials prepared in $|B\rangle$ or $|D\rangle$ respectively. It is not possible to write down the optimum threshold for each N analytically due to the complicated shape of $B(n)$ and $D(n)$, so the optimum position must be found computationally by considering the overlap of the two distributions. The shape of $B(n)$ and $D(n)$ for N pixels is easiest to determine by histogramming either experimental or M-C simulated data (the approach used in this thesis) although it is also possible to find $B(n)$ and $D(n)$ numerically from the single-pixel distributions, see section 5.3. A plot of the discrimination error ϵ with pixel number is shown for simulations in [figure 5.5(b), curve T], where the optimum thresholds were found by histogramming the M-C simulated data. The spatial fluorescence distribution is that expected from a diffraction-limited imaging system with numerical aperture $\sin \alpha = 0.25$ and magnification $\mathcal{M} = 62$, where the ion's Airy disc covers ~ 42 pixels⁴. The fluorescence rates were chosen to be roughly similar to experimentally observed rates at $R_B t_b = 54$ photons per exposure, $R_D = 0.03$ photons per pixel. The other camera settings for this simulation were chosen to match an experiment to be described in chapter 6.

As discussed in the previous section, the readout noise is increased by \sqrt{N} when N pixels are combined during analysis. In addition to this, pixels far from the centre of the ion image will only contribute a small amount of ion fluorescence, contributing mainly dark counts and CIC noise which serve only to increase the shot-noise and widen $B(n)$. Hence a value of N too large will increase ϵ . Conversely, summing too few pixels

⁴This is the same numerical aperture as imaging system C (used for the experiments in chapter 6), but with a $10\times$ larger magnification.

will not collect enough ion fluorescence to separate the bright histogram $B(n)$ from the dark histogram $D(n)$. Consequently there is an optimum value of N which optimises discrimination (in the figure, $N_{opt} = 26$, giving $\epsilon = 1.33(3) \times 10^{-4}$). The choice of optimum exposure time t_b is, as with the PMT, a trade-off between collecting enough photons and the $D_{5/2}$ lifetime τ ; it is investigated in chapter 6 using simulations.

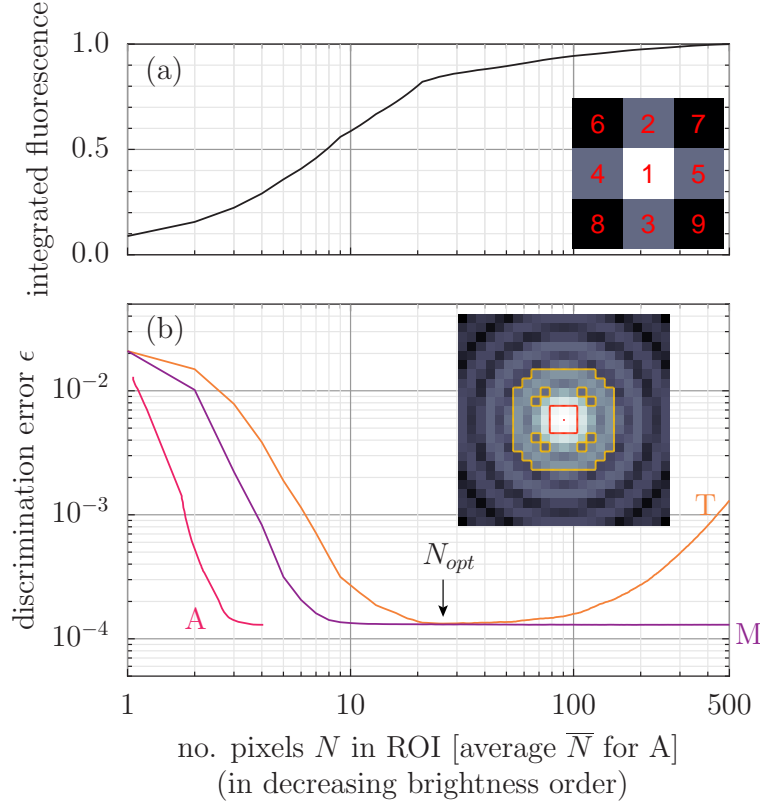


Figure 5.5: (a) Integrated fluorescence signal from a diffraction-limited single-ion image using an imaging system with numerical aperture $\sin \alpha = 0.25$, where the ion's Airy disc covers ~ 42 pixels. INSET: central nine pixels of image labelled in decreasing brightness order. (b) Variation of discrimination error with number of pixels N included in analysis, 2×10^7 simulated M-C trials of a single ion with $R_B t_b = 54$ photons per exposure, $\lambda^D = 0.03$ photons per pixel (including $\lambda_{CIC} = 0.018$ photoelectrons per pixel). These fluorescence rates and the other camera settings for this simulation were chosen to be similar to experiments with $t_b = 400 \mu s$ to be described in chapter 6. T: Threshold method (orange), M: Maximum likelihood method (purple), A: Adaptive maximum likelihood method (pink). The statistical error in the simulations is $\sim 3 \times 10^{-6}$ at the minimum ϵ . The optimum ROI size for method T is labelled by N_{opt} . INSET: Long exposure image (contrast enhanced) showing position of ion (\cdot) and the ROIs containing the brightest {9, 101} pixels.

Maximum likelihood method

Although the spatial distribution of the ion fluorescence (parameterised by w_i) was mentioned in the previous section, the threshold analysis method itself does not take this into account when determining the ion's state from the counts $\{n_i\}$ in an N -pixel

ROI. In the “spatial” maximum likelihood analysis we compare the likelihoods p_B and p_D , which are the probabilities that a particular set of counts $\{n_i\}$ could have been generated by an ion prepared in $|B\rangle$ or $|D\rangle$ respectively. The likelihoods are computed in a similar way to those in section 3.2.3, although with no decay terms in p_D as we have no time dependence.

$$p_B = \prod_{i=1}^N B_i(n_i) \quad p_D = \prod_{i=1}^N D_i(n_i) \quad (5.8)$$

Here $B_i(n_i)$ is the probability of observing n_i counts on pixel i from a bright ion; similarly for $D_i(n_i)$. Knowledge of the spatial distribution of fluorescence is included in this analysis as the probability distributions $B_i(n)$ and $D_i(n)$ are different for each pixel. These distributions could be obtained by histogramming independent control data or produced using the model in (5.6). In the latter case, $B_i(n)$ requires λ_i^B for a bright ion from (5.7), $D_i(n)$ requires λ_i^D for a dark ion. These could be obtained from a pair of long exposures (with and without an ion in the trap) if the parameters describing the camera were already known.

The discrimination error ϵ with varying pixel number N is shown for 2×10^7 simulated trials in [figure 5.5(b), curve M]. An analysis with $N = 8$ pixels allows us to reach within 10% of the minimum ϵ for the maximum likelihood analysis, compared to $N = 20$ to reach within 10% of the minimum ϵ for the threshold analysis. This demonstrates that the maximum likelihood method makes more efficient use of the data. Nevertheless the minimum $\epsilon = 1.30(3) \times 10^{-4}$ reached is similar as both are limited by errors caused by the $D_{5/2}$ decay rate ($\epsilon_D \approx t_b/\tau \approx 3 \times 10^{-4}$ for a typical $400 \mu\text{s}$ camera exposure). An additional advantage of the maximum likelihood method is the slightly reduced sensitivity to N and the removal of the requirement to choose a threshold position, to which the threshold method is very sensitive.

Adaptive maximum likelihood method

An analogous method to that discussed in section 3.2.4 can be used to reduce further the *average* number of pixels \overline{N} required to determine the qubit state. A spatially adaptive method only uses sufficient pixels for the estimated error in the identification to fall below some required cutoff e_c , resulting in a lower average \overline{N} . It is also necessary to impose a cutoff in N (a maximum ROI size) in case the cutoff error is not reached.

Computationally, it is easier to consider the likelihood ratio p_B/p_D which is a good approximation to the exact Bayesian error⁵, see (3.13).

In practice the adaptive technique does not allow a speed-up in CCD readout time through a reduction in the number of pixels because individual on-demand readout of pixels anywhere in the CCD is not possible with the current commercially available EMCCD camera architectures. Even so, performing the adaptive analysis allows us to gain an insight into the number of pixels over which most useful information is spread. An adaptive analysis of simulated data is shown in [figure 5.5(b), curve A]. The method reaches within 10% of its minimum ϵ with only $\bar{N} = 2.96$; which is impressive given that these first three pixels only contain 22% of the total ion fluorescence, see figure 5.5(a).

5.2.3 Multiple exposures: spatial and temporal resolution

The largest cause of error for the single exposure readout methods discussed above is due to the ion making a $|D\rangle \rightarrow |B\rangle$ transition during the exposure time t_b . As with the PMT readout, one might hope to identify some of these decay events by the use of Time-Arrival Resolved Detection of Ion States (TARDIS)⁶. Photon arrival-time information is collected by dividing the exposure up into M shorter exposures (labelled by j) each of length t_s .

Threshold method

After the entire detection period $t_b = Mt_s$ is over we obtain a set of counts $\{n_{ji}\}$ where n_{ji} is the number of counts on pixel i of exposure j . For the threshold analysis method, we compare the total counts $\sum_{j=1}^M \sum_{i=1}^N n_{ji}$ within an N -pixel region from M exposures with a threshold value in order to decide the ion state. The total counts recorded in many trials can be histogrammed for the bright and dark trials separately; the optimum threshold is that which optimises the discrimination between these histograms, as before.

A further complication lies in the choice of t_s . Unlike with the PMT, there is now a penalty associated with making t_s too short and increasing the number of temporal divisions M within the total integration time t_b since there is extra noise associated with the readout of each exposure. The effect of changing t_s is investigated in chapter

⁵We can then use logarithms to prevent underflow.

⁶With the camera, the TARDIS allows us to explore both spatial and temporal dimensions, and can screen out cosmic rays :-)

6 using simulations. Having chosen an exposure length t_s and performed an experiment (or simulation), we can investigate the error with changing M as we did for the PMT data but with the complication that we must additionally choose the optimum number of pixels N to include in the analysis. An example is shown in [figure 5.6, curve T].

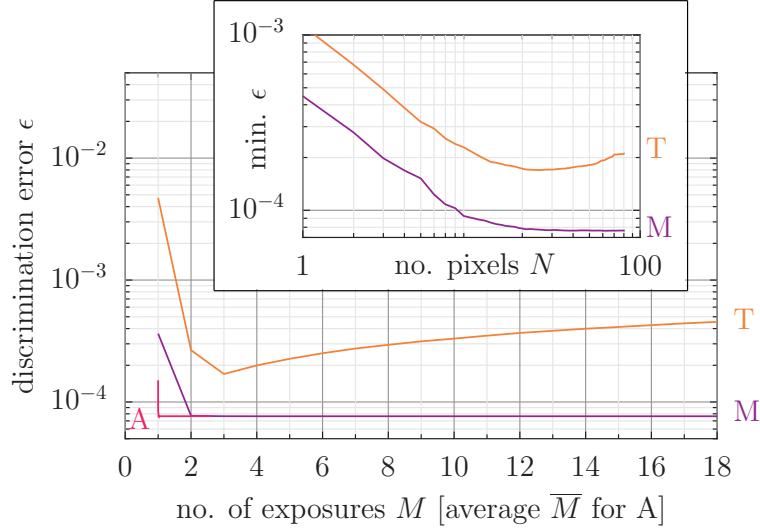


Figure 5.6: Variation of discrimination error with number of exposures M included in analysis and optimal ROI size N , from 2×10^7 simulated M-C trials of a single ion imaged by a diffraction-limited system with numerical aperture $\sin \alpha = 0.25$ (the ion’s Airy disc covers ~ 42 pixels). The camera settings and fluorescence rates were chosen to be similar to those seen in the experiment to be described in section 6.3 which had $t_s = 200 \mu\text{s}$: $R_B t_s = 27$ photons per exposure with λ_j^D increasing linearly with exposure number j from 0.0571 to 0.1897 photons per pixel. T: Threshold method (orange), M: Maximum likelihood method (purple), A: Adaptive maximum likelihood method (pink). INSET: Minimum ϵ achievable with N pixels in ROI. The statistical error in the simulations is $\sim 2 \times 10^{-6}$ at the minimum ϵ .

Maximum likelihood method

The likelihoods to be calculated for a “spatio-temporal” maximum-likelihood analysis are similar to those for the PMT analysis but are modified to take into account the spatial information. The likelihood $p_B = P(\{n_{ji}\} | B)$ is modified from (3.7) to become:

$$p_B = \prod_{j=1}^M p_{B_j} \quad \text{where:} \quad p_{B_j} = \prod_{i=1}^N B_{ji}(n_{ji}) \quad (5.9)$$

where p_{B_j} is the probability of observing the set of counts $\{n_{j1} \dots n_{jN}\}$ in exposure j from a bright ion and $B_{ji}(n_{ji})$ is the probability of observing n_{ji} counts on pixel i of exposure j from a bright ion. Allowing independent distributions for each j allows for different background levels which are present in practice (§6.3).

The likelihood p_D allows for the spontaneous decay of the ion into the bright state

in exposure j' with a probability (t_s/τ) . It is similar to (3.11) but is modified to:

$$p_D = \left(1 - \frac{Mt_s}{\tau}\right) \prod_{j=1}^M p_{D_j} + \left(\frac{t_s}{\tau}\right) \sum_{j'=1}^M \prod_{j=1}^{j'-1} p_{D_j} \prod_{j=j'}^M p_{B_j} \quad (5.10)$$

where: $p_{D_j} = \prod_{i=1}^N D_{ji}(n_{ji})$

with $D_{ji}(n_{ji})$ being the probability of observing n_{ji} counts on pixel i of exposure j from a dark ion. In (5.10) we have made the same approximations as for the PMT analysis: that $t_s, t_b \ll \tau$ and that when a decay happens, the count rate changes from R_D to R_B at the start of the sub-bin, thus eliminating the need for the complicated distribution like $X(n_j)$ in (3.9) for the PMT. Although t_s can be an appreciable fraction of t_b , this vast simplification in the analysis outweighs any small reduction in ϵ that might be obtained without the approximations (§3.3.1).

An example analysis on simulated data is shown in [figure 5.6, curve M]. This shows the variation of ϵ with number of exposures M , where we have chosen the ROI size N so that we reach the minimum ϵ in the fewest exposures.

Adaptive maximum likelihood method

The likelihoods in (5.9) and (5.10) can be used to perform a *temporally* adaptive analysis of the data, such that a high fidelity is reached using fewer exposures on average (smaller \overline{M}). This is similar to the temporally adaptive method for the PMT described in section 3.2.4 and similarly we impose both a required estimated error e_c and a cutoff number of exposures in case e_c is not reached. Once again, the likelihood ratio p_B/p_D is simpler to use computationally than the exact Bayesian error. Adaptively changing N at the same time is not considered; instead a fixed choice of N is made such that we reach the minimum ϵ with the smallest \overline{M} .

In common with the spatial adaptive technique described in section 5.2.2, this temporally adaptive method offers little practical speed-up in state-detection due to the CCD architecture and overhead in CCD read time. Nevertheless the analysis still offers an insight into the temporal performance of the maximum likelihood method.

5.2.4 Extension to multiple ion readout

Up until now the discussion of analysis techniques has been restricted to the case of a single ion. This is now relaxed and we consider a linear string of ions labelled by k . For each ion we still label the pixels $i = 1 \dots N$ in brightness order so that the pixels containing the most information about ion k are included first. The arguments already presented regarding the disadvantage of taking too many pixels still apply here, but now there is an extra disadvantage to making N large: we will start to take pixels which contain the image of neighbouring ions. This increasing “cross-talk” from the neighbouring ion images will increase our discrimination error. Even for diffraction-limited optics there will be some overlap between the ions’ images (depending on the ion-ion spacing), so there are now three sources of discrimination error to be considered: the statistical overlap of probability distributions describing the output from the camera for bright and dark ions, $|D\rangle \rightarrow |B\rangle$ decay during measurement, and cross-talk from neighbouring ions.

Single exposure

We first extend the single-exposure readout discussed in section 5.2.2 to cover detection of ions within a string. The threshold method can be used on each ion independently, where the optimum thresholds are chosen separately for each ion in the string. The spatial maximum likelihood methods can also be applied to each ion independently by computing the likelihoods:

$$p_B = \prod_{i=1}^N B_{ki}(n_{ki}) \quad p_D = \prod_{i=1}^N D_{ki}(n_{ki}) \quad (5.11)$$

where $B_{ki}(n_{ki})$ is the probability of recording n_{ki} counts on the i th brightest pixel of ion k when that ion is bright, and $D_{ki}(n_{ki})$ is the probability of recording n_{ki} counts on the same pixel when that ion is dark. The spatial maximum likelihood method should be significantly more immune to cross-talk errors than the threshold method, since it requires fewer pixels and effectively gives less weight to pixels which are further from the ion of interest. Even so, it is possible to improve the method further by taking into account the states of the neighbouring ions in our analysis. The state of a neighbouring ion k' has a significant effect on the distributions $D_{ki}(n)$ for ion k , depending on whether

the neighbour k' is bright or dark. The distributions $B_{ki}(n)$ are also affected. The effects are largest for large i when we are considering a pixel closer to ion k' than ion k , although such a pixel may still contain useful information about the state of k .

This information can be extracted in the analysis by allowing independent probability distributions $B_{\nu ki}(n)$ and $D_{\nu ki}(n)$ for the i th brightest pixel of ion k depending on the four possible states $\{\nu\} = \{00, 01, 10, 11\}$ of the two nearest-neighbour ions, where 1 denotes a bright ion, 0 a dark ion. If cross-talk between ions is fairly small, we need only consider the effects of nearest-neighbour ions and can ignore the states of ions further from k . When analysis of an ion string image starts we have no knowledge of the states of any of the ions and hence no knowledge of ν . We necessarily begin analysis with a guess for the state of the string, perhaps $[\dots 0000\dots]$, and then start to measure the state of each qubit assuming $\nu = [00]$. As analysis proceeds, the original guess for the state of the string can be updated to provide better estimates of ν . Once the whole string has been analysed, a second iteration is performed where the calculations are repeated with the new values of ν . Iterations continue until the inferred state of the string becomes stable⁷. An optimum choice of ROI size N_k must also be made for each ion; in this thesis the same N is chosen for all ions k .

The iterative method of accounting for neighbouring ions can be trivially extended to provide a simpler iterative threshold method, where different thresholds for each ν are defined for each ion k . These thresholds can either be found from an inspection of experimental histograms or by numerical calculation, see section 5.3. This analysis method is mentioned for completeness; it does not take into account the ions' spatial distribution and hence the maximum likelihood method will outperform it.

An example of each analysis method is shown in figure 5.7, applied to simulated trials for a four-ion string with a diffraction-limited imaging system. The readout error ϵ_x includes only the statistical errors and cross-talk between ion images; it does not include the error due to $|D\rangle \rightarrow |B\rangle$ decay. The value of ϵ_x rises quickly for both threshold methods as the ROI begins to overlap neighbouring ions. Both maximum likelihood methods are significantly more immune to cross-talk; when taking neighbouring ions into account (method MN) there is no penalty to increasing the ROI size even when it completely overlaps neighbouring ions.

⁷A maximum number of iterations can be enforced in the rare event that the state of the string does not stabilise and oscillates between two outcomes.

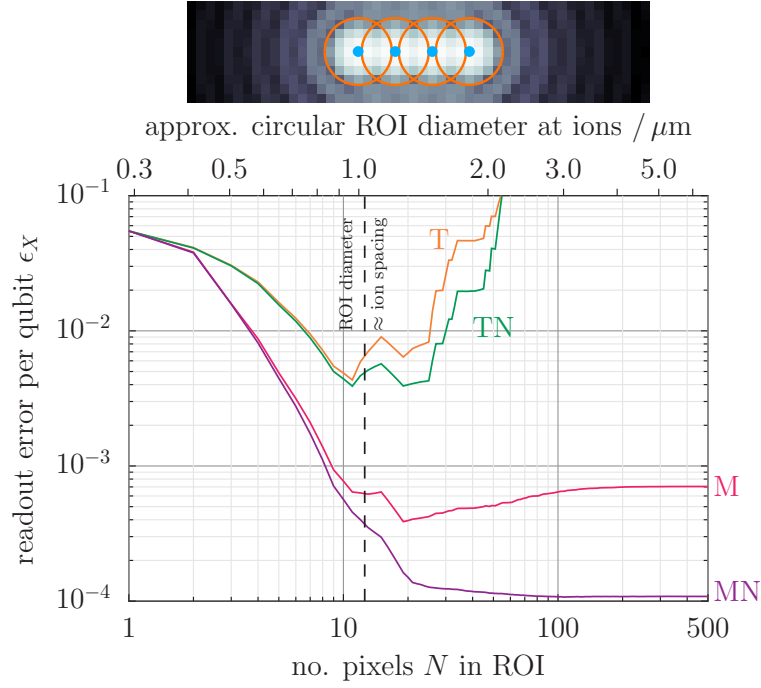


Figure 5.7: Readout error ϵ_x per qubit (not including decay) for a four-ion string (averaged over all 16 states of the four-ion string) vs. ROI size N around each ion. From $16 \times (2 \times 10^6)$ M-C simulated trials for a diffraction-limited system with numerical aperture $\sin \alpha = 0.25$ and ions equally separated by $1.03 \mu\text{m}$ in the object plane, corresponding to 4 pixels on the CCD. The ions' Airy radius is $0.938 \mu\text{m}$ in the object plane, and the fluorescence rates are the same as those in figure 5.5 but scaled to a shorter exposure time of $t_b = 250 \mu\text{s}$, giving $R_B t_b = 33.75$ photons per exposure, $\lambda^D = 0.0255$ photons per pixel. Threshold (T, orange) and maximum likelihood (M, pink) methods ignoring neighbours. Threshold (TN, green) and maximum likelihood (MN, purple) methods taking into account nearest neighbour states. ABOVE: Long exposure image of the 50×11 pixel area showing position of ions (\bullet , blue) and the Airy disc around each (solid lines, orange).

Multiple exposures

The “spatio-temporal” methods of analysis in section 5.2.3 can be straightforwardly extended to cover the detection of multiple ions, taking into account neighbours as described above. The likelihoods that the set of counts seen for ion k over M exposures are calculated according to equations (5.9) and (5.10), but the spatial part of the probabilities are modified to:

$$p_{B_j} = \prod_{i=1}^N B_{\nu kji}(n_{kji})$$

where $B_{\nu kji}(n_{kji})$ is the probability of observing n_{kji} counts on the i th brightest pixel of ion k in exposure j from a bright ion with neighbours in state ν . p_{D_j} is similarly constructed. The correct choice of ν is no longer obvious as the neighbouring ions could make a $|D\rangle \rightarrow |B\rangle$ transition during the multi-exposure detection period, leading to different values of ν_j for each value of j . This change in neighbour states is a second-order effect compared to the change due to decay of our ion-of-interest, so to simplify matters one could neglect the possibility of neighbours decaying and just use the same value of ν for the whole analysis, performing iterations over the whole calculation of p_B and p_D .

For the simpler non-iterative method (ignoring the neighbouring ions) the index ν is omitted and only one pair of bright and dark distributions is needed for each pixel of each exposure for each ion.

5.2.5 Quantifying the readout error

For the readout of a single ion, section 3.2.1 defined the average discrimination error as $\epsilon = (\epsilon_B + \epsilon_D)/2$ where ϵ_B is the fraction of trials where an ion prepared in the bright state was incorrectly measured to be dark (similarly for ϵ_D). This choice of definition reflects the fact that the discrimination errors for the two qubit states can be significantly different, therefore any evaluation of an “average” error needs to reflect the number of trials prepared in each state to avoid bias.

Following this premise, the average discrimination error for an ion in a string is defined the same way, but with ϵ_B and ϵ_D computed as the average over the fractional

errors for each neighbour state⁸:

$$\epsilon_B = (\epsilon_B^{00} + \epsilon_B^{01} + \epsilon_B^{10} + \epsilon_B^{11})/4 \quad (5.12)$$

where the superscripts give the neighbour state ν and ϵ_B^{00} is the fraction of trials prepared in $|B\rangle$ with $\nu = [00]$ which have been incorrectly identified as “D”. The rationale behind choosing this definition is the same as for a single ion— for some analysis methods the discrimination errors for different neighbour states can be significantly different and the number of trials prepared with each neighbour-type may not be the same. This difference in discrimination error is not the case for iterative methods which effectively remove the cross-talk, nevertheless this definition is still appropriate as our analysis method has depended on the value of ν .

There is one caveat to this definition which applies when quoting an average error in the case of poor statistics. If, for example, only one trial with an incorrect identification is seen within the whole data set then (5.12) may give a significant variation in ϵ depending on the qubit preparation and value of ν measured for the offending trial. Unless there is reason⁹ to expect that errors are more likely to occur for a certain qubit state (and value of ν) then a more simplistic measure of the error would be appropriate, such as $\epsilon = 1/N_{\text{exp}}$ for a single incorrect identification in N_{exp} trials. Generally in our data sets these different methods of calculating ϵ are consistent within statistical uncertainty.

5.3 Simulation methods

5.3.1 Obtaining thresholds from simulated distributions

The single-ion discrimination error for the threshold method can be simulated by computing the overlap of the probability distributions $B(n)$ and $D(n)$ expected for trials prepared in $|B\rangle$ or $|D\rangle$ respectively. These distributions describe the probability of measuring a total of n counts in an N -pixel ROI and are easiest to determine by histogramming experimental or M-C simulated data. Nevertheless, it is possible to find these distributions computationally using the model presented in section 5.1.3.

Since the pixels have been read individually from the CCD, the full distribution

⁸For an ion at the end of a string the definition must be modified to contain only two terms as there is only one neighbouring ion.

⁹For example, the use of a non-iterative analysis method that does not correct well for cross-talk.

$B(n)$ for a single ion in a single exposure is obtained by convolving the single-pixel distributions $B_i(n)$ together for each pixel i we add to the analysis ROI. Each $B_i(n)$ has the form of (5.6) with the appropriate λ_i^B for pixel i from a bright ion, see (5.7). In the absence of decay, the distribution $D(n)$ would be a convolution of the $D_i(n)$ for each pixel in the ROI, where the $D_i(n)$ also have the form of (5.6) with λ_i^D for a dark ion, see (5.7). With a finite lifetime τ for the $|D\rangle$ state, the distributions for each pixel must be modified—in a single-exposure trial for example, each $D_i(n)$ also contains weighted amounts of (5.6) with λ_i between the values of λ_i^D and λ_i^B in (5.7) corresponding to occasions where the ion decays at $t < t_b$ and begins to fluoresce. An expression for this is not easy to write down in closed form, but the function can easily be computed numerically.

The distributions for multiple-exposure trials can be computed by making $B(n)$ a convolution of $B_{ji}(n)$ with λ_{ji}^B for pixel i of exposure j for a bright ion, similarly for $D(n)$ (taking care to include the decay possibility). For a multiple ion readout experiment, we must take care to make the distributions $B(n)$ and $D(n)$ for the specific ion k and neighbour state ν we are interested in, by convolving the appropriate $B_{\nu ki}(n)$ for each pixel i . If we wish to ignore neighbour states in the analysis, for each ion k we average over the distributions with each value of ν .

Once the distributions $B(n)$ and $D(n)$ have been calculated, the threshold which optimises discrimination between them can be found, and hence ϵ , in a similar fashion to (3.16) for the PMT simulation. For multiple ion readout, simply calculating the overlap of theoretical distributions is not sufficient to simulate the error from an iterative threshold method which takes into account the states of neighbouring ions; this analysis method must be simulated using Monte-Carlo methods¹⁰. Nevertheless, computation of the theoretical distributions for each ν can still provide the positions of the optimum thresholds which are required before beginning analysis of either simulated or real trials.

Computation of the theoretical distributions for many-pixel ROIs is relatively slow due to the many convolutions involved. For this reason, theoretical calculations for $B(n)$ and $D(n)$ were only used to determine the optimum thresholds for the iterative threshold method. All other simulations of threshold analyses shown in this thesis were produced by examining the histograms built from the M-C simulated data generated to

¹⁰For small cross-talk the overlap of distributions gives almost the same ϵ as a full M-C simulation.

investigate maximum likelihood methods.

5.3.2 Monte-Carlo simulations

Monte-Carlo (M-C) simulations were performed in a similar way to the PMT simulations described in section 3.3 using programs written in the Fortran 95 language and using the NAG Fortran library. Simulated trials prepared in $|B\rangle$ were generated by picking a random number for each pixel from the relevant distribution $B_{\nu kji}(n)$ to produce an exposure (or set of exposures) to be analysed in the same way as a real experiment. Simulated trials prepared in $|D\rangle$ involved first picking a random number from an exponential distribution to provide the decay time t_* of the ion. Any exposures ending before this time were simulated by picking numbers from $D_{\nu kji}(n)$ distributions, while any exposures beginning after t_* were produced from $B_{\nu kji}(n)$ distributions. For the exposure in which the decay occurred a new distribution ought to be made with the λ_i scaled appropriately between the two values in (5.7). Since the generation of an entirely new set of distributions is slow, the closest match to the exact distribution set was picked from a library of “decay” distributions generated in advance and containing N_{div} distribution sets with λ_i evenly spaced between the dark and bright values. The simulations in figures 5.5 and 5.6 were made using this method. $N_{\text{div}} = 20$ was chosen to simulate single-exposure trials, and $N_{\text{div}} = 10$ for multiple-exposure sequences.

The simulations require as their input realistic choices for the camera parameters G , μ , σ and λ_{CIC} as well as knowledge of the spatial distribution of ion fluorescence across the CCD giving the set of $\{\lambda_i^B, \lambda_i^D\}$ for bright and dark ions. For an ideal camera (with no fixed-pattern noise) the set of $\{\lambda_i^B, \lambda_i^D\}$ is described by the fluorescence rates R_B and R_D and the spatial distribution $\{w_i\}$ for an ion; for a diffraction-limited system with a circular aperture this distribution can be found from the Airy function. Values for the parameters describing the camera are listed in a performance data sheet supplied by the manufacturer [172].

Before the experiments in the next chapter were performed, preliminary simulations of an ideal system were performed to check the suitability of EMCCD cameras for qubit readout. In practice, using simulations to make a systematic search for the optimum exposure times t_b and t_s for use in the experiments was not feasible as these values will depend on the exact distribution of ion fluorescence across the CCD. Since our

imaging system is not diffraction-limited, this shape must be obtained experimentally and will vary if the imaging system drifts or the focus is changed. Using the values of $\{\lambda_i^B, \lambda_i^D\}$ taken from experimental data can also incorporate fixed-pattern noise into the simulation. In addition, the parameters describing the camera operation may vary from those listed in the data sheet— in particular, gain ageing effects have been documented in EMCCD devices [170]. Accordingly, to produce simulations which are more closely comparable with our experimental data we obtained values for all parameters by fitting experimental data with the models described in this chapter. Presentation of detailed simulation results is therefore deferred until after a discussion of the experiments in the following chapter.

Chapter 6

CCD readout experiments

6.1 Experimental methods

As discussed in the previous chapter there are three contributions to the discrimination error for multi-qubit readout using a CCD array: the statistical overlap of probability distributions describing the output from the camera for bright and dark ions, $|D\rangle \rightarrow |B\rangle$ decay during measurement, and cross-talk from neighbouring ions. The first two sources of error were also important for PMT readout although their effects are now modified due to the extra noise sources inherent in EMCCDs. For comparison with the PMT detector these two error sources were studied by performing experiments on single ions. The cross-talk noise source is peculiar to the case of multiple ions and as such was studied separately in an experiment designed to eliminate the effect of decay from $D_{5/2}$.

Details of specific experimental sequences are presented with each experiment, but the general schemes are as follows. For single-ion experiments the ion was repeatedly prepared with high fidelity in a known initial state. The preparation is followed by a detection period and the recorded data is then analysed to determine the ion's state using the various protocols discussed in the previous chapter. The identification is compared with the known preparation, enabling a measurement of ϵ after many repeats of this process. To estimate the cross-talk contribution, we repeatedly measure the state of a four-ion string or “qunybble”¹ [173]. Since we are not able to prepare all 16 possible states of the qunybble deterministically with a high fidelity, we prepare a random state and sandwich our “test” detection period between “pre-” and “post-” detection periods. These two extra detection periods are used to select only trials in

¹A nybble is half a byte, hence a qunybble is four qubits.

which the measured qunybble state remains constant, thus both eliminating decay errors and providing the known preparation with which to compare the outcome of analysis on the “test” exposure.

The EMCCD camera used for these experiments was an iXon^{EM}+ DU-897 back-illuminated device on loan from Andor Technology plc. This model has a frame-transfer CCD with a 512×512 pixel active image area and a $16 \mu\text{m} \times 16 \mu\text{m}$ pixel size. Control of the camera is via a PCI interface card installed in a Windows PC running the Andor SOLIS software. The operation settings were chosen to minimise the noise sources discussed in section 5.1.1. The CCD detector head is Peltier-cooled with a fanned heatsink and the lowest stable temperature set-point of -80°C was chosen. The highest electron-multiplier (EM) gain setting was selected, nominally $\times 1000 \text{ e}^- / \text{e}^-$. Minimum noise from the readout amplifier was obtained by use of the lowest 1 MHz ADC rate and the highest pre-amplifier gain setting of $5.1\times$, which was admissible as we did not expect to have enough signal to saturate the ADC. The CIC noise was minimised by use of the fastest vertical shift-speed: $0.3 \mu\text{s}$ to shift charge on the CCD sensor downwards by one row. To move all the charge off the CCD at this speed it was necessary to increase the amplitude of the vertical clock voltage by $+2 \text{ V}$. For these settings, the data sheet [172] specifies a CCD sensitivity of $\beta = 4.16 \text{ e}^-$ per ADC count n .

The operation of the camera must be synchronised with the state-preparation and readout laser pulses which are managed by the experimental control program running on a separate PC, as described in chapter 2. Although it is possible in principle to trigger CCD exposures from an external source via an SMB connector on the camera, this operation mode was observed to give noisier images compared to those obtained using the “internal” trigger mode. It is possible that this is due to differences in the “keep-clean cycle”: this is the process by which charge is removed from the idling CCD and discarded to prevent the pixels becoming saturated with dark current [174]. To obtain lower noise images we allowed the camera to operate in internal trigger mode and used the “fire” output from the camera to trigger the rest of the experimental sequence on the experimental control computer. The “fire” output is a TTL compatible output which presents a high voltage for the duration of each exposure.

A program written in the AndorBasic language (and running from within the SOLIS software) was used to control the data acquisition from the camera and to save

the pixel values from a sub-region of the CCD to file. The program also provided an output reflecting the total counts in an ROI around the ion(s) in order to monitor their fluorescence in real time during the experiment; it was not possible to do this using a PMT without significantly reducing the signal at the CCD.

The data in this chapter were taken with imaging system C shown in figure 2.6 where modifications had been made to maximise the collection efficiency to $\eta = 1.0(1)\%$, not including the quantum efficiency Q of the detector. An additional interference filter² was introduced to reduce the level of scatter from the 854 nm and 866 nm lasers to which the CCD is also sensitive (unlike the PMT). The magnification of the system was measured to be 6.2(1) and the objective has a numerical aperture of $\sin \alpha = 0.25$, where α is half the angle subtended by the objective lens at the ion.

A summary of the experimental parameters used for the experiments described in this chapter are summarised in table 6.1, including the camera settings and laser intensities. The 397 nm and 866 nm lasers were in general tuned as close to resonance as possible from the red side of the transition in order to maximise fluorescence. The magnetic field at the trap was measured by Dr David Szwer to be 1.9356(1) G; at this field we measure $R_B \sim 53000 \text{ s}^{-1}$ (compared to $R_B = 55800 \text{ s}^{-1}$ at 3.0(1) G).

Expt. settings		Camera settings	
I_{397}	$5I_{sat}$	Gain, G	1000 e^-/e^-
I_{866}	$33I_{sat}$	R/O speed	1 MHz
I_{393}	$0.007I_{sat}$	PAG	$5.1 \times$
I_{854}	$\sim 23I_{sat}$	excess clock	+2 V
B field	1.9356(1) G	vert. shift time	$0.3 \mu\text{s}$
Imaging system	C	cooling T	-80°C
...see figure	2.6		
η^*	1.0(1)%		

Table 6.1: Parameters used for the camera readout experiments, including the EMCCD settings where “R/O speed” indicates the readout speed and “PAG” is the pre-amplifier gain setting. The “vertical shift time” is defined in the text. The saturation intensity I_{sat} is that for the relevant transition in each case; the definition used is that given in (2.1). The imaging system efficiency η^* quoted here excludes the quantum efficiency Q of the camera.

For the single ion experiments, the errors due to imperfect preparation of the $|D\rangle$ state must be calculated and corrected for exactly as described in section 4.3.1 for the PMT experiments. The delay t_{delay} between shelving and detection is specified in the description of each experiment. The shelving rate $1/t_{shelve}$ due to the competition of the

²SEMROCK “brightline” 337/50, $T = 94(5)\%$ at 397 nm.

393 nm laser with the $|D\rangle$ lifetime τ was measured by performing a simple experiment to measure the number of occasions where the ion was shelved in 500 repeats of a shelve–detect–desheve sequence with a varying length shelving pulse $t_{393} : 0 \rightarrow 200 \mu\text{s}$ and a $500 \mu\text{s}$ PMT detection period. A fit of the results provided a measurement of $t_{\text{shelve}} = 17.5(3) \mu\text{s}$.

As mentioned in the previous chapter, an exhaustive search for the optimal exposure times t_b (or t_s) using simulations was not practical before the experiments were performed. To make the best possible choice of exposure times we performed quick experimental tests to find the minimum possible ϵ using threshold discrimination in a square ROI around a single ion.

6.1.1 Characterisation of camera properties

The parameters G , μ and σ describing the action of the EMCCD were obtained by fitting “dark” exposures, either from the experimental data set itself or from separate background data. To obtain the best statistics when fitting, a histogram was made including the counts from every pixel in the exposure. This was then fitted by (5.6) using a routine which included a sequence of fits with and without logarithmic weighting³. An example of such a fit is shown in figure 6.3; the effect of serial register CIC can be seen where the data does not match the fit. Once the values of G , μ and σ have been obtained, histograms for each pixel i are fitted separately to acquire the values of $\{\lambda_i^B, \lambda_i^D\}$ for bright and dark exposures. Care was taken to avoid bias in the fit caused by bins in the histograms with low statistics (generally ≤ 1 event) by removing such bins from the histogram before fitting. These fitted parameters were used to construct the $B_i(n)$ and $D_i(n)$ distributions needed for maximum likelihood analyses of trials using the function described in section 5.1.3. Using the fitted λ_i^D for each pixel enabled us to include fixed pattern noise in the analysis. For computational reasons, both the camera data and theoretical distributions were usually scaled so that n was in the range $0 \rightarrow 512$; this still provided adequate resolution for the calculations. The results presented in [43] use more simplistic distributions for analysis, but the results presented in this chapter agree within the statistical uncertainty.

³The values of μ and σ which come from the $n = 0$ photon peak are fitted best on a non-logarithmic scale, while accurate fits for G and λ require a logarithmic scaling to give more weight to the “tail” at $n > 0$ photons.

To verify the camera behaviour a succession of exposures was taken with the shutter closed (to minimise background light) and a variety of camera settings. These were analysed and the variation of noise parameters (σ and λ_{CIC}) with camera settings are shown in figure 6.1; the trends are explained by the arguments in section 5.1.1. Several frames were taken with the same settings; by looking at the variation in parameters obtained from these frames together with fits to simulations made with known theoretical distributions we estimate the fitting routine returns parameters with accuracies:

$$\Delta\mu \approx 0.05\% \quad \Delta\sigma \approx 0.5\% \quad \Delta G \approx 2\% \quad \Delta\lambda \approx 10\%$$

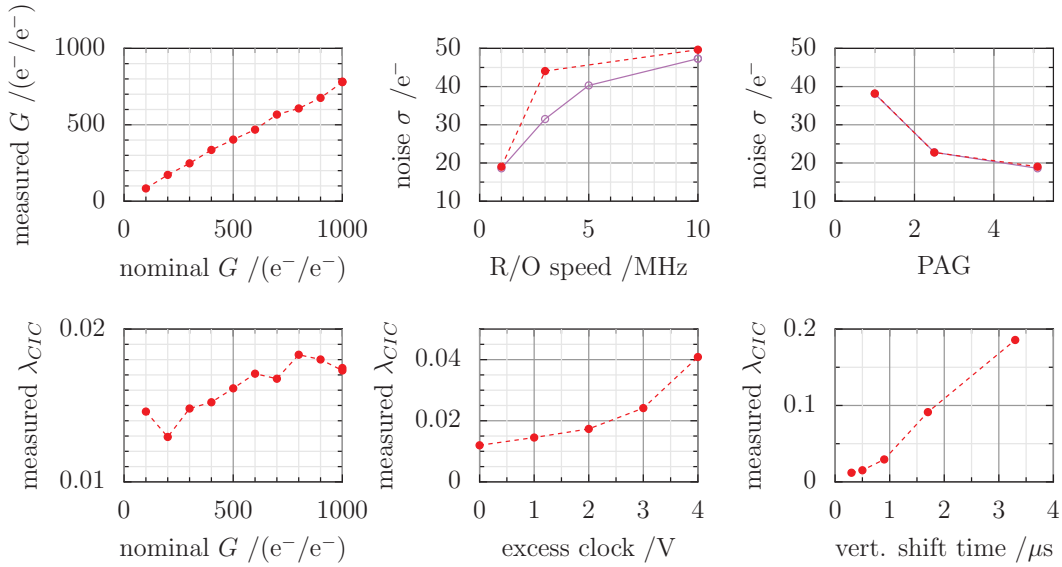


Figure 6.1: Fitted parameters (red \bullet) obtained from exposures with changing camera settings and a closed shutter. The settings held constant in each case match those used for experiments described in this chapter, namely $G = 1000\text{e}^-/\text{e}^-$, 1 MHz readout (R/O) speed, $5.1\times$ pre-amplifier gain (PAG), $0.3\mu\text{s}$ vertical shift time and +2 V clock voltage. The values supplied by the manufacturer are also shown (blue \circ).

Table 6.2 shows the fitted parameters for the readout experiments described in this chapter and compares them with those specified by the camera manufacturer [172]. The fitted parameters are largely self-consistent between experiments with identical camera settings, with the exception of μ which was observed to vary during the course of an experiment (“baseline drift”). The average value of λ_i^D seen in the exposures with the shutter shut should be dominated by CIC, although it may contain a small amount of residual thermal dark current. The larger λ_i^D and λ_{CIC} seen for the experiments in section 6.3 can possibly be attributed to the different operational mode of the camera.

	Spec.	Shutter	Expt. in section:		
		closed	6.2	6.3	6.4
Mode	-	KS	KS	FK	KS
μ /counts	370	368.1(2)	366.2(2)	376.9(2)	365.6(2)
σ /e ⁻	18.6	19.09(9)	18.67(9)	19.1(1)	18.67(9)
G /(e ⁻ per e ⁻)	1000	778(16)	819(16)	838(17)	817(16)
average λ_i^D /photons	-	0.018(2)	0.022(2)	0.066(7)	0.027(3)
...in exposure time t_b	-	400 μ s	400 μ s	200 μ s	400 μ s
$\Rightarrow \lambda_{CIC}$	0.005	0.018(2)	-	0.026(3)	-

Table 6.2: Fitted parameters for the experiments that follow compared with values supplied by the camera manufacturer in [172]. The operational mode of the camera for the experiment is specified by KS (Kinetic Series) and FK (Fast Kinetics). The average dark count λ_i^D for all pixels in the dark frames is given as photoelectrons per pixel (s) over an integration time t_b . Where an estimate of the CIC noise has been made this is provided as λ_{CIC} electrons per pixel. The specified thermal count rate is 2.3×10^{-4} e⁻/pixel/s at -97°C .

6.2 Single qubit, single exposure experiment

Method

The sequence shown in figure 6.2 was repeated several times, each sequence records one “B” trial with the ion prepared in $|B\rangle$, and one “D” trial, prepared in $|D\rangle$. The camera was operated in “kinetic series” mode with a 400 μ s exposure, and a 50×10 pixel ROI near the frame-transfer region was selected for readout. In this camera mode the ROI is transferred quickly after exposure to the covered storage area of the CCD (from which it is read out slowly). The transfer is estimated to take $512 \times 0.3 \mu\text{s} \approx 154 \mu\text{s}$ and the lasers were turned off during the frame-transfer period to prevent build up of background scatter⁴. The laser sequence in figure 6.2 is triggered by the falling edge of the “fire pulse”, indicating the end of the “B” exposure. During the “B” exposure the 854 nm laser was also illuminating the ion to prevent shelving (see section 4.3.3). There was a small delay of 15(1) μ s between the end of the 1 ms long 393 nm shelving pulse and the start of the “D” exposure which, together with the finite shelving rate of the 393 nm laser, gives a correction of $\delta = 2.8(1) \times 10^{-5}$ to ϵ_D due to imperfect preparation of $|D\rangle$, where the uncertainty will be dominated by the statistical uncertainty $\sqrt{\delta/N_{\text{exp}}^D}$ expected in N_{exp}^D trials prepared in $|D\rangle$.

Viewing the summed pixels from the “B” frames in time order allowed us to identify and remove regions of the data set where the ion was heated so as to cause a drop in fluorescence over several consecutive sequence repeats; 51874 sequences were retained

⁴The lasers were actually turned off for a total time of 500 μ s, comfortably longer than the transfer period.

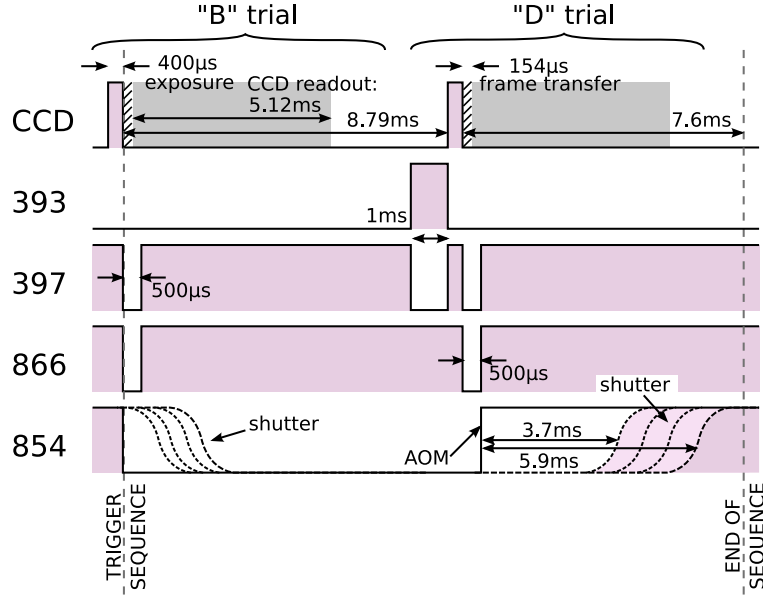


Figure 6.2: Sequence diagram for single qubit, single exposure experiment. The sequence is triggered by the CCD exposure and repeats with a constant 18.38 ms period. The CCD exposure is indicated by the pink pulses; the hatched areas represent the frame transfer time during which lasers are extinguished to minimise background light; the grey areas indicate the readout time for 10 rows of pixels. Shutter jitter is indicated by the dashed lines.

for analysis. The effect of the amplifier baseline μ drifting over the course of the data acquisition was removed by fitting the data with an exponential decay; the value of μ dropped by ~ 5.5 counts with a time constant of ~ 600 sequence repeats.

Results

The pixel order was chosen from a long exposure image created by summing all "B" trials in the data set; the spread of information over the pixels can be seen in figure 6.5(a). For $N \lesssim 100$ pixels (taken in brightness order) the ROI is roughly circular and centred on the ion. The brightest pixel contains around 10% of the information— on average containing 4.1 photons in 400 µs. The average count for a pixel in the "D" trials was 0.022(2) photons. We see a total of 49(1) photons over the whole 500 pixel ROI and estimate that around 25% of photons fall outside this region. This gives an estimated fluorescence rate of $\sim 164 \times 10^3 \text{ s}^{-1}$ at the CCD. Comparing this with the $53 \times 10^3 \text{ s}^{-1}$ rate seen using the PMT at 1.9356(1) G, this gives a rough estimate of $Q = 50\%$ for the camera, which is comparable to the nominal efficiency quoted by the manufacturer [175] at 397 nm.

The results from analyses of the data with the protocols described in section 5.2.2 are shown in figure 6.5(b) for changing ROI size N . For each analysis method, the error

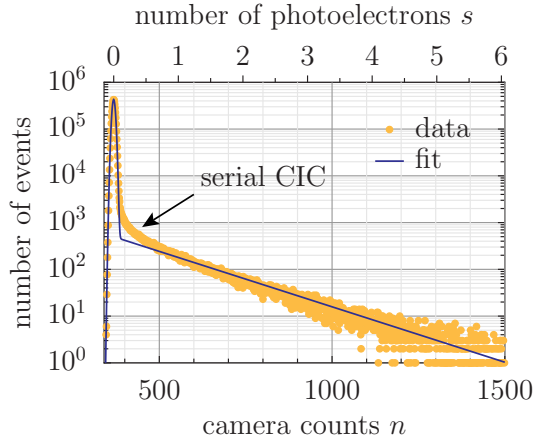


Figure 6.3: Example of fitted dark counts for 5×10^6 pixels taken using the same camera settings as the readout experiments with a closed shutter.

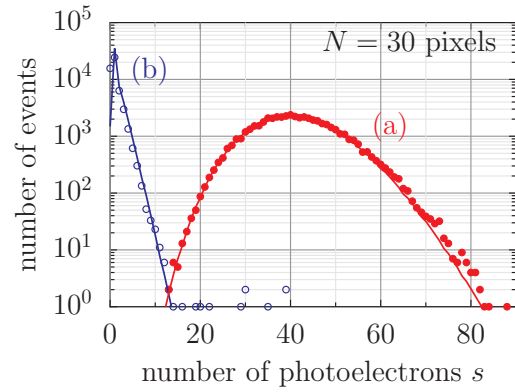


Figure 6.4: Experimental histograms of photoelectrons s for $N = 30$ pixels around one ion, $t_b = 400 \mu\text{s}$. 51874 trials prepared in each of $|B\rangle$ (\bullet) and $|D\rangle$ (\circ). Theoretical probability distributions (solid lines) for (a) $B(s)$ (b) $D(s)$ (with no decay).

bars are larger than the apparent scatter in the values of ϵ because the same data set was used to create the entire curve, so results at different N are not independent.

The optimum thresholds used were those which optimised discrimination of the experimental histograms as our theoretical model does not include the serial register CIC noise. An example of the experimental and theoretical histograms is shown in figure 6.4 for an $N = 30$ ROI. In the absence of a background data set, the camera parameters and $\{\lambda_i^B, \lambda_i^D\}$ for constructing the $B_i(n)$ and $D_i(n)$ distributions for maximum likelihood analyses were extracted by fitting the experimental data set itself. Although the “D” trials may contain instances of $|D\rangle \rightarrow |B\rangle$ decay, high-count data points from these events are not expected to affect the λ_i^D obtained from fits as they have low statistics and are removed from the histogram before fitting (see section 6.1.1).

The threshold method reaches a minimum of $\epsilon = 1.0(4) \times 10^{-4}$ (with $\epsilon_B = 0$) using an ROI of 26 pixels, while the maximum likelihood reaches an error of $\epsilon = 1.1(4) \times 10^{-4}$ (with $\epsilon_B = 0$) in only 15 pixels, demonstrating that this method is indeed more efficient at using the information. The adaptive analysis shows that the same error can be achieved using an average $\overline{N} = 3.1$ pixels which contain on average only 22% of the total fluorescence signal.

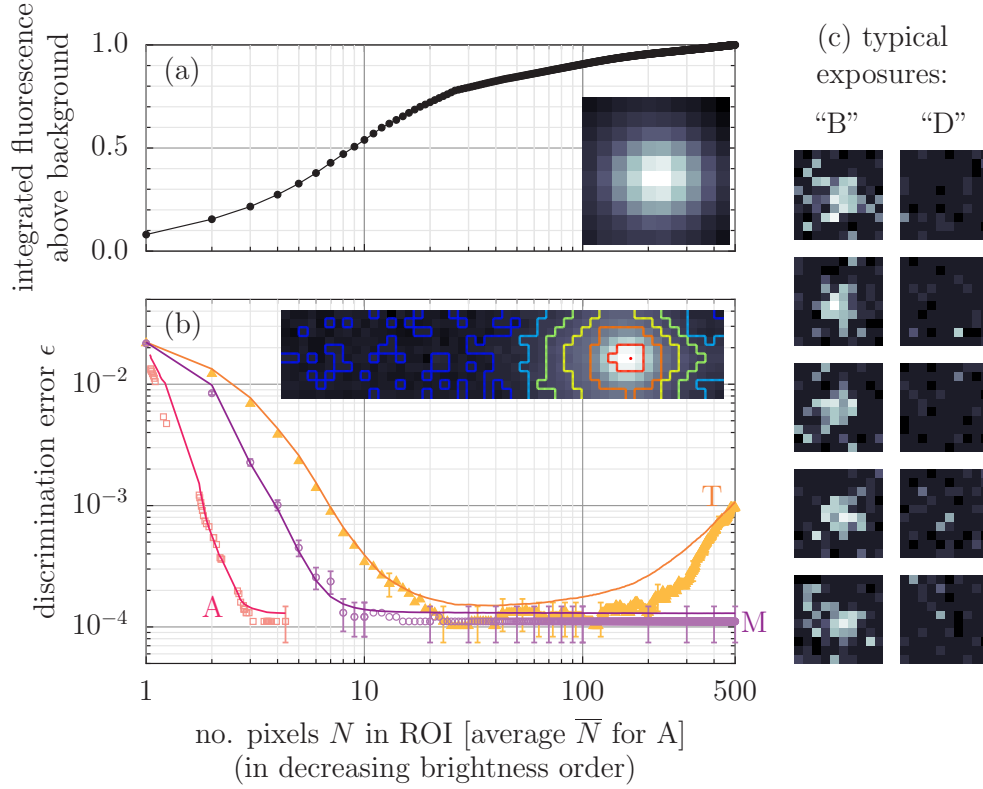


Figure 6.5: (a) Integrated fluorescence signal above background vs. ROI size N , for a single ion. INSET: Long exposure image. (b) Readout error ϵ vs. ROI size N using single $400\mu\text{s}$ exposures. Solid lines show the results of 2×10^7 simulated trials with the same parameters. T: Threshold method (orange), M: Maximum likelihood method (purple), A: Adaptive maximum likelihood method (pink). INSET: Full 50×10 acquisition area showing ROIs containing the brightest $\{10, 50, 100, 150, 200, 300\}$ pixels. (c) Typical $400\mu\text{s}$ exposures for trials prepared in $|B\rangle$ and $|D\rangle$.

Simulations

After obtaining information about the camera and fluorescence distribution from the experiment, simulations were performed to find the optimum value of t_b which would have given the lowest ϵ . A value of $\lambda_{CIC} = 0.018$ was chosen based on the investigations in section 6.1.1 (see table 6.2). Figure 6.6(a) shows the results of several sets of 10^7 simulations of this experiment with varying t_b . The lowest points of these curves are plotted in figure 6.6(b) which shows the minimum possible ϵ with exposure time t_b ; figure 6.6(c) shows the optimum ROI needed to achieve this. The threshold analysis gives a minimum possible ϵ of $1.42(3) \times 10^{-4}$ with an optimum t_b between $440 \mu\text{s}$ and $480 \mu\text{s}$, not far from our experimental choice. It turns out that the lowest possible ϵ of $0.92(2) \times 10^{-4}$ using a maximum likelihood analysis occurs at the shorter time of $t_b = 260 \mu\text{s}$, at the expense of using a larger ROI ($\bar{N} = 7.6$); as the exposure time is decreased, the average number of pixels required increases to ensure a similar amount of information is included in the analysis. The non-adaptive maximum likelihood method M is not shown in figure 6.6 for clarity; for each t_b it took $N > 100$ pixels to reach the asymptotic error ϵ_∞ . In comparison, the adaptive method A reached the same minimum ϵ (within the statistical uncertainty) while requiring a much smaller ROI size \bar{N} .

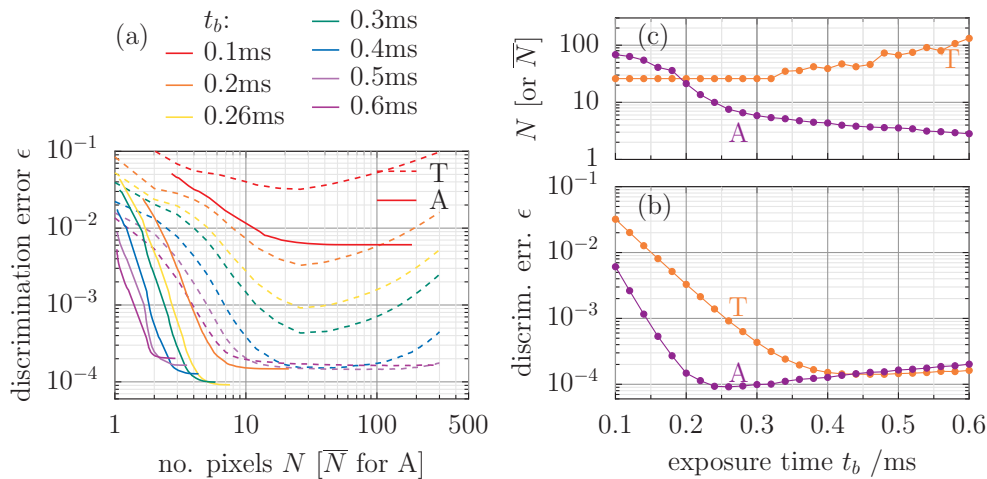


Figure 6.6: Simulations of 2×10^7 single-ion, single-exposure trials with varying t_b and $\lambda_{CIC} = 0.018$ (a) ϵ vs. N . (b) Minimum ϵ for each t_b possible when using (c) optimum N (or \bar{N}). T: Threshold method, A: Adaptive maximum likelihood method.

6.3 Single qubit, multiple exposure experiment (time resolved)

Method

To achieve time-resolved detection the EMCCD was operated in “fast kinetics” mode where the data for each trial was acquired as 21 exposures of $t_s = 200 \mu\text{s}$ with minimal ($6 \mu\text{s}$) dead-time between them. By operating in this mode, several smaller images can be held on the storage area of the CCD and the time-consuming readout deferred until later. Although only a 10×10 pixel ROI was saved for analysis, the images held on the CCD were 20 rows apart to minimise cross-talk between frames⁵. The experimental sequence is shown in figure 6.7 and is triggered by the rising edge of the CCD “fire” pulse. The $570 \mu\text{s}$ shelving pulse of 393 nm light overlaps the first three exposures and so these are discarded from all trials, leaving 18 exposures for analysis. There is a $10(1) \mu\text{s}$ delay from the end of the shelving pulse to the start of the first retained exposure, which together with the finite shelving rate of the 393 nm laser gives a correction of $\delta = 2.4(1) \times 10^{-5}$ to ϵ_D due to the imperfect preparation of $|D\rangle$. During the readout of the “D” exposures from the CCD the ion is deshelled with 854 nm light and the 397 nm light is tuned ~ 120 MHz to the red in order to cool the ion (in case of collisional heating). The collection of the “B” exposures begins after a second trigger; during these exposures the 854 nm light remains on in order to prevent shelving of the ion by 393 nm leakage. The whole D-B sequence was repeated many times and 2×33946 trials were retained for analysis after removing regions of the data set with low fluorescence in several consecutive “B” trials (ion heating).

An independent “background” data set was acquired to match these experiments. The pulse sequence for this data set is similar to figure 6.7 but with the 393 nm shelving pulse removed and the 397 nm light constantly illuminating the ion. To provide a dark “D” trial with no shelving (and thus no decay) the 866 nm light was turned off during the first set of exposures in the sequence. This has negligible effect on the background light levels due to the interference filter in the imaging system which prevents 866 nm light from reaching the CCD. We also discard the first three exposures from each trial so that the data is comparable with the readout experiments. In total, 14920 each of

⁵With 20 rows each, a maximum of 25 images can be held on the 512×512 pixel storage region.

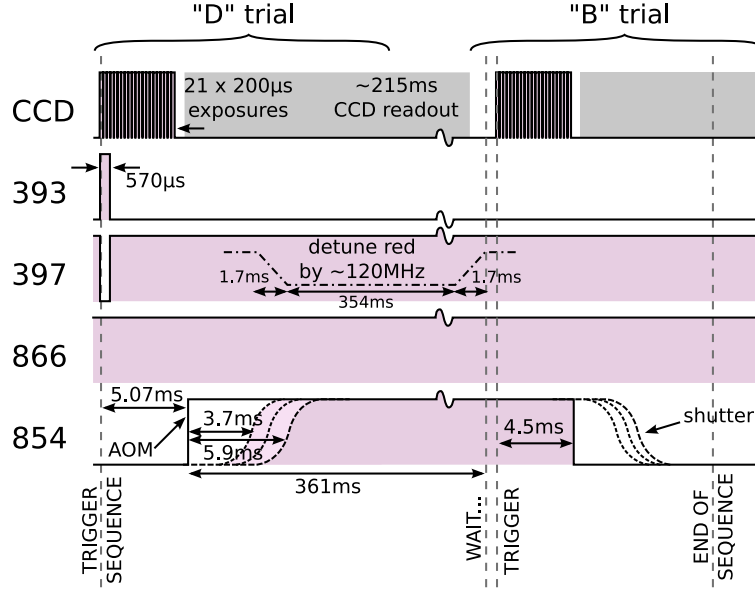


Figure 6.7: Sequence diagram for single qubit, multiple exposure experiment. The sequence is triggered by the first CCD exposure in a sequence of 21 exposures making up the “D” trial. The 21 CCD exposures are indicated by the blocks of narrow pink pulses; the grey areas indicate the readout time for 21×20 rows of pixels. The camera control software imposes a long ($\sim 560(10)$ ms) delay between “fast kinetic” series, we make use of this time to tune the 397 nm laser further to the red of the atomic transition to cool the ion; this is represented by the dash-dotted line. After the “D” trial, the experimental control computer waits to receive a second trigger from the camera indicating the start of the “B” trial. Shutter jitter is indicated by the dashed lines.

“B” and “D” background trials were retained for fitting.

Results

The camera parameters and dark $\{\lambda_{ji}^D\}$ were obtained from the “D” exposures in the background data set. The average photon count per pixel in exposure 1 (of 18) is 0.066(7), increasing to 0.20(2) by exposure 18 as later exposures have had longer to accumulate scattered background light and also undergo more vertical shifts (thus possibly accumulating more parallel CIC noise). For this reason, separate analysis distributions $B_{ji}(n)$ and $D_{ji}(n)$ were used for each exposure j . The average dark counts for each dark exposure j were fitted with a linear regression line which indicates an increase of ≈ 0.0078 photons per $200 \mu\text{s}$ exposure on top of a baseline $\lambda_{CIC} \approx 0.026(3)$ photons.

The bright $\{\lambda_{ji}^B\}$ were taken from fits to the experimental data itself as the fluorescence had drifted to a different level to that seen in the background data. The average number of fluorescence photons contained in the 10×10 pixel ROI varies from 18.6(5) to 21.7(6) between exposures 1 and 18. This could be due to intensity modulation of the 397 nm laser during each trial caused by for example an AOM switch-on transient.

(A similar systematic effect was seen in the time-resolved PMT data in chapter 4.)

Figure 6.8 shows examples of the first five exposures from a bright and a dark trial. Also shown is an example of a cosmic ray event which occurred in the eighth exposure of one of the “B” trials; this was the only cosmic ray seen in all of the camera data presented in this thesis. The event is characterised by very high count values— scaling for gain, these would be equivalent to over 100 photons each on six of the pixels (two of these pixels are saturated at a count equivalent to 323 photons). This is consistent with the often high energy of the particles.

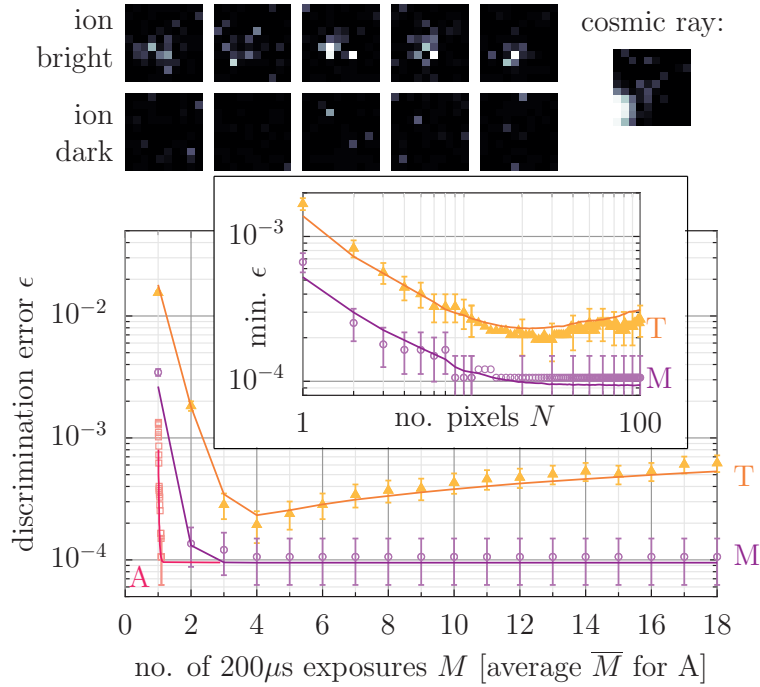


Figure 6.8: Readout error ϵ vs. number of $200\mu\text{s}$ exposures M included in analysis with optimal N for a single ion. Solid lines show the results of 2×10^7 simulated trials with the same parameters. T: Threshold method (orange), M: Maximum likelihood method (purple), A: Adaptive maximum likelihood method (pink). INSET: Minimum ϵ achievable with N pixels in ROI. ABOVE: Typical experimental frames (1–5) for ions prepared in $|B\rangle$ and $|D\rangle$. “B” exposure showing the single cosmic ray event seen in any of our data sets (the brightest pixels were completely saturated, at $2^{16} - 1$ counts).

The results of the TARDIS analyses with the protocols described in section 5.2.3 are shown in figure 6.8 and compared with the expected ϵ computed from 2×10^7 simulated trials with the same parameters. The threshold analysis was performed using thresholds obtained from the experimental data itself and an optimal ROI of 24 pixels; the lowest ϵ achieved was $1.9(6) \times 10^{-4}$ (with $\epsilon_B = 0$) using $M = 4$ exposures. The maximum likelihood analysis reaches $\epsilon = 1.1(4) \times 10^{-4}$ ($\epsilon_B = 0$) with $M \geq 4$ and an optimum ROI of 37 pixels. This is no lower than ϵ obtained experimentally for a single $400\mu\text{s}$

exposure—the extra temporal information gained has been offset by the increase in read noise caused by splitting the exposure up into several shorter ones. This was not the case with the PMT, which had no read noise and therefore negligible penalty to sub-dividing the detection period⁶. An adaptive analysis with an ROI of $N = 29$ reaches the same ϵ in only $\overline{M} = 1.1$ exposures ($230 \mu\text{s}$). Even if it were possible to terminate the detection sequence before all 18 exposures had been taken, the adaptive method would not allow a practical speedup (without a dramatic change in camera architecture) since the CCD read-time is larger than the $200 \mu\text{s}$ exposure time⁷.

Simulations

The fluorescence distribution $\{\lambda_{ji}^B\}$ seen in the experiment was used in simulations to estimate the readout error had the experiment been performed with a range of exposure times t_s . The same average background λ_j^D was used for all pixels⁸ i in each exposure j ; this was also derived from the experimental data and a value of $\lambda_{CIC} = 0.02$ was assumed.

A simulation using only exposure $j = 1$ with $t_s = 200 \mu\text{s}$ reaches $\epsilon = 2.43(1) \times 10^{-3}$ at $N = 100$ pixels using a spatial maximum likelihood analysis. In contrast, the $t_b = 200 \mu\text{s}$ simulation of the non-time-resolved experiment from Figure 6.6 gives a readout error of $1.57(3) \times 10^{-4}$ with the same ROI, an order of magnitude lower. This difference in ϵ is due to the higher level of background in the time-resolved experiment. The exposure time $t_b = 200 \mu\text{s}$ is not far from the optimal value in Figure 6.6 but for this experiment it is much too short: the higher background level requires a longer exposure time.

Figure 6.9(a) shows the results of several sets of simulations of this experiment with varying t_s . Only the threshold and adaptive maximum likelihood methods are shown; the non-adaptive maximum likelihood method reaches the same ϵ as the adaptive method but uses a larger number of exposures M . The lowest points of these curves are plotted in figure 6.9(b) which shows the minimum possible ϵ with exposure time t_s ; figure 6.9(c) shows the number of exposures M needed to achieve this. Each simulation point is plotted at its respective optimum ROI size N . For the threshold simulations, the

⁶The PMT did have a short ($< 43 \text{ ns}$) dead-time between $10 \mu\text{s}$ counting bins.

⁷The readout time for one 20 row exposure with our camera is $\approx 1 \text{ ms}$ at the fastest possible read rate of 10 MHz . It is not possible to read out less than complete 512-pixel rows.

⁸Removing fixed-pattern noise from the simulation in this way makes negligible difference to the final ϵ obtained.

average size of N is 23 pixels and the average N for the adaptive method simulations is 89 pixels. The threshold analysis gives a minimum ϵ of $2.23(3) \times 10^{-4}$ using two $t_s = 400 \mu s$ exposures. The adaptive method shows the trade-off between temporal resolution and added noise per exposure. As t_s is reduced, the average number of exposures \overline{M} increases to maintain similar total integration time t_b but ϵ does not decrease as the temporal resolution is improved below $t_s \approx 200 \mu s$ — rather, at the smallest t_s , ϵ appears to start increasing. With the addition of a new free parameter M , the maximum likelihood method becomes less sensitive to the choice of t_s and the lowest ϵ of $0.91(2) \times 10^{-4}$ is possible with t_s between $100 \mu s$ and $200 \mu s$. This minimum ϵ is the same (within the uncertainty) as the minimum $\epsilon = 0.92(2) \times 10^{-4}$ at $t_b = 260 \mu s$ from the simulations of a single exposure experiment in figure 6.6. This implies that even when the exposure times t_b and t_s are optimised, no improvement is gained by splitting up the exposure to obtain temporal information.

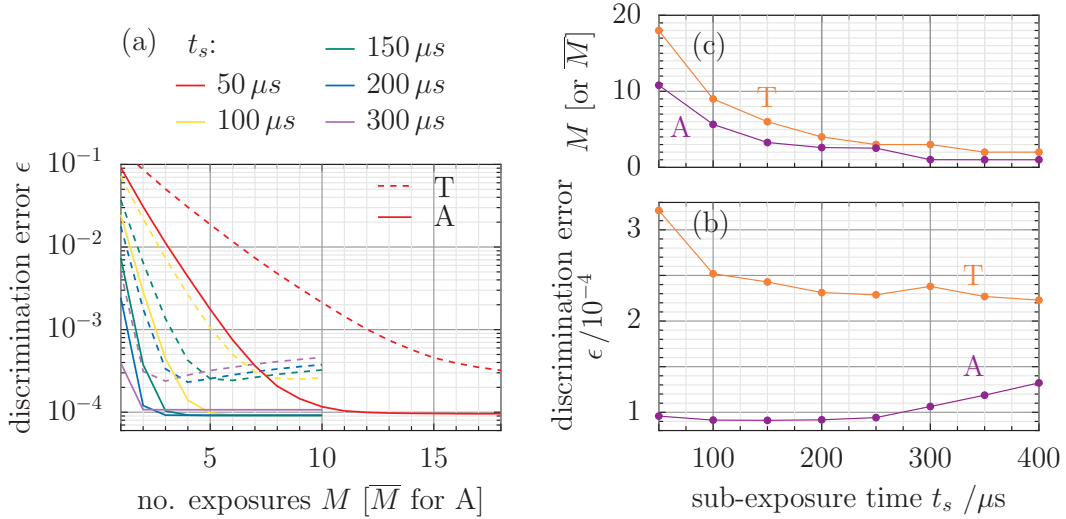


Figure 6.9: Simulations of 2×10^7 single-ion time-resolved trials with varying t_s and $\lambda_{CIC} = 0.02$. (a) ϵ vs. M . (b) Minimum ϵ for each t_s possible when using (c) optimum M (or \overline{M}). T: Threshold method (orange), A: Adaptive maximum likelihood method (purple). Each simulation is plotted with its optimum ROI size N ; the average size of N for method T(A) was 23(89). Error bars on each point are smaller than the symbol size.

6.4 Four ion “qunybble” experiment, single exposure

Method

As mentioned in section 6.1, we are not able to prepare all 16 possible states of the qunybble (four-ion string) deterministically with a low error $\sim 10^{-5}$ as we did in the

previous single-ion experiments. Instead, we prepare a random state and sandwich our “test” detection period between a “pre-” and “post-” detection. These two extra detection periods are used to select only trials in which the measured qunybble state remains constant, thus both eliminating errors due to qubit decay and providing the known preparation with which to compare the outcome of analysis on the test exposure. Eliminating errors due to qubit decay means that we are able to measure the error due to cross-talk between ion images separately.

For this experiment, the camera was operated in “kinetic series” mode with an experimental sequence involving six $400\,\mu\text{s}$ exposures with an ROI of 50×10 . The sequence begins with a “check” exposure in which all ions should be bright. The falling edge of the “fire” pulse from this exposure triggers the laser sequence shown in figure 6.10. After each exposure all lasers are turned off for $500\,\mu\text{s}$ to allow the data to be moved to the “storage” region without acquiring any more background scatter. A $12\,\mu\text{s}$ shelving pulse from the $393\,\text{nm}$ laser shelves each ion with a probability $\sim 50\%$ to prepare a random state of the qunybble. The remaining five exposures follow. The middle exposure of these represents our “test” exposure and each pair either side of this are summed to provide the “pre-” and “post-” measurements respectively. Just before the end of the sequence the $397\,\text{nm}$ laser is tuned $\sim 73\,\text{MHz}$ to the red to improve cooling and try to reduce decrystallisation of the string.

We removed all regions where ions heated/decrystallised by examining all of the “check” exposures in the data set. These also allowed us to correct for synchronisation changes between the laser and camera control PCs. We were left with 30100 sequences in the data set, giving 120400 qubit trials.

A similar two-exposure sequence was used to record “background” data where the first exposure (“B”) contained all ions in $|B\rangle$ and the second exposure (“D”) was taken with no $866\,\text{nm}$ light so that all ions appeared dark. The “D” exposures were fitted to obtain the camera parameters.

Results

The qunybble state that was prepared in each trial was determined by analysing the “pre-” and “post-” measurements using a double-threshold method to improve our confidence in the identifications as follows. For each ion k , a 5×7 pixel ROI was chosen,

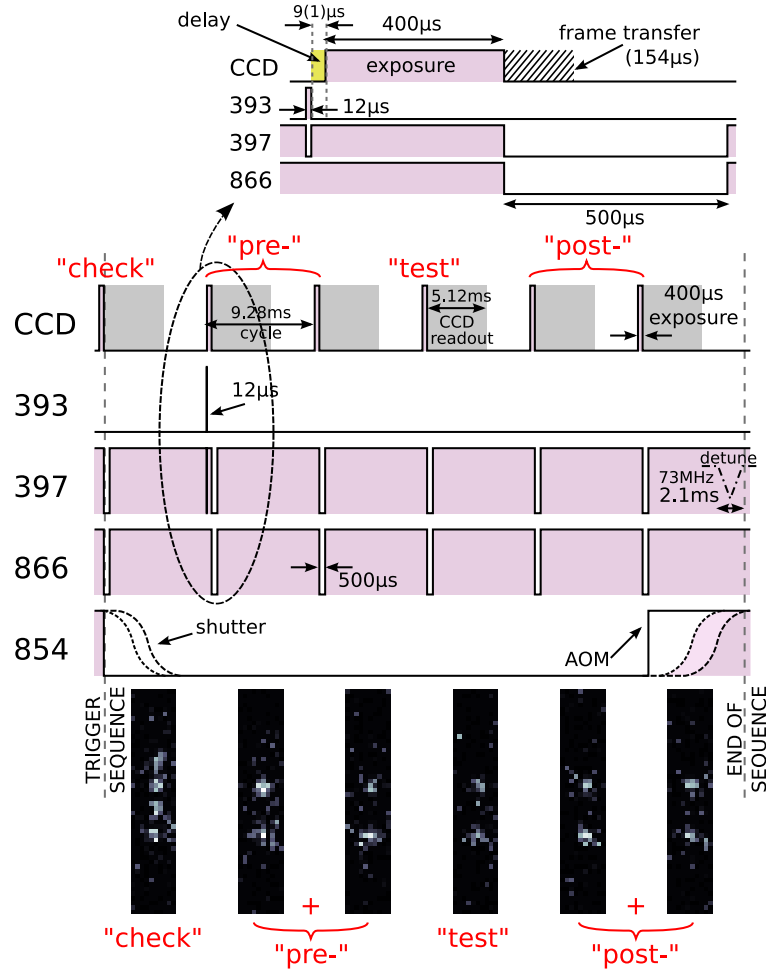


Figure 6.10: Sequence diagram for the “qunybble” experiment, showing a single trial of six exposures. The CCD exposures are indicated by pink pulses; the grey areas indicate the readout time for 10 rows of pixels. The sequence is triggered at the end of the “check” CCD exposure. The expanded region of the diagram (above) shows more detail including the timing of the 393 nm shelving pulse. The hatched area represents the frame transfer time during which lasers are extinguished to minimise background light after each exposure. After the sixth and final exposure, the 397 nm laser is briefly tuned ~ 73 MHz to the red of the atomic transition to cool the ions; this is represented by the dash-dotted line. Shutter jitter is indicated by the dashed lines. BELOW: Typical experimental frames (1–6) for a qunybble trial in state [1010].

centred on the brightest pixel for that ion. For each pre- and post- measurement, the counts inside this region were summed and two thresholds were used to decide the state of the ion; measurements with a count value beneath the lower threshold were determined to be dark (0) and those with count values higher than the upper threshold identified as bright (1). Experiments with a count value between the two thresholds were marked as “uncertain” and discarded from analysis. The results from the pre- and post- measurements were compared and those where ion identifications did not match were also discarded (this removes all trials where a $|D\rangle \rightarrow |B\rangle$ decay occurs)⁹. The spacing between the two thresholds was the same for all ions but the exact position of the lower threshold was optimised separately for each ion by first minimising the number of mismatching qunybble trials in the data set and then fine-tuned by minimising the number of qubit trials discarded from the data set. In total, we retained 95% of the qubit trials, removing 5846 from the data set. An example histogram from the “pre-” measurements showing the double thresholds is presented in figure 6.11.

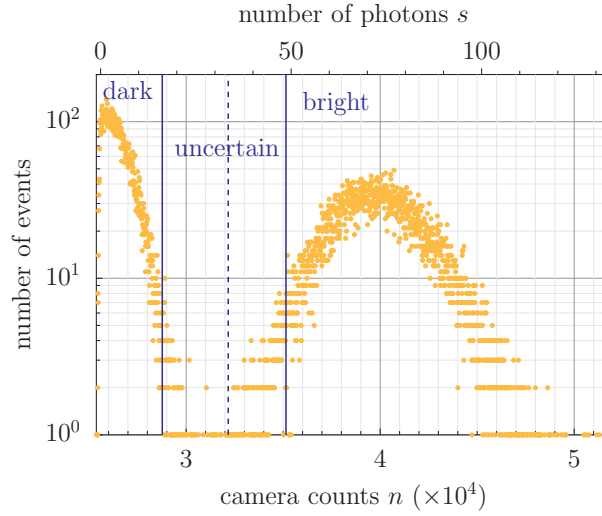


Figure 6.11: Example histogram of the total counts in a 5×7 pixel ROI around ion 1 after summing the two “pre-” exposures. Solid lines show the optimal upper and lower thresholds used to identify the state of the ion; the position of the thresholds was adjusted, keeping their separation constant, to minimise the number of qubit trials discarded from the data set. The dashed line indicates the single-threshold position which would minimise the number of mismatching qunybble trials.

Long exposure images of the qunybble states are shown in figure 6.12. The distribution of qunybble state preparations is also shown in figure 6.12 and analysis of this data gives a probability of shelving a single ion of $p = 0.459(8)$, with no significant bias

⁹Several $|B\rangle \rightarrow |D\rangle$ events were also observed (and discarded); the number of such events is consistent with the observed imperfect extinction of the 393 nm AOM.

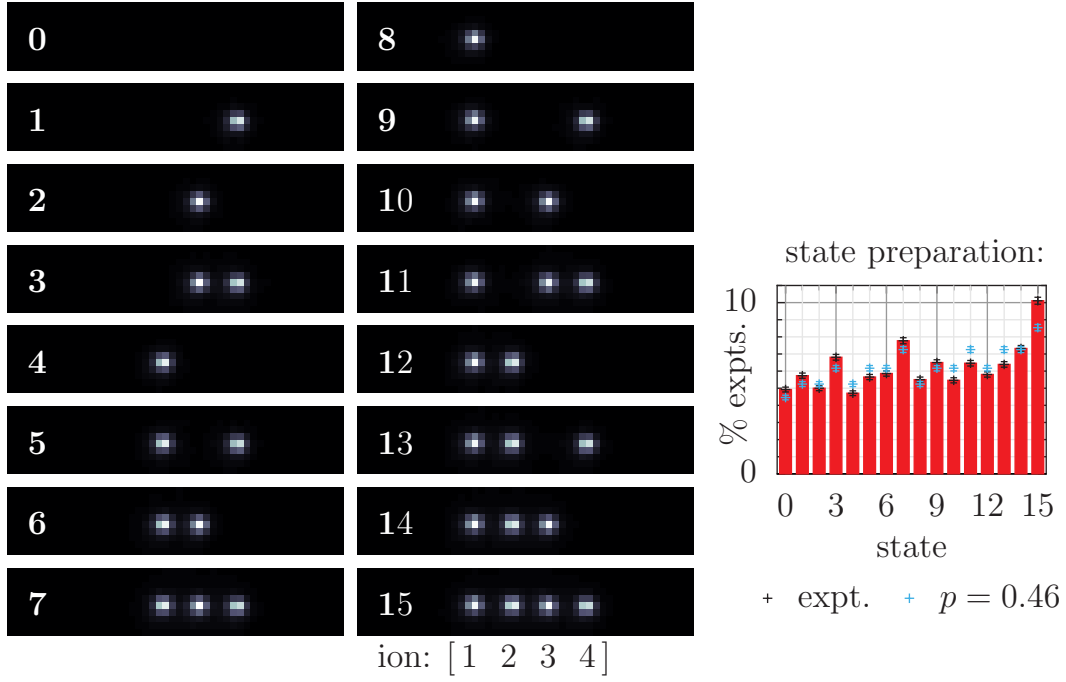


Figure 6.12: Long exposure images obtained by averaging over all “test” exposures determined to have each qunybble value $0 \dots 15$. The scale is $2.6 \mu\text{m}$ per pixel in the object plane and the mean ion spacing is $14 \mu\text{m}$ in the trap. Images 1,2,4,8 were used to find the pixel brightness order for each ion independently. RIGHT: percentage of trials prepared in each qunybble state, error-bars show the statistical error in the experimental preparations (black) and the preparations expected given a probability $p = 0.46$ of shelving a single ion (blue).

obvious from the post-selection. This is not consistent with the shelving probability $p = 0.496(6)$ calculated from the $12 \mu\text{s}$ long 393 nm shelving pulse, but the smaller value of p could be explained by a drift in the intensity of the 393 nm laser throughout the experiment. The long exposure images for qunybbls $\{1, 2, 4, 8\}$ were used to order the pixels according to brightness for each ion independently.

The results of analyses of the “test” exposure using the protocols described in section 5.2.4 are shown in figure 6.13 along with the results of M-C simulations for comparison. The optimal threshold positions were chosen from a computation of the theoretical distributions (see section 5.3) but analyses performed using thresholds found by histogramming the data itself give results which agree within the uncertainty. Both threshold methods reach a minimum cross-talk error (not including decay error) of $\epsilon_x = 6.8(8) \times 10^{-4}$ per qubit (averaged over all qunybble preparations) after which ϵ_x rises sharply for $N \gtrsim 25$ as the ROI diameter begins to exceed the $14 \mu\text{m}$ mean ion spacing. Taking the states of nearest neighbours into account improves ϵ_x slightly for larger ROIs. The amount of cross-talk with N is shown in figure 6.14 when picking pixels in brightness order for ion 2. At an ROI of $N = 25$, the nearest-neighbour ions

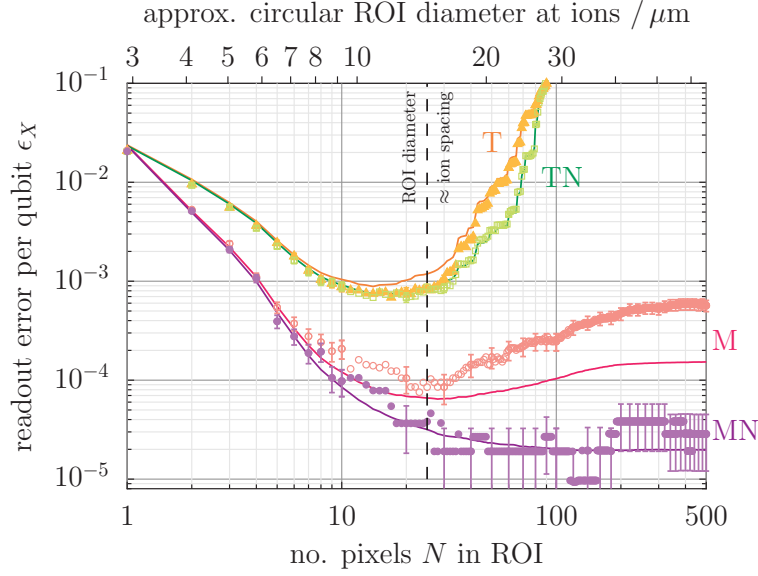


Figure 6.13: Readout error ϵ_x per qubit (averaged over all qunybble states) vs. ROI size N around each ion. Solid lines show the results of 2×10^6 simulated trials of each qunybble value with the same parameters. Threshold (T, orange) and maximum likelihood (M, pink) methods ignoring neighbours. Threshold (TN, green) and maximum likelihood (MN, purple) methods taking into account nearest neighbour states.

contribute cross-talk at a level of $\approx 4.0\%$ of the signal from ion 2, with the next-nearest neighbour contributing at a level of $\approx 0.9\%$. The cross-talk for ion 3 is slightly higher than that from ion 1 since it is slightly closer to ion 2.

The average photon numbers $\{\lambda_{qi}\}$ for all the pixels i in the exposure were found for each of the qunybble states q by fitting the histogrammed data from the pre- and post-exposures (before the images were summed). Although these histograms may contain instances of $|D\rangle \rightarrow |B\rangle$ decay, the resulting bins at high counts have few entries and are removed from the data before fitting. The $\{\lambda_{qi}\}$ were then used to create theoretical distributions for each i, q ; serial CIC noise was included by replacing the theoretical probabilities for $n = 0 \rightarrow 4$ (where n are the scaled camera counts) with probabilities derived from the actual data. This set of distributions was then used to create $B_{\nu ki}(n)$ and $D_{\nu ki}(n)$ for the maximum likelihood analyses. Since they are derived from the pre- and post- data only, they are independent of the test exposure itself.

Ignoring the states of neighbouring ions, the maximum likelihood method reaches a minimum cross-talk error of $\epsilon_x = 0.8(3) \times 10^{-4}$ at $N = 23$, after which it increases as the ROIs begin to overlap neighbouring ions. Nevertheless, this increase is not as marked as for the threshold methods as the maximum likelihood method gives less weight to pixels added later in the analysis. The experimental data in figure 6.13 appears to disagree

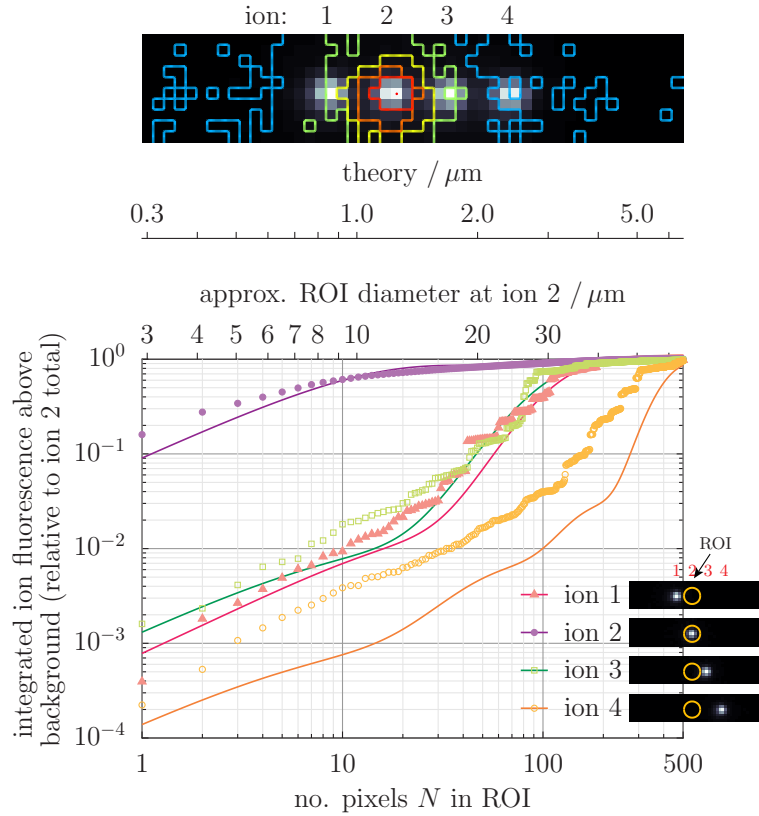


Figure 6.14: Cross-talk affecting ion 2 in a string of four ions. Filled circles (●) show the integrated fluorescence from ion 2 when adding pixels to the ROI in order of decreasing brightness (the order is found from images in which only ion 2 was fluorescing); fluorescence from the other ions is integrated using the same pixel order. Data for each ion are obtained from images where only the ion in question is bright (see key, inset). Up to $N \sim 100$ pixels the ROI is roughly circular and centred on ion 2 with a diameter in the object plane given by the upper abscissa. Theory (solid lines) shows cross-talk for a diffraction-limited system with ions spaced ten times closer, on a ten-times magnified upper abscissa. ABOVE: image of the full 50×10 acquisition area with contours showing ROIs containing the brightest $\{10, 25, 50, 100, 250\}$ pixels around ion 2.

with the simulation at larger N .

An iterative maximum likelihood analysis which takes into account the states of nearest neighbours reaches an average cross-talk error of $\epsilon_x = 0.2(1) \times 10^{-4}$ and is even zero for certain N . There is now no penalty to increasing the ROI size to overlap neighbouring ions. The close agreement with the simulation in figure 6.13 indicates that any systematic effects (such as correlated errors which would be common to the “pre-”, “post-” and “test” exposures) are below the statistical uncertainty.

The value of ϵ_x represents only the additional error due to cross-talk from neighbouring ions and does not include the effects of decay. Combining this with the result from the single-ion experiment in section 6.2 which does include decay then we estimate a net readout fidelity approaching 99.99% for a four-ion string is possible with the camera for our imaging system, despite the significant ($\approx 4.0\%$) cross-talk.

By generalising the analysis method to include next-nearest neighbours $\{\nu\} = \{000, \dots, 111\}$ we can investigate the level of cross-talk from these further ions. The analysis provides no further reduction in ϵ_x or N and so we conclude that any effect is at or below the $\sim 10^{-5}$ level.

6.5 Simulations

A selection of single-ion simulations with changing exposure time have already been presented with the experiments discussed in this chapter. This section presents further simulations of camera readout in different scenarios. We first investigate the dependence of the cross-talk error ϵ_x on the level of cross-talk between ion images using simulations of a four-ion string in which we change the ions’ separation. We then investigate the effect of spatial resolution on the analysis methods by changing how many pixels the ions’ images are spread over; we consider both single- and multiple- ion detection. We then discuss the effect of photon arrival rates (R_B and R_D) and exposure times. The “photon counting mode” offered by commercial EMCCDs is evaluated. Finally, we present simulations to investigate the cross-talk error ϵ_x for ions in a surface trap at Oxford.

6.5.1 Changing cross-talk (ion separation)

The cross-talk described in section 6.4 is limited by imperfections in our imaging system. For an ideal diffraction-limited imaging system with the same numerical aperture $\sin \alpha = 0.25$, similar nearest-neighbour cross-talk is obtained only when the ions are ten times closer together (and imaged with a ten-times greater magnification, $\mathcal{M} = 62$). The theoretical cross-talk expected from such a system is plotted in figure 6.14 (solid lines). For this magnification, the pixel size becomes $(16/62) \approx 0.26 \mu\text{m}$ per pixel in the object plane. The radius of the ions' Airy discs is $0.938 \mu\text{m}$ in the object plane (or 3.6 pixels) and the ions are separated by ≈ 1.54 times the Airy radius.

The effect of changing the separation of the ions (and hence the cross-talk) was investigated by performing simulations of four equally spaced ions imaged on a 50×11 pixel area with the choice of magnification and numerical aperture above. The pixel means $\{\lambda_{qi}\}$ were found according to (5.7) where the weighting w_i for each pixel was found by integrating the Airy function over each square pixel. A total fluorescence rate of $R_B = 164 \times 10^3 \text{ s}^{-1}$ was used (see estimation in section 6.2) with a background rate of $R_D = 17.5 \text{ s}^{-1}$ per pixel, chosen to be between the values seen in section 6.2 and section 6.4. The CIC noise was set at $\lambda_{CIC} = 0.018$ per pixel and an exposure time of $t_b = 250 \mu\text{s}$ was used as this was found to be approximately optimal according to the single-ion simulations presented in figure 6.6. A total of 2×10^6 simulated trials were performed for each qunybble value; the results are shown in figure 6.15.

The cross-talk error ϵ_X is shown in the lower plot of figure 6.15 and decreases as the ion separation is increased and the amount of cross-talk between ion images is reduced. For large ion separations the value of ϵ_X obtained from the two maximum likelihood methods (M,MN) begins to converge since cross-talk becomes negligible and therefore little improvement is obtained by including the states of neighbouring ions in the analysis. At extremely large separations the value of ϵ_X is expected to tend towards the residual error arising from the effective overlap between “B” and “D” fluorescence distributions which are widened by Poisson statistics and EMCCD readout noise. As the ion separation is reduced, the iterative maximum likelihood method offers a significant improvement over the simpler threshold method: ϵ_X is reduced by two orders of magnitude when the ion spacing is equal to the Airy radius (the Rayleigh criterion) and ϵ_X can be reasonably small even when the ion spacing is reduced below this limit.

We noted above that the nearest-neighbour cross-talk seen in the experiment in section 6.4 looks qualitatively similar to that expected from a diffraction-limited imaging system where the ions are separated by $\approx 1.54\times$ the Airy radius (figure 6.14). Figure 6.15 shows the simulated discrimination error for such a diffraction-limited system to be $\epsilon_x = 0.42(2) \times 10^{-5}$ with a slightly smaller ion separation of $1.5\times$ the Airy radius. In comparison, simulations of our experimental system (figure 6.13) imply $\epsilon_x = 2.0(1) \times 10^{-5}$. Therefore, a diffraction-limited system with ion spacing decreased by a factor of 10 (compared to our experiment) is expected to significantly out-perform our system.

The discrepancy between the value of ϵ_x obtained using an experimentally derived fluorescence distribution and that using Airy distributions arises because the results of the analyses depend sensitively on the entire shape of the fluorescence distribution. Consequently it is not possible to predict the value of ϵ_x that will be obtained in an experiment by examining only a single parameter which has been used to characterise the cross-talk — the whole shape of the distribution must be known. Nevertheless, to give some general idea of how the cross-talk scales with ion separation in a diffraction-limited system, the upper plot in figure 6.15 attempts to quantify it by finding the amount of signal from the nearest (and next-nearest) neighbour which falls inside an ROI around the ion of interest, as a fraction of the amount of signal from the ion itself. This quantity depends on the ROI size chosen; figure 6.15 shows the value when the ROI diameter is equal to the ion separation.

6.5.2 Spatial resolution on the CCD

The effect of combining the contents of several pixels was considered in section 5.1.3, where it was shown that spreading the information over several pixels followed by the addition of pixels after readout from the CCD will increase the width of the resulting distribution when compared to placing the same number of photoelectrons on a single pixel. In a readout experiment there is a further noise source which is added *per pixel* from the scattered light background R_D . Will these per-pixel effects cause an increase in ϵ when multiple pixels are included in a maximum likelihood analysis, or will the extra information contained in the spatial distribution of the fluorescence offset this increase in noise?

To answer this question, 2×10^7 simulations were performed, consisting of a single

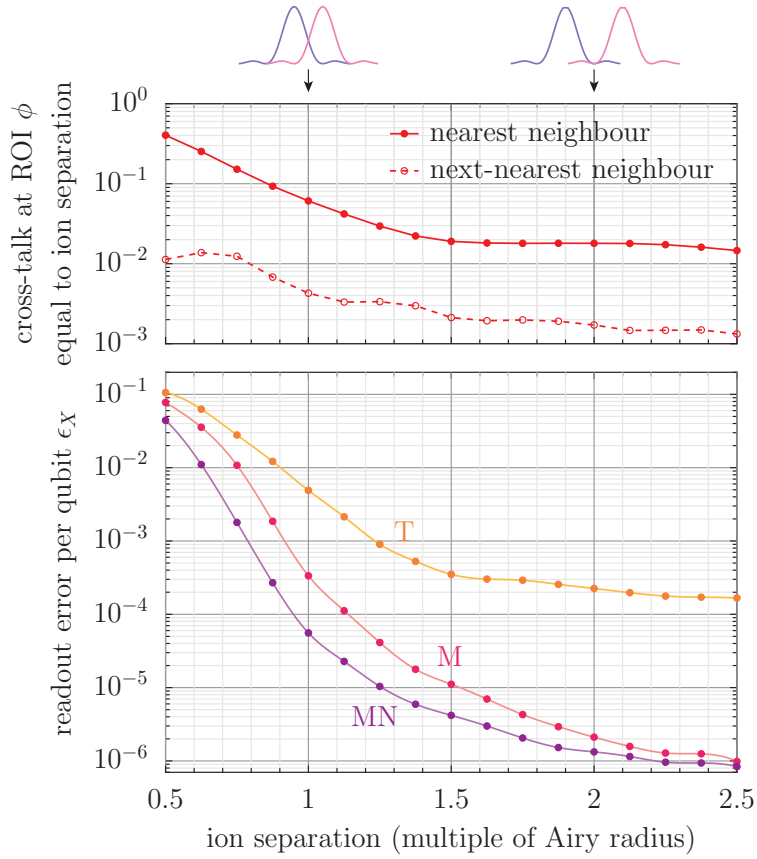


Figure 6.15: LOWER PLOT: Readout error ϵ_X per qubit (averaged over all qunybble states) vs. ion separation as a multiple of the Airy radius ($0.94\mu\text{m}$), from 2×10^6 simulated trials of each qunybble value for an ideal diffraction-limited imaging system with numerical aperture $\sin \alpha = 0.25$. Error bars on each point are smaller than the symbol size, solid lines are spline fits to guide the eye. Threshold (T, orange) and maximum likelihood (M, pink) methods ignoring neighbours, maximum likelihood (MN, purple) method taking into account nearest neighbour states. UPPER PLOT: Cross-talk between ions, quantified as the amount of fluorescence from neighbouring ions (as a fraction of the signal from the ion itself) falling within an ROI with a diameter equal to the ion separation.

ion imaged on a 23×23 pixel region using a diffraction-limited imaging system with magnification $\mathcal{M} = 60$ and all other parameters as in section 6.5.1. Only the 300 brightest pixels were included in the simulation; the ion's Airy disc covered ~ 39 pixels. The results of this simulation are compared in figure 6.16(a) with the results of simulations where the same total signal from the ion is contained on a single pixel.

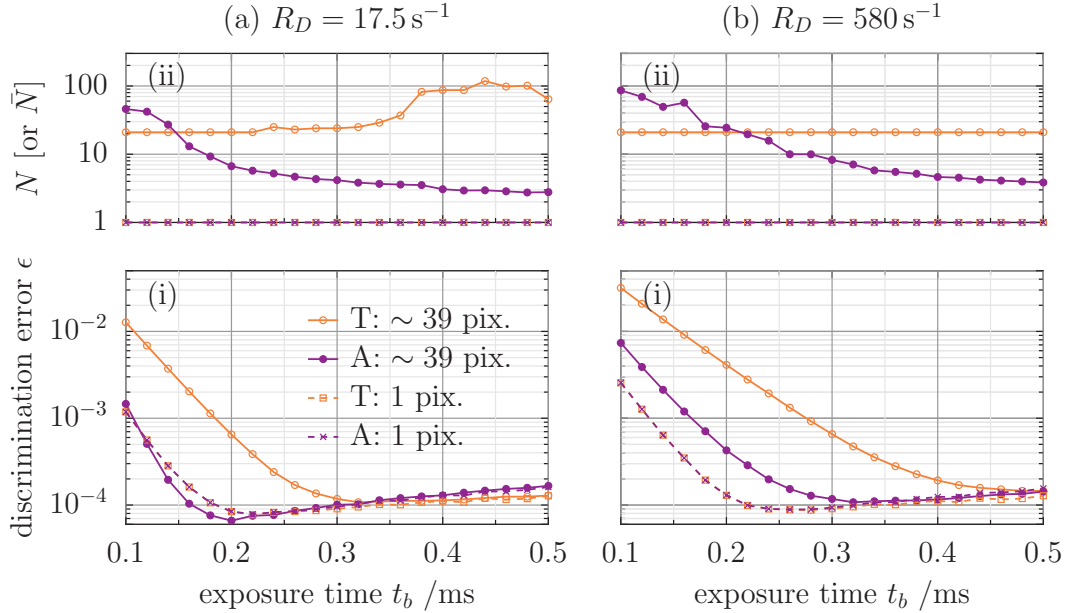


Figure 6.16: Simulations of 2×10^7 single-ion trials for an ideal diffraction-limited imaging system with varying t_b and $\lambda_{CIC} = 0.018$. Plots show a comparison between simulations where the signal is an Airy function with the disc covering ~ 39 pixels (solid lines) with a situation where the same total signal is contained on a single pixel (dashed lines). (i) Minimum ϵ for each t_b possible when using (ii) optimum N (or \bar{N}). T: Threshold method (orange), A: Adaptive maximum likelihood method (purple). Error bars on each point are smaller than the symbol size. (a) Simulations with a background rate of $R_D = 17.5 \text{ s}^{-1}$ per pixel. (b) Increased background scatter of $R_D = 580 \text{ s}^{-1}$ per pixel.

For a threshold analysis pixels are added together and so ϵ is increased when the signal is spread over more pixels, as explained in section 5.1.3 and shown in [figure 6.16(a),(i)]. Spreading the information over several pixels appears to provide a small advantage below $t_b \approx 250 \mu\text{s}$ when using the maximum likelihood analysis. For a single pixel at short t_b the threshold and maximum likelihood methods give the same results as each other. At longer t_b decay dominates and the number of pixels appears not to make a difference as the two simulations agree for each analysis method within the statistical uncertainty.

If the background R_D per pixel is increased, one might expect that at some point the additional background will outweigh the advantage of the spatial information when the ion signal is spread over the CCD. Figure 6.16(b) shows the results of similar sim-

ulations, but with an increased rate of scattered light background. Focussing all of the ion fluorescence on a single pixel now indeed provides the lower ϵ .

For multiple ions the spatial resolution becomes more important as it is this which enables us to distinguish cross-talk from neighbouring ions. The sensitivity of the analysis methods described in section 5.2.4 to the spatial resolution is investigated in figure 6.17. The spacing of the four ions was kept constant at one Airy radius while the magnification \mathcal{M} was changed so that the number of pixels per Airy radius increased. The rest of the parameters were the same as those in section 6.5.1. The minimum cross-talk error ϵ_x for method MN occurs when the Airy radius is five times the pixel side, meaning that the Airy disc is spread over ≈ 79 pixels. For higher resolutions, ϵ_x is increased by the extra noise added per pixel, while for lower resolutions the reduced spatial information becomes an issue.

In summary, when using a CCD to read a *single* ion, the choice of spatial resolution will depend on the background scattered light level. For our background levels, spreading the image over several pixels actually confers a slight advantage, whereas for high scattered background light a single-pixel image is preferable (in which case a PMT would be more appropriate). For readout of multiple ions at once (where CCDs excel) a reasonably high spatial resolution may be required to reach the lowest ϵ_x possible, although the exact choice of magnification will depend on the background light level, ion separation and fluorescence distribution. Imaging each ion in the string onto a separate single pixel would only be advisable if the ions were well separated (meaning the cross-talk between the ion images was low), this will be discussed in section 7.1.1.

In many EMCCDs it is possible to combine the pixel contents on the CCD before readout, known as “binning” which has the effect of reducing spatial resolution. As already discussed in section 5.1.3, binning pixel contents horizontally will always increase readout noise¹⁰ relative to simply imaging the same image onto fewer pixels. Therefore, if a lower resolution is desirable (e.g. to reduce readout time by minimising N) then a better option would be to reduce the imaging system magnification instead.

¹⁰Vertical binning occurs before the gain register and so does not affect the readout noise.

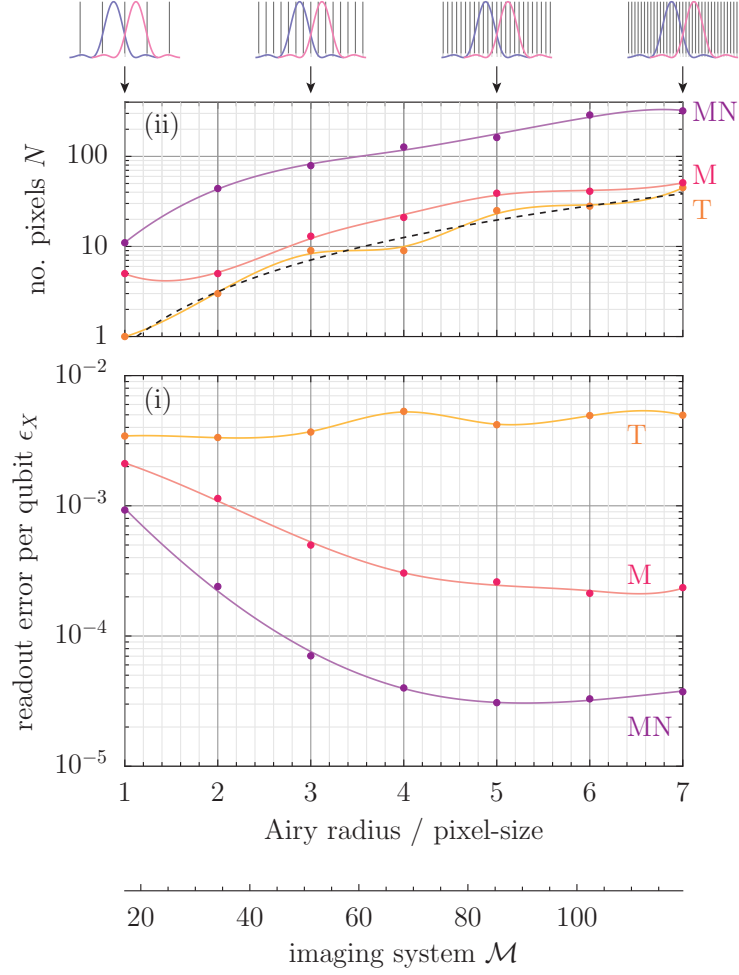


Figure 6.17: LOWER PLOT: Readout error ϵ_X per qubit for a qunybble (averaged over all qunybble states) with changing CCD spatial resolution, where the abscissa shows the number of CCD pixels spanning the Airy radius of an ion. Also shown is the corresponding magnification for an ideal diffraction-limited imaging system with numerical aperture $\sin \alpha = 0.25$ and CCD pixels of size $16 \mu\text{m} \times 16 \mu\text{m}$. Data is taken from $16 \times (2 \times 10^6)$ simulated qunybble trials with a constant ion separation of one Airy radius. Error bars on each point are smaller than the symbol size, solid lines are spline fits to guide the eye. Threshold (T, orange) and maximum likelihood (M, pink) methods ignoring neighbours, maximum likelihood (MN, purple) method taking into account nearest neighbour states. UPPER PLOT: Optimum ROI size N necessary to reach the minimum ϵ_X in the lower plot. Also shown is the approximate value of N at which the ROI diameter equals the ion spacing (dashed line). The pixel spacing is indicated by the grid lines in the sketches above.

6.5.3 Discussion of photon arrival rates and exposure times

The number of parameters affecting ϵ in EMCCD experiments is much larger than for PMT readout and the associated increase in computing time prevents us from making a detailed exploration of the parameter space as we did for the PMT. Although the distributions from the camera have a more complicated non-Poissonian shape, we can still draw some conclusions by appealing to the same arguments made for the PMT readout presented in section 3.3.3.

For the PMT experiments we considered the arrival rate of fluorescence photons $R_B\tau$ compared to the $|D\rangle$ -state lifetime τ and the relative rates of signal and background photons R_B/R_D . We also considered the total exposure time t_b/τ necessary to reach the minimum discrimination error ϵ . When considering readout using the EMCCD we now have an extra parameter in the number of pixels N needed for analysis. This will depend on the spatial distribution of ion fluorescence $\{w_i\}$ (which we shall not investigate further) as well as the photon arrival rates and exposure time. The background light collection now becomes a per-pixel effect and there is an additional source of background in the CIC noise which does not depend on exposure time. Since CIC noise is broadly similar from camera to camera we shall not consider the effect of changing CIC rates further.

To reach the lowest possible ϵ we must integrate as much ion signal as possible in our detection. For a single detection bin, we stop integrating in time when the errors due to ion decay outweigh the advantage of gathering more fluorescence. We stop integrating in space when the extra noise added per pixel outweighs the extra information included.

For both PMT readout and EMCCD readout, an increase in $R_B\tau$ will mean that a similar amount of information can now be collected in a shorter t_b , resulting in a lower ϵ as the decay effect is reduced. When using the EMCCD, one can choose instead to reduce the ROI size N , and collect the same amount of information within fewer pixels. An increase in $R_B\tau$ also gives a reduction in the cross-talk error ϵ_x for multiple ion readout with the EMCCD as the signal-to-noise ratio is improved.

As for the PMT, when R_D is increased the variances of the count distributions for dark and bright ions increase (see discussion in section 3.3.3). More information must be gathered to optimise discrimination between them: this can be accomplished with a longer integration time t_b or by inclusion of more pixels in the analysis (increased N).

Figure 6.16 shows the results of two pairs of simulations (a) and (b), which differ in their rate of scattered light background. For both the single-pixel and Airy function simulations, an increase in R_D causes the minimum value of ϵ to increase and move towards longer t_b . For example, when considering the Airy function simulations analysed with the adaptive maximum likelihood method, the minimum error increases from $\epsilon = 0.66(2) \times 10^{-4}$ at $t_b = 200 \mu\text{s}$ with $R_D = 17.5 \text{ s}^{-1}$ per pixel to $\epsilon = 1.08(2) \times 10^{-4}$ at $t_b = 320 \mu\text{s}$ with $R_D = 580 \text{ s}^{-1}$ per pixel.

A comparison of the two upper plots in figure 6.16(ii) shows that a greater average number of pixels \bar{N} are needed for the adaptive analysis at any given t_b when the background rate R_D is higher.

6.5.4 The EMCCD in photon-counting mode

Many EMCCDs offer a “photon-counting mode” [176] where each pixel is assigned a value “0” or “1” indicating the absence or presence of a photoelectron in the pixel. This identification is made by comparing the count in each pixel to a pre-determined threshold. The mode is proposed as a route to circumventing the excess noise factor F associated with the EMCCD gain process thus to re-gain the full quantum efficiency.

Once the count value n for each pixel i has been mapped to $\{0, 1\}$, the data can be analysed by one of the protocols described in section 5.2. The binary mapping makes maximum likelihood analyses somewhat simpler: the probability distributions $B_i(n)$ and $D_i(n)$ for each pixel now only need to be found and stored for $n \in \{0, 1\}$.

To avoid losing too much information, the readout must be conducted in such a way that there is a negligible probability of counting > 1 photon per pixel. The experiment presented in section 6.2 had ~ 4 photons on the brightest pixel with $t_b = 400 \mu\text{s}$, implying that for typical values of R_B in our experiment, the exposures should be $< 100 \mu\text{s}$. To integrate for long enough to reach the lowest ϵ , the readout would need to consist of several such exposures. Since extra CIC noise is added per-pixel and per-exposure, this sort of detection sequence would probably result in an increased ϵ (see earlier discussion in section 6.3). Indeed, figure 6.9 already shows some evidence of ϵ increasing as t_s gets shorter than $100 \mu\text{s}$. If the exposure time is not sufficiently short, then the preliminary threshold used to map the data to $\{0, 1\}$ is removing some of the information that was contained in the full count distribution. Thus the photon-counting mode is unlikely to

result in a lower ϵ than seen in the experiments and simulations described earlier in this chapter.

6.5.5 Imaging ions in a surface trap

The Oxford group has recently trapped ions in a multi-zone gold-on-quartz microfabricated planar ion trap, designed and fabricated by David Allcock. This work is described in Allcock *et al.* [133]. The ions are held $150\text{ }\mu\text{m}$ above the surface of the ion trap, which is mirror-like with an upper bound of 50 nm on the surface roughness. Individual electrodes are isolated from each other by gaps where the gold is removed; these gaps are $5\text{ }\mu\text{m}$ in width near the ion position [Figure 6.18(a)].

When imaging the ions normal to the plane of the trap, the mirror-like surface reflects more light from the ions into the imaging system, improving the collection efficiency η by up to $\sim 50\%$ when compared with a different non-surface-electrode trap used previously in the same apparatus. This increase in η can reduce the readout error ϵ for single ion detection with the PMT, see section 3.3.3. Contrariwise, this reflection is not advantageous when detecting multiple ions with an EMCCD. When the ion itself is in focus, its image reflected from the trap surface will be out of focus, resulting in a wide background “pedestal” of fluorescence which will increase cross-talk between neighbouring ions.

Figure 6.18(b) shows an image of a single ion in the surface trap with a scale of $1.67(5)\text{ }\mu\text{m}$ per pixel in the object (ion) plane. The scattered light extends over a large region around the ion. The spatial extent of this scatter can not be explained by imperfections in the imaging system alone: it is mostly due to reflection from the trap surface, and is exacerbated by specular reflection off the edges of an isolation gap directly beneath the ion. [Figure 6.18(e), curve (i)] shows the proportion of ion fluorescence on each pixel of a horizontal transect through this image.

Linear crystals of up to three ions have been successfully trapped and crystallised in the surface trap. To investigate the effect of the extra cross-talk on the discrimination error ϵ_x , simulations were performed using the fluorescence distribution expected from the surface trap. The fraction of ion signal w_i on each pixel was obtained from the single-ion image [figure 6.18(b)]; three such images were superimposed at the positions¹¹ of

¹¹The images are offset by 5 pixels diagonally, or $\approx 11.8\text{ }\mu\text{m}$ in the object plane.

the ions when three are held in the trap [figure 6.18(c)]. Fluorescence and background levels, exposure time and camera settings were chosen to match those used in section 6.5.1, 2×10^5 simulated trials were performed for each state of the three-ion string. The discrimination error ϵ_X obtained is shown [figure 6.18(f), curve (i)] using an iterative maximum likelihood analysis to minimise the effects of cross-talk between images; the analysis reaches a minimum of $\epsilon_X = 1.19(2) \times 10^{-3}$ at $N = 245$ pixels.

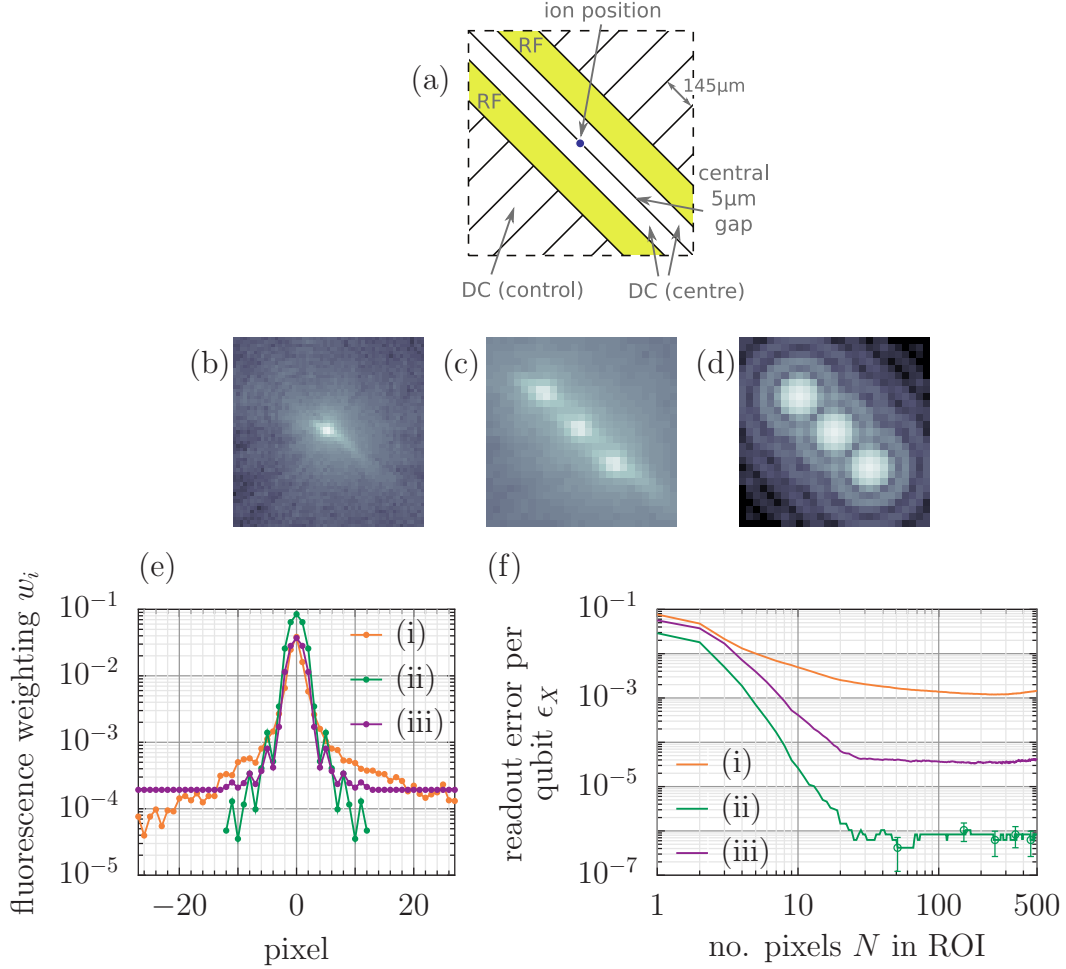


Figure 6.18: (a) Diagram of electrode layout for the surface trap (from Allcock *et al.* [133]) showing the ion location relative to the electrode structure. The RF electrodes are shown in yellow; between these are the central DC electrodes which are separated by a $5 \mu\text{m}$ insulating gap. The DC control electrodes either side are used to provide the axial confinement. IMAGES: (b) Fluorescence from a single surface-trapped ion, 55×55 -pixel image. Each pixel is $1.67(5) \mu\text{m}$ at the ion. (c) Three superimposed images of a single ion at the positions of ions in a three-ion crystal (23×23 -pixel image). Ions are separated by 5 pixels diagonally. (d) Diffraction-limited image of ions separated by 5 pixels diagonally, for a system with numerical aperture $\sin \alpha = 0.25$ and pixel size $0.26 \mu\text{m}$ at the ion. PLOTS: (e) Proportion of fluorescence w_i on each pixel along a horizontal transect through a single ion: (i) surface-trapped ion, (ii) diffraction-limited ions described above, and (iii) the same diffraction-limited image with a baseline added to every pixel. (f) Readout error ϵ_X per qubit (averaged over all states of the three-ion string) with changing number of pixels N included in the iterative maximum likelihood analysis (method MN).

For comparison, simulations were made for three ions imaged by a diffraction-limited

imaging system with numerical aperture $\sin \alpha = 0.25$ [figure 6.18(d)]. The ions were imaged with the same separation in pixels on the CCD but with a higher magnification such that the pixel size corresponds to $0.26 \mu\text{m}$ in the object plane. The ion separation is $1.95\times$ the Airy radius. These settings were chosen so that the central fluorescence peak of each ion is similar in cross-section to that seen experimentally [figure 6.18(e)]. [Figure 6.18(f), curve (ii)] shows that the discrimination error reaches $\epsilon_x = 4(3) \times 10^{-7}$ by $N = 51$ pixels, this is almost three orders of magnitude lower than that found from the experimental fluorescence distribution. Adding a baseline weight of $w_i = 2 \times 10^{-4}$ to every pixel [figure 6.18(e), curve (iii)] to simulate the reflected ion image increases the minimum discrimination error by almost two orders of magnitude to $\epsilon_x = 3.3(3) \times 10^{-5}$, therefore we infer that it is the relatively low pedestal of fluorescence around the experimental ion image that is responsible for the high ϵ_x . The value of ϵ_x appears very sensitive to the shape of the fluorescence distribution $\{w_i\}$.

6.6 Conclusions for EMCCD readout

In this chapter we have presented experiments in which the state of a single ion was measured using an EMCCD with a discrimination error of $\epsilon = 1.1(4) \times 10^{-4}$ (with $\epsilon_B = 0$) in only 15 pixels and a $400 \mu\text{s}$ exposure time using a spatial maximum likelihood method; this fidelity is comparable to that achieved with the PMT in chapter 4.

An experiment designed to investigate the cross-talk between ion images in a string *without the effect of decay* gave an additional readout error of $\epsilon_x = 0.2(1) \times 10^{-4}$ using an iterative maximum likelihood method which takes into account the states of the nearest neighbours. Combining this with the result from the single ion experiment (which includes decay) and simulations, we estimate a net readout fidelity exceeding 99.99% would be possible for a four-ion “qunybble” in our conventional (non-surface) ion trap, despite the significant ($\approx 4.0\%$) cross-talk between images (mainly due to imperfections in our imaging system). We have also presented simulations which indicate that this level of fidelity would be achievable with the ions spaced $10\times$ closer together (at $1.4 \mu\text{m}$, or $\sim 1.5\times$ their Airy radii) if our imaging system were diffraction-limited.

The effect of the next-nearest neighbours on ϵ_x was shown to be at or below the $\sim 10^{-5}$ level, so we conclude that the cross-talk is short range and we can extend this method to long ion strings. Since $\epsilon_x \ll \epsilon$ we expect a similar fidelity for two-dimensional

arrays of ions. The whole 512×512 pixel CCD array could be used to image an array of $100 \times 100 = 10\,000$ ions simultaneously (allowing a 5×5 pixel ROI per ion). The exposure time of 250–400 μs would then be negligible compared with the readout time of data from the EMCCD, as all pixels must be read serially through a single output amplifier. At the fastest readout speed of 0.1 $\mu\text{s}/\text{pixel}$, this would take $\approx 26\text{ ms}$ for the whole CCD, or of order $\sim 2.6\text{ }\mu\text{s}$ per ion. An EMCCD architecture which allowed parallel pixel readout would offer a significant speedup as image data for all ions could be read from the CCD simultaneously.

The classical computing time required for image processing is $< 0.1\text{ }\mu\text{s}/\text{pixel}$ ¹², since the basic spatial maximum likelihood analysis can be performed using just one floating point operation and one comparison per pixel. The log-likelihood ratio $\ln(p_B/p_D)$ can be updated by adding the relevant entry from a stored “difference” distribution $[\ln(B_i(n_i)) - \ln(D_i(n_i))]$, followed by a comparison of the resulting value with zero to determine the ion state. The adaptive method involves a further comparison of $|\ln(p_B/p_D)|$ with $\ln(e_c)$. The iterative version with nearest-neighbours is more complex, but reasonable speed could be achieved by calculation of $\ln(p_B/p_D)$ for all neighbour states ν as each pixel is added to the ROI, together with a few more comparisons. The main resource cost would be the storage of the “difference” distribution for each ion ($\sim 1\text{ kB}/\text{pixel}$, allowing 128 values of n_i for the distribution in double-precision). Table 6.3 summarises the classical computing resource costs for the analysis methods used in this chapter.

Method	Speed	Memory requirement [16-bit integers]
T	12 ns/pixel	2 bytes/pixel
M	14 ns/pixel	256 bytes/pixel
MN	25 ns/pixel [avg.]	1024 bytes/pixel

Table 6.3: Processing speeds for analysis of the “qunybble” experiment (section 6.4) on a typical 1.7 GHz PC. Memory requirements are also shown, assuming 16-bit integer arithmetic (which is sufficient if log distributions are used). For method MN the analysis time is an average; it varies in practice because of the iterative method.

An ideal camera architecture can be envisaged where a smaller $\sim 10\text{--}20$ pixel ROI around each ion can be read out pixel-by-pixel in decreasing brightness order through its own dedicated gain stage and output amplifier. Classical image processing could be carried out by a small microprocessor underneath each ROI. Since the image processing

¹²Measured on a typical 1.7 GHz PC.

time per pixel is no longer than the pixel readout time, this would enable feedback from the adaptive analysis to reduce the average number of pixels read out. Such an architecture would enable state identification to be performed in parallel for all ions in the array. Complementary metal-oxide-semiconductor (CMOS) technology (an alternative to CCD technology) can incorporate ADCs fabricated into each pixel, thus allowing integration of pixel arrays with on-chip image processing. Development of these technologies is ongoing [177, 178] however historically CMOS detectors suffer from higher read noise and dark current and lower fill-factors than their CCD counterparts. Combining CMOS and CCD technologies into a “scientific CMOS” (sCMOS) architecture aims to combine the lower noise performance of CCDs with the fast readout of CMOS devices [179], nevertheless at low light-levels these devices are still out-performed by EMCCDs.

Related experiments on ion detection with an EMCCD have been performed by F. Zähringer and co-workers at Innsbruck University. Previous work on multiple ion detection was published by Acton *et al.* [39], who imaged three $^{111}\text{Cd}^+$ ions separated by $\sim 4\mu\text{m}$ with an ICCD. A thresholding method was used to discriminate between ion states based on a 28×28 pixel ROI around each ion, binned into a 7×7 array of “superpixels” on the CCD. This method allowed them to read out the state of a single ion with a fidelity $> 99.4\%$; cross-talk reduced this fidelity to $\sim 98\%$ for readout of ions within the three ion string. Our fidelities compare favourably with this although some of the improvement must be attributed to the fact that our ion spacing was $\approx 1.9\times$ larger (when compared to the respective wavelengths of the imaging light)¹³.

The discrimination methods described in this and the previous chapter can also be extended to the detection of neutral atoms in an optical lattice, an alternate system for QIP. In this system a slightly different problem can be solved by camera detection: determining which of the single-occupancy lattice sites actually contains an atom. This has applications not only in the “push-out” readout scheme for neutral atoms (described in chapter 1), but also in initial loading of the lattice and when observing subsequent interactions between atoms in neighbouring lattice sites. Cooling light is applied to the whole array and the presence or absence of fluorescence at each lattice site corresponds to the presence or absence of an atom. Instead of the “decay” of an atomic state, we

¹³At $\lambda = 214\text{nm}$, the Airy radius for $^{111}\text{Cd}^+$ ions is smaller than that for $^{40}\text{Ca}^+$ with $\lambda = 397\text{nm}$ when considering an imaging system with the same numerical aperture. However, in practice it may be more difficult to make diffraction-limited optics at the shorter wavelength.

must instead consider the probability of atoms “hopping” from one site to another; this can be interpreted as providing “D” \rightarrow “B” as well as “B” \rightarrow “D” transition rates at each lattice site. The hopping rate depends on the lattice depth; it can be as high as our qubit decay rate ($\sim 1 \text{ s}^{-1}$) or as small as $5 \times 10^{-6} \text{ s}^{-1}$ [68].

Such a detection scenario is addressed by Nelson *et al.* [68] who used a diffraction-limited system to image a three-dimensional (3D) array of caesium atoms spaced by $4.9(1) \mu\text{m}$ in an optical lattice. The imaging system had a small enough depth-of-field ($2.8 \mu\text{m}$) to be able to image one plane of atoms at a time. They used a least-squares method to obtain a preliminary map of the lattice occupancy with an error of 1.0% when determining the presence/absence of an atom at a lattice site; two iterations of the procedure were calculated to reduce the error to 3×10^{-4} . The exposure used was relatively long at 50 ms; the spatial maximum likelihood methods discussed in this chapter could easily be extended to discrimination of atoms in a 3D array and may lead to similarly high fidelities with a reduction in exposure time.

The atom spacing in [68] is larger than the diffraction limit of their imaging system. The problem of discriminating lattice occupation below this limit was considered by Karski *et al.* [67], whose one-dimensional lattice spacing (433 nm) was $\frac{1}{4} \times$ the Airy radius for their imaging system. They used a least-squares method to determine the number of lattice sites separating the caesium atoms in the lattice from a 1 s exposure image. They quote a fidelity of 68.8%–99.4% for inferring the correct number of lattice sites between two atoms spaced by 4 lattice sites or fewer (i.e. below the diffraction limit), and 97.7%–99.8% for atoms spaced by 5–29 lattice sites. Making a direct comparison with the work presented in this chapter is hard, nevertheless figure 6.15 demonstrates that the iterative maximum likelihood method can discriminate ions with reasonable fidelity even below the diffraction limit: a fidelity of $\approx 95\%$ seems possible at $\frac{1}{2} \times$ the Airy radius for a diffraction-limited version of our imaging system with a $250 \mu\text{s}$ exposure. With negligible pumping between “B” and “D” states there would be no penalty to increasing exposure time to achieve an even better fidelity. However, we recall that for practical QIP the readout time needs to be kept as low as possible for successful error-correction (ideally fast, or no longer than, the logic gate time, namely $\sim 50 \mu\text{s}$ for trapped ions).

Nelson *et al.* used a long-wavelength optical lattice, while Karski *et al.* considered a short-wavelength lattice that was more sparsely filled. More recently, Bakr *et al.* [69]

have demonstrated detection of the presence (or absence) of atoms in a short-wavelength optical lattice with a fidelity of 98% with an exposure of ~ 1 s. An innovative solid immersion microscope was used, where the polished surface of a hemispherical lens is placed only a few μm from the 2D ^{87}Rb gas under study; this provided a detection efficiency of $\eta = 0.1$ and a numerical aperture of $\sin \alpha = 0.8$, giving a diffraction limit of ~ 520 nm at the 780 nm detection wavelength. The measured resolution of the lattice sites was $\sim 570 \times 630$ nm, compared to the 640 nm lattice spacing. The occupation of the lattice sites was determined by fitting point-spread functions at the position of each lattice site on an image obtained with an exposure from 0.2–1 s. The main source of infidelity was atom loss from the lattice, which occurs with a $1/e$ lifetime of ~ 30 s, this represents a $|B\rangle \rightarrow |D\rangle$ transition rate. The methods described in this thesis could be straightforwardly applied to such a scenario and may increase the fidelity by mitigating the effect of cross-talk between neighbouring lattice sites.

Chapter 7

Conclusion

7.1 Scalable readout of trapped ions

The single-shot readout fidelities of 99.99% achieved in the experiments presented in this thesis exceed the readout threshold of 99.9% for fault-tolerant quantum computation (QC) suggested by Steane [49] and are quantum non-demolition (as discussed in chapter 1). With an average readout time of $145\,\mu\text{s}$, or $91\,\mu\text{s}$ to reach 99.9%, the method is already relatively fast, but an increase in the photon detection efficiency to the (still modest) value of 2% would reduce the single qubit readout time by an order of magnitude to $\lesssim 10\,\mu\text{s}$. The parallel EMCCD readout demonstrated in the latter part of this work appears capable of accessing a similar 99.99% fidelity for readout of four ions in a string (a “qunybble”), despite the presence of $\sim 4\%$ optical cross-talk between neighbouring ion images.

The net detection efficiency of our imaging system is currently $\eta = 0.22\%$, including the $Q \approx 20\%$ quantum efficiency of the PMT at 397 nm. An improvement in detected count rate could be achieved by a detector with a higher Q ; recent advancements in PMT technology¹ have resulted in efficiencies as high as 40% around 400 nm. There is much more scope to improve the collection efficiency by increasing the solid angle over which scattered photons are collected. Moving the objective lens closer to the ions could be achieved by in-vacuum refractive [180] or Fresnel lenses [181]. Dielectric surfaces too close to the ions can however perturb the trap potential; this effect can be reduced by coating the surfaces with a conductive layer of indium tin oxide [181], although this may also decrease transmission through the lens. Shu *et al.* [153] have demonstrated

¹see for example the Hamamatsu “ultra bialkali” PMT range.

an (electrically conductive) spherical aluminium reflective mirror placed behind the ion. This allows a numerical aperture of 0.63 but the aberrations introduced by the mirror require correcting with a compensating lens outside the vacuum can. Even so, the image remains far from diffraction-limited, which would cause excessive cross-talk for camera detection of multiple ions, although such a scheme has great potential for single-ion PMT detection where the spatial properties of the image are less critical.

When determining the state of a single ion, the PMT provides the fastest read time for a given fidelity. The ability to record temporal information means that maximum likelihood methods can be used to make the scheme more immune to the effects of qubit decay and cosmic rays, while the likelihood information can be used to make a faster “adaptive method” and could also be exploited for quantum error correction. In contrast, the extra noise associated with camera readout outweighs any temporal information gained when splitting up the exposure, so these advantages are not possible. The time taken to read information from the camera’s CCD array adds significant overhead for readout of a single ion, nevertheless when performing parallel readout of a larger array of ions the readout time *per ion* can be reasonable. Indeed, for an array of ions the time taken to split and shuttle them to separate readout zones might outweigh the time to read them simultaneously with the camera. Additionally, the spatial information from the camera together with the spatial maximum likelihood analysis methods developed in this thesis means that the reduction in the error due to cross-talk possible (when imaging ion arrays) is more significant than any reduction in error that would be obtained with a time-resolved detection. The spatial resolution also means that camera detection is resistant to cosmic rays.

The fidelities and speeds presented in this thesis compare favourably to those reported elsewhere in the literature (figure 1.4), including measurements of qubits in other architectures, and is believed to be the highest fidelity qubit measurement (or operation of any sort) reported to date.

7.1.1 Towards a large-scale architecture

A viable scheme for a scalable ion trapping architecture which could support tens or hundreds of ions is that of microscale segmented traps [13, 14] with computation, storage and readout zones between which ions could be shuttled. To perform parallel readout of

many ions at once, the region(s) containing the ions must be imaged onto a CCD camera by an imaging system with a high resolution and diffraction-limited performance over a large flat field. This could be achieved using a large multi-element objective to image the entire array, an array of high numerical aperture refractive microlenses, or an array of phase Fresnel lenses. Fresnel lenses are attractive as a scalable technique as whole arrays can be fabricated on a single substrate, requiring only one alignment step with the ion trap microchip [181]. The image quality is less important if the output of each microlens is instead coupled to a separate fibre; the fibre outputs could be directed to separate PMTs for parallel readout. If the light from each ion is not perfectly coupled into its own fibre, the resulting cross-talk could limit the final discrimination error. This situation is modelled in figure 7.1, omitting the effect of qubit decay. We assume detectors whose count probabilities are Poisson distributed. Each ion is (imperfectly) imaged onto a single-pixel detector and for simplicity we consider only this single pixel to make a decision about each ion's state.² As we have omitted spatial information and qubit decay, the maximum likelihood method is equivalent to a threshold method. For small cross-talk, we assume that an iterative method (such as that in section 5.2.4) provides the states of neighbouring ions so that we can always pick the optimum threshold using (3.1) to discriminate the state of the ion-of-interest. The figure shows three situations which differ in the number of neighbouring ions which provide cross-talk. At small cross-talk, the readout error ϵ_X is limited by the overlap of Poisson distributions with means $(R_B + R_D)t_b$ and $R_D t_b$. For a linear chain of ions, a cross-talk level of $\sim 5\%$ results in an additional error ϵ_X which is at a level similar to the effect of qubit decay, $\frac{1}{2}(t_b/\tau) = 1.8 \times 10^{-4}$ at $t_b = 420 \mu\text{s}$.

Lenses require manual alignment and can take up a great deal of valuable solid angle near the ion trap which is needed for laser access. Optical fibres directly integrated into the ion trap chip could be aligned during the trap fabrication and would leave more space for laser access out of the plane of the trap chip. The fibres could be used for high numerical aperture fluorescence collection (as well as additional laser beam delivery). Van Devender *et al.* [182] have integrated a flat-ended quartz fibre into a surface electrode Paul trap by recessing it behind a hole in the trap substrate in order

²The cross-talk due to imperfect imaging means that information is present on neighbouring detectors; as for the CCD detection, a spatial maximum likelihood method could be used to retrieve this information.

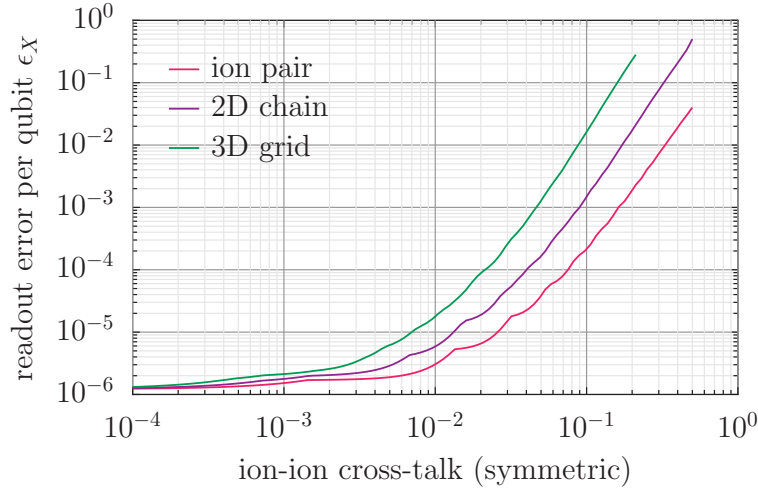


Figure 7.1: Readout error ϵ_X per qubit with changing cross-talk between detectors. Simulations assume each qubit is imaged by an ideal detector which (in the absence of cross-talk) detects fluorescence at a rate $R_B = 55800\text{s}^{-1}$, with background $R_D = 442\text{s}^{-1}$ and a detection time $t_b = 420\mu\text{s}$ to match the PMT experiments presented in chapter 4. As cross-talk increases, the signal on the detector from its own qubit drops, while the signal from the neighbouring qubit(s) increases. Qubit decay error is not included. Three cases are shown: a pair of ions (pink), an ion in a two-dimensional (2D) linear chain (purple), and an ion in a three-dimensional (3D) grid with four nearest-neighbours (green).

to minimise the perturbation to the trapping potential from the dielectric surface. The numerical aperture of 0.37 is limited by the fibre acceptance angle.

Lenses can be formed directly on fibre ends by using a fibre splicer to first join a section of fibre with a different refractive index and then to create curvature on the bare end. Fresnel lenses can also be milled into fibre ends.

Fibre integration can be used to form cavities on chips, a technique which has been used for some time in the field of cavity QED and fluorescence detection with neutral atoms [183] (cavities can increase the collection efficiency of light from trapped ions via the Purcell effect). Cavity QED with trapped ions is currently being pursued at Sussex University and Innsbruck University.

7.2 Application of methods to other ions

All trapped ion species commonly used for quantum information studies can be read out via resonance fluorescence. We shall discuss the discrimination fidelities possible for each ion species, concentrating on time-resolved PMT detection and dividing the ions into groups depending on the features of their atomic structure. In the discussion which follows we shall neglect the effect of scattered light background (which is highly

dependent on the experimental situation) and consider only pumping between qubit states as a limitation to the readout fidelity. In any case, we showed in chapter 3 that the fidelity is relatively insensitive to the rate of background scatter.

Before leaving the subject of background light, it should be mentioned that alternative cycling transitions exist for calcium or similar ions which can be used to significantly reduce background scatter; this could be employed in microfabricated traps where scattered light levels can be significantly higher due to the small ion-electrode distances. Hendricks *et al.* [184] suggest pumping light at 733 nm and 866 nm (resonant with the $S_{1/2} \leftrightarrow D_{3/2}$ and $D_{3/2} \leftrightarrow P_{1/2}$ transitions) could be used to drive a cycling transition where the emitted light at 397 nm is at a sufficiently different wavelength from the pumping beams to mean that there is essentially no background from the laser light when an appropriate filter is employed. They demonstrate a similar pumping scheme with 729 nm and 854 nm light via the $D_{5/2}$ and $P_{3/2}$ levels but note that the fluorescence levels are around a factor of 5 lower than the conventional scheme for calcium employed in this thesis. This means it would only lead to a reduction in ϵ if the scatter were at the level $R_B/R_D \lesssim 1$ (see figure 3.15).

7.2.1 Direct readout of an optical qubit

For alkali earth ions with low-lying D levels and a similar structure to $^{40}\text{Ca}^+$, readout of the optical qubit is similar. As for calcium, the $|B\rangle \rightarrow |D\rangle$ rate is negligible compared to the $|D\rangle \rightarrow |B\rangle$ decay rate. The important parameter is how fast the fluorescence can be detected compared to the rate of decay from the metastable D state; this is parameterised by $R_B\tau$. The important parameters for optical qubit readout are listed in table 7.1 (and plotted in figure 7.4) for various ions, along with an estimate of the minimum possible discrimination error ϵ and corresponding detection time t_c . These are calculated using equations (3.20) and (3.19) assuming a completely saturated transition and no background scattered light. An imaging system with a net efficiency of $\eta = 1\%$ is assumed; recent advances in PMT manufacture mean that a quantum efficiency of 40% is now attainable for all of the detection wavelengths in table 7.1. The very long 35 s lifetime of the $D_{5/2}$ state in Ba^+ makes this species particularly attractive for high fidelity readout.

	Ca ⁺	Sr ⁺	Ba ⁺
λ	397 nm	422 nm	493 nm
A_{21}	$1.32 \times 10^8 \text{ s}^{-1}$	$1.27 \times 10^8 \text{ s}^{-1}$	$9.53 \times 10^7 \text{ s}^{-1}$
τ	1.168 s	0.39 s	35 s
R_B at $\eta = 1\%$	$3.30 \times 10^5 \text{ s}^{-1}$	$3.18 \times 10^5 \text{ s}^{-1}$	$2.38 \times 10^5 \text{ s}^{-1}$
calculated ϵ	1.7×10^{-5}	4.7×10^{-5}	9.6×10^{-7}
calculated t_c	39 μs	37 μs	67 μs
reported R_B	55800 s^{-1}	58000 s^{-1}	2100 s^{-1}
reported R_D	442 s^{-1}	2000 s^{-1}	50 s^{-1}
reported R_B/R_D	126	20	42
<i>ref.</i>	[this work]	[185, 186]	[187, 40]

Table 7.1: Predicted minimum discrimination error ϵ and corresponding detection time t_c for optical qubits in alkali earth ions with low-lying D-states. The wavelength λ and coefficient A_{21} are given for the detection transition, τ is the lifetime of the $D_{5/2}$ level. R_B is estimated at saturation and we take $R_D = 0$ and $\eta = 1\%$ (PMT quantum efficiencies are similar for all λ in the table). Recently reported signal and background rates R_B , R_D are also given.

7.2.2 Readout of hyperfine qubits

Hyperfine qubits stored in the ground level of trapped ions can exhibit very long coherence times as they are no longer limited by a relatively short lifetime of the upper qubit level, as is the case for optical qubits. Two (F, M_F) states are chosen to store the qubit, usually with each state in a different F sub-level (the sub-levels are split in energy by the hyperfine interaction). Readout begins by selectively exciting population in only one of the qubit states.

Ions with a closed transition to a P level

Ions with a closed transition which are candidates for quantum information processing include $^9\text{Be}^+$, $^{25}\text{Mg}^+$, $^{67}\text{Zn}^+$, $^{111,113}\text{Cd}^+$, $^{199,201}\text{Hg}^+$ and $^{171,173}\text{Yb}^+$. In these ions (most of which have no low-lying metastable D-levels) resonance fluorescence is driven by directly exciting the $S \leftrightarrow P$ transition. Two common methods exist for selectively exciting only one of the ground-level hyperfine qubit states on a closed transition; these are described in Acton *et al.* [39] and are discussed below. The rate of state-to-state pumping for each of these methods is an important factor for readout fidelity and depends on the method and atomic properties. We shall refer to the (F, M_F) state of a level such as $S_{1/2}$ using the notation $S_{1/2}^{F, M_F}$.

General method This method can be used for ions with a general nuclear spin I . The relevant energy levels are shown in figure 7.2. Population in the “bright” $S_{1/2}^{I+1/2, I+1/2}$

state is excited with σ^+ polarised light to the $P_{3/2}^{I+3/2, I+3/2}$ state, from which it can only decay back to the bright state. Population in the “dark” $S_{1/2}^{I-1/2, I-1/2}$ state is not excited as the laser is detuned from this transition by $\Delta = \omega_{HFS} - \omega_{HFP}$ (the difference in hyperfine splittings of the two levels, typically several GHz). Detection fidelity is limited by imperfect laser polarisation which causes $|B\rangle \rightarrow |D\rangle$ pumping, and off-resonant $|D\rangle \rightarrow |B\rangle$ pumping of the dark state.

Special case method This method can be applied for ions which have $I = 1/2$ such as $^{111,113}\text{Cd}^+$, $^{199}\text{Hg}^+$ and $^{171}\text{Yb}^+$. The relevant energy levels are shown in figure 7.3. One qubit state is chosen to be $S_{1/2}^{0,0}$, with the other in one of the $S_{1/2}^{1, M_F}$ states. A laser beam containing all polarisations (σ^+ , σ^- , π) is applied between the $S_{1/2}^{F=1}$ sub-level and the $P_{1/2}^{0,0}$ state. Decays back into the “dark” $S_{1/2}^{0,0}$ qubit level are prevented by selection rules and the excitation of this state (to $P_{1/2}^{F=1}$) is suppressed by the hyperfine detuning. Off-resonant pumping of the $S_{1/2}^{0,0}$ state to the $P_{1/2}^{F=1}$ sub-level leads to $|D\rangle \rightarrow |B\rangle$ transitions; off-resonant pumping of population in $S_{1/2}^{F=1}$ to $P_{1/2}^{F=1}$ leads to a $|B\rangle \rightarrow |D\rangle$ rate (the dominant rate as the $P_{1/2}$ hyperfine splitting is smaller).

Both $|B\rangle \rightarrow |D\rangle$ and $|D\rangle \rightarrow |B\rangle$ transitions during the detection period can be included in the sort of time-resolved maximum likelihood analysis presented in this thesis. The discrimination fidelity is again limited by $R_B \tau_{ss}$, the rate at which information is collected compared to the state-to-state pumping rate $1/\tau_{ss}$.³ The off-resonant excitation rate is proportional to the laser intensity and is also a function of atomic properties such as the transition linewidth, branching ratios and hyperfine splittings (the latter determine the detuning of the laser from transitions causing state-to-state pumping). For small laser intensities, $R_B \tau_{ss}$ is independent of the intensity, but for larger laser intensities $R_B \tau_{ss}$ decreases and ϵ increases, as the fluorescence transition begins to saturate while the off-resonant excitation rate ($1/\tau_{ss}$) continues to rise. Transition rates due to imperfect laser polarisation depend on the polarisation purity achievable, but similarly continue to increase after the fluorescence transition has saturated. Coherent population trapping [125] can also reduce R_B , and hence increase ϵ .

The general resonance fluorescence method above requires the specific choice of the

³A detailed calculation would incorporate different $|B\rangle \rightarrow |D\rangle$ and $|D\rangle \rightarrow |B\rangle$ rates as they can affect ϵ differently (see section 3.2.4).

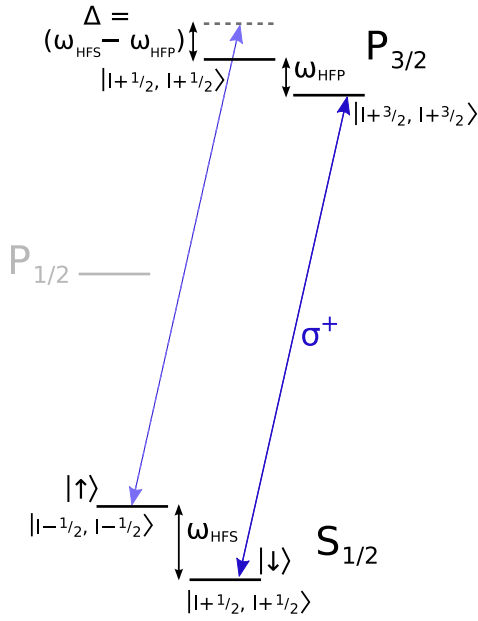


Figure 7.2: GENERAL METHOD: energy level diagram showing selective excitation of the “bright” $S_{1/2}^{I+1/2, I+1/2}$ state in an ion with nuclear spin I . Levels are labelled by $|F, M_F\rangle$ quantum numbers. Off-resonant excitation of the “dark” qubit state is also shown (dashed arrow); the laser is detuned by $\Delta = \omega_{HFS} - \omega_{HFP}$ from this transition.

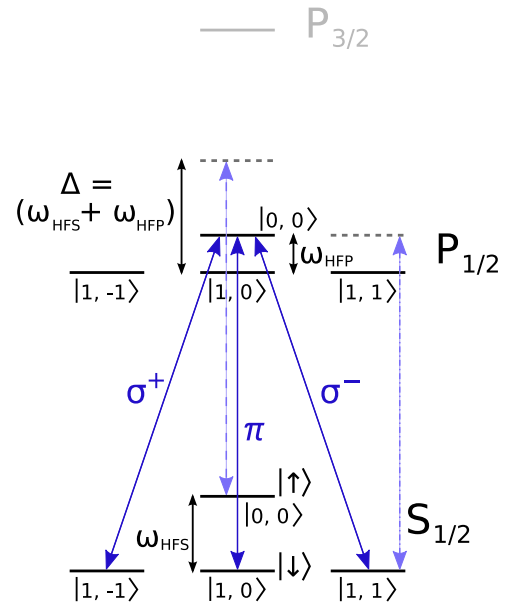


Figure 7.3: SPECIAL CASE METHOD: energy level diagram showing selective excitation of the “bright” qubit state in one of the $S_{1/2}^{1, M_F}$ states in an ion with nuclear spin $I = 1/2$. Levels are labelled by $|F, M_F\rangle$ quantum numbers. Off-resonant excitation of the “dark” qubit state is shown (dashed arrow) which causes dark→bright pumping. Bright→dark pumping is caused by off-resonant excitation from $S_{1/2}^{F=1}$ to $P_{1/2}^{F=1}$; an example of such a transition is shown (dash-dotted arrow).

$S_{1/2}^{F, M_F}$ “stretched” (maximal M_F) state for one of the qubit states. In some cases, a different pair of “clock” states⁴ represents a more robust choice for quantum information storage. Direct readout of clock states may have larger ϵ as the off-resonant excitation rate may be larger; the fidelity can be improved by mapping to the stretched states before readout. The mapping will also have an error associated with it (due to imperfect π -pulses, for example).

In the general scheme described, a single off-resonant excitation can result in pumping from one qubit state to the other. The pumping rate can be reduced by a “shelving” process which maps the population in the $|D\rangle$ qubit state to an auxiliary state from which several scattering events must occur before the qubit is pumped to $|B\rangle$. In $^9\text{Be}^+$ in the intermediate field regime ($B = 119\text{ G}$), Langer [148] shows that the optimum mapping is from $|D\rangle = S_{1/2}^{1, +1}$ to $S_{1/2}^{2, -2}$; at least four scattering events then separate this state from $|B\rangle = S_{1/2}^{2, +2}$. Again, the infidelity of the shelving process will contribute to the overall error in qubit readout.

Ions with no closed transition to a P level

For ground-level hyperfine qubits stored in ions with low-lying D-levels (such as in $^{43}\text{Ca}^+$, $^{87}\text{Sr}^+$, $^{135,137}\text{Ba}^+$), the metastable D-level can be used to increase readout fidelity. By “shelving” one of the qubit states in a D-level which does not participate in the cycling transition (effectively mapping to an optical qubit, see section 3.1.3), the limitation then becomes infidelities in the mapping. David Szwer [137] has modelled mapping for $^{43}\text{Ca}^+$ using a simple optical pumping method; he notes that the optimum fidelity for a (low-field) clock state qubit would be achieved by transferring to a stretched state qubit before mapping to the $D_{5/2}$ level. Mapping on the $S \rightarrow D$ transition (e.g. by rapid adiabatic passage) is also possible [136]. The overall discrimination error is a combination of mapping errors and the optical qubit error already discussed.

The myriad schemes for increasing the readout fidelity of hyperfine qubits prohibit a more thorough investigation here. Some theoretical results from the literature are summarised in table 7.2 and plotted in figure 7.4 for comparison.

⁴Clock states are separated by a transition whose energy is independent of magnetic field to first order. These may be $M_F = 0$ states at low B -field, or other M_F states at intermediate B -field.

	$^{171}\text{Yb}^+$	$^{111}\text{Cd}^+$	$^{199}\text{Hg}^+$	$^{43}\text{Ca}^+$
λ	369.5 nm	226.5 nm	194 nm	397 nm
estimated ϵ	1.5×10^{-3}	3.5×10^{-3}	5.7×10^{-4}	4.3×10^{-4}
scheme	$I = 1/2$ case	$I = 1/2$ case	$I = 1/2$ case	map to optical
includes CPT?	✓	×	×	✓
ref.	[125]	[39]	[39]	[137]

Table 7.2: Predicted minimum discrimination error ϵ for a selection of hyperfine qubits. The wavelength λ is given for the detection transition. ϵ is estimated assuming $\eta = 1\%$ (PMT quantum efficiencies are similar for all λ in the table); the table indicates whether the estimate includes the effect of coherent population trapping (CPT), the presence of which reduces R_B and increases ϵ . The estimated error for $^{43}\text{Ca}^+$ includes both mapping and fluorescence detection errors.

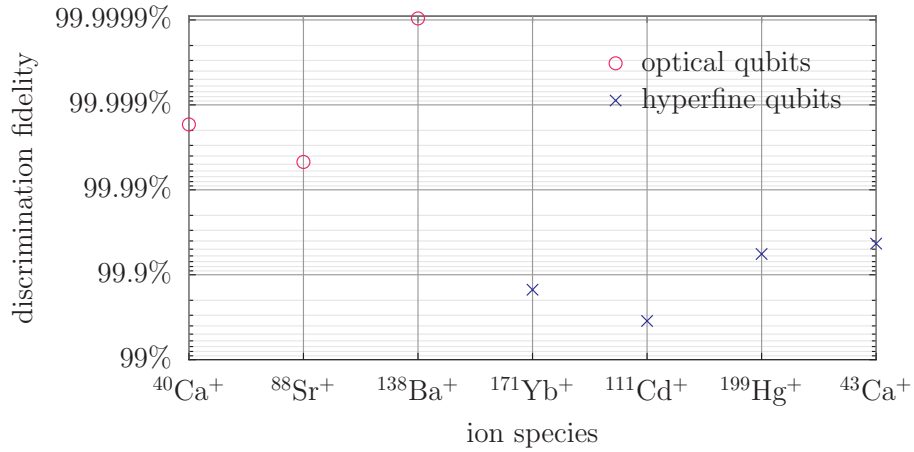


Figure 7.4: Predicted maximum readout fidelity ($1 - \epsilon$) for a selection of optical and hyperfine trapped ion qubits. The data shown here is given in tables 7.1 and 7.2 and assumes an imaging system efficiency of $\eta = 1\%$.

7.3 Application of methods to other systems

The maximum likelihood analysis methods used in this thesis are also applicable to readout of qubits in other architectures. Temporal maximum likelihood analyses can be applied in schemes where the readout fidelity is limited by qubit relaxation during the time over which a signal is integrated; resonance fluorescence with spontaneous decay is just one example of this. We discuss both the neutral atom and solid-state systems for quantum computation which were described in chapter 1. Linear optics and NMR implementations will not be included as the measurement schemes are very different to those in solid-state and atomic systems.

7.3.1 Neutral atoms

Atoms in a lattice are an alternate approach to creating a network of many qubits for QC and also lend themselves to quantum condensed matter simulations as interactions between the sites can be tuned. A common readout method consists of a “push-out” of all atoms in one state, followed by fluorescence detection to determine which atoms remain (see section 1.2.1). The spatial maximum likelihood methods for camera detection developed in this thesis can be applied to interpretation of the fluorescence data (see discussion in section 6.6), although the main limitation to fidelity may lie in the push-out step.

An alternative (non-destructive) method of detection involves the addition of a cavity to increase the number of photons detected. Interpretation of fluorescence coupled out of the cavity can be performed using the time-resolved methods presented here, or the resonant frequency of the cavity can be monitored (this exhibits a state-dependent shift). Gehr *et al.* [73] exploit this and have adapted the maximum likelihood protocols from this thesis (and published in [41]) to achieve 99.92% readout fidelity.

7.3.2 Superconducting qubits

Measurements of superconducting qubits (in particular, charge qubits) that are continuous and QND in character could be analysed with the methods presented for PMT readout in this thesis. Indeed, the “optimal nonlinear filter” developed by Gambetta *et al.* [76] in the context of superconducting qubit readout appears similar to the temporal maximum likelihood analysis discussed in this work.

Examples of continuous QND measurement in charge qubits can be found in references [86, 87, 88], details of which were discussed in section 1.2.2. In these examples, information on the qubit state is collected over time while transitions between the qubit states can occur during the measurement period. The fidelity of latching measurements (such as those involving a Josephson bifurcation amplifier [93, 94]) is often limited by the effect of qubit relaxation before latching occurs, nevertheless if the latched state itself has a finite lifetime then maximum likelihood techniques may be of use.

7.3.3 Quantum dots

The maximum likelihood scheme has obvious application to optical time-resolved measurements of quantum dot qubits [188]. It can also be applied to electrical measurements such as the continuous charge-sensing technique used by Barthel *et al.* [105]. In this reference, a quantum point contact gives an output signal with sub- μs time resolution which the authors integrate over a measurement time (limited by the T_1 relaxation of the qubit) before applying a threshold to discriminate states; this is an ideal scenario to apply a temporal maximum likelihood technique. The other methods discussed in section 1.2.3 involve measuring the presence or absence of a current pulse to discriminate between qubit states; in this case a threshold is sufficient.

7.3.4 Atomic impurities in semiconductors

The electrical method used in reference [106] relies on measuring the presence or absence of a current pulse in a similar fashion to many quantum dot measurements. Optical measurement of NV centres (see Wrachtrup *et al.*, [107]) is analogous to fluorescence readout in trapped ions, with transitions between qubit states during readout; maximum likelihood methods could identify these transitions.

7.4 Measurement-based quantum computation

Measurement-based QC [189] is formally equivalent to the normal “circuit” model of gates and measurements but the realization is very different. The computational resource is an entangled two-dimensional “cluster state”: large entangled states of qubits are created off-line before the computation begins (independent of the algorithm to be implemented), and the computation then proceeds by single qubit measurements in a

certain order in different bases. A review of measurement-based QC has recently been published by Briegel *et al.* [190].

High-fidelity measurements are very important to achieve a fault-tolerant computation in this architecture while gate fidelities are important only for the creation of the initial cluster-state; post-selection and entanglement purification [191] can be used to improve the quality of this state. Fast measurement is also important as the speed of the processor is limited by the measurement time. It was this requirement which motivated Stock and James [46] to propose state-dependent ionisation to allow readout of trapped-ion qubits on a nanosecond timescale.

The adaptive maximum likelihood methods presented in this thesis allow the most efficient use of fluorescence data to allow high-fidelity measurements in the shortest possible time (for a given required fidelity). Furthermore, the likelihoods provide an indication of the confidence in the result which could be exploited in the computation.

An architecture that lends itself particularly well to measurement-based QC is that of neutral atoms in an optical lattice. While the camera detection methods already discussed may not necessarily be applicable to measurement during the computation (due to the large readout-time overhead when measuring only a few qubits), they could be used to provide a high-quality map of the lattice occupation to start with.

7.5 Final remarks

In summary, this work demonstrates readout of single and multiple qubits with a fidelity of 99.99%, believed to be the highest reported fidelity to date and above the threshold required for fault-tolerant quantum computation. The temporal maximum likelihood methods employed can mitigate the effect of qubit decay and screen out cosmic rays in the photodetector; these methods are applicable to electrical and optical readout in other atomic and solid-state systems. The camera readout demonstrated provides parallel readout of many qubits. The iterative spatial maximum likelihood method presented can reduce the error due to cross-talk between nearby ions or atoms, even when they are spaced close to the diffraction limit. The methods are also applicable to detection of site-filling in atomic lattices.

Appendix A

Monte-Carlo Simulation Code

An example section of M-C simulation code (Fortran 95) to generate and analyse a “dark” trial (for an ion prepared in $|D\rangle$) is shown below. The trial is generated by picking random numbers to represent the photons detected by a photomultiplier tube in $\langle n_{\text{subbins}} \rangle$ contiguous counting bins of length $\langle t_{\text{sub}} \rangle$; the simulated trial is stored in the variable `SimBin` which is later analysed by a variety of methods. The analyses are *independent* of the known preparation of the ion in the simulation.

```
! ***** GENERATE |D> TRIAL *****
rnum = G05KAF(IGEN, ISEED) ! get a random number
tdecay = -(tau/tsub)*log(1.0D0-rnum) ! find D->B decay time
SimBin = 0 ! this will contain the photon numbers in each (10us) subbin
if (tdecay >= dble(nsubbins)) then ! ion decays after detection period
  do n = 1, nsubbins ! generate an all dark trial
    rnum = G05KAF(IGEN, ISEED)
    ! turn into a Poissonian distributed random number with mean RD*tsub
    ! (cumDprobs contains a cumulative Poisson distribution with mean above)
    do while (cumDprobs(SimBin(n)+1) < rnum)
      SimBin(n) = SimBin(n) + 1;
    enddo
  enddo
else ! there has been a decay during detection
  beforebins = floor(tdecay) ! # dark subbins
  afterbins = nsubbins - beforebins - 1 ! # bright subbins
  if (beforebins /= 0) then ! generate the dark bins
    do n = 1, beforebins
      rnum = G05KAF(IGEN, ISEED)
      do while (cumDprobs(SimBin(n)+1) < rnum)
        SimBin(n) = SimBin(n) + 1;
      enddo
    enddo
  endif
  ! generate sub-bin containing the decay from Poisson dist. with mean lambda
  lambda = RD*tsub + (1.0D0 - (tdecay - dble(beforebins))) * RB*tsub
  call poissondist(DECAYprobs, maxx, lambda) ! get Poisson dist. for decay bin
  DECAYprobs = DECAYprobs / sum(DECAYprobs)
  cumDECAYprobs = 0.0D0
  do j = 1, maxx ! form cumulative distribution
    cumDECAYprobs(j:maxx) = cumDECAYprobs(j:maxx) + DECAYprobs(j)
  enddo
  rnum = G05KAF(IGEN, ISEED) ! get a random number
  do while (cumDECAYprobs(SimBin(beforebins+1)+1) < rnum)
    SimBin(beforebins+1) = SimBin(beforebins+1) + 1;
  enddo
endif
```

```

enddo
if (afterbins /= 0) then ! generate the bright bins (after decay)
  do n = beforebins+2, nsubbins
    rnum = G05KAF(IGEN, ISEED) ! get a random number
    ! ...convert to Poissonian distributed with mean (RD+RB)*tsub
    do while (cumBprobs(SimBin(n)+1) < rnum)
      SimBin(n) = SimBin(n) + 1;
    enddo
  enddo
endif
endif
! ***** ANALYSE TRIAL *****
pB = 1; pDsum = 1; pDafter = 0
StateEST = 1.0D0; pixtot = 0
do n = 1, nsubbins
  pixtot = pixtot + SimBin(n) ! cumulative photon counts in n*tsub
  ! build histogram of D experiments for later analysis with method T:
  Dhists(n, pixtot+1) = Dhists(n, pixtot+1) + 1
  ! update likelihoods pD and pB:
  pB = pB*Bprobs(SimBin(n)+1) ! product of B(n)
  pDafter = (pDafter + pDsum)*Bprobs(SimBin(n)+1)
  pDsum = pDsum*Dprobs(SimBin(n)+1) ! product of D(n)
  pD = (1.0D0 - real(n, kind=r18)*tsub/tau)*pDsum + (tsub/tau)*pDafter
  ! method M analysis:
  if (pB <= pD) then ! identify as "D"
    nDdark(n) = nDdark(n) + 1 ! keep track of # dark identifications
  end if
  ! method A analysis: (change pDsum to pD for method AD)
  if (pB <= pDsum) then ! identify as "D"
    isdark = 1; esterr = pB/(pDsum+pB)
  else ! identify as "B"
    isdark = 0; esterr = pDsum/(pDsum+pB)
  end if
  do iec = 1, Nec ! loop to test range of e_c values
    if (StateEST(iec) > ec(iec)) then
      StateEST(iec) = esterr
      StateID(iec) = isdark
      StateN(iec) = real(n, kind=r18)
    endif
  enddo
  ! keep track of # "D" identifications in whole M-C simulation:
  nDdarkEC(n, :) = nDdarkEC(n, :) + StateID
  ! keep track of average # subbins and Bayesian est_error:
  avND(n, :) = avND(n, :) + StateN
  avErrD(n, :) = avErrD(n, :) + StateEST
enddo

```

Appendix B

Photon counting publication

Following is a copy of a paper published in Physical Review Letters [41] describing the photomultiplier readout discussed in Chapters 3 and 4.

© The American Physical Society

Appendix C

CCD camera publication

Following is a copy of a paper published in Physical Review A [43] describing the EMCCD camera readout discussed in Chapters 5 and 6.

© The American Physical Society

Bibliography

- [1] R. P. Feynman. Simulating physics with computers. *International Journal Of Theoretical Physics*, 21(6-7):467–488, 1982. (cited on page 1).
- [2] D. Deutsch. Quantum computational networks. *Proceedings Of The Royal Society Of London Series A— Mathematical Physical And Engineering Sciences*, 425(1868):73–90, September 1989. (cited on page 1).
- [3] D. Deutsch. Quantum-theory, the Church-Turing principle and the universal quantum computer. *Proceedings Of The Royal Society Of London Series A— Mathematical Physical And Engineering Sciences*, 400(1818):97–117, 1985. (cited on page 1).
- [4] D. Deutsch and R. Jozsa. Rapid solution of problems by quantum computation. *Proceedings Of The Royal Society Of London Series A— Mathematical Physical And Engineering Sciences*, 439(1907):553–558, December 1992. (cited on page 1).
- [5] P. W. Shor. Algorithms for quantum computation— discrete logarithms and factoring. *35th Annual Symposium On Foundations Of Computer Science, Proceedings*, pages 124–134, 1994. (cited on page 2).
- [6] P. W. Shor. Polynomial-time algorithms for prime factorization and discrete logarithms on a quantum computer. *SIAM Journal On Computing*, 26(5):1484–1509, October 1997. (cited on page 2).
- [7] R. L. Rivest, A. Shamir, and L. Adleman. Method for obtaining digital signatures and public-key cryptosystems. *Communications of the ACM*, 21(2):120–126, 1978. (cited on page 2).
- [8] L. K. Grover. Quantum mechanics helps in searching for a needle in a haystack. *Physical Review Letters*, 79(2):325–328, July 1997. (cited on page 2).
- [9] C. H. Bennett and G. Brassard. Quantum cryptography: Public key distribution and coin tossing. In *Proceedings of the IEEE International Conference on Computers, Systems and Signal Processing, Bangalore, India*. IEEE, New York, 1984. (cited on page 2).
- [10] Army Research Office (USA). ARDA quantum computation roadmap. [online] http://qist.lanl.gov/qcomp_map.shtml, 2005. (cited on page 2).
- [11] H. Häffner, C. F. Roos, and R. Blatt. Quantum computing with trapped ions. *Physics Reports— Review Section Of Physics Letters*, 469(4):155–203, December 2008. (cited on pages 2, 5).
- [12] D. P. DiVincenzo. The physical implementation of quantum computation. *Fortschritte Der Physik— Progress Of Physics*, 48(9-11):771–783, 2000. (cited on page 2).

- [13] D. J. Wineland, C. Monroe, W. M. Itano, D. Leibfried, B. E. King, and D. M. Meekhof. Experimental issues in coherent quantum-state manipulation of trapped atomic ions. *Journal Of Research Of The National Institute Of Standards And Technology*, 103(3):259–328, May 1998. (cited on pages 3, 176).
- [14] D. Kielpinski, C. Monroe, and D. J. Wineland. Architecture for a large-scale ion-trap quantum computer. *Nature*, 417(6890):709–711, June 2002. (cited on pages 3, 176).
- [15] M. A. Rowe, A. Ben-Kish, B. Demarco, D. Leibfried, V. Meyer, J. Beall, J. Britton, J. Hughes, W. M. Itano, B. Jelenkovic, C. Langer, T. Rosenband, and D. J. Wineland. Transport of quantum states and separation of ions in a dual RF ion trap. *Quantum Information & Computation*, 2(4):257–271, July 2002. (cited on page 3).
- [16] M. D. Barrett, J. Chiaverini, T. Schaetz, J. Britton, W. M. Itano, J. D. Jost, E. Knill, C. Langer, D. Leibfried, R. Ozeri, and D. J. Wineland. Deterministic quantum teleportation of atomic qubits. *Nature*, 429(6993):737–739, June 2004. (cited on pages 3, 7, 9).
- [17] C. E. Pearson, D. R. Leibbrandt, W. S. Bakr, W. J. Mallard, K. R. Brown, and I. L. Chuang. Experimental investigation of planar ion traps. *Physical Review A*, 73(3):032307, March 2006. (cited on page 3).
- [18] W. K. Hensinger, S. Olmschenk, D. Stick, D. Hucul, M. Yeo, M. Acton, L. Deslauriers, C. Monroe, and J. Rabchuk. T-junction ion trap array for two-dimensional ion shuttling, storage, and manipulation. *Applied Physics Letters*, 88(3):034101, January 2006. (cited on page 3).
- [19] A. Kastler. Quelques suggestions concernant la production optique et la détection optique d’une inégalité de population des niveaux de quantification spatiale des atomes— application à l’expérience de Stern et Gerlach et à la résonance magnétique. *Journal De Physique Et Le Radium*, 11(6):255–265, 1950. (cited on page 3).
- [20] J. Brossel, A. Kastler, and J. Winter. Création optique d’une inégalité de population entre les sous-niveaux Zeeman de l’état fondamental des atomes. *Journal De Physique Et Le Radium*, 13(12):668–668, 1952. (cited on page 3).
- [21] W. B. Hawkins and R. H. Dicke. The polarization of sodium atoms. *Physical Review*, 91(4):1008–1009, 1953. (cited on page 4).
- [22] C. F. Roos, M. Chwalla, K. Kim, M. Riebe, and R. Blatt. ‘Designer atoms’ for quantum metrology. *Nature*, 443(7109):316–319, September 2006. (cited on page 4).
- [23] D. M. Lucas, B. C. Keitch, J. P. Home, G. Imreh, M. J. McDonnell, D. N. Stacey, D. J. Szwer, and A. M. Steane. A long-lived memory qubit on a low-decoherence quantum bus. *arXiv:0710.4421v1 [quant-ph]*, 2007. (cited on pages 4, 23, 51).
- [24] C. Langer, R. Ozeri, J. D. Jost, J. Chiaverini, B. DeMarco, A. Ben-Kish, R. B. Blakestad, J. Britton, D. B. Hume, W. M. Itano, D. Leibfried, R. Reichle, T. Rosenband, T. Schaetz, P. O. Schmidt, and D. J. Wineland. Long-lived qubit memory using atomic ions. *Physical Review Letters*, 95(6):060502, August 2005. (cited on pages 4, 51).
- [25] R. Blatt and D. Wineland. Entangled states of trapped atomic ions. *Nature*, 453(7198):1008–1015, June 2008. (cited on page 4).

- [26] J. I. Cirac and P. Zoller. Quantum computations with cold trapped ions. *Physical Review Letters*, 74(20):4091–4, May 1995. (cited on page 5).
- [27] K. Mølmer and A. Sørensen. Multiparticle entanglement of hot trapped ions. *Physical Review Letters*, 82(9):1835–1838, March 1999. (cited on page 5).
- [28] D. Leibfried, B. DeMarco, V. Meyer, D. Lucas, M. Barrett, J. Britton, W. M. Itano, B. Jelenkovic, C. Langer, T. Rosenband, and D. J. Wineland. Experimental demonstration of a robust, high-fidelity geometric two ion-qubit phase gate. *Nature*, 422(6930):412–415, March 2003. (cited on page 5).
- [29] J. Benhelm, G. Kirchmair, C. F. Roos, and R. Blatt. Towards fault-tolerant quantum computing with trapped ions. *Nature Physics*, 4(6):463–466, June 2008. (cited on pages 5, 6, 23, 49).
- [30] J. P. Home, M. J. McDonnell, D. M. Lucas, G. Imreh, B. C. Keitch, D. J. Szwer, N. R. Thomas, S. C. Webster, D. N. Stacey, and A. M. Steane. Deterministic entanglement and tomography of ion-spin qubits. *New Journal Of Physics*, 8:188, September 2006. (cited on page 5).
- [31] C. Ospelkaus, C. E. Langer, J. M. Amini, K. R. Brown, D. Leibfried, and D. J. Wineland. Trapped-ion quantum logic gates based on oscillating magnetic fields. *Physical Review Letters*, 101(9):090502, August 2008. (cited on pages 5, 6).
- [32] F. Mintert and C. Wunderlich. Ion-trap quantum logic using long-wavelength radiation. *Physical Review Letters*, 87(25):257904, December 2001. (cited on pages 5, 6).
- [33] J. Chiaverini and W. E. Lybarger. Laserless trapped-ion quantum simulations without spontaneous scattering using microtrap arrays. *Physical Review A*, 77(2):022324, February 2008. (cited on page 5).
- [34] M. A. Rowe, D. Kielpinski, V. Meyer, C. A. Sackett, W. M. Itano, C. Monroe, and D. J. Wineland. Experimental violation of a Bell’s inequality with efficient detection. *Nature*, 409(6822):791–794, February 2001. (cited on page 5).
- [35] R. Reichle, D. Leibfried, E. Knill, J. Britton, R. B. Blakestad, J. D. Jost, C. Langer, R. Ozeri, S. Seidelin, and D. J. Wineland. Experimental purification of two-atom entanglement. *Nature*, 443(7113):838–841, October 2006. (cited on pages 5, 6, 23).
- [36] P. Staunum and M. Drewsen. Trapped-ion quantum logic utilizing position-dependent ac Stark shifts. *Physical Review A*, 66(4):040302–1, October 2002. (cited on page 5).
- [37] P. C. Haljan, P. J. Lee, K.-A. Brickman, M. Acton, L. Deslauriers, and C. Monroe. Entanglement of trapped-ion clock states. *Physical Review A*, 72(6):062316, December 2005. (cited on pages 5, 6).
- [38] C. Monroe, C. A. Sackett, D. Kielpinski, B. E. King, C. Langer, V. Meyer, C. J. Myatt, M. Rowe, Q. A. Turchette, W. M. Itano, and D. J. Wineland. Scalable entanglement of trapped ions. In E. Arimondo, P. De Natale, and M. Inguscio, editors, *Atomic Physics 17, Proceedings of the 17th International Conference*, pages 173–186, AIP Conf. Proc. 551, Melville, 2001. (cited on pages 6, 23, 57).
- [39] M. Acton, K.-A. Brickman, P. C. Haljan, P. J. Lee, L. Deslauriers, and C. Monroe. Near-perfect simultaneous measurement of a qubit register. *Quantum Information & Computation*, 6(6):465–482, September 2006. (cited on pages 6, 7, 23, 171, 180, 184).

- [40] M. R. Dietrich, N. Kurz, T. Noel, G. Shu, and B. B. Blinov. Hyperfine and optical barium ion qubits. *Physical Review A*, 81(5):052328, May 2010. (cited on pages 6, 23, 180).
- [41] A. H. Myerson, D. J. Szwer, S. C. Webster, D. T. C. Allcock, M. J. Curtis, G. Imreh, J. Sherman, D. N. Stacey, A. M. Steane, and D. M. Lucas. High-fidelity readout of trapped-ion qubits. *Physical Review Letters*, 100:200502, May 2008. (cited on pages 6, 12, 23, 25, 51, 185, 191).
- [42] D. B. Hume, T. Rosenband, and D. J. Wineland. High-fidelity adaptive qubit detection through repetitive quantum nondemolition measurements. *Physical Review Letters*, 99(12):120502, September 2007. (cited on pages 6, 23, 61, 86, 102, 106).
- [43] A. H. Burrell, D. J. Szwer, S. C. Webster, and D. M. Lucas. Scalable simultaneous multiqubit readout with 99.99% single-shot fidelity. *Physical Review A*, 81(4):040302, April 2010. (cited on pages 7, 25, 140, 197).
- [44] C. F. Roos, M. Riebe, H. Häffner, W. Hänsel, J. Benhelm, G. P. T. Lancaster, C. Becher, F. Schmidt-Kaler, and R. Blatt. Control and measurement of three-qubit entangled states. *Science*, 304(5676):1478–1480, June 2004. (cited on page 7).
- [45] M. Riebe, H. Häffner, C. F. Roos, W. Hänsel, J. Benhelm, G. P. T. Lancaster, T. W. Körber, C. Becher, F. Schmidt-Kaler, D. F. V. James, and R. Blatt. Deterministic quantum teleportation with atoms. *Nature*, 429(6993):734–737, June 2004. (cited on pages 7, 9).
- [46] R. Stock and D. F. V. James. Scalable, high-speed measurement-based quantum computer using trapped ions. *Physical Review Letters*, 102(17):170501, May 2009. (cited on pages 7, 187).
- [47] W. Paul and M. Raether. Das elektrische massenfilter. *Zeitschrift Für Physik*, 140(3):262–273, 1955. (cited on page 7).
- [48] L.-M. Duan and C. Monroe. Quantum networks with trapped ions. (*to appear in:*) *Reviews of Modern Physics*, 2010. (cited on page 7).
- [49] A. M. Steane. How to build a 300 bit, 1 giga-operation quantum computer. *Quantum Information & Computation*, 7(3):171–183, March 2007. (cited on pages 8, 25, 102, 111, 175).
- [50] E. Knill. Quantum computing with realistically noisy devices. *Nature*, 434(7029):39–44, March 2005. (cited on page 8).
- [51] D. Hanneke, J. P. Home, J. D. Jost, J. M. Amini, D. Leibfried, and D. J. Wineland. Realization of a programmable two-qubit quantum processor. *Nature Physics*, 6(1):13–16, January 2010. (cited on page 8).
- [52] J. D. Jost, J. P. Home, J. M. Amini, D. Hanneke, R. Ozeri, C. Langer, J. J. Bollinger, D. Leibfried, and D. J. Wineland. Entangled mechanical oscillators. *Nature*, 459(7247):683–U84, June 2009. (cited on page 9).
- [53] J. P. Home, D. Hanneke, J. D. Jost, J. M. Amini, D. Leibfried, and D. J. Wineland. Complete methods set for scalable ion trap quantum information processing. *Science*, 325(5945):1227–1230, September 2009. (cited on page 9).

- [54] S. Gulde, M. Riebe, G. P. T. Lancaster, C. Becher, J. Eschner, H. Häffner, F. Schmidt-Kaler, I. L. Chuang, and R. Blatt. Implementation of the Deutsch-Jozsa algorithm on an ion-trap quantum computer. *Nature*, 421(6918):48–50, January 2003. (cited on page 9).
- [55] J. Chiaverini, J. Britton, D. Leibfried, E. Knill, M. D. Barrett, R. B. Blakestad, W. P. Itano, J. D. Jost, C. Langer, R. Ozeri, T. Schaetz, and D. J. Wineland. Implementation of the semiclassical quantum Fourier transform in a scalable system. *Science*, 308(5724):997–1000, May 2005. (cited on page 9).
- [56] J. Chiaverini, D. Leibfried, T. Schaetz, M. D. Barrett, R. B. Blakestad, J. Britton, W. M. Itano, J. D. Jost, E. Knill, C. Langer, R. Ozeri, and D. J. Wineland. Realization of quantum error correction. *Nature*, 432(7017):602–605, December 2004. (cited on page 9).
- [57] K.-A. Brickman, P. C. Haljan, P. J. Lee, M. Acton, L. Deslauriers, and C. Monroe. Implementation of Grover’s quantum search algorithm in a scalable system. *Physical Review A*, 72(5):050306, November 2005. (cited on page 9).
- [58] A. Friedenauer, H. Schmitz, J. T. Glueckert, D. Porras, and T. Schaetz. Simulating a quantum magnet with trapped ions. *Nature Physics*, 4(10):757–761, October 2008. (cited on page 9).
- [59] H. Häffner, W. Hänsel, C. F. Roos, J. Benhelm, D. Chek-al kar, M. Chwalla, T. Körber, U. D. Rapol, M. Riebe, P. O. Schmidt, C. Becher, O. Gühne, W. Dür, and R. Blatt. Scalable multiparticle entanglement of trapped ions. *Nature*, 438(7068):643–646, December 2005. (cited on page 9).
- [60] P. Maunz, S. Olmschenk, D. Hayes, D. N. Matsukevich, L. M. Duan, and C. Monroe. Heralded quantum gate between remote quantum memories. *Physical Review Letters*, 102(25):250502, June 2009. (cited on page 9).
- [61] J. Clarke and F. K. Wilhelm. Superconducting quantum bits. *Nature*, 453(7198):1031–1042, June 2008. (cited on pages 10, 13, 15).
- [62] M. J. Curtis. *Measurement-Selected Ensembles in Trapped-Ion Qubits*. PhD thesis, University of Oxford, 2010. (cited on pages 10, 31).
- [63] A. Lengwenus, J. Kruse, M. Volk, W. Ertmer, and G. Birkel. Coherent manipulation of atomic qubits in optical micropotentials. *Applied Physics B— Lasers And Optics*, 86(3):377–383, February 2007. (cited on page 11).
- [64] S. Kuhr, W. Alt, D. Schrader, I. Dotsenko, Y. Miroshnychenko, A. Rauschenbeutel, and D. Meschede. Analysis of dephasing mechanisms in a standing-wave dipole trap. *Physical Review A*, 72(2):023406, August 2005. (cited on pages 11, 23).
- [65] M. P. A. Jones, J. Beugnon, A. Gaetan, J. Zhang, G. Messin, A. Browaeys, and P. Grangier. Fast quantum state control of a single trapped neutral atom. *Physical Review A*, 75(4):040301, April 2007. (cited on pages 11, 23).
- [66] D. Schrader, I. Dotsenko, M. Khudaverdyan, Y. Miroshnychenko, A. Rauschenbeutel, and D. Meschede. Neutral atom quantum register. *Physical Review Letters*, 93(15):150501, October 2004. (cited on pages 11, 23).
- [67] M. Karski, L. Forster, J. M. Choi, W. Alt, A. Widera, and D. Meschede. Nearest-neighbor detection of atoms in a 1D optical lattice by fluorescence imaging. *Physical Review Letters*, 102(5):053001, February 2009. (cited on pages 11, 172).

- [68] K. D. Nelson, X. Li, and D. S. Weiss. Imaging single atoms in a three-dimensional array. *Nature Physics*, 3(8):556–560, August 2007. (cited on pages 11, 172).
- [69] W. S. Bakr, J. I. Gillen, A. Peng, S. Folling, and M. Greiner. A quantum gas microscope for detecting single atoms in a Hubbard-regime optical lattice. *Nature*, 462(7269):74–U80, November 2009. (cited on pages 11, 172).
- [70] F. Henkel, M. Krug, J. Hofmann, W. Rosenfeld, M. Weber, and H. Weinfurter. Highly-efficient state-selective sub-microsecond photoionization detection of single atoms. *arXiv:1008.1910v1 [quant-ph]*, 2010. (cited on pages 11, 23).
- [71] E. M. Purcell. Spontaneous emission probabilities at radio frequencies. *Physical Review*, 69(11-1):681, 1946. (cited on page 12).
- [72] J. Bochmann, M. Mücke, C. Guhl, S. Ritter, G. Rempe, and D.L. Moehring. Lossless state detection of single neutral atoms. *Physical Review Letters*, 104:203601, 2010. (cited on pages 12, 23).
- [73] R. Gehr, J. Volz, G. Dubois, T. Steinmetz, Y. Colombe, B. L. Lev, R. Long, J. Estève, and J. Reichel. Cavity-based single atom preparation and high-fidelity hyperfine state readout. *arXiv:1002.4424v1 [quant-ph]*, 2010. (cited on pages 12, 23, 185).
- [74] S. Gleyzes, S. Kuhr, C. Guerlin, J. Bernu, S. Deleglise, U. B. Hoff, M. Brune, J. M. Raimond, and S. Haroche. Quantum jumps of light recording the birth and death of a photon in a cavity. *Nature*, 446(7133):297–300, March 2007. (cited on pages 12, 23).
- [75] C. Guerlin, J. Bernu, S. Deleglise, C. Sayrin, S. Gleyzes, S. Kuhr, M. Brune, J. M. Raimond, and S. Haroche. Progressive field-state collapse and quantum non-demolition photon counting. *Nature*, 448(7156):889–U1, August 2007. (cited on page 12).
- [76] J. Gambetta, W. A. Braff, A. Wallraff, S. M. Girvin, and R. J. Schoelkopf. Protocols for optimal readout of qubits using a continuous quantum nondemolition measurement. *Physical Review A — Atomic, Molecular, and Optical Physics*, 76(1):012325–, 2007. (cited on pages 13, 57, 185).
- [77] J. M. Martinis, S. Nam, J. Aumentado, and C. Urbina. Rabi oscillations in a large Josephson-junction qubit. *Physical Review Letters*, 89(11):117901, September 2002. (cited on pages 13, 24).
- [78] M. Ansmann, H. Wang, R. C. Bialczak, M. Hofheinz, E. Lucero, M. Neeley, A. D. O’Connell, D. Sank, M. Weides, J. Wenner, A. N. Cleland, and J. M. Martinis. Violation of Bell’s inequality in Josephson phase qubits. *Nature*, 461(7263):504–506, September 2009. (cited on pages 13, 14, 16, 24).
- [79] N. Katz, M. Ansmann, R. C. Bialczak, E. Lucero, R. McDermott, M. Neeley, M. Steffen, E. M. Weig, A. N. Cleland, J. M. Martinis, and A. N. Korotkov. Coherent state evolution in a superconducting qubit from partial-collapse measurement. *Science*, 312(5779):1498–1500, June 2006. (cited on page 14).
- [80] A. Lupascu, T. Saito, S. amd Picot, P. C. de Groot, C. J. P. M. Harmans, and J. E. Mooij. Quantum non-demolition measurement of a superconducting two-level system. *Nature Physics*, 3:119–125, Feb 2007. (cited on pages 14, 16, 24).

- [81] D. A. Bennett, L. Longobardi, V. Patel, W. Chen, and J. E. Lukens. RF-SQUID qubit readout using a fast flux pulse. *Superconductor Science & Technology*, 20(11):S445–S449, November 2007. (cited on pages 14, 24).
- [82] Y. Nakamura, Y. A. Pashkin, and J. S. Tsai. Coherent control of macroscopic quantum states in a single-Cooper-pair box. *Nature*, 398(6730):786–788, April 1999. (cited on page 14).
- [83] J. Koch, T. M. Yu, J. Gambetta, A. A. Houck, D. I. Schuster, J. Majer, A. Blais, M. H. Devoret, S. M. Girvin, and R. J. Schoelkopf. Charge-insensitive qubit design derived from the Cooper pair box. *Physical Review A*, 76(4):042319, October 2007. (cited on page 14).
- [84] D. Vion, A. Aassime, A. Cottet, P. Joyez, H. Pothier, C. Urbina, D. Esteve, and M. H. Devoret. Manipulating the quantum state of an electrical circuit. *Science*, 296(5569):886–889, May 2002. (cited on page 14).
- [85] S. M. Girvin, M. H. Devoret, and R. J. Schoelkopf. Circuit QED and engineering charge-based superconducting qubits. *Physica Scripta*, T137:014012, December 2009. (cited on page 15).
- [86] A. Wallraff, D. I. Schuster, A. Blais, L. Frunzio, J. Majer, M. H. Devoret, S. M. Girvin, and R. J. Schoelkopf. Approaching unit visibility for control of a superconducting qubit with dispersive readout. *Physical Review Letters*, 95(6):060501, August 2005. (cited on pages 15, 24, 186).
- [87] A. Aassime, G. Johansson, G. Wendin, R. J. Schoelkopf, and P. Delsing. Radio-frequency single-electron transistor as readout device for qubits: Charge sensitivity and backaction. *Physical Review Letters*, 86(15):3376–3379, April 2001. (cited on pages 15, 186).
- [88] K. W. Lehnert, K. Bladh, L. F. Spietz, D. Gunnarsson, D. I. Schuster, P. Delsing, and R. J. Schoelkopf. Measurement of the excited-state lifetime of a microelectronic circuit. *Physical Review Letters*, 90(2):027002, January 2003. (cited on pages 15, 186).
- [89] O. Astafiev, Y. A. Pashkin, T. Yamamoto, Y. Nakamura, and J. S. Tsai. Single-shot measurement of the Josephson charge qubit. *Physical Review B*, 69(18):180507, May 2004. (cited on pages 15, 24).
- [90] J. Lisenfeld, A. Lukashenko, M. Ansmann, J. M. Martinis, and A. V. Ustinov. Temperature dependence of coherent oscillations in Josephson phase qubits. *Physical Review Letters*, 99(17):170504, October 2007. (cited on page 15).
- [91] I. Siddiqi, R. Vijay, F. Pierre, C. M. Wilson, M. Metcalfe, C. Rigetti, L. Frunzio, and M. H. Devoret. RF-driven Josephson bifurcation amplifier for quantum measurement. *Physical Review Letters*, 93(20):207002, November 2004. (cited on page 15).
- [92] I. Siddiqi, R. Vijay, M. Metcalfe, E. Boaknin, L. Frunzio, R. J. Schoelkopf, and M. H. Devoret. Dispersive measurements of superconducting qubit coherence with a fast latching readout. *Physical Review B*, 73(5):054510, February 2006. (cited on page 15).
- [93] N. Boulant, G. Ithier, P. Meeson, F. Nguyen, D. Vion, D. Esteve, I. Siddiqi, R. Vijay, C. Rigetti, and F. Pierre. Quantum nondemolition readout using a

- Josephson bifurcation amplifier. *Physical Review B*, 76(1):014525, July 2007. (cited on pages 15, 24, 186).
- [94] F. Mallet, F. R. Ong, A. Palacios-Laloy, F. Nguyen, P. Bertet, D. Vion, and D. Esteve. Single-shot qubit readout in circuit quantum electrodynamics. *Nature Physics*, 5(11):791–795, November 2009. (cited on pages 15, 24, 186).
 - [95] J. Majer, J. M. Chow, J. M. Gambetta, J. Koch, B. R. Johnson, J. A. Schreier, L. Frunzio, D. I. Schuster, A. A. Houck, A. Wallraff, A. Blais, M. H. Devoret, S. M. Girvin, and R. J. Schoelkopf. Coupling superconducting qubits via a cavity bus. *Nature*, 449(7161):443–447, September 2007. (cited on page 16).
 - [96] B. R. Johnson, M. D. Reed, A. A. Houck, D. I. Schuster, L. S. Bishop, E. Ginossar, J. M. Gambetta, L. DiCarlo, L. Frunzio, S. M. Girvin, and R. J. Schoelkopf. Quantum non-demolition detection of single microwave photons in a circuit. *arXiv:1003.2734v1 [cond-mat.mes-hall]*, 2010. (cited on page 16).
 - [97] R. Hanson and D. D. Awschalom. Coherent manipulation of single spins in semiconductors. *Nature*, 453(7198):1043–1049, June 2008. (cited on pages 17, 19).
 - [98] R. Hanson, L. P. Kouwenhoven, J. R. Petta, S. Tarucha, and L. M. K. Vandersypen. Spins in few-electron quantum dots. *Reviews Of Modern Physics*, 79(4):1217–1265, October 2007. (cited on pages 17, 18).
 - [99] R. J. Young, S. J. Dewhurst, R. M. Stevenson, P. Atkinson, A. J. Bennett, M. B. Ward, K. Cooper, D. A. Ritchie, and A. J. Shields. Single electron-spin memory with a semiconductor quantum dot. *New Journal Of Physics*, 9:365, October 2007. (cited on page 17).
 - [100] M. Atatüre, J. Dreiser, A. Badolato, and A. Imamoglu. Observation of Faraday rotation from a single confined spin. *Nature Physics*, 3(2):101–105, February 2007. (cited on page 17).
 - [101] M. H. Mikkelsen, J. Berezovsky, N. G. Stoltz, L. A. Coldren, and D. D. Awschalom. Optically detected coherent spin dynamics of a single electron in a quantum dot. *Nature Physics*, 3(11):770–773, November 2007. (cited on page 17).
 - [102] J. M. Elzerman, R. Hanson, L. H. W. van Beveren, B. Witkamp, L. M. K. Vandersypen, and L. P. Kouwenhoven. Single-shot read-out of an individual electron spin in a quantum dot. *Nature*, 430(6998):431–435, July 2004. (cited on pages 17, 24).
 - [103] R. Hanson, L. H. W. van Beveren, I. T. Vink, J. M. Elzerman, W. J. M. Naber, F. H. L. Koppens, L. P. Kouwenhoven, and L. M. K. Vandersypen. Single-shot readout of electron spin states in a quantum dot using spin-dependent tunnel rates. *Physical Review Letters*, 94(19):196802, May 2005. (cited on pages 17, 24).
 - [104] T. Meunier, I. T. Vink, L. H. W. van Beveren, F. H. L. Koppens, H. P. Tranitz, W. Wegscheider, L. P. Kouwenhoven, and L. M. K. Vandersypen. Nondestructive measurement of electron spins in a quantum dot. *Physical Review B*, 74(19):195303, November 2006. (cited on pages 18, 24).
 - [105] C. Barthel, D. J. Reilly, C. M. Marcus, M. P. Hanson, and A. C. Gossard. Rapid single-shot measurement of a singlet-triplet qubit. *Physical Review Letters*, 103(16):160503, October 2009. (cited on pages 18, 24, 186).

- [106] A. Morello, J. J. Pla, F. A. Zwanenburg, K. W. Chan, H. Huebl, M. Mottonen, C. D. Nugroho, C. Yang, J. A. van Donkelaar, A. Alves, D. N. Jamieson, C. C. Escott, L. C. L. Hollenberg, R. G. Clark, and A. S. Dzurak. Single-shot readout of an electron spin in silicon. *arXiv:1003.2679v1 [cond-mat.mes-hall]*, 2010. (cited on pages 19, 24, 186).
- [107] J. Wrachtrup and F. Jelezko. Processing quantum information in diamond. *Journal Of Physics— Condensed Matter*, 18(21):S807–S824, May 2006. (cited on pages 19, 24, 186).
- [108] M. Steiner, P. Neumann, J. Beck, F. Jelezko, and J. Wrachtrup. Universal enhancement of the optical readout fidelity of single electron spins at nitrogen-vacancy centers in diamond. *Physical Review B*, 81(3):035205, January 2010. (cited on page 19).
- [109] L. Jiang, J. S. Hodges, J. R. Maze, P. Maurer, J. M. Taylor, D. G. Cory, P. R. Hemmer, R. L. Walsworth, A. Yacoby, A. S. Zibrov, and M. D. Lukin. Repetitive readout of a single electronic spin via quantum logic with nuclear spin ancillae. *Science*, 326(5950):267–272, October 2009. (cited on page 19).
- [110] M. V. G. Dutt, L. Childress, L. Jiang, E. Togan, J. Maze, F. Jelezko, A. S. Zibrov, P. R. Hemmer, and M. D. Lukin. Quantum register based on individual electronic and nuclear spin qubits in diamond. *Science*, 316(5829):1312–1316, June 2007. (cited on page 19).
- [111] E. Fraval, M. J. Sellars, and J. J. Longdell. Method of extending hyperfine coherence times in $\text{Pr}^{3+}:\text{Y}_2\text{SiO}_5$. *Physical Review Letters*, 92(7):077601, February 2004. (cited on page 20).
- [112] E. Fraval, M. J. Sellars, and J. J. Longdell. Dynamic decoherence control of a solid-state nuclear-quadrupole qubit. *Physical Review Letters*, 95(3):030506, July 2005. (cited on page 20).
- [113] S. E. Beavan, E. Fraval, M. J. Sellars, and J. J. Longdell. Demonstration of the reduction of decoherent errors in a solid-state qubit using dynamic decoupling techniques. *Physical Review A*, 80(3):032308, September 2009. (cited on page 20).
- [114] J. H. Wesenberg, K. Mølmer, L. Rippe, and S. Kröll. Scalable designs for quantum computing with rare-earth-ion-doped crystals. *Physical Review A*, 75(1):012304, January 2007. (cited on page 20).
- [115] J. Mlynek, N. C. Wong, R. G. Devoe, E. S. Kintzer, and R. G. Brewer. Raman heterodyne-detection of nuclear magnetic-resonance. *Physical Review Letters*, 50(13):993–996, 1983. (cited on page 20).
- [116] J. J. Longdell and M. J. Sellars. Experimental demonstration of quantum-state tomography and qubit-qubit interactions for rare-earth-metal-ion-based solid-state qubits. *Physical Review A*, 69(3):032307, March 2004. (cited on page 20).
- [117] P. Kok, W. J. Munro, K. Nemoto, T. C. Ralph, J. P. Dowling, and G. J. Milburn. Linear optical quantum computing with photonic qubits. *Reviews Of Modern Physics*, 79(1):135–174, January 2007. (cited on pages 20, 21).
- [118] T. D. Ladd, F. Jelezko, R. Laflamme, Y. Nakamura, C. Monroe, and J. L. O’Brien. Quantum computers. *Nature*, 464(7285):45–53, March 2010. (cited on page 21).

- [119] S. Takeuchi, J. Kim, Y. Yamamoto, and H. H. Hogue. Development of a high-quantum-efficiency single-photon counting system. *Applied Physics Letters*, 74(8):1063–1065, February 1999. (cited on page 21).
- [120] G. J. Pryde, J. L. O’Brien, A. G. White, S. D. Bartlett, and T. C. Ralph. Measuring a photonic qubit without destroying it. *Physical Review Letters*, 92(19):190402, May 2004. (cited on page 21).
- [121] J. A. Jones. NMR quantum computation: A critical evaluation. *Fortschritte Der Physik— Progress Of Physics*, 48(9-11):909–924, 2000. (cited on page 21).
- [122] L. M. K. Vandersypen, C. S. Yannoni, and I. L. Chuang. *Encyclopedia of Nuclear Magnetic Resonance*, volume 9: “Advances in NMR”, chapter “Liquid State NMR Quantum Computing”, pages 687–697. John Wiley & Sons Ltd., 2002. (cited on page 21).
- [123] J. A. Jones and M. Mosca. Approximate quantum counting on an NMR ensemble quantum computer. *Physical Review Letters*, 83(5):1050–1053, 1999. (cited on page 22).
- [124] N. A. Gershenfeld and I. L. Chuang. Bulk spin-resonance quantum computation. *Science*, 275(5298):350–356, 1997. (cited on page 22).
- [125] S. Olmschenk, K. C. Younge, D. L. Moehring, D. N. Matsukevich, P. Maunz, and C. Monroe. Manipulation and detection of a trapped Yb^+ hyperfine qubit. *Physical Review A*, 76(5):052314, November 2007. (cited on pages 23, 181, 184).
- [126] A. H. Myerson. High-precision qubit readout and microfabricated ion traps for quantum information processing. First year report, University of Oxford, 2007. (cited on pages 22, 42).
- [127] R. C. Thompson, S. Donnellan, D. R. Crick, and D. M. Segal. Applications of laser cooled ions in a Penning trap. *Journal Of Physics B— Atomic Molecular And Optical Physics*, 42(15):154003, August 2009. (cited on page 28).
- [128] P. K. Ghosh. *Ion Traps*. International Series of Monographs on Physics. Oxford University Press, 1995. (cited on page 28).
- [129] C. J. S. Donald. *Development of an Ion Trap Quantum Information Processor*. PhD thesis, University of Oxford, 2000. (cited on pages 29, 36, 37, 39, 84).
- [130] L. Deslauriers, S. Olmschenk, D. Stick, W. K. Hensinger, J. Sterk, and C. Monroe. Scaling and suppression of anomalous heating in ion traps. *Physical Review Letters*, 97(10):103007, September 2006. (cited on page 30).
- [131] D. J. Berkeland and M. G. Boshier. Destabilization of dark states and optical spectroscopy in Zeeman-degenerate atomic systems. *Physical Review A*, 65(3):033413, March 2002. (cited on pages 30, 38, 84).
- [132] B. Keitch. *A Quantum Memory Qubit in Calcium-43*. PhD thesis, University of Oxford, 2007. (cited on pages 30, 42).
- [133] D. T. C. Allcock, J. A. Sherman, D. N. Stacey, A. H. Burrell, M. J. Curtis, G. Imreh, N. M. Linke, D. J. Szwer, S. C. Webster, A. M. Steane, and D. M. Lucas. Implementation of a symmetric surface electrode ion trap with field compensation using a modulated Raman effect. *New Journal Of Physics*, 12:053026, 2010. (cited on pages 30, 167, 168).

- [134] D. M. Lucas, A. Ramos, J. P. Home, M. J. McDonnell, S. Nakayama, J.-P. Stacey, S. C. Webster, D. N. Stacey, and A. M. Steane. Isotope-selective photoionization for calcium ion trapping. *Physical Review A*, 69(1):012711, January 2004. (cited on pages 30, 33).
- [135] J. Benhelm, G. Kirchmair, C. F. Roos, and R. Blatt. Experimental quantum-information processing with $^{43}\text{Ca}^+$ ions. *Physical Review A*, 77(6), 2008. (cited on pages 32, 51).
- [136] C. Wunderlich, T. Hannemann, T. Körber, H. Häffner, C. Roos, W. Hänsel, R. Blatt, and F. Schmidt-Kaler. Robust state preparation of a single trapped ion by adiabatic passage. *Journal Of Modern Optics*, 54(11):1541–1549, 2007. (cited on pages 32, 51, 183).
- [137] D. J. Szwer. *High Fidelity Readout and Protection of a $^{43}\text{Ca}^+$ Trapped Ion Qubit*. PhD thesis, University of Oxford, 2009. (cited on pages 32, 33, 34, 35, 37, 38, 39, 42, 51, 183, 184).
- [138] P. A. Barton, C. J. S. Donald, D. M. Lucas, D. A. Stevens, A. M. Steane, and D. N. Stacey. Measurement of the lifetime of the $3d^2D_{5/2}$ state in $^{40}\text{Ca}^+$. *Physical Review A*, 62(3):032503, September 2000. (cited on pages 34, 48, 54, 90, 92, 93, 94).
- [139] Hamamatsu. *Photomultiplier Tubes: Basics and Applications*, third edition, 2006. [online] http://sales.hamamatsu.com/assets/applications/ETD/pmt_handbook_complete.pdf. (cited on page 38).
- [140] K. Schätzel, R. Kalström, B. Stampa, and J. Ahrens. Correction of detection-system dead-time effects on photon-correlation functions. *Journal Of The Optical Society Of America B— Optical Physics*, 6(5):937–947, May 1989. (cited on page 44).
- [141] H. Dehmelt. Proposed $10^{14}\delta\nu > \nu$ laser fluorescence spectroscopy on Tl^+ monocation oscillator II. *Bulletin Of The American Physical Society*, 20(1):60–60, 1975. (cited on page 48).
- [142] T. Sauter, W. Neuhauser, R. Blatt, and P. E. Toschek. Observation of quantum jumps. *Physical Review Letters*, 57(14):1696–1698, October 1986. (cited on page 48).
- [143] W. Nagourney, J. Sandberg, and H. Dehmelt. Shelved optical electron amplifier—observation of quantum jumps. *Physical Review Letters*, 56(26):2797–2799, June 1986. (cited on page 48).
- [144] J. C. Bergquist, R. G. Hulet, W. M. Itano, and D. J. Wineland. Observation of quantum jumps in a single atom. *Physical Review Letters*, 57(14):1699–1702, October 1986. (cited on page 48).
- [145] S. C. Webster. *Raman Sideband Cooling and Coherent Manipulation of Trapped Ions*. PhD thesis, University of Oxford, 2005. (cited on pages 49, 51).
- [146] M. J. McDonnell. *Two-Photon Readout Methods for an Ion Trap Quantum Information Processor*. PhD thesis, University of Oxford, 2003. (cited on page 49).
- [147] D. J. Szwer. A $^{43}\text{Ca}^+$ trapped-ion qubit. First year report, University of Oxford, 2006. (cited on page 51).
- [148] C. E. Langer. *High-fidelity quantum information processing with trapped ions*. PhD thesis, University of Colorado, Boulder, 2006. (cited on pages 55, 57, 69, 71, 183).

- [149] K. F. Riley, M. P. Hobson, and S. J. Bence. *Mathematical Methods for Physics and Engineering*. Cambridge University Press, 2nd edition, 2002. (cited on page 56).
- [150] M. C. Teich, R. A. Campos, and B. E. A. Saleh. Statistical properties of cosmic-ray showers at ground-level determined from photomultiplier-tube background registrations. *Physical Review D*, 36(9):2649–2665, November 1987. (cited on page 80).
- [151] A. T. Young. Cosmic ray induced dark current in photomultipliers. *The Review of Scientific Instruments*, 37(11):1472–1481, Nov 1966. (cited on page 80).
- [152] D. N. Stacey. Saturation of an electric dipole transition— alternative version. Technical report, University of Oxford, June 1999. (cited on page 84).
- [153] G. Shu, N. Kurz, M. R. Dietrich, and B. B. Blinov. Efficient fluorescence collection from trapped ions with an integrated spherical mirror. *Physical Review A*, 81(4):042321, 2010. (cited on pages 86, 175).
- [154] M. D. Barrett, B. DeMarco, T. Schaetz, V. Meyer, D. Leibfried, J. Britton, J. Chiaverini, W. M. Itano, B. Jelenkovic, J. D. Jost, C. Langer, T. Rosenband, and D. J. Wineland. Sympathetic cooling of $^9\text{Be}^+$ and $^{24}\text{Mg}^+$ for quantum logic. *Physical Review A*, 68(4):042302, October 2003. (cited on page 91).
- [155] Max Born. *Atomic Physics*. Blackie & son limited, 8th edition, 1969. (cited on page 92).
- [156] NIST. Atomic spectra database version 3. [online] <http://physics.nist.gov/PhysRefData/ASD/index.html>, November 2009. (cited on pages 92, 94).
- [157] C. Froese Fischer. MCHF, ab initio. [online] http://www.vuse.vanderbilt.edu/~cff/mchf_collection/, 6th August 2002. (cited on pages 93, 94).
- [158] M. Roberts, P. Taylor, G. P. Barwood, W. R. C. Rowley, and P. Gill. Observation of the $^2\text{S}_{1/2}$ – $^2\text{F}_{7/2}$ electric octupole transition in a single $^{171}\text{Yb}^+$ ion. *Physical Review A*, 62(2):020501, August 2000. (cited on page 93).
- [159] K. Hosaka, S. A. Webster, P. J. Blythe, A. Stannard, D. Beaton, H. S. Margolis, S. N. Lea, and P. Gill. An optical frequency standard based on the electric octupole transition in $^{171}\text{Yb}^+$. *IEEE Transactions On Instrumentation And Measurement*, 54(2):759–762, April 2005. (cited on page 93).
- [160] D. E. Osterbrock. Transition probabilities of forbidden lines. *Astrophysical Journal*, 114(3):469–472, 1951. (cited on page 94).
- [161] D. R. Crick, S. Donnellan, D. M. Segal, and R. C. Thompson. Magnetically induced electron shelving in a trapped Ca^+ ion. *Physical Review A*, 81(5):052503, May 2010. (cited on page 94).
- [162] P. Jerram, P. Pool, R. Bell, D. Burt, S. Bowring, S. Spencer, M. Hazelwood, I. Moody, N. Catlett, and P. Heyes. The LLLCCD: Low light imaging without the need for an intensifier. *Sensors And Camera Systems For Scientific, Industrial, And Digital Photography Applications Ii*, 4306:178–186, 2001. (cited on page 111).
- [163] A. G. Basden, C. A. Haniff, and C. D. Mackay. Photon counting strategies with low-light-level CCDs. *Monthly Notices Of The Royal Astronomical Society*, 345(3):985–991, November 2003. (cited on pages 112, 118).
- [164] J. R. Janesick. *Scientific Charge-Coupled Devices*. SPIE Press, 2001. (cited on pages 113, 114, 116).

- [165] S. Tulloch. Investigation into L3 CCD performance [online] <http://www.ing.iac.es/~smt/publications/Publications.htm>. Technical Report 128, University of Durham & ING, August 2003. (cited on pages 114, 120).
- [166] S. Tulloch. Photon counting and fast photometry with L3 CCDs. *Ground-Based Instrumentation For Astronomy, Pts 1-3*, 5492:604–614, 2004. (cited on page 114).
- [167] S. Tulloch. Introduction to EMCCDs [online] <http://www.qucam.com/>. Technical report, QUCAM, June 2009. (cited on page 114).
- [168] M. S. Robbins and B. J. Hadwen. The noise performance of electron multiplying charge-coupled devices. *IEEE Transactions On Electron Devices*, 50(5):1227–1232, May 2003. (cited on page 115).
- [169] G. C. Holst. *CCD Arrays, Cameras and Displays*. SPIE Optical Engineering Press, 1996. (cited on pages 116, 117).
- [170] Andor. Andor technology learning centre. [online] <http://www.andor.com/learning/>, December 2009. (cited on pages 117, 121, 136).
- [171] R. N. Tubbs. *Lucky Exposures: Diffraction-limited astronomical imaging through the atmosphere*. PhD thesis, University of Cambridge, 2009. (cited on page 118).
- [172] Andor. *iXon+ DU-897BI Performance Sheet*. Andor Technology, February 2008. (cited on pages 119, 135, 138, 141, 142).
- [173] J.-Å. Larsson. No information flow using statistical fluctuations and quantum cryptography. *Physical Review A*, 69(4):042317, April 2004. (cited on page 137).
- [174] Andor. *iXon Users Guide (version 3.6)*. Andor Technology, 2007. (cited on page 138).
- [175] Andor. *iXon+ DU-897BI Specification Sheet*. Andor Technology, 4 edition, February 2008. (cited on page 143).
- [176] Andor. *iXon^{em}+ back-illuminated EMCCDs*. Technical report, October 2009. (cited on page 166).
- [177] J. P. Crooks, S. E. Bohndiek, C. D. Arvanitis, R. Speller, H. XingLiang, E. G. Villani, M. Towrie, and R. Turchetta. A CMOS image sensor with in-pixel ADC, timestamp, and sparse readout. *IEEE Sensors Journal*, 9(1-2):20–28, January 2009. (cited on page 171).
- [178] K. Ito, B. Tongprasit, and T. Shibata. A computational digital pixel sensor featuring block-readout architecture for on-chip image processing. *IEEE transactions on circuits and systems I— regular papers*, 56(1):114–123, January 2009. (cited on page 171).
- [179] C. Coates, B. Fowler, and G. Holst. sCMOS: Scientific CMOS technology, a high-performance imaging breakthrough. White paper, Andor Technology, Fairchild Imaging and PCO AG, June 2009. (cited on page 171).
- [180] M. Almendros, J. Huwer, N. Piro, F. Rohde, C. Schuck, M. Hennrich, F. Dubin, and J. Eschner. Bandwidth-tunable single-photon source in an ion-trap quantum network. *Physical Review Letters*, 103(21):213601, November 2009. (cited on page 175).

- [181] E. W. Streed, B. G. Norton, J. J. Chapman, and D. Kielpinski. Scalable, efficient ion-photon coupling with phase Fresnel lenses for large-scale quantum computing. *Quantum Information & Computation*, 9(3-4):203–214, March 2009. (cited on pages 175, 177).
- [182] A. P. VanDevender, Y. Colombe, J. Amini, D. Leibfried, and D. J. Wineland. Efficient fiber optic detection of trapped ion fluorescence. *arXiv:1004.0668v1 [quant-ph]*, 2010. (cited on page 177).
- [183] M. Wilzbach, A. Haase, M. Schwarz, D. Heine, K. Wicker, X. Liu, K. H. Brenner, S. Groth, T. Fernholz, B. Hessmo, and J. Schmiedmayer. Detecting neutral atoms on an atom chip. *Fortschritte Der Physik—Progress Of Physics*, 54(8-10):746–764, August 2006. (cited on page 178).
- [184] R. J. Hendricks, J. L. Sorensen, C. Champenois, M. Knoop, and M. Drewsen. Doppler cooling of calcium ions using a dipole-forbidden transition. *Physical Review A*, 77(2):021401, February 2008. (cited on page 179).
- [185] A. G. Sinclair, M. A. Wilson, and P. Gill. Improved three-dimensional control of a single strontium ion in an endcap trap. *Optics Communications*, 190(1-6):193–203, April 2001. (cited on page 180).
- [186] V. Letchumanan, M. A. Wilson, P. Gill, and A. G. Sinclair. Lifetime measurement of the metastable $4d\ ^2D_{5/2}$ state in $^{88}\text{Sr}^+$ using a single trapped ion. *Physical Review A*, 72(1):012509, July 2005. (cited on page 180).
- [187] N. Kurz, M. R. Dietrich, G. Shu, R. Bowler, J. Salacka, V. Mirgon, and B. B. Blinov. Measurement of the branching ratio in the $6P_{3/2}$ decay of Ba(II) with a single trapped ion. *Physical Review A*, 77(6):060501, June 2008. (cited on page 180).
- [188] C. Y. Lu, Y. Zhao, A. N. Vamivakas, C. Matthiesen, S. Falt, A. Badolato, and M. Atature. Direct measurement of spin dynamics in InAs/GaAs quantum dots using time-resolved resonance fluorescence. *Physical Review B*, 81(3):035332, January 2010. (cited on page 186).
- [189] M. A. Nielsen. Quantum computation by measurement and quantum memory. *Physics Letters A*, 308(2-3):96–100, February 2003. (cited on page 186).
- [190] H. J. Briegel, D. E. Browne, W. Dür, R. Raussendorf, and M. Van den Nest. Measurement-based quantum computation. *Nature Physics*, 5(1):19–26, January 2009. (cited on page 187).
- [191] W. Dür and H. J. Briegel. Entanglement purification and quantum error correction. *Reports On Progress In Physics*, 70(8):1381–1424, August 2007. (cited on page 187).